An Exploration of the Effect of Temperature on Different Alloys in a Supercritical Carbon Dioxide Environment

by

Michael William Dunlevy

B.S. Chemical Engineering
University of Massachusetts Lowell, 2007

SUBMITTED TO THE DEPARTMENT OF NUCLEAR SCIENCE AND ENGINEERING IN PARTIAL FULFILLMENT OF THE REQUIREMENTS FOR THE DEGREE OF
MASTER OF SCIENCE IN NUCLEAR SCIENCE AND ENGINEERING
AT THE
MASSACHUSETTS INSTITUTE OF TECHNOLOGY

SEPTEMBER 2009

Signature of Author: _____
// Department of Nuclear Science and Engineering
August 14, 2009

Certified by: _____
Ronald G. Ballinger
Professor of Nuclear Science and Engineering and Materials Science and Engineering
Thesis Supervisor

Certified by: _____
Thomas J. McKrell
Research Scientist
Thesis Reader

Accepted by: _____
Jacquelyn C. Yanch
Professor of Nuclear Science and Engineering
Chair, Department Committee on Graduate Students

This page intentionally left blank

An Exploration of the Effect of Temperature on Different Alloys in a Supercritical Carbon Dioxide Environment

By

Michael William Dunlevy

Submitted to the Department of Nuclear Science & Engineering
on August 14, 2009 in Partial Fulfillment of the
Requirements for the Degree of Master of Science in
Nuclear Science and Engineering

Abstract

In the constant effort to increase efficiency, safety margins, and lower cost, a new breed of nuclear reactors, Generation IV, is being developed in which supercritical carbon dioxide (SCO_2) is a prime coolant candidate. SCO_2 allows for higher efficiencies, reduced pumping power, lower plant temperature, and more compactness compared to the other gas coolants currently being examined. However, limited corrosion data currently exists for materials that are potential pressure boundary candidates under high pressures and temperatures in SCO_2 environments. The goal of this investigation was to understand the effect of temperature on corrosion on potential structural materials in a SCO_2 environment

A total of 7 different alloys, 6 nickel based and 1 austenitic stainless steel (AUSS), were examined in three sets of experiments. The experiments exposed the specimens to SCO_2 at temperatures ranging from 650 °C to 750 °C, pressures from 12.5 to 20 MPa, and for durations of up to 1000 hours. The nickel based alloys demonstrated very promising results as the weight gain rates were almost an order of magnitude lower than the stainless steel. The average nickel based sample exposed to SCO_2 at a temperature of 750 °C and a pressure of 12.5 MPa showed a weight gain rate of 0.0063 mg/cm^2*day, while the stainless steel sample had a weight gain rate of 0.096 mg/cm^2*day after a duration of 1000 hours. This was expected as the combination of nickel and chromium forms a higher integrity and more stable passive film than iron and chromium. Additionally, nickel has a lower oxygen affinity than iron and therefore the migration of cations into the scale is lower. The chromium content for the AUSS 316L was also the lowest, which most likely contributed to the high oxidation rates.

The tests conducted at 750 °C and 12.5 MPa showed the highest weight gain rates for the nickel based alloys, which was expected as the corrosion rate should follow an Arrhenius trend. The effect of pressure was small compared to the effect of temperature as a 43% reduction in pressure and a 5% increase in temperature produced significantly higher corrosion rates in the nickel based alloys. The AUSS 316L, behaved counter-intuitively as the highest temperature experiment, 750 °C and 12.5 MPa, had the lowest weight gain rate. This behavior may be explained by the increase in temperature, which caused an increase in the diffusion rate within the alloy. This facilitated a faster growth rate of an inner "healing" layer composed of chromium rich oxide, which may have restricted the outward diffusion of cations and inward diffusion of anions.

Thesis Supervisor: Ronald G. Ballinger, PhD
Title: Professor of Nuclear Science and Engineering and Materials Science and Engineering

Thesis Reader: Thomas J. McKrell, PhD
Title: Research Scientist, Nuclear Science & Engineering

Acknowledgements

I would like to thank Professor Ballinger for his academic support, encouragement, and valuable insight. I would also like to thank Dr. Thomas McKrell for his extraordinary patience, understanding, and direction in helping me deal with all of the irregularities involved with the research process and showing me that each challenge was a new opportunity to learn and grow.

I am also appreciative of my labmates: Michael Short, Jon Gibbs, Tim Lucas, Julian Benz, and Joseph Hubley for the many late nights spent "researching" at the various establishments around Boston and for their help in the laboratory. I would like to thank Tatiana Kish as well for her dedicated research assistance. Narine Malkhasyan also deserves my gratitude for her moral support and proof reading prowess; without her encouragement I would not be where I am today.

Finally, I would like to thank the Defense Nuclear Facilities Safety Board for both their moral and financial support throughout my studies at MIT.

Table of Contents

List of Figures

List of Tables

1. Introduction

As the world's energy demand continues to increase, new energy sources are required. Nuclear energy accounts for about 14% of the world's energy supply, and will become even more vital as an energy source in a carbon constrained energy market (1). In the constant effort to increase efficiency, safety margins, and lower cost, a new breed of nuclear reactors, Generation IV, is being developed. Currently, there are at least six designs for generation IV reactors, for some of which supercritical carbon dioxide (SCO_2) is a prime coolant candidate (2). By utilizing the sudden property changes of carbon dioxide near its critical point (31.1 °C and 7.38 MPa), the compression work can be reduced due to the significant increase in density. This in turn allows for higher efficiencies, reduced pumping power, lower plant temperature, and more compactness compared to the other gas coolants currently being examined (3). However, limited corrosion data currently exists for materials that are potential pressure boundary candidates under high pressures and temperatures in SCO_2 environments (4).

Although gaseous carbon dioxide was used as a coolant in the British advanced gas reactors (AGR), little material performance data exists for materials in a SCO_2 environment at temperatures proposed for the Generation IV designs (4) (5). Therefore corrosion of structural materials in this pressure and temperature regime may be a serious concern and more information is needed in order to determine material suitability under these conditions. The purpose of this thesis was to investigate the effect of temperature on corrosion of potential structural and pressure boundary materials in a SCO_2 environment.

1.1 Advantages and Disadvantages

The use of SCO_2 as a coolant in Generation IV gas cooled fast reactors (GFR) has significant advantages over other potential coolants. The most important of these is the achievement of higher efficiency at lower temperatures than would be required for other coolant gases, such as helium. Additionally, the overall plant layout for a SCO_2 cooled GFR will be more compact due to smaller size requirements for turbomachinery, as a result of high fluid and power densities for SCO_2. The temperatures and pressures that are being investigated for these reactors range from 550 °C to 850 °C and 20 to 25 MPa. A temperature of at least 800 °C is needed for helium to achieve the same thermal efficiency of 46%, which SCO_2 achieves at

550 °C. However there is a trade off: higher pressures are required for SCO_2 use compared to helium, 20 MPa vs. 8 MPa (6). This disadvantage is countered by the fact that very few structural metals retain their mechanical properties at temperatures above 550 °C.

2. Background

Corrosion can be a direct cause in the failure of equipment and structural components; therefore it is imperative to understand the thermodynamics behind the various corrosion reactions and how different alloys are affected by corrosion.

2.1 Ellingham Diagram

An Ellingham diagram is a plot of the change in Gibbs free energy versus temperature for reactions between a metal and an oxidizing environment, which can be used to determine the ease of reducing or oxidizing a given metal. Whether a metal is oxidized or reduced is dependent upon the operating oxygen or carbon monoxide partial pressure. If the temperature is known, the Ellingham diagram can be used to determine the equilibrium oxygen or carbon monoxide concentration for the metal's redox reaction. If the concentration of oxygen or carbon monoxide is greater than the equilibrium concentration, the redox reaction is driven towards the oxidation of the metal, and if it is lower, the oxide on the metal is reduced. The metals that have the least negative Gibbs free energy (the top of the diagram) are the most noble (gold, silver, platinum) and therefore the oxide is the least stable and is easily reduced. The more negative the Gibbs free energy of the metal, the more thermodynamically stable the oxide is and the harder it is to reduce. The diagram illustrates which oxides are more thermodynamically stable, but no information about the kinetics or integrity of the oxide can be ascertained from the Ellingham diagram. It is the integrity of the oxide that dictates whether metal loss will occur or not. For example, if a dense and well bonded oxide forms, it will act as a barrier to further metal loss, but if the oxide has low integrity (spallation), significant metal loss can occur. Typically as temperature and partial pressure of oxygen or carbon monoxide increases, the overall oxide stability decreases (7). Figure 1 illustrates an Ellingham diagram with the relevant reactions for this testing regime circled in red.

According to the Ellingham diagram, at 700°C the carbon monoxide dissociation reaction:

$$2C + O_2 \Leftrightarrow 2CO \quad [1]$$

becomes more favorable than the carbon dioxide dissociation reaction.

$$C + O_2 \Leftrightarrow CO_2 \quad [2]$$

Both of the above reactions are capable of causing the reduction of Ni, Fe, and Co oxides if there is free carbon in the material. The addition of the carbon monoxide dissociation reaction is undesirable as it may aggravate the reduction of Ni or Fe based protective oxide scales, causing spallation, and may also add another potential oxidation reaction. However, this should not be a problem for chromium oxides as they are not reduced by the carbon monoxide dissociation reaction until temperatures rise considerably above 1000 °C, well beyond the scope of this test. Since many of the materials being considered for SCO_2 service contain many, if not all, of the above elements, it is important to understand the effect of temperature on the corrosion behavior of these materials over the temperature range 600-800 °C.

Ellingham Diagrams

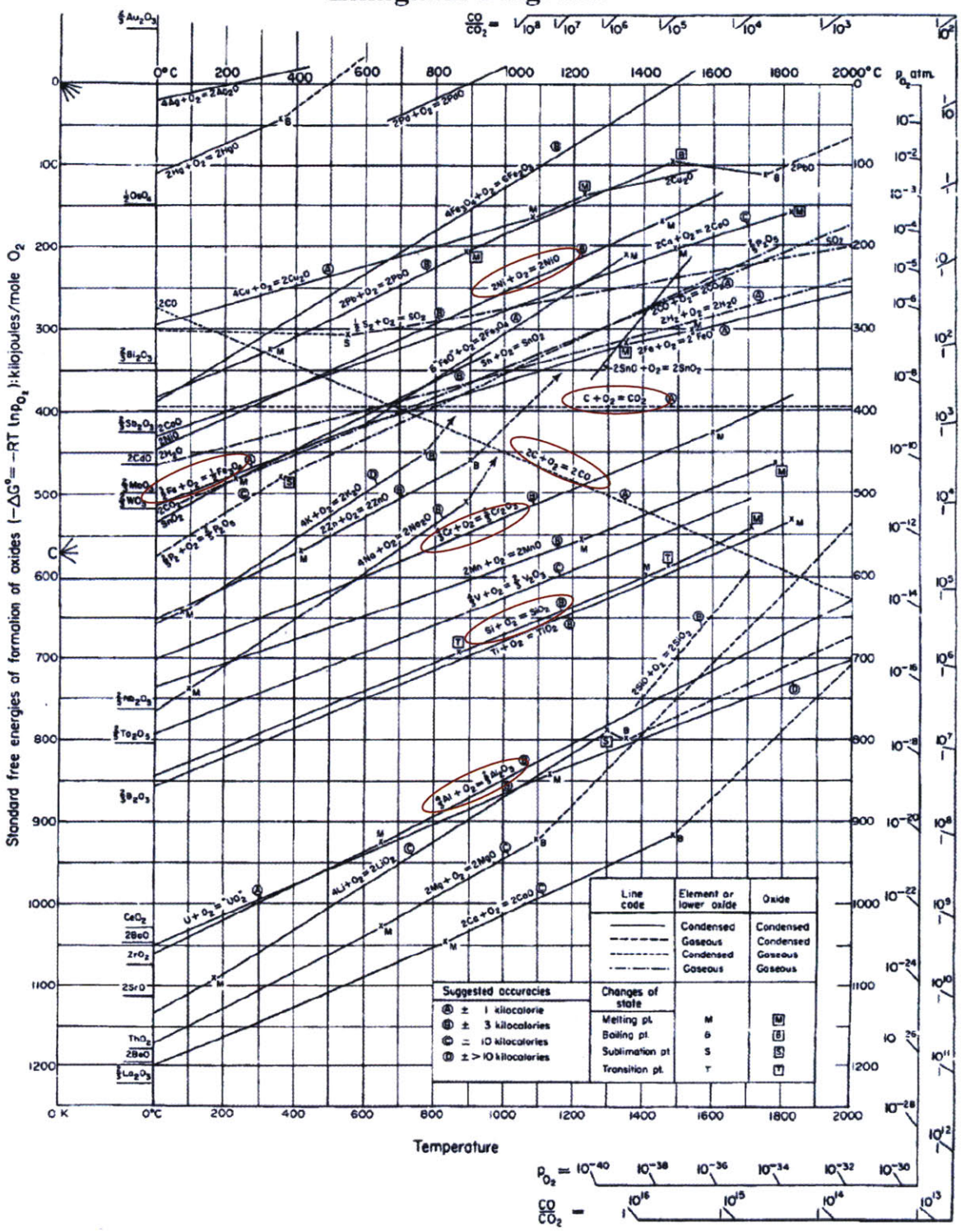

Figure 1: Ellingham Diagram (7)

2.2 Oxidation

Oxidation corrosion is a significant concern for materials in high temperature and pressure environments. There are two types of oxidation scales that can form on metals: protective and non-protective (breakaway). Protective oxide formation on metals is beneficial as it slows the inward diffusion of atmospheric species across the scale and the outward diffusion of metal cations (8) (9). Generally, the adherence of the oxide film depends on the density difference between the oxide and metal. In addition, for SCO_2 corrosion, the protective oxide layer is sustained as long as the underlying metal has the ability to absorb the carbon produced by the reduction of CO_2 and CO. If the underlying metal becomes saturated with carbides, a more porous and fractured layer of oxide, breakaway oxide, can form at the oxide-metal interface. The carbon produced during breakaway oxidation is absorbed into the scale, which destroys adherence and increases the porosity. This allows for rapid CO_2 access to the base of the scale (8). In this case, diffusion of cations and anions across the scale is no longer hindered by a protective oxide. Breakaway can also occur if the chromium content beneath the oxide layer becomes depleted and is not sufficient to maintain the formation of the protective Cr_2O_3 layer (10). Breakaway causes a non-protective oxide film to grow at a linear rate, which significantly increases the weight gain. Figure 2 illustrates that protective oxidation has a high initial weight gain then levels off, while breakaway has a continuous linear weight gain. Breakaway oxidation is undesirable as it can lead to the loss of cross-sectional area for load bearing components, as well as cause moving components to seize, mechanical failure, and spallation (8). This phenomenon has been discovered in the past on some ferritic steels used in the British advance gas reactors (AGR) cooled with gaseous CO_2 (10) (11).

The time to reach breakaway oxidation depends on the following: temperature, H_2O and CO concentrations, silicon content, surface area to volume ratio, and surface geometry (8). As there are four oxidizing surfaces on the corners, three on the edges, and one on the planar surface, corrosion at the edges and corners of materials are a concern as they oxidize more rapidly than the planar surface (8).

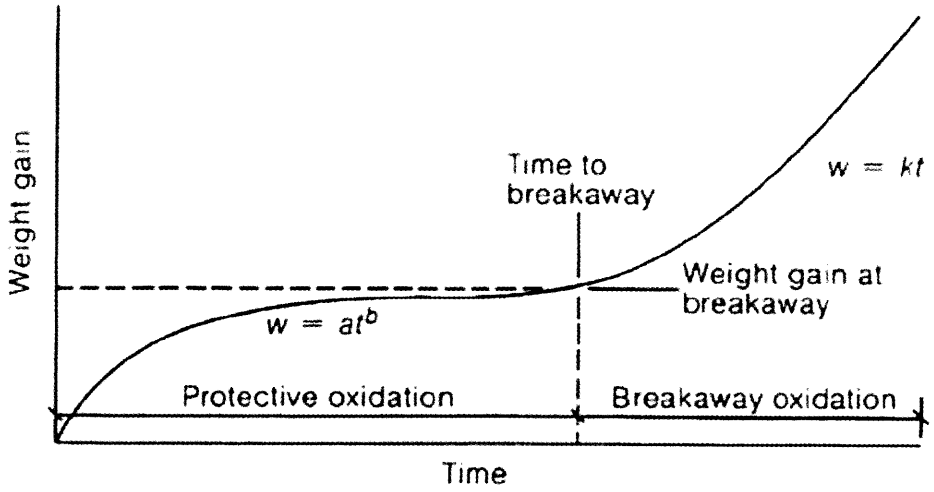

Figure 2: Protective Oxidation versus Breakaway Oxidation (12)

In order to achieve a protective oxide the following characteristics are desirable: 1) resistance to oxygen and metal ion transport across the oxide and into the bulk interface, 2) free from imperfections (pores, cracks, and other short circuit transport paths), 3) free from thermal stresses at the desired operating temperature, 4) adherent in order to resist spallation, 5) high melting point, 6) low vapor pressure to resist sublimation, 7) similar thermal expansion coefficients compared to the bulk matrix to prevent oxide cracking, and 8) having Pilling-Bedworth ratio (PB ratio) greater than 1 (9) (13).

The PB ratio correlates the porosity of a metal oxide with the specific density. The PB ratio of a metal oxide is defined as the ratio of the volume of metal oxide produced, to the consumed metal volume as shown in equation 3. Typically PB ratios greater than 1 are adherent and protective due to the formation of a moderate compressive stress in the oxide. However, ratios that are excessively large have a high compressive stress which can lead to spallation and buckling of the oxide. Metal oxides that have PB ratios lower than 1 tend to form a tensile stress within the oxide and are porous and non-protective (9). The oxides of interest for this testing regime all have PB ratios greater than 1: 2.02 for Cr_2O_3, 2.15 for SiO_2, 1.28 for Al_2O_3, and 2.10 for Fe_3O_4. However, oxides that react at the atmosphere/oxide interface may not necessarily introduce a compressive stress within the oxide, which therefore invalidates the PB-ratio predictions (9).

$$\text{PB Ratio} = \frac{\text{Volume of Oxide Produced}}{\text{Volume of Metal Consumed}} = \frac{Wd}{nDw} \quad [3]$$

W= Molecular weight of the metal oxide

d= Density of the pure metal

n= Number of metal atoms in the oxide

D= Density of the metal oxide

w=Atomic weight of the pure metal

Generally, oxidation is responsible for the loss of resistance to creep, stress rupture strength, and thermal cycling fatigue. Thermal cycling fatigue and creep can cause protective oxide spallation, which may significantly accelerate the corrosion process (13). Three main types of oxide scales can form on the nickel alloys being used in this testing regime: chromia, alumina, and silica scales. These scales are generally reliable, adherent, and protective, depending on the density difference between the oxide and metal. Additionally, the iron based alloy that was used, austenitic stainless steel (AUSS) 316L, can form either iron scales, chromia scales, or an iron-chromia spinel.

2.2.1 Chromia Oxide

A continuous chromia oxide layer is one of the more protective oxides; the scale is dense, adherent, resistant to oxygen and metal ion transport across the oxide, and stable up to about 900 °C. At temperatures above 900 °C the chromium scale becomes volatile as it reacts with oxygen to form CrO_3.

In order to form a continuous protective chromium oxide film, typically an alloy needs to have at least 12 wt % chromium (9). In alloys with lower chromium content, a continuous Cr_2O_3 oxide layer generally does not form due to insufficient chromium content. The chromium can also react with the carbon present in the alloy's matrix, or carbon deposited during the oxidation

reaction to form carbides. The carbides deplete the bulk matrix of chromium preventing the formation of a continuous Cr_2O_3 scale (14).

In nickel-chromium alloys with greater than 12% Cr content, chromia oxide scale grows in stages. Initially, both nickel and chromium are oxidized at the metal environment interface. The nickel oxide, NiO, forms at a faster rate and forms the first complete external scale. However, NiO has a high dissociation pressure causing oxygen to be supplied at a high enough potential to react with elemental nickel and chromium causing the formation of chromia oxide or spinel ($NiCr_2O_4$) at the alloy oxide interface. At this point there is insufficient chromium content at the oxide/metal interface to form a continuous oxide layer. An internal oxidation front then penetrates the alloy, which creates further oxidation at the alloy scale interface. Eventually, chromium metal diffuses, mostly through the grain boundaries, to the metal scale interface to form a more complete chromia scale. The internal oxidation front aids chromium diffusion that extends the protective chromia scale in a stepwise manner. Finally a complete chromia layer is formed by the growth of the stepwise terraces (13). As the Cr_2O_3 scale grows chromium is removed from the base alloy causing a chromium depleted zone. Eventually the subsurface chromium can get depleted to the point where there is not enough chromium present to heal the protective Cr_2O_3 layer.

The rate of formation of the chromia oxide is dependent on the following: 1) external oxygen and internal cation flux through the scale and surface region, 2) the alloy's interdiffusion coefficient, 3) the chromium concentration gradient, 4) oxygen concentration, and 5) grain size, which becomes less important at a higher chromium concentration (13). Once a continuous scale is formed the subsequent oxidation rate is determined by the scales effectiveness as a barrier to inward diffusion of oxygen and other corrodents, and the outward diffusion of metal ions (15). Generally, the oxidation rate follows a parabolic trend as demonstrated in Figure 2 by the protective oxidation line.

2.2.2 Alumina Oxide

For alloys with 15% chromium content or higher it generally takes at least 3-4% aluminum to form a complete alumina scale and the amount of aluminum content needed to form a complete oxide generally decreases with increasing chromium content (13) (16). The mechanism for alumina oxide formation is similar to that of chromium; however less base metal

oxide is observed on the surface, which may be attributed to chromium acting as an oxygen scavenger preventing oxygen diffusion into the alloy (13) (17). The growth rate of the alumina scale is roughly an order of magnitude slower than that of the chromia scale. This causes the continuous chromia oxide layer to form first at the surface. Eventually, as oxygen diffuses through the external chromia oxide scale an internal Al_2O_3 oxide may form at the Cr_2O_3/base alloy interface (16). Alloys that lack sufficient aluminum content to form a continuous protective alumina oxide are prone to internal oxidation at the grain boundaries close to the alloy/scale interface.

2.2.3 Silica Oxide

Silica is thermodynamically more stable than chromia and tends to form beneath or at the alloy/chromia interface (18). Typically 4 - 7 wt % silicon is needed in an alloy in order to form a continuous amorphous SiO_2 layer. However, the continuous layers easily develop imperfections and enable the transport of the base metal cations to the surface (19). Even 0.05% silicon is sufficient to form a partial-healing layer of SiO_2 underneath the external scale (18). The underlying silica oxide layer is slow to develop compared to both the alumina and chromia scales due to a slower rate of diffusivity and the limited population density of internal silica precipitates (13). This internal silica layer can play a paramount role in oxidation reduction because it can limit diffusing cations and anions to and from the surface and due to its structure can aid the formation of the external chromia layer (20). However, some studies have shown decreased adherence of scales causing spallation in chromium-iron-nickel stainless steels with greater than 0.95 wt% silicon in CO_2 atmospheres (21).

2.2.4 Iron Oxide

The iron oxide that is likely to form on the AUSS 316L in SCO_2 at temperatures above 500 °C is magnetite, Fe_3O_4 (8). Magnetite is one of the least thermodynamically stable oxides, having a Gibbs free energy of roughly -210 kJ/mole O_2 (chromia and silica oxide have Gibbs free energies of roughly -580 kJ/mole O_2 and -740 kJ/mole O_2 respectively) (7). Magnetite also forms a lower integrity protective film than chromia oxide which makes it is easier for metal cations and atmospheric anions to diffuse through the scale. Additionally, the incorporation of carbon into the magnetite scale decreases scale adherence and can lead to breakaway oxidation

(4). Spallation of the film on cold-worked surfaces can also be a problem at temperatures greater than 650°C.

2.3 Oxidation Resistance

A number of rare earth elements, reactive elements (RE), such as yttrium, hafnium, and zirconium can be added to the alloy in order to improve oxidation resistance and mechanical properties. The improvement is caused by two effects: 1) the adhesion of chromia (not alumina) scales is improved, which increases the alloy's resistance to thermal cycling exposure and 2) the oxide growth rate may be inhibited (22) (23).

Many studies have suggested that sulfur plays a detrimental role in alloy scale adhesion, which may be attributed to sulfur segregation to the metal-scale interface (24) (25). However, with the addition of RE the unfavorable role that sulfur plays can be mitigated by either scavenging the sulfur or by some other mechanism. With the addition of RE, sulfur is no longer found to segregate to the metal scale interface (23) (25).

The oxide growth rate is reduced by the addition of RE because the outward diffusion of Cr is inhibited, which is the normal chromia oxide growth path. The RE cations segregate to the Cr_2O_3 grain boundaries, which reduces the Cr flux along the grain boundary. This causes the grain boundary diffusivity of cations to be lower than the grain boundary diffusivity of anions, which controls the oxidation rate (26).

Another way to enhance oxidation resistance is to increase the content of nickel and decrease the content of iron in alloys, as nickel has a lower oxygen affinity than iron, which results in a lower diffusion of cations into the scale (13). However, in most nickel based alloys, minor concentrations of manganese are present, which negatively influences the oxidation resistance in chromia forming alloys. Mn appears to rapidly diffuse through the chromia scale and form a stable spinel ($MnCr_2O_4$) on the outer surface which thickens with time, increasing the overall oxidation rate (27). Titanium is another alloying element that forms a more thermodynamically stable oxide than chromia. Titanium, like manganese, rapidly diffuses through the chromia oxide and can form an oxide on the outer surface which thickens with time; however the effect is much less substantial than manganese. Table 1 shows a list of different alloying elements used and their major effects. Other factors such as grain size, the degree of

cold work, texture, surface finish, diffusion coefficients, differences in coefficient of expansion between scale and base alloy, and gas solubility can all influence oxidation rates (13).

Table 1: Effects of Alloying Elements in High Temperature Alloys (28)

Alloying Element	Main Feature
Cr	Improves oxidation and carburization resistance, which enhances corrosion resistance.
Si	Improves oxidation, nitriding, sulfidation, and carburization resistance. Acts with Cr to improve high temperature degradation. However, in some environments could cause spallation.
Al	Improves oxidation and sulfidation resistance.
Mo	Improves high temperature strength, creep resistance. Detrimental for oxidation resistance at high temperatures.
W	Behaves similarly to Mo.
Nb	Increases short term creep strength and beneficial in carburizing environments.
C	Improves strength, and is beneficial to carburization resistance. Adversely affects oxidation resistance.
Ti	Improves age hardening strength.
Mn	Positively effects high temperature strength and creep. Detrimental to oxidation resistance. Increases solubility to N.
Co	Reduces rate of sulfur diffusion which increases sulfidation resistance. Improves solid solution strength.
Ni	Improves carburization, nitridation, chlorination resistance, oxidation resistance. Detrimental to sulfidation resistance.
Y + RE	Improves scale adherence and spallation resistance of oxide layers. Improves oxidation, sulfidation, and carburization resistance.

2.4 Material Selection Criteria

Under oxidizing conditions, mild steels are generally employable up to a temperature of 350 °C, ferritic steels up to 550 °C depending on the silicon and reactive element (RE) content in the alloy, austenitic stainless steels up to 700 °C, and nickel based alloys at temperatures greater than 700 °C (8). The projected operating temperature of the SCO_2 cooled GFR is between 550 – 800 °C. Based on the low operating temperature for mild steels, they will not be examined any further.

2.4.1 Ferritic Alloys

Ferritic alloy is a term applied to Fe-Cr steels in which the iron is in the ferrite phase with a body centered cubic structure. The morphology and composition of the oxide typically depends on the chromium content and other minor constituents. For example ferritic steels containing less than 12% chromia typically form a duplex scale, a magnetite (Fe_3O_4) outer oxide with an underlying iron-chromium spinel. Ferritic steels with a chromium composition between 12-20% can either form a duplex spinel oxide or a continuous outer oxide layer of Cr_2O_3. If the Cr composition is greater than 20% only external Cr_2O_3 scale forms. 9% Cr ferritic steels have been studied extensively due to their wide use in a CO_2 environment during the British AGR campaign.

Laboratory tests have shown that 9% Cr with low Si content (0.06 %) steel initially forms a protective oxide at temperatures of 560 °C; after 4000 hours breakaway oxidation occurs (10) (11). Typically the protective external oxide is maintained until the underlying iron-chromium spinel, which acts as a carbon sink, is saturated with carbides causing the oxide to become more porous, which initiates breakaway oxidation. This was a major concern for AGR's as bolts, welds, and other structural materials failed due to breakaway oxidation (5). However, depending on the silicon content, the time to breakaway oxidation can be slowed down or even stopped. Ferritic steels with greater than 0.45 wt % Si showed no signs of breakaway after 30,000 hours at 500 °C (11). Other factors that affect the time to breakaway are temperature, gas composition, specimen geometry, thickness, and surface finish (4).

As the projected life-time of a nuclear power plant is 40 years and utilities want to extend this to 60 years it is very important to have reliable structures, pressure vessels and

turbomachinery. Some ferritic alloys that were potential structural candidates, HT9, F91, and HCM12A (T122), have been examined in a SCO_2 environment at temperatures of 600 °C and 650 °C and a pressure of 20 MPA for times ranging from 500-3,000 hours. These alloys showed significant spallation of the external oxide and oxide growth rates more than 2 orders of magnitude higher than nickel alloys and austenitic stainless steels (3) (29) (30). However, PM2000, a RE stabilized ferritic steel, performed exceptionally well in the supercritical environment, displaying excellent corrosion resistance. Due to the performance data collected previously on ferritic alloys in both gaseous CO_2 and SCO_2 environments, ferritic alloys were not examined in this testing regime (30) (3) (12).

2.4.2 Austenitic Alloys

Austenitic stainless steels (AUSS) is a term applied to Fe-Cr alloys that contain at least 16% Cr, a maximum of 0.15% C, and have a face centered cubic structure. AUSS have a number of beneficial properties including: high temperature strength due to the close-packed structure, which inhibits atomic diffusion required for thermal creep and excellent corrosion resistance (8). The excellent corrosion resistance can be attributed to the protective oxide's low porosity and high density sealing the metal off from the environment. Typically initial oxidation rates of AUSS are high then stabilize out once a complete protective oxide is formed, as Figure 2 illustrates.

Generally Cr_2O_3 oxide forms on the surface, however if the oxide is damaged or if the initial surface nucleation is iron oxide (perhaps due to chromium depletion) a duplex spinel oxide may form. Initially the spinel oxide starts off with a parabolic growth rate much faster than the Cr_2O_3, but over a long period of time the oxidation rates become comparable. This is due to an inner "healing" layer of chromium rich oxide and precipitates, which restrict the outward diffusion of cations. Depending on the silicon content of the AUSS, an underlying thin layer of silica oxide can form as well further promoting healing layer formation. Increasing the temperature increases the rate in which the healing layer is formed due to the increase in diffusion. The rate of healing layer formation is so essential that some studies have shown that the corrosion rate of AUSS at 650 °C was less than at 600 °C and at 550 °C (32). Peak oxidation rates were often observed in the 550-600 °C temperature range as Figure 3 demonstrates (32).

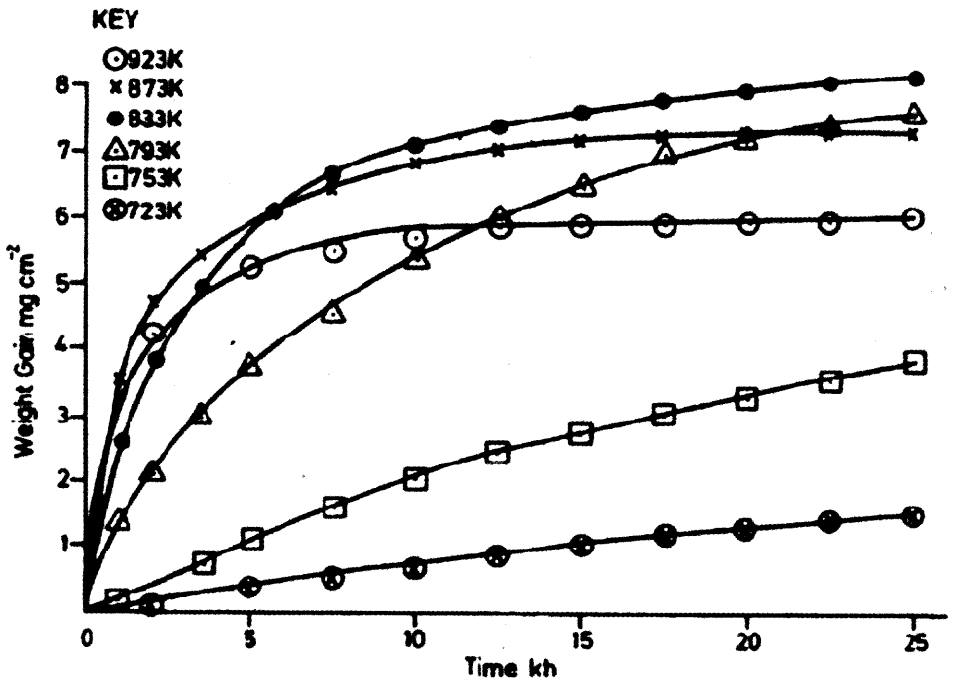

Figure 3: Oxidation of Wrought 321 Steel at Different Temperatures (32)

A number of other factors also affect the rate of healing layer formation, including: grain size, surface finish, amount of cold work on the surface, chromium content, and silicon content. Smaller grain sizes promotes faster healing layer growth (32). Some studies have shown that smaller grain sizes produced full healing layers more than four times faster than larger grain sizes (33). Heavily cold worked surfaces recrystallize at high temperatures, which produces fine grain structures that promotes chromium diffusion and faster healing layer formation (33). However, heavily cold worked surfaces introduce strain, which may lead to spallation.

In CO_2 environments, both oxygen and carbon can be transferred to the AUSS by the following reactions:

$$M + CO_2 \rightarrow MO + CO \quad [4]$$

$$2M + CO_2 \rightarrow 2MO + [C] \quad [5]$$

$$M + CO \rightarrow MO + [C] \quad [6]$$

These reactions can inject carbon into the bulk material forming carbides. Carbides cease to form once a complete healing layer is established. Unlike the ferritic alloys, breakaway oxidation cannot occur through the deposition of carbon in the healing layer. One laboratory

experiment oxidized a thin (100 micron) AUSS foil at 600 °C in a CO_2 environment (32). The experiment exhibited that the carbon injection from reactions 4-6 prevented the healing layer from forming, but the outer protective oxide was maintained and no breakaway oxidation was observed. This demonstrated that under normal operation conditions the deposition of carbon within the oxide to form carbides should not lead to breakaway (32). However, at temperatures greater than 425 °C sensitization may occur in the AUSS causing the formation of chromium carbides at the grain boundary.

Sensitization occurs at the temperature range of 425 °C to 815 °C when chromium reacts with carbon forming insoluble chromium carbides ($Cr_{23}C_6$ or Cr_7C_3) that first precipitate out on the grain boundary. The precipitation of chromium causes the bulk matrix to be depleted of chromium. Without sufficient chromium content in the bulk matrix, a protective oxide may not form causing the alloy to be susceptible to intergranular corrosion. However, if there is either niobium or titanium present in the alloy they will preferentially react with carbon generally preventing sensitization. Sensitization can also occur in nickel based alloys, and ferritic stainless steels, but at higher temperatures (9).

AUSS containing 18% Cr were extensively used as structural materials in the British AGRs and exhibited excellent corrosion resistance, with low lifetime metal loss during service (4). 5% Cr AUSS were also used in the highest temperature regions in the AGRs and showed adequate corrosion resistance. Recent Japanese data has also shown promising results for type 316 AUSS, which was exposed to 600 °C and 10 MPa SCO_2, after 10,000 hours of exposure a total weight gain of $10^{-4}g/cm^2$ was observed (31).

2.4.3 Nickel Based Alloys

Nickel based alloys can withstand some of the harshest environments, temperatures exceeding 650 °C, while still retaining most of its strength. One main reason for nickels excellent performance is its ability to resist oxidation. Nickel has a lower oxygen affinity than iron and therefore the diffusion of cations into the scale is lower, which decreases oxidation rates compared to iron based alloys (34).

Typically nickel based alloys contain greater than 15% Cr and up to 8% Al and Ti. Additionally Co, Mo, W, Ta, Hf, Nb, B, Zr, and C can be added in order to improve strength,

corrosion resistance, and creep resistance. The elemental additions can be classified as γ formers (elements that tend to partition with the bulk γ matrix), γ' formers (elements that partition to the γ' precipitates), carbide formers, and elements that segregate to the grain boundaries (34).

The γ phase for nickel alloys is the continuous bulk matrix and is a face centered cubic (FCC) nickel-based austenitic phase. Typically, alloying elements that are considered γ formers are group V, VI, and VII elements. The atomic diameters for these elements are very similar to nickel, differing only by 3-13% (34).

The γ' phase is the primary strengthening phase of nickel alloys. Aluminum and titanium are the primary constituents of the γ' and are added in amounts to precipitate a high volume fraction, up to 70% in the matrix. This phase has an ordered coherent $L1_2$ crystal structure, which is also FCC, but has a slightly different lattice parameter compared to the bulk matrix. The lattice mismatch between the precipitates and the matrix create coherency strains that impede dislocation migration resulting in precipitation hardening. Additionally, the formations of carbides contribute to strength and high temperature stability (35).

Carbides also tend to form in nickel alloys and generally consist of Group IV or V metals with an FCC crystal structure. Results vary on whether carbides are detrimental or advantageous to the nickel alloy properties. However, the general opinion is that carbides are beneficial by increasing rupture strength at high temperature (34).

Nickel-based alloys offer a number of advantages compared to iron based alloys including oxidation resistance, strength at high temperature, and good low temperature ductility. However, little to no experimental data is reported for nickel based alloys exposed to either gaseous CO_2 or SCO_2. Therefore nickel-based alloys were the focus of this testing regime

2.5 Effect of Pressure

The effect of pressure on corrosion processes for steel is not fully understood. In one experiment it was found that the pressure of CO_2 between 1.96 MPa to 4.14 MPa was independent of oxidation rate for 20Cr-25Ni-Nb steel (8) (36). Other experiments in which the pressure of CO_2 was varied between 1 and 4 MPa showed little change on oxidation rate as well (37). However, another experiment demonstrated that an increase in pressure from 1.48 MPa – 2.85 MPa increased the parabolic weight gain rate constant by roughly 45% (8) (38). Overall, it

seems as if the relative corrosion mechanism stays the same and the oxidation rates are comparable at different pressures (4) (37). However, a few general trends have been noted at higher pressures: increased localized corrosion (pitting), and a higher carbon content on the inner oxide layer (4) (8).

3. Experimental Approach

Based on the extensive research that has been conducted on ferritic and AUSS alloys, the primary focus of this testing regime were nickel based superalloys. Additionally one AUSS alloy, 316L, was used in order to compare the work done in this thesis to previous work using similar exposure conditions.

3.1 Materials

The following seven materials were included in the testing program: AUSS 316L, Inconel 690, 693, 718, 725, 740, and 740+. Alloy 740+ is a modified version of alloy 740 that promotes microstructural stability at temperatures up to 760 °C. All of the Ni-base alloys were supplied by Special Metals, Inc. The chemical compositions of the materials used are provided in Table 2. A total of 16 samples (10 large samples and 6 small samples) of each alloy were machined from the base metal.

Table 2: Composition of Materials Used in Testing Regime

	AUSS 316 L	Inconel 690 (40)	Inconel 693 (40)	Inconel 718 (40)	Inconel 725 (40)	Inconel 740 (40)	Inconel 740+ (40)
C	0.02	<0.05	<0.15	<.08	<0.3	0.041	-
Mn	0.89	<0.050	<1.0	<0.35	<0.35	-	-
Fe	69.57	7.0-11.0	2.5-6.0	11.10-22.50	2.3-14.3	0.75	1.06
S	0.004	<0.015	<0.01	<0.015	<0.010		-
Si	0.65	<0.50	<0.5	<0.35	<0.20	0.132	0.306
Cu	0.35	<0.50	<0.5	<0.30	-	-	-
Ni	10.11	>58.0	53.3-64.3	-	55.0-59.0	48.48	48.93
Ni+Co	-	-	-	50.00-55.00	-	-	-
Co	-	-	-	<1.00	-	20.19	20.01
Cr	16.24	27.0-31.0	27.0-31.0	17.00-21.00	19.0-22.5	25.49	24.37
Al	-	-	2.5-4.0	0.20-0.80	<0.35	1.22	1.35
Ti	-	-	<0.10	0.65-1.15	1.0-1.7	1.11	1.53
Mo	2.12	-	-	2.80-3.30	7.0-9.5	0.075	0.544
Nb	-	-	0.5-2.5	-	2.75-4.0	2.06	1.56
Nb+Ta	-	-	-	4.75-5.50	-	-	-
B	-	-	-	<0.006	-	0.001	-
W	-	0.48	-	-	-	-	-
Zr	-	-	-	-	-	0.003	0.21

3.2 Sample Nomenclature

Figure 4 illustrates the samples nomenclature. The LA represents Los Alamos National Laboratory as they were the technical interface for this research which was sponsored by the United States Department of Energy. The number next to LA represents the series number, which depended on the experiment. Three different experiments were completed and the following series numbers were used: LA1, LA2, and LA3. The LA1 samples were exposed to a temperature and pressure of 714 °C and 20 MPa using the large autoclave, the LA2 samples were exposed to a temperature and pressure of 650 °C and 12.5 MPa using the small autoclave, and the LA3 samples were exposed to a temperature and pressure of 750 °C and 12.5 MPa using the large autoclave. The number immediately following the dash represents the alloy designation number (see Table 3 for a list of alloys) and the final number represents the sample number for the specific alloy. For the LA1 and LA2 series 6 duplicate copies of each alloy were used and only 4 for the LA3 series.

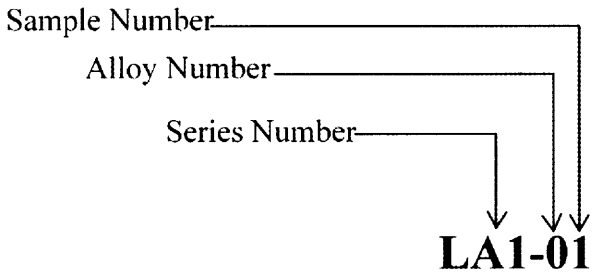

Figure 4: Sample Nomenclature

Table 3: Alloy Designations

Alloy	Alloy Number
Inconel 690	0
Inconel 693	1
Inconel 718 with end grains	2
Inconel 725 with end grains	3
Inconel 740	4
Inconel 740+	5
AUSS 316L	6
Inconel 718 Without end grains	7
Inconel 725 Without end grains	8

3.3 Sample Preparation

Two types of circular samples, "large" and "small, were electro discharged machined (EDM) out of a larger base material. The samples were EDMed perpendicular to the rolling direction with the exception of alloys 718 and 725, which were cut both perpendicular and parallel to the rolling direction. The samples that were cut parallel to the rolling direction were expected to have a higher corrosion rate due to the exposed endgrains and grain boundaries causing a higher concentration of stress and an easier diffusion path, which Figure 5 illustrates. The large samples were roughly 1.76 cm (0.694 in) in diameter with a thickness of 0.043 cm (0.017 in), while the small samples were about 0.55 cm (0.216 in) in diameter with a thickness of about 0.15 mm (0.006 in). A large surface area to volume ratio with a small edge area to total area was desirable, as the edges or other high stress areas of the sample would be preferentially corroded (41). Figure 6 and Figure 7 show photographs of both the large and small samples.

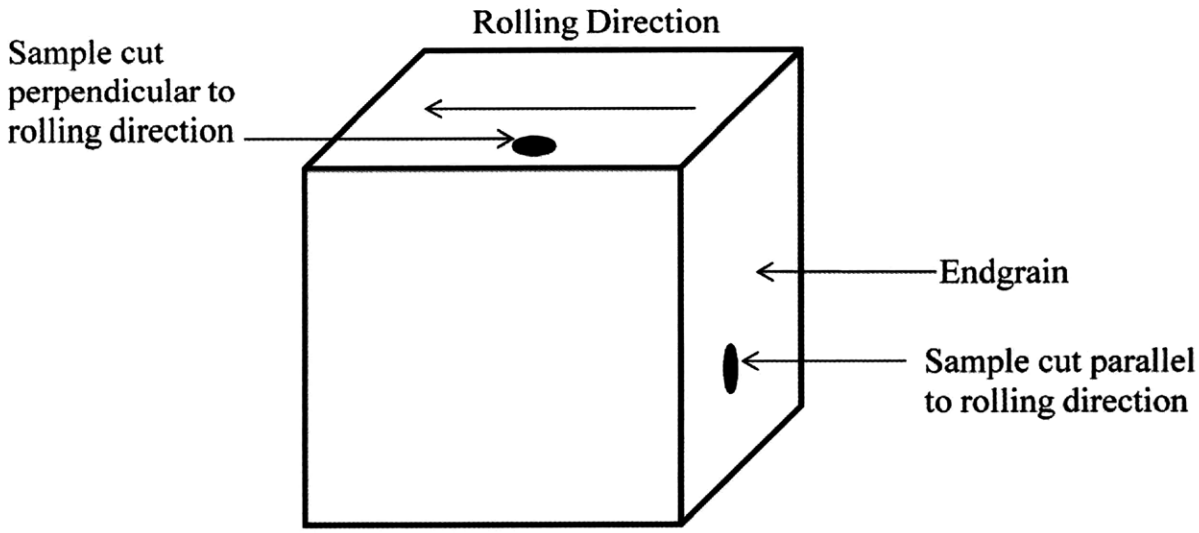

Figure 5: Sample Orientation with Respect to the Rolling Direction

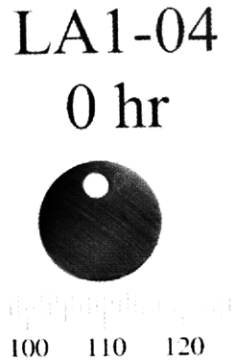

Figure 6: Large Sample

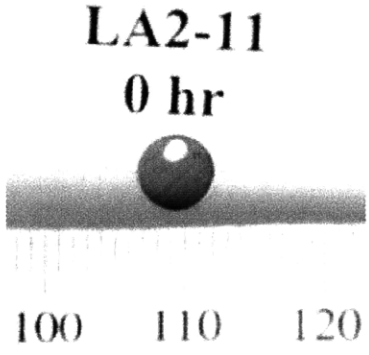

Figure 7: Small Sample

The LA1 and LA2 samples were polished by hand as uniformly as possible using 320 grit sandpaper to remove the oxide that formed from the EDMing process. The samples were then polished with 600 grit sandpaper; 800 grit sandpaper was used for the final surface finish. For the LA3 samples as well as alloys 7 and 8 for the LA2 series, a new polishing technique was used in which the samples were bonded to a circular plate using Crystalbond™ adhesive. The plate was then attached to an Automet 3 Autopolisher and polished using an Ecomett Variable Speed Grinder-Polisher. The following polishing regiment was used with the Autopolisher:

1) 320 grit sandpaper until oxide was removed (typically 30-120 seconds), with a speed of 130 rpm, and a force of 3 lbs per sample
2) 800 grit sandpaper for 5 minutes ,with a speed of 150 rpm, and a force of 4 lbs per sample

This method of polishing led to flatter, more uniform surfaces as the pressure and speed of the polisher was controlled. After the samples were polished, the circular plate to which the samples were bonded was heated up to about 100 °C with acetone in order to remove the Crystalbond™ from the samples.

Once polished, the samples were marked with a unique identification number that was laser etched onto the surface. The numbers that were laser etched onto the large samples had the following dimensions: 2 mm in height, 0.05 mm in depth; and those etched onto the small samples were 0.7 mm in height and had a depth of 0.025 mm. The laser etching was done at a power that was too high for the LA3 series, and alloys 8 and 9 of the LA2 series, which caused plastic deformation of the sample on the opposite side of the number and scorching on roughly one third of the samples. Figure 8 and Figure 9 show photographs of a sample from the LA2 and LA3 series that had plastic deformation occur on the opposite side of the laser etch.

After the samples were laser etched, each sample was ultrasonically cleaned in ethyl alcohol for ten minutes at room temperature. The samples were then immediately rinsed with distilled water, dried, then stored in a desiccator until use. This was done to ensure no moisture from the atmosphere was adsorbed onto the surface.

Figure 8: LA2 Series Sample with Plastic Deformation on the Opposite Side of the Etch

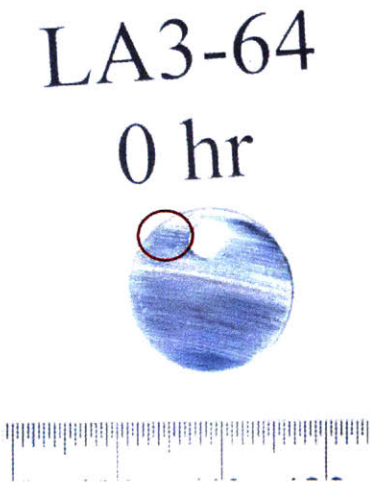

Figure 9: LA3 Series Sample with Plastic Deformation on the Opposite Side of the Etch

3.4 Equipment

3.4.1 Autoclaves

Two high-pressure autoclaves were used concurrently to test the corrosion behavior of a variety of materials (listed in Table 2) in a SCO_2 environment. The "large autoclave" had an internal diameter of 2.5 cm (1 in) and was 152.4 cm (60 in) long. The "small autoclave" had an internal diameter of 1.3 cm (0.5 in) and was 106.7 cm (42 in) long. Both autoclaves were made of Alloy 625; however, the large autoclave had two penetrations, one on each side so both ends

could be opened, while the small autoclave only had one penetration. Figure 10 illustrates that the larger autoclave could withstand a slightly higher pressure and temperature than the smaller one. This plot was generated using the yield strength data for alloy 625 at different temperatures (42) and the formula for circumferential stress in a thick walled cylinder, Equation 7 (43). The large autoclave also had two aluminum heat sinks, in which the purpose was to prevent the overheating of the carbon steel bolt that secured the sealing plug, bolted on each side of the autoclave as shown in Figure 15. The two heat sinks had an inner diameter of 7.6 cm (3 in), an outer diameter of 15.2 cm (6 in), were 12.7 cm (5 in) long, and had 9 fins. The small autoclave had only one aluminum heat sink which had a 3.8 cm (1.5 in) inner diameter, a 14 cm (5.5 in) outer diameter, was 7.6 cm (3 in) long, and had 5 fins.

$$\sigma_c = [(p_i r_i^2 - p_o r_o^2) / (r_o^2 - r_i^2)] - [r_i^2 r_o^2 (p_o - p_i) / r_o^2 (r_o^2 - r_i^2)] \quad [7]$$

σ_c = stress in circumferential direction

p_i = internal pressure in the tube or cylinder

p_o = external pressure in the tube or cylinder

r_i = internal radius of tube or cylinder

r_o = external radius of tube or cylinder

r = radius to point in tube or cylinder wall

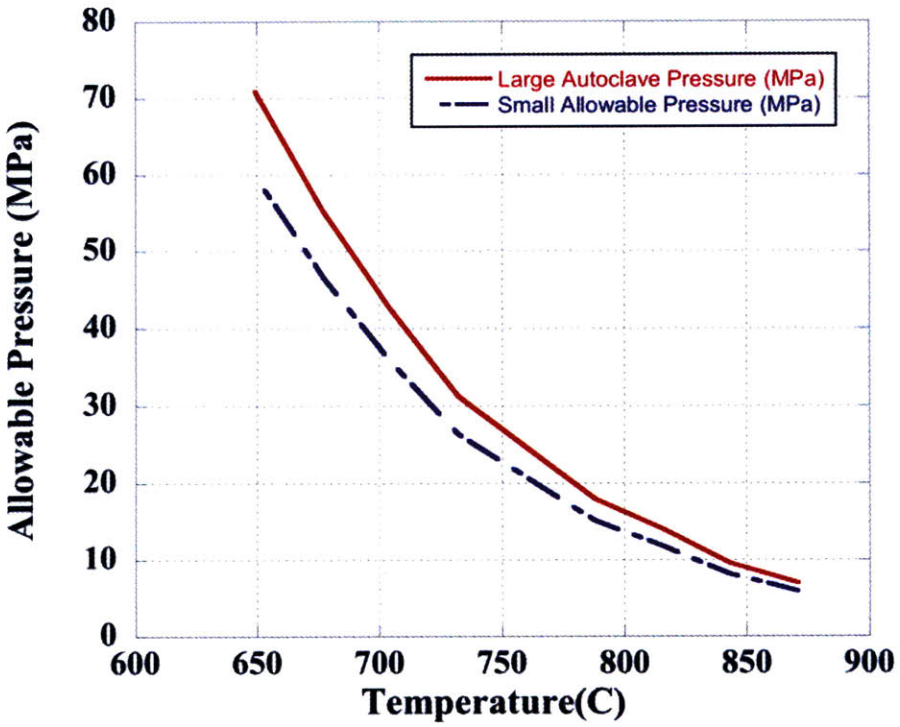

Figure 10: Allowable Pressure vs. Temperature Curve for Both Autoclaves Based on the ASME Code

3.4.2 Furnaces

The large autoclave used a Thermcraft Split Tube Furnace model number TSP-3.75-0-24-3C-J8927/1A with a Watlow 988B-11CD-AARG temperature controller. The small autoclave used a Lindberg Blue Tube Furnace; model number STF55346COMC-1 with built in temperature controllers. Both furnaces had 3 independent heated zones, where the heated lengths were 15.2 cm (6 in) for zone 1, 30.5 cm (12 in) for zone 2, and 15.2 cm (6 in) for zone 3 for a total heated length of 61 cm (24 in). The large autoclave furnace had a power of 5,000 watts, while the small autoclave had a power of 3,830 watts. The furnace controller measurements were obtained from thermocouples located in the center of each zone as Figure 11 demonstrates. As discussed in Section 4.4, Temperature Profiling, the outside temperature measured by the controllers were not representative of the internal temperatures.

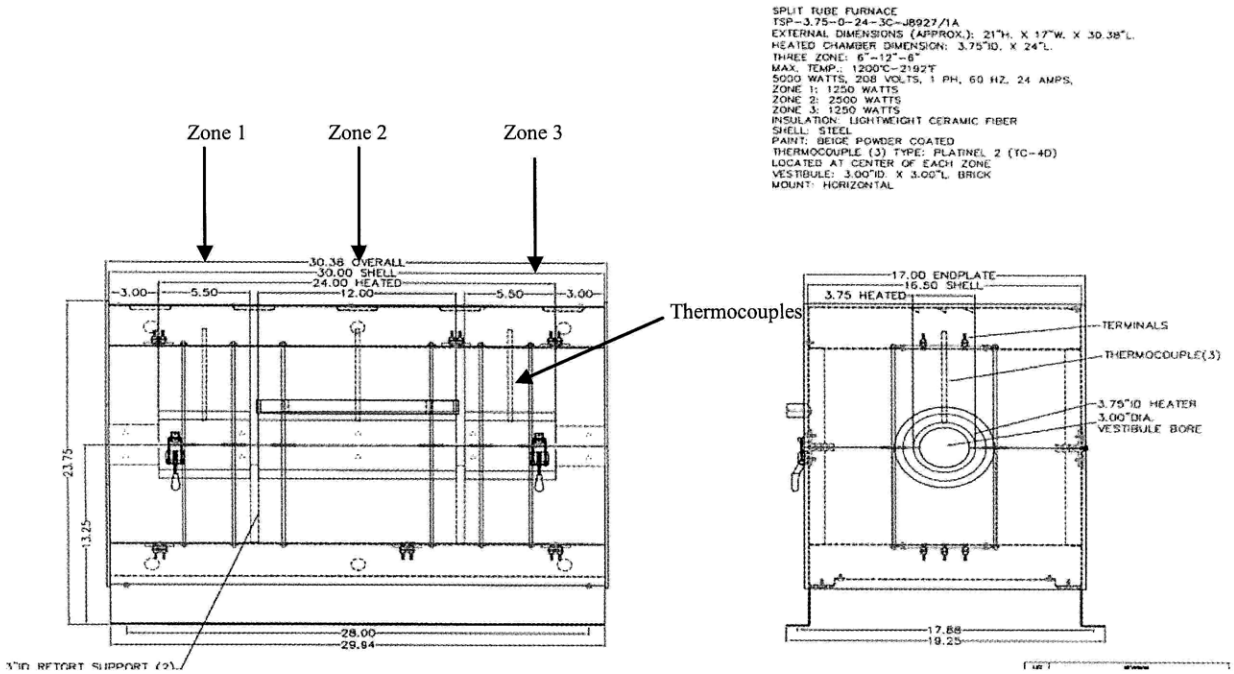

Figure 11: Location of Thermocouples for Thermcraft Furnace Temperature Controllers

3.4.3 Sample Trains

Sample trains were used to suspend the test specimens in the autoclaves.

Table 4 illustrates the sample train dimensions for both autoclaves. The sample train tubes were machined in order to accommodate the rod from which the samples were suspended. Alumina washers were used as spacers between each sample to ensure that the samples did not come in direct contact with each other. Type 316 6.4 mm (0.25 in) stainless steel tubing was used around the large sample train rod in the spaces not occupied by samples. This was done to ensure that the samples would have the same orientation during loading and unloading operations. Figure 12 illustrates the large autoclave sample train with samples loaded and the dummy sample instrumented with a thermocouple.

The small sample train had a slightly different setup than the large autoclave. The surface area of the washers were nearly half that of the test specimens. This caused concerns that if the washers were in direct contact with the samples, the SCO_2 would be shielded from the samples. Therefore the samples and washers were separated in order to prevent this effect from happening as Figure 13 illustrates.

Table 4: Sample Train Dimensions

	Large Autoclave Sample Train	Small Autoclave Sample Train
Tube outer diameter	2.38 cm	0.95cm
Tube length	20.32 cm	30.48 cm
Rod outer diameter	0.33 cm	0.078 cm
Rod length	17.46 cm	27.69 cm
Washer outer diameter	0.56 cm	0.24 cm
Material	99.7% Alumina	99.7% Alumina

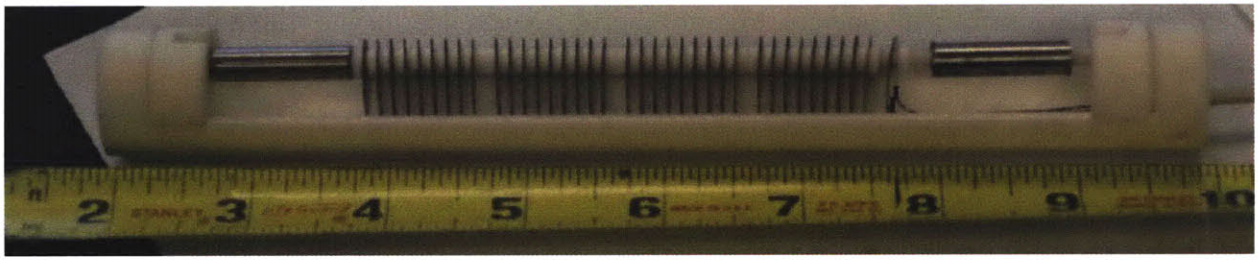

Figure 12: Large Autoclave Loaded Sample Train

Figure 13: Small Autoclave Loaded Sample Train

3.4.4 Data Acquisition

Six K-type thermocouples were spot welded to the large autoclave and four to the small autoclave outer surface. These thermocouples directly produced a voltage and sent the signal to a National Instruments CA-1000 data acquisition system, which interpreted the voltage as a temperature. Additionally, Omega PX605 and PX615 Transducers were used to measure the pressure in the system. The transducers converted the pressure in the system to a current by the physical deformation of a strain gauge, which was bonded to a diaphragm. The strain produced an electrical resistance proportional to the pressure (44). The current was then converted to a

voltage and the signal was sent to the CA-1000 data acquisition system. The CA-1000 interfaced with a Dell Precision 420 computer and the data was read and recorded using a visual basic program.

3.5 Experimental Setup

3.5.1 Large Autoclave Experimental Apparatus

Figure 14 illustrates the line diagram for the experiment, while Figure 15 shows an image of the experimental setup. CO_2 gas, part number CD SFX15A from Airgas, (the purity used was 99.9999% with the following certified contaminants: $H_2O < 250$ ppb, total condensable hydrocarbons < 1 ppb, total halocarbons < 1 ppb) was drawn from one of two gas cylinders (the second cylinder was for redundancy in case the first cylinder emptied during operation) at 4 MPa for the 20 MPa experiments and at 2 MPa for the 12.5 MPa experiments with a flow rate of approximately 320 cm^3/hr. From the cylinder the gas traveled through 6.4 mm (0.25 in) type 316 stainless steel tubing and the stream was then split and went to either a DYCOR LC100m residual gas analyzer (RGA) with a Pfeiffer vacuum system or to a Haskel AGT-15/30 compressed air driven gas booster pump, which increased the pressure to the desired value and brought the CO_2 into the supercritical regime. Both the pump and the tubing following the pump were wrapped in 25 watt Omegalux heating tape in order to prevent the CO_2 gas from liquefying.

The SCO_2 then flowed from the booster pump through a high pressure rupture disk, an Omega PX615 pressure transducer, and through an emergency bleed valve. The CO_2 then traveled into the autoclave which contained the test specimens. The outlet stream from the autoclave was then routed to either a gas bubbler or the RGA. The approximate flow rate of the CO_2 was determined via the gas bubbler. The average bubble rate was 1 bubble every two seconds and the average bubble size was about 0.7 cm. Using the volume of a sphere, the flow rate through the system was calculated to be roughly 320 cm^3/hr

The sampling process for the RGA involved the migration of the various species through a capillary tube from the autoclave. The capillary tube caused the decrease in pressure necessary for operation with the RGA, which is under vacuum. The different molecules and atoms in the system migrated at different rates; thus the arrival rate of species to the sampling system did not necessarily correspond to their concentrations in the autoclave. Additionally, the RGA ionized

the molecules in the autoclave causing the spectra to contain not only signal from species present in the autoclave, but also the decomposition products of these species as well. For example, if there was pure CO_2 in the system the RGA would get a signal peak from both carbon dioxide and its decomposition products: carbon monoxide, carbon, and oxygen even though the decomposition species may not be present in the system. Therefore the RGA gave a qualitative measurement with respect to the concentration in which the inlet and outlet gas compositions can be compared.

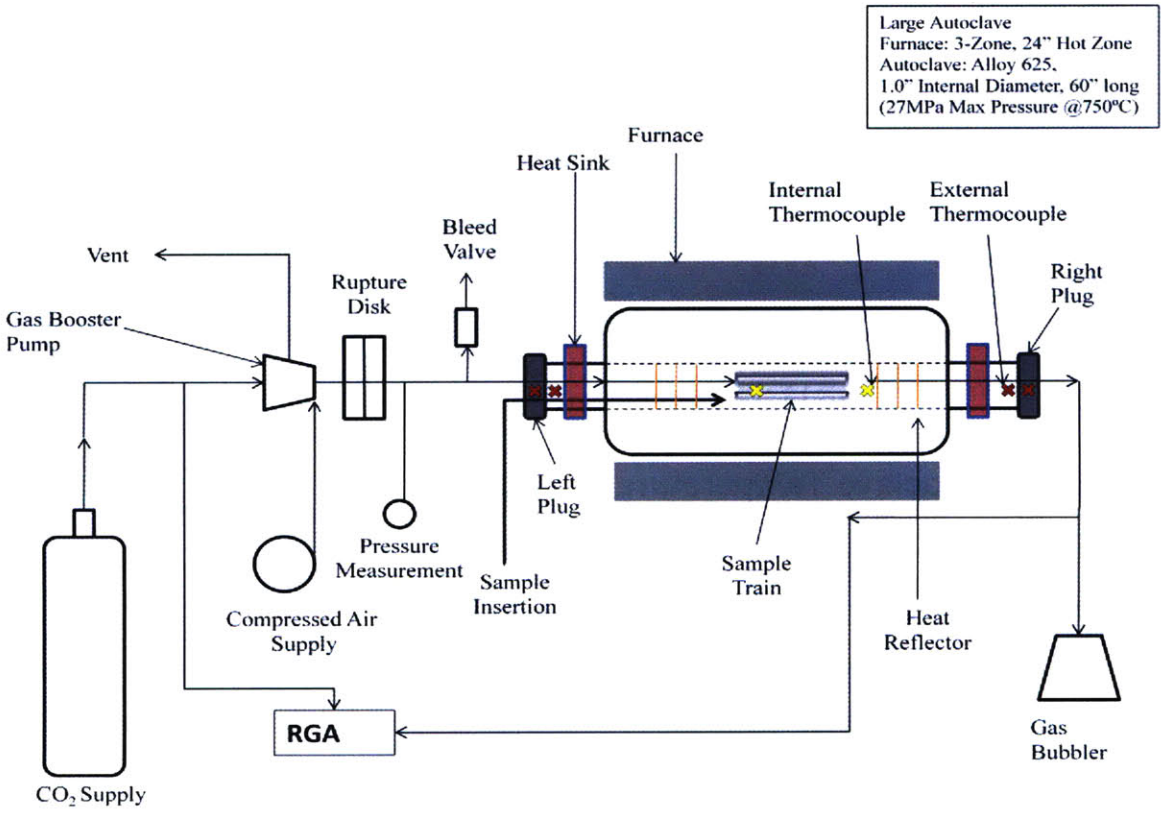

Figure 14: Line Diagram of Large Autoclave Experimental Apparatus

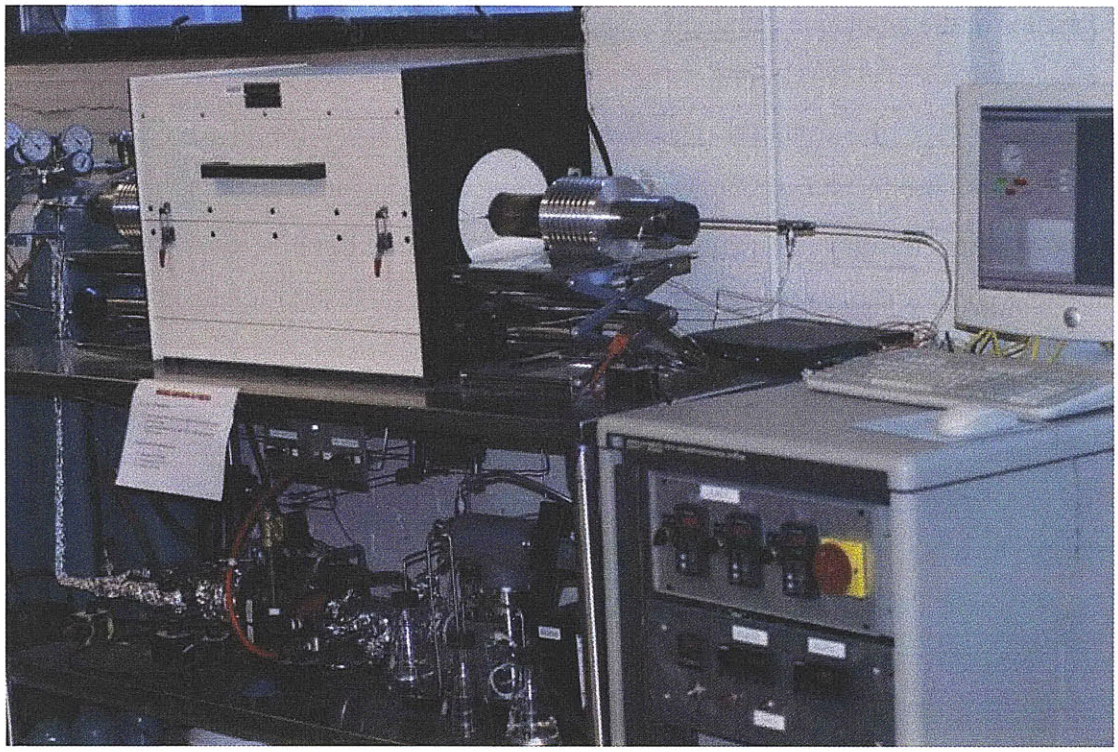

Figure 15: Large Autoclave Experimental Apparatus

3.5.2 Large Autoclave Temperature Measurements

Figure 14 shows the locations of the four external and two internal K-type thermocouples that were used. Two of the external thermocouples were spotwelded on the bolts that secure both sealing plugs, which sealed the large autoclave. The plugs would most likely fail first due to the high stress concentrations in the root of the threads. Therefore it was imperative to limit the maximum temperature of the carbon steel bolts to less than 300 °C, which is lower than the bolts tempering temperature.

Internally a dummy sample was instrumented with K-type 24 gauge bare thermocouple wire. This was achieved by running the wire through a 0.5 mm (0.020 in) Conax MHC2-020-A2-T fitting which created a pressure boundary that separated the outside atmosphere from the internal environment. Once past the fitting the wire then traveled through a 3.2 mm (0.125 in) dual bore 99.7% alumina tube which prevented the two wires from making contact with each other. This ceramic tube was contained inside the 6.4 mm (0.25 in) stainless steel CO_2 inlet tube, which was inside the left plug. The thermocouple wire was then spotwelded to a dummy sample, which was also the first sample suspended in the sample train. The temperature reading on the

dummy sample was assumed to be representative of the rest of the samples. Additionally, there was a 3.2 mm (0.125 in) type K thermocouple that entered the autoclave from the right plug and was located roughly 5.1 cm (2 in) away from the sample train.

Surrounding the ceramic tube were three 6.1 cm (2.4 in) diameter 316 stainless steel heat reflectors that were roughly 15.2 cm (6 in) away from the sample train and were spaced 1.9 cm (0.75 in) apart. These heat reflectors were wire tied to the stainless steel gas inlet tube to ensure they did not shift during loading and unloading operations. Each heat reflector also had six small holes in it to promote CO_2 flow into the autoclave. The purpose of the heat reflectors was to reflect the radiative heat back to the center of the autoclave, which resulted in a decrease in the plugs operating temperature. As discussed in Section 4.3, The Effect of Heat Reflector Position, the placement of these heat reflectors had a significant impact on the internal temperature of the autoclave. Figure 16 illustrates the internal thermocouple and heat reflector setup for the left plug. A similar heat reflector setup was used for the right plug, in which the three heat reflectors surrounded the 3.2 mm (0.125 in) thermocouple. These heat reflectors were not wire tied together, but they never moved because the right plug was never shifted during operation.

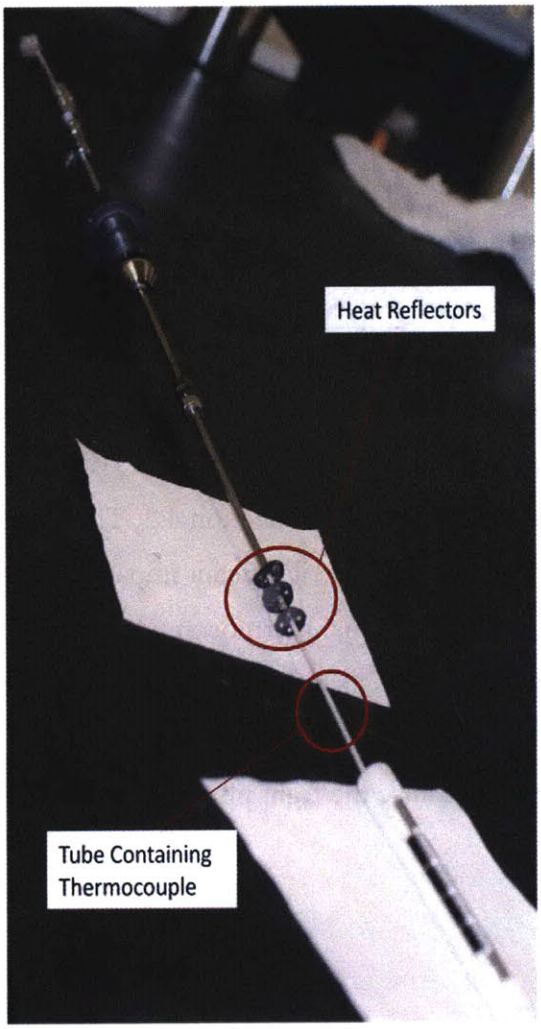

Figure 16: Internal Temperature Setup and Heat Reflector Location for the Left Plug

3.5.3 Small Autoclave Experimental Apparatus

The small autoclave setup was very similar to the large autoclave except for a few key features. A line diagram and an image of the small autoclave setup are shown in Figure 17 and Figure 18. The small autoclave had only one penetration, the inner diameter was 1.3 cm (0.5 in), and the autoclave was 106.7 cm (42 in) long. Additionally, the CO_2 effluent exited through a 1.6 mm (0.0625 in) 316 stainless tube, which was housed inside the 6.4 mm (0.25 in) 316 stainless steel CO_2 inlet tube. This was done because there was only one penetration in this autoclave.

In order to measure the internal temperature of the autoclave an Omega type K TJ36-CAXL-020U-60" thermocouple probe was used. The thermocouple was inserted into a 0.5 mm

(0.020 in) Conax MHC2-020-A2-T fitting and through the CO_2 inlet tube. Since there was a ceramic sheath on this probe, it could not be directly spotwelded to a dummy sample without compromising the integrity of the probe. Due to the tight clearances inside the small autoclave an alternate probe could not be used. Consequently, the temperature probe was mounted to the sample train 7 cm (2.8 in) away from the inlet using Resbond™ 907. This high temperature ceramic adhesive was guaranteed not to out-gas, thus, the data collected from the samples would not be compromised. As demonstrated in section 4.3, The Effect of Pressure, having the thermocouple in direct contact with the sample train was fairly representative of the actual sample temperature. Figure 19 illustrates the temperature measurement setup.

The small autoclave did not use heat reflectors; it was found that the temperature of the plug was low enough so that the material was well below the tempering point. Also this setup utilized a SC Hydraulic GBT 15/30 compressed air gas booster pump and an Omega PX605 pressure transducer.

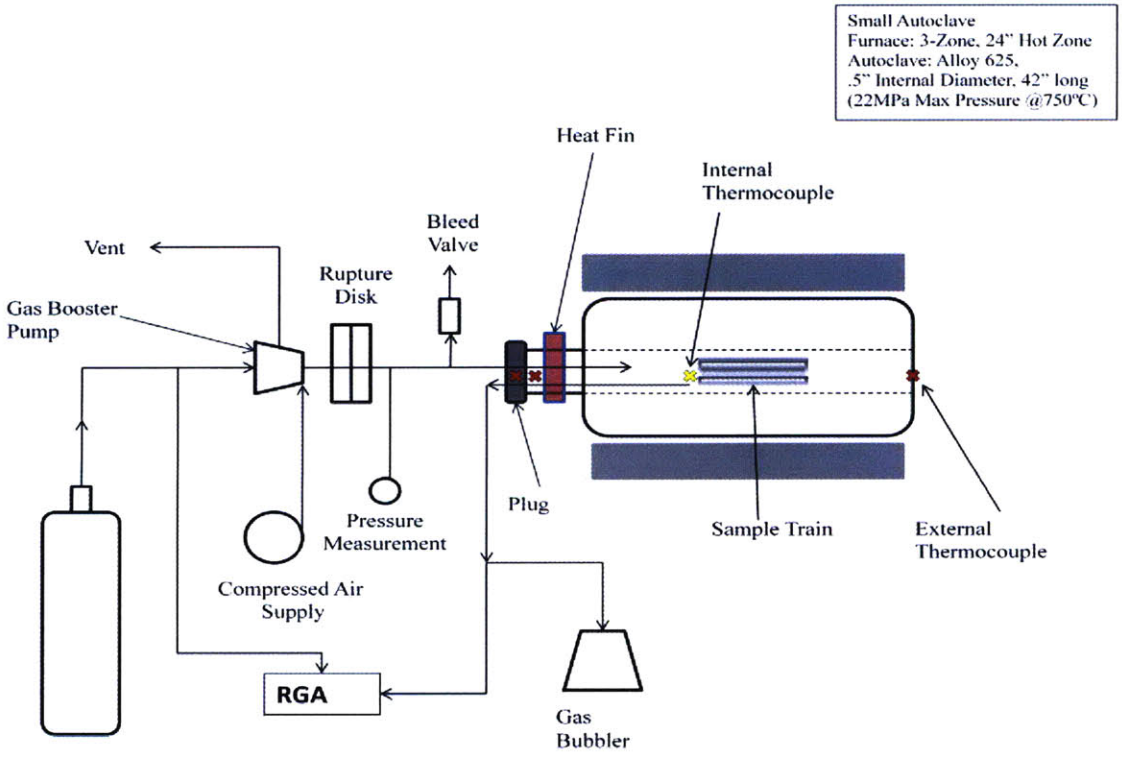

Figure 17: Line Diagram of Large Autoclave Experimental Apparatus

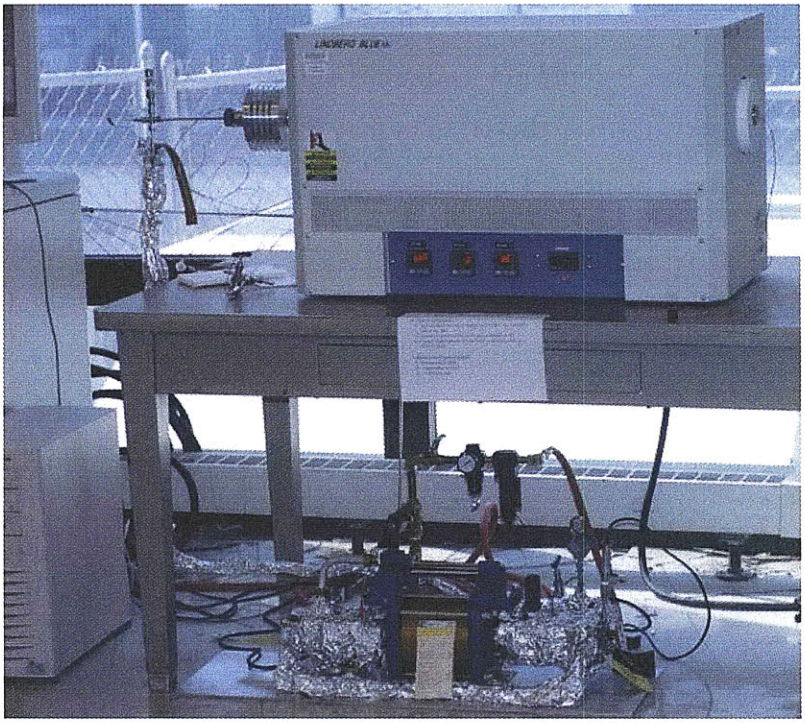

Figure 18: Small Autoclave Experimental Apparatus

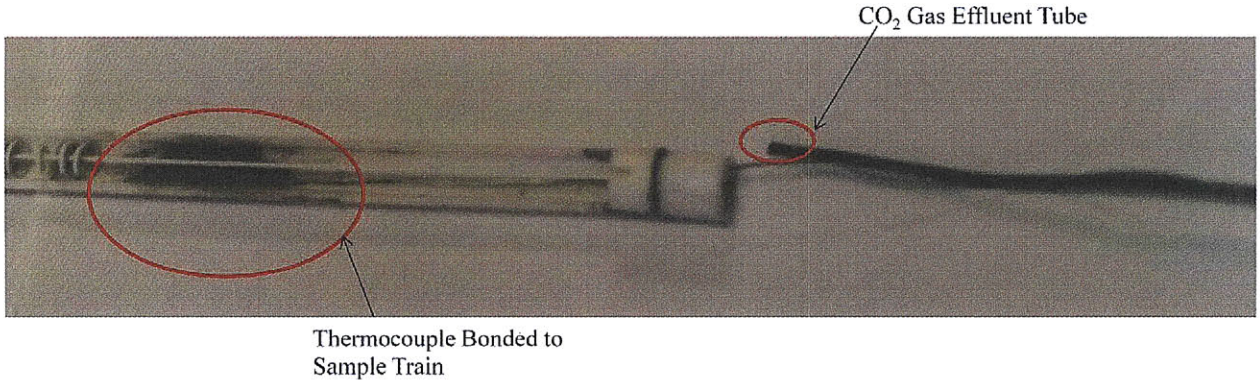

Figure 19: Small Autoclave Internal Temperature Measurement Setup

3.6 Operating Procedure

In order to ensure consistent gas composition throughout the testing regime a baseline RGA measurement was obtained from all CO_2 cylinders. Then the samples were loaded onto the sample train with the internal thermocouples properly positioned in the autoclave. The sample train was then loaded into the autoclave, the plug was tightened to form a seal, and the autoclave was placed into the furnace. All of the fittings were tightened, the outer thermocouples were spotwelded in place, and the Omegalux heat tape was set to 3.6 W. The high temperature alarms

were set to 15 °C above the desired operating temperature and the high pressure alarms were set to 1 MPA above the desired operating pressure. If an alarm tripped, the controller relay would latch causing the system to shutdown. The data acquisition programs were also initialized.

The first CO_2 cylinder was set to the desired pressure of either 2 MPa or 4 MPa, depending on the pressure required for the experiment. The second cylinder was set roughly 0.5 MPa lower than the first cylinder. Thus, if the first tank emptied and the second tank supplied CO_2 into the system, the system pressure would drop noticeably alerting the operator of an empty tank. Next, the compressed air regulator on the gas booster pump was tightened until the pressure of the system reached 6 MPa. The controller temperature was set to 140 °C, and the CO_2 flow rate through system was set to about 1000 cm^3 per hour to purge the system of impurities. After roughly 24 hours the purge was completed, as verified by the RGA data, and the flow rate through system was lowered to about 320 cm^3 per hour.

The controller temperature was increased slowly, 200 °C every 30 minutes to ensure the autoclaves did not heat up too quickly causing excess thermal stress. Once the desired system temperature was achieved, the pressure was increased via the gas booster regulator to the desired set-point. Flow rate was again adjusted to roughly 320 cm^3 per hour to adjust for the increase that occurred as a result of system pressurization. After every 250 hours the system was shutdown to weigh and photodocument the samples. Additionally, one sample from each alloy was removed from the test regime for recording purposes.

3.7 Test Matrix

Table 5 shows the test matrix that was used during this experiment. A total of 3 tests were performed with temperatures ranging from 650 °C to 750 °C, pressures ranging from 12.5 MPa to 20 MPa, measurements at intervals of 250 hours, and a total run time of 500 or 1,000 hours. LA-2 and LA-3 were completed at 12.5 MPa rather than 20 MPa due to autoclave operating temperature and pressure limitations. As discussed in Section 4.4, Temperature Profiling, the furnace controller reading was not representative of the actual internal temperature. So in order to get a relatively uniform internal temperature of 750 °C within the large autoclaves, the controller had to be set to 810 °C for zone 1, 760 °C for zone 2, and 810 °C for zone 3. Due

to safety concerns, the assumed outside temperature of the autoclave was 810 °C and according to Figure 10 the maximum allowable pressure at 810°C was 14 MPa.

Table 5: Test Matrix

Test Series	Temperature	Pressure	Measurement Time	Total Run Time	Number of Samples per Alloy
LA-1	714 °C	20 MPa	250 hours	500 hours	6
LA-2	650 °C	12.5 MPa	250 hours	500 hours	6
LA-3	750 °C	12.5 MPa	250 hours	1000 hours	4

3.8 Sample Characterization Measurements

Before the experiments were conducted, the sample geometry was measured using vernier calipers and a micrometer, photodocumented using a Nikon D80 camera with 60mm lens, and weighed using a Mettler Toledo XS105 Dual Range Scale that had a range and accuracy of 20.00001g ± .02 mg.

During each measurement interval the autoclave would be shut down and the samples removed from the sample train. Each sample was then photodocumented and weighed using the same equipment. These measurements were used in order to determine both the weight gain and to characterize the change in surface morphology. One sample of each alloy was then removed from the testing regime during each time period and stored in the desiccator for archival purposes. The rest of the specimens were then returned to the autoclave.

After a sample was removed, it was coated in gold using a sputter deposition technique in order to make the sample conductive. The surface morphology of the sample was then analyzed using a Topcon ABT150S Scanning Electron Microscope (SEM). The SEM was used to visually explore the surface conditions in order to observe any abnormal oxide growth, unique corrosion behavior, new phases not originally in the sample, and elemental segregation. Furthermore, Electron Dispersive X-ray Spectroscopy (EDX) was used to quantify the elemental composition of each specimen.

Further analysis was done by cutting each sample in half using a LECO VC-50 diamond saw. The half samples were then mounted in either Buehler Epo-Kwick or Buehler Epoxicure Epoxy in order to perform the polishing. Buehler flat edge filler was also mixed in with the

epoxy around the sample in order to promote better edge retention. The samples were mounted with the exposed surface orthogonal with respect to the polishing surface in order to examine the thin cross section of the sample. Once the epoxy cured the half-samples were finely polishing. The purpose of polishing each sample was to clearly see the different interfaces between the oxide layers and to reveal any grain boundary attack that may have occurred. The following polishing regiment was used with the Automet 3 Autopolisher:

1. 60 grit silicon carbide sand paper, 150 rpm, 3 lbs per sample, until plane
2. 360 grit silicon carbide sand paper, 150 rpm, 5 lbs per sample, 2 minutes
3. Trident wheel with 9 micron Metadi supreme diamond suspension, 150 rpm, 6 lb per sample, 5 minutes
4. Cleaned with deionized water in ultrasonic cleaner for 2 minutes and then rinsed with ethanol
5. Trident wheel with 3 micron Metadi supreme diamond suspension, 150 rpm, 6 lb per sample, 5 minutes
6. Cleaned with deionized water in ultrasonic cleaner for 2 minutes and then rinsed with ethanol
7. ChemoMet wheel with MasterPrep 0.05 micron colloidal silica suspension, 150 rpm, 6 lb per sample, 5 minutes
8. Cleaned with deionized water in ultrasonic cleaner for 2 minutes, rinsed with ethanol, and the dried

Each sample was then coated with gold using a diffusion dusting technique and further analyzed with the SEM and EDX. The purpose of the gold coating was to make the sample conductive. By looking at the cross section of the sample, the composition and number of different oxide layers that were formed should be able to be observed. However, the samples were very thin, which caused significant charging to occur from the mounting compound. The charging caused an unclear SEM image, and not much detail could be ascertained from the sectioned sample. Therefore, a conductive mounting compound should be used in future work.

Microstructural analysis was also conducted on Inconel 693 in order to observe if there were any differences between the as-received material and the material exposed to the high temperature and pressure SCO_2. Both the as-received material and LA1-12 (Inconel 693, T=750 °C, P=20 MPa, time = 500 hours) were finely polished based on the four step polishing procedure for nickel-based superalloys provided by Buehler (51). Both samples were then

etched in acid in order to reveal structural characteristics that were not evident on the as-polished specimens.

The samples were initially etched in modified glyceregia (60 mL glycerol, 50 mL hydrogen chloride, and 10 mL nitric acid), for 30 seconds. However, no microstructural information was revealed on the as-received sample, while the sample exposed to the SCO_2, LA1-12, revealed both grain boundaries and precipitates as shown in Figure 99. Therefore a stronger acid, modified Kalling's solution (25 mL hydrogen chloride, 25 mL ethanol, and 0.5g cupric chloride), was used for 30 seconds to etch the as-received samples. This acid was also tried on LA1-12, but the acid was to strong and over-etched the specimen even after 5 seconds of exposure. After etching, both samples were then observed under a Zeiss optical microscope.

4. The Effect of Autoclave Zone Temperature and Pressure on Sample Temperature

4.1 Temperature

Temperature plays a very crucial role in the oxidation rate of metals. In fact for most thin or thick film forming materials, the oxidation rate increases with temperature according to the Arrhenius equation, shown in equation 8 (45).

$$\text{Reaction Rate Constant} = A \exp\left(\frac{-\Delta E}{RT}\right) \quad [8]$$

A = Pre-Exponential Factor

ΔE = Change in Activation Energy

R = Gas Constant

T = Absolute Temperature

Given typical activation energies this equation predicts that, the rate of oxidation increases by a factor of two for each increase in temperature of 15 °C. This indicates that the temperature plays a very important role in the oxidation rate and it is therefore imperative to have accurate temperature measurements inside the autoclave.

Extensive temperature profiling work was completed on both the large and small autoclaves. It was determined that the difference between the internal temperature of the

autoclave and the furnace temperature controller was as high as 50 °C. The internal pressure also played a critical role in the actual temperature inside the autoclave. In the large autoclave the pressure was increased from 6 MPa to 20 MPa at a constant controller temperature setting of 750 °C. As a result the internal temperature decreased almost 30 °C from 745 °C to 715 °C. A similar trend occurred in the small autoclave as well.

4.2 The Effect of Pressure

4.2.1 Large Autoclave Temperature Profile

Figure 20 shows that there were four external temperature measurement locations and two internal locations throughout the large autoclave. The temperature profile setup included an internal thermocouple that was spotwelded to a dummy sample. Two stainless steel tubes were installed on both sides of the sample to ensure that the sample was stationary in the center of the sample train during loading and unloading operations. Two ceramic washers were also placed on both sides of the sample to prevent the sample from thermally bonding with the stainless steel tube, which is shown in Figure 21. The sample train was then positioned in the middle of the central heated zone of the autoclave. The right thermocouple was 15.2 cm (6 in) away from the middle of the central heated zone, 5.1 cm (2 in) away from the right edge of the sample train, and made no contact with the sample train or walls of the autoclave. The heat reflectors during this test were 15.2 cm (6 in) away from the sample train.

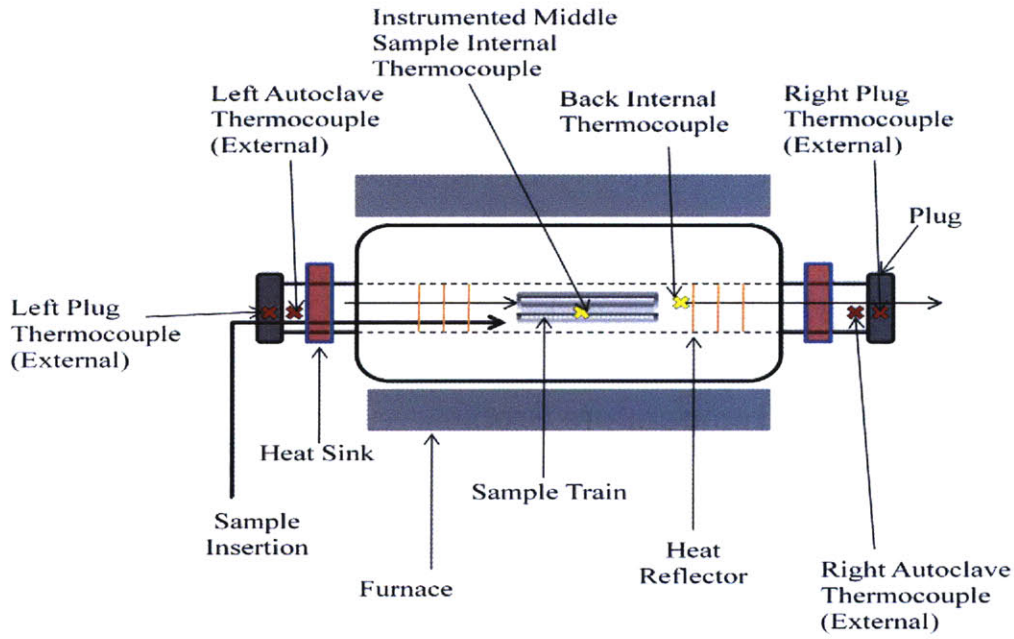

Figure 20: Thermocouple Layout for Large Autoclave

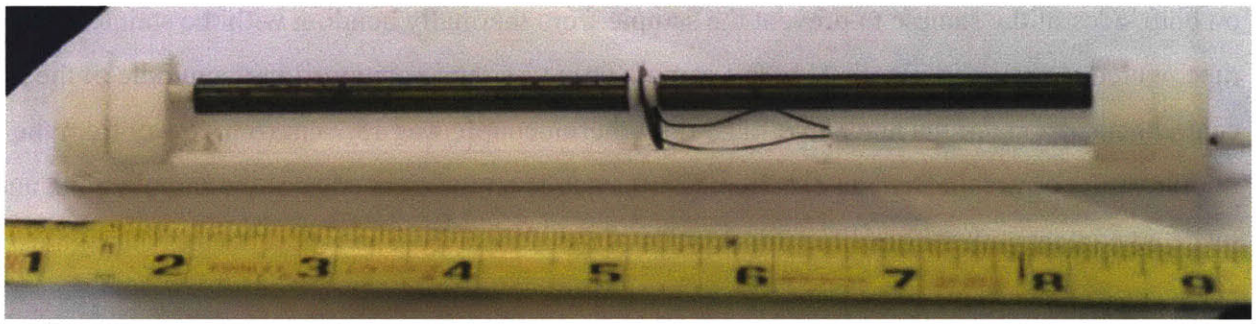

Figure 21: Large Autoclave Temperature Profile Setup

Figure 22 shows that as the pressure increased from 6 MPa to about 20 MPa with a constant controller temperature setting of 750 ºC the temperature of the middle internal thermocouple decreased almost 30 ºC from 745 ºC to 715 ºC. This can most likely be attributed to conduction through the autoclave; as the pressure increases, the density of the SCO_2 increases as well, making it a more effective heat transfer medium. This theory is also supported by the fact that the four external thermocouple temperature readings increased. The reading of the two external thermocouples positioned in front of the heat sinks increased about 55 ºC, while the two plug thermocouples increased by about 25 ºC. This demonstrates that as the SCO_2 fluid becomes denser it also becomes more conductive; conducting heat outwardly.

It was also found that if the thermocouple was not in contact with the autoclave wall or an object touching the autoclave wall the temperature reading would be significantly decreased. Figure 22 shows the back thermocouple readout was roughly 70 °C lower than that of the internal middle thermocouple at 6 MPa and 150 °C lower at 20 MPa. The back thermocouple was in the heated zone of the furnace in-between zones 2 and 3; however it did not make contact with either the sample train or the autoclave walls. Theoretically, the internal temperature should have been fairly uniform within the heated length, so the difference in temperature between the back thermocouple and the dummy sample that was instrumented can most likely be attributed to heat conduction through the wall of the autoclave, into the sample train, and into the sample.

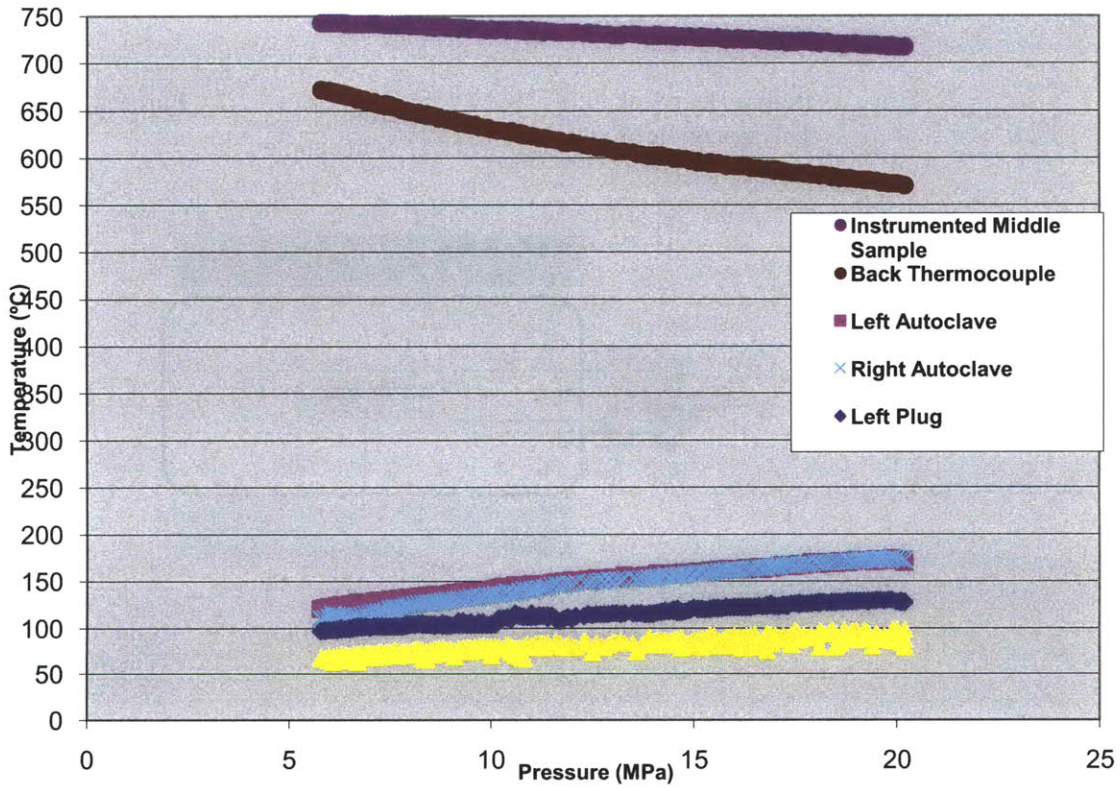

Figure 22: Effect of Pressure on Internal Temperature at a Constant Controller Temperature of 750 °C for the Large Autoclave

4.2.2 Small Autoclave

The small autoclave thermocouple setup was different compared to the large autoclave due to both size restrictions and the number of penetrations. There were three external

thermocouples and only one internal thermocouple for this setup as shown in Figure 23. Only one internal thermocouple could be used due to the single penetration and could not be directly mounted to a sample. Instead a 0.5 mm (0.020 in) thermocouple was placed inside a 3.2 mm (0.125 in) stainless steel tube, which was inside the sample train as shown in Figure 24. Care was taken to ensure the thermocouple was in direct contact with the tube as conduction from the autoclave walls played a very important role in temperature. The stainless steel tube was crimped at both the center and at the end. This ensured the internal thermocouple was locked in place at the center of the sample train and the tube would not slide out of the sample train during loading. As discussed in section 4.3, The Effect of Heat Reflector Position, attaching the thermocouple to some kind of thermal mass that was in contact with the autoclave wall was a fair representation of the temperature on an instrumented sample.

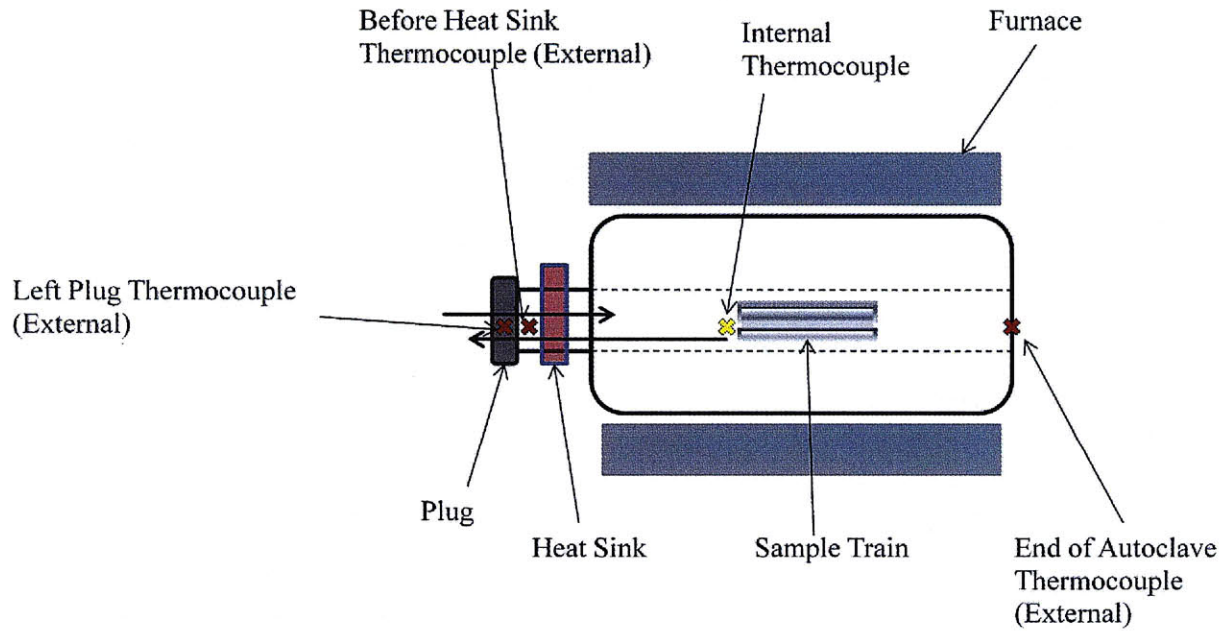

Figure 23: Thermocouple Layout for Small Autoclave

Figure 24: Small Autoclave Temperature Profile Setup

The small autoclave exhibited the same trend with internal temperature as the large autoclave when the pressure was varied at a constant controller temperature. In this case all three zones of the furnace were set to a constant temperature of 650 ºC and the pressure was increased from 2 MPa to 17 MPa. As Figure 25 shows the internal temperature reading decreased by almost 80 ºC during the pressure transient. As the internal temperature decreased, the readouts of the thermocouples on the outside of the autoclave increased as well, which may be due to the increase in density of SCO_2 resulting in it becoming a more effective heat transfer medium.

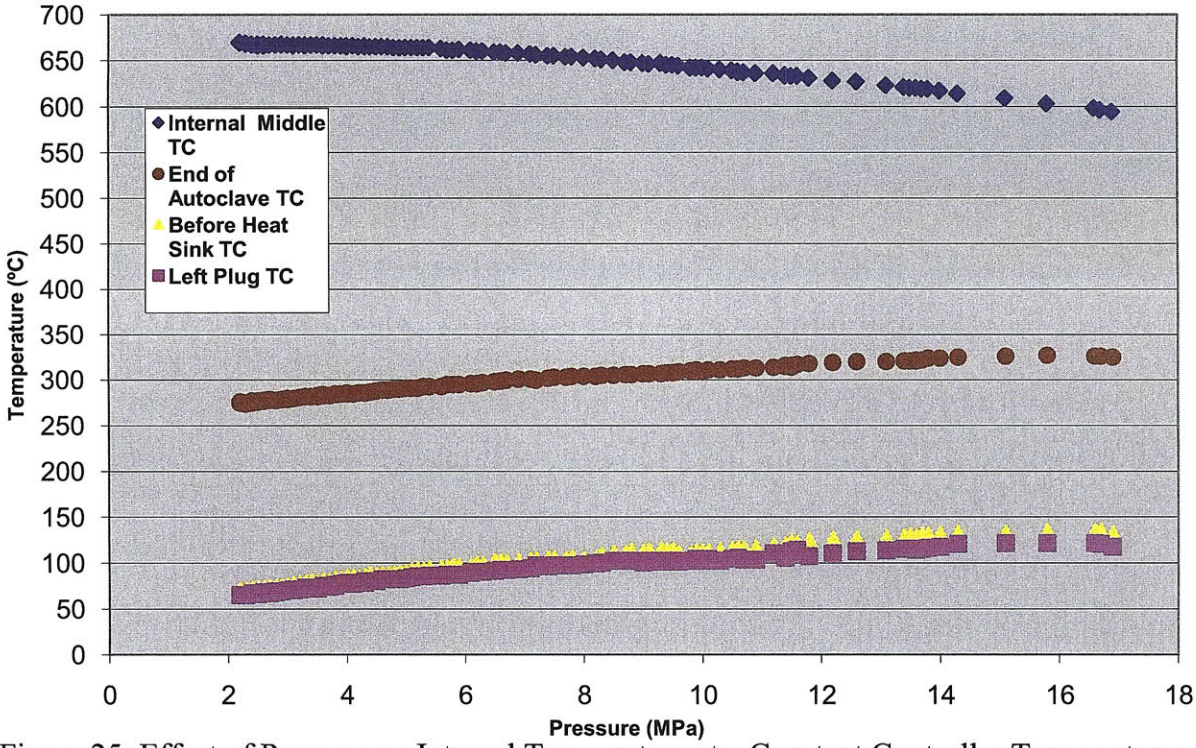

Figure 25: Effect of Pressure on Internal Temperature at a Constant Controller Temperature of 650 °C for the Small Autoclave

4.3 The Effect of Heat Reflector Position

Extensive temperature profiling was performed on both the large and small autoclaves as temperature is a critical parameter in corrosion rate. A controller temperature of 650 °C and a pressure of 20 MPa were used as a calibration point for temperature profiling as these were the previous operating conditions for tests run as part of an earlier program.

Eight temperature profiling trials were completed and it was concluded that the biggest effect on the internal temperature was the location of the heat reflectors as shown in Figure 16. For trials 1-5 the temperature profile setup was similar to that used in the small autoclave, as discussed above. This setup consisted of a 3.2 mm (0.125 in) internal thermocouple in which the heat reflectors were mounted on, as shown in Figure 26. The internal thermocouple was positioned in a 6.4 mm (0.250 in) stainless steel tube, which was inside the sample train. The middle and ends of the tube were crimped to ensure the thermocouple stayed in placed and so the tube could not be pushed out of the sample train during loading and unloading. For trials 6 and 8

the temperature profile setup was identical to that shown in Figure 21; for trial 7 the setup was the same except the instrumented sample was moved to 1.27 cm (0.5 in) away from the sample train inlet.

For trials 1-4 the heat reflector position was not held constant as Figure 26 shows because it was unknown how important position was. For each of these trials the heat reflectors were moved further away from the sample train than the previous trial as a result of loading operations. During trial 5 the three heat reflectors were wire tired together with spacing between each reflector being about 19 mm (0.75 in). The heat reflectors for this trial were placed 15.2 cm (6 in) away from the sample train. However, the reflectors were not wire tied to the gas effluent tube; they just rested on top of the internal 6.4 mm (0.250 in) thermocouple. It is the author's judgment that the heat reflectors shifted to about 19.1 cm (7.5 in) away from the sample train inlet during loading operations for trial 5.

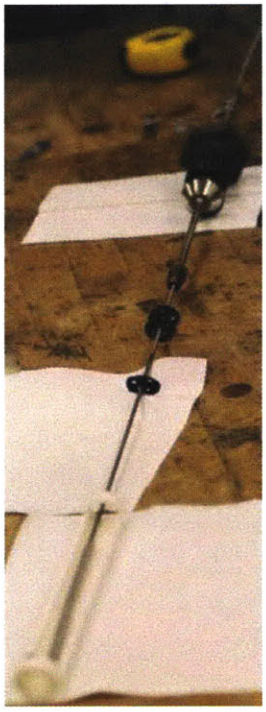

Figure 26: The Experimental Setup for Temperature Profiles 1-4

Trials 1-4 in Figure 27 show that as the heat reflectors are moved further away from the sample train the internal temperature of the system decreased. During trial 5 when the heat reflectors were moved to roughly 19 cm (7.5 in) away from the sample train the internal temperature increased roughly 20 °C compared to that of trial 4. During trials 6 and 8 the heat

reflectors were tied to the CO_2 effluent tube at a distance of 15.24 cm (6 in) and the thermocouple was mounted directly to a sample. These tests showed repeatability as the setup was changed in between trials and the temperature measurements were within one degree Celsius of each other. When the instrumented sample was moved roughly 10.2 cm (4 in) toward the inlet of the sample train, the internal temperature decreased about 7 °C under the same conditions and position in the autoclave. This shows that the temperature inside the autoclave may not be uniform and zones 1 and 3 need to be adjusted to a higher value then zone 2 to achieve a more homogeneous temperature.

There is about a 7 °C difference between trial 1 and trials 7 and 8. Both setups had the same thermocouple position in the autoclave, however in trials 7 and 8 the thermocouple was mounted directly to the sample, and the heat reflector position was most likely further away in trial 1. Based on the trend in Figure 27 the difference in temperature between trial 1 and trials 7 and 8 can most likely be attributed to the heat reflector position and not by the difference in thermocouple setup. This theory is also supported by comparing trial 5 with trials 7 and 8, in which the heat reflectors were roughly 3.8 cm (1.5 in) further away from the sample train. In this case the temperature difference was roughly 12 °C and may be attributed to the difference in heat reflector positioning.

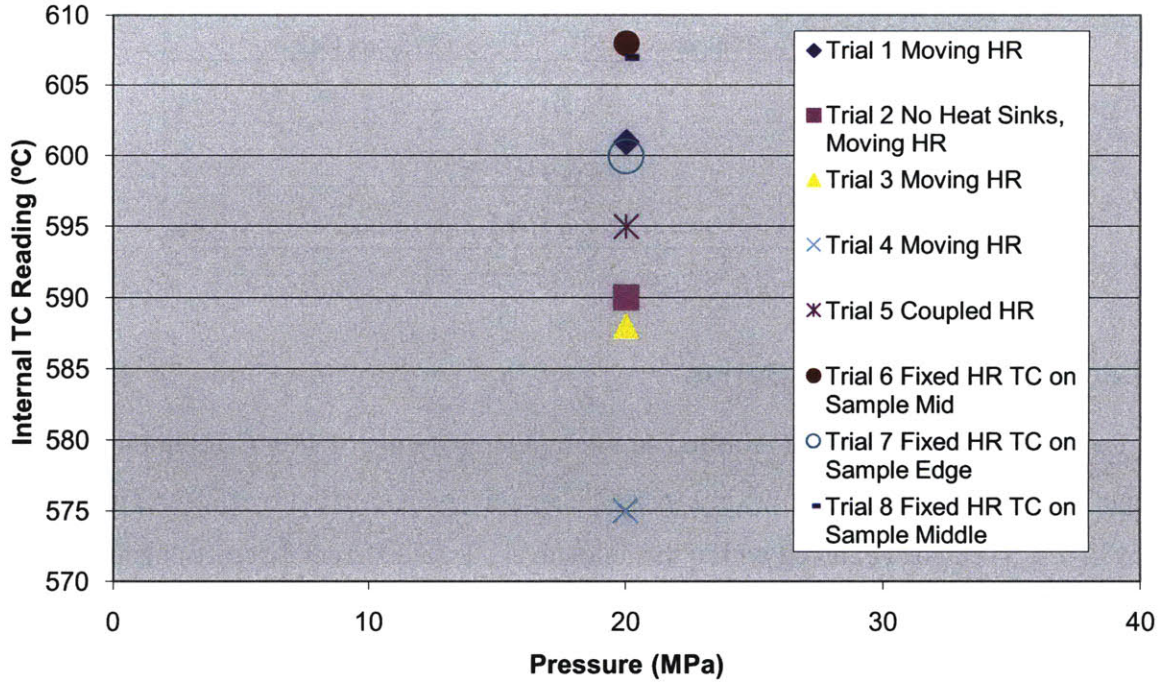

Figure 27: Temperature Profile Data at a Controller Temperature of 650 °C for the Large Autoclave

4.4 Temperature Profiling

4.4.1 Large Autoclave LA1 Series

The LA1 series of experiments were conducted with a controller setting of 750 °C and a pressure of 20 MPa. At this time during the testing regime, the importance of thermocouple positioning inside the autoclave was unknown, and it was assumed that the controller setting represented the actual internal temperature. However, during subsequent temperature profiling it was determined that the controller temperature and the internal temperature for this test varied by more than 30 °C. Therefore a thorough temperature profile was completed under the same conditions. It was determined that the internal temperature was 714 ± 6 °C, with the coolest temperature being at the edges of the sample train. Table 6 illustrates the temperature profiling results that correspond to these conditions.

Table 6: LA1 Series Temperature Data with All Three Controllers Set at 750 °C

	Internal Temperature (°C)	Pressure (MPa)
TC 1.3 cm away from inlet	707	20
TC 10.2 cm away from inlet trial 1	718	19.9
TC 10.2 cm away from inlet trial 2	720	20.1

4.4.2 Large Autoclave LA3 Series

The LA3 series experiment required an internal temperature of 750 °C. Demonstrated by the temperature profiling work shown in Figure 28, an average temperature of 750 °C with an accuracy of ± 3 °C can be achieved within the autoclave. Two different distances inside the sample train were used for the profiling, 1.3 cm (0.5 in) and 10.2 cm (4 in) away from the inlet. These distances were chosen because they represent the first position in which a sample can be positioned and the midpoint of the sample train. Symmetry was assumed so only the inlet was profiled.

The temperature of an end sample was roughly 6 °C cooler than a middle sample. Figure 28 illustrates the internal temperature profiling data of an instrumented sample as a function of the trial number. Table 7 shows the corresponding zone temperatures for each trial. Based on this data, trial 7 produced the most uniform internal temperature at 750 °C with zone settings of 810 °C, 760 °C, and 810 °C respectively. Only one trial for the mid and edge temperatures were completed at these settings. However, trial 2 produced a consistently higher temperature reading than trial 1 under the same conditions making it a more conservative data set.

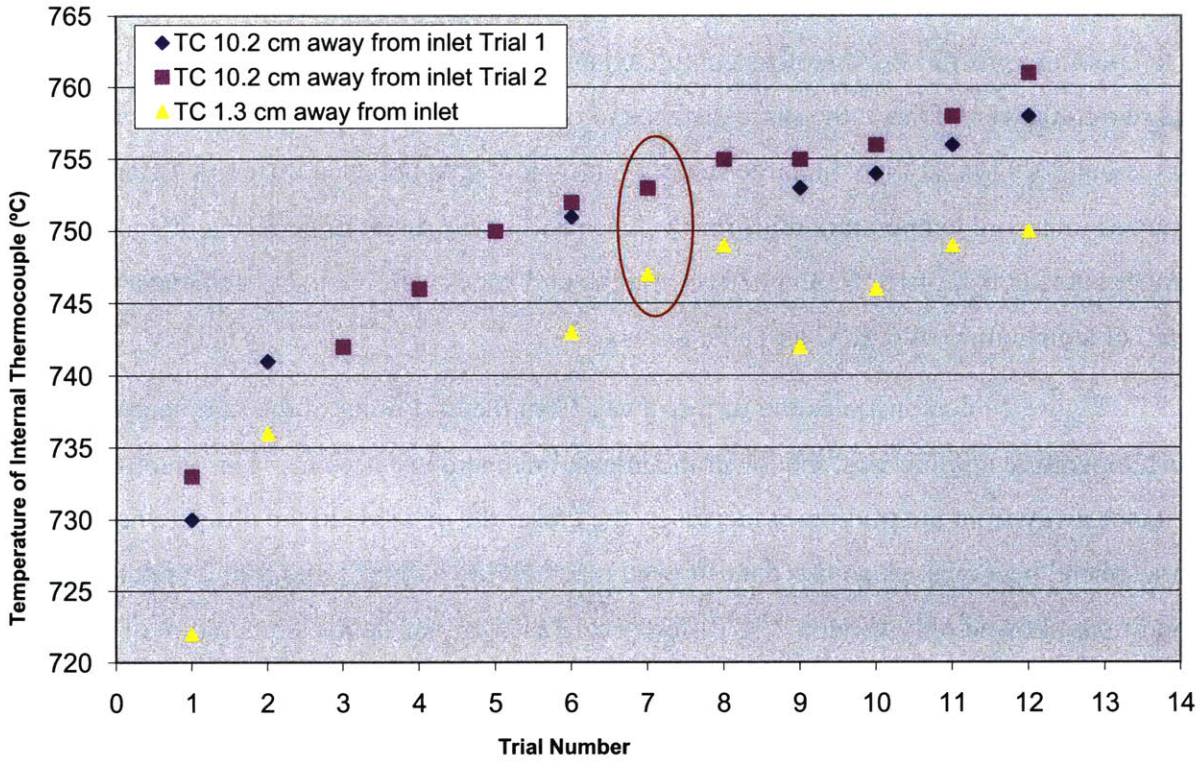

Figure 28: Large Autoclave Temperature Profile Data at 12.5 MPa

Table 7: Large Autoclave Zone Temperatures for the Different Trials

Trial #	Zone 1	Zone 2	Zone 3
1	750	750	750
2	800	750	880
3	760	760	760
4	780	760	780
5	790	760	790
6	800	760	800
7	810	760	810
8	815	760	815
9	770	770	770
10	780	770	780
11	790	770	790
12	800	770	800

4.4.3 Small Autoclave Temperature Profile

The LA2 series of experiments required a temperature of 650 °C in the small autoclave. A temperature profile was therefore completed at three different distances along the sample train and two trials were done at the same distance to ensure repeatability. As the small sample train was about 50% longer than the large sample train, more data points at different distances were required to ensure temperature uniformity. The profile was run at three different zone 2 temperatures 600 °C, 610 °C, and 620 °C and the end zones were varied to achieve a uniform internal temperature of 650 °C as Table 8 shows.

Figure 29 demonstrates the further away from the mid-point of the sample train (15.2 cm) the temperature reading was, the lower the internal temperature became. This is intuitive, as the distance away from the mid-point increases, the closer the distance to the ultimate heat sink, the atmosphere, becomes. Also this data showed repeatability as trial 1 and trial 2 under the same conditions showed only about a 2 °C difference. Based on this data a temperature of roughly 650 °C was achieved by using the following zone temperatures: 690 °C, 600 °C, and 690 °C.

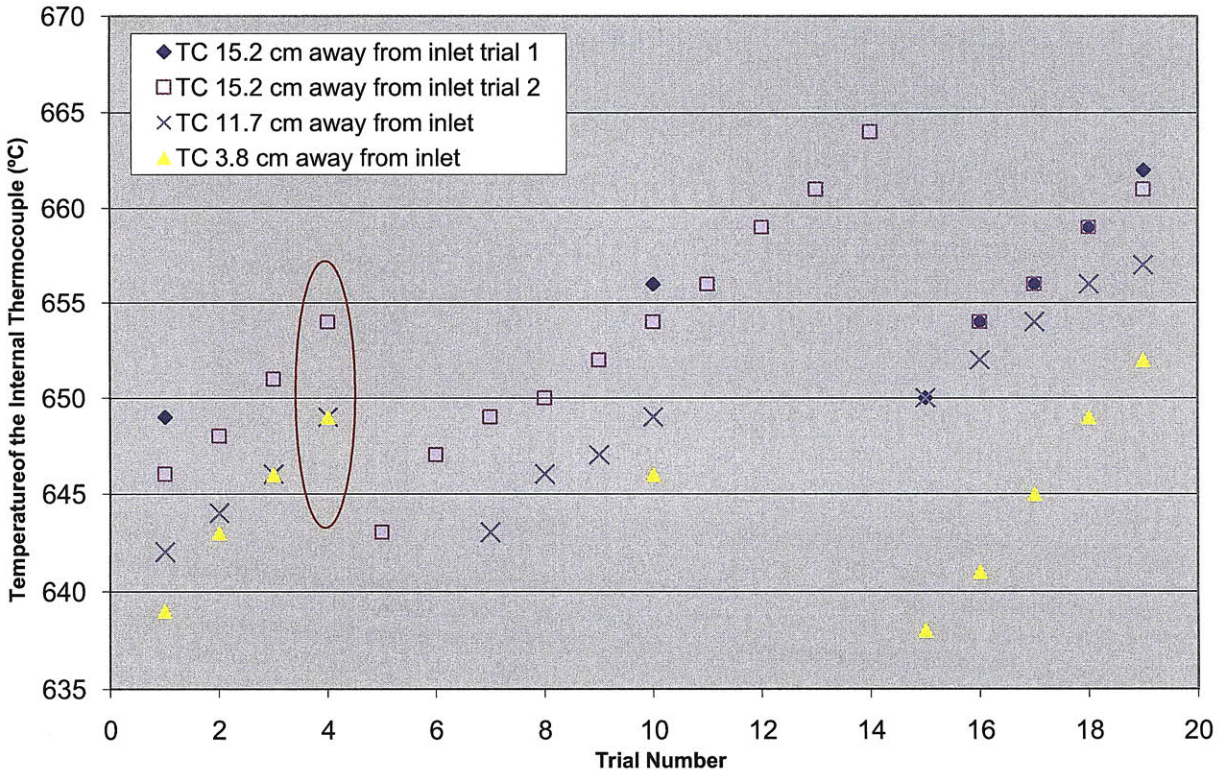

Figure 29: Small Autoclave Temperature Profile Data at 12.5 MPa

Table 8: Small Autoclave Zone Temperatures for the Different Trials

Trial #	Zone 1	Zone 2	Zone 3
1	660	600	660
2	670	600	670
3	680	600	680
4	690	600	690
5	610	610	610
6	620	610	620
7	630	610	630
8	640	610	640
9	650	610	650
10	660	610	660
11	670	610	670
12	680	610	680
13	690	610	690
14	700	610	700
15	620	620	620
16	630	620	630
17	640	620	640
18	650	620	650
19	660	620	660

5. Results and Discussion

The purpose of this thesis was to investigate the effect of temperature on the corrosion of potential structural and pressure boundary materials in a SCO_2 environment. Three sets of experiments were run (LA1, LA2, and LA3) at temperatures of 714 °C, 650 °C, and 750 °C and pressures of 20 MPa, 12.5 MPa, and 12.5 MPa respectively. These temperatures were selected as they are the likely operating temperature of the Generation IV gas cooled fast reactor, where SCO_2 is a prime coolant candidate. Ideally, a pressure of 20MPa would have been used throughout the testing regime, however due to autoclave operating temperature and pressure limitations some of the experiments had to be run at 12.5 MPa. Additionally, it was important to understand the effect that the carbon monoxide dissociation reaction, $2C + O_2 \leftrightarrow 2CO$, had on the oxidation rate, as it became more thermodynamically favorable than the carbon dioxide dissociation reaction, $C + O_2 \leftrightarrow CO_2$, at temperatures greater than 700°C. Understanding the potential effect of the carbon monoxide dissociation reaction was important as it could introduce a new oxidation mechanism significantly affecting the rate of weight gain.

5.1 Weight Gain Analysis

The amount of weight an alloy gained over a period of time in an environment was very important in determining how susceptible an alloy was to corrosion as it indicated the formation of an oxide layer. Therefore it was necessary to analyze the weight gain, and weight gain rate for the given alloys in the testing regime. The weight gain rates in the subsequent graphs were calculated using equations 9 and 10.

$$\text{Rate of Weight Gain} = \frac{\text{(Final Weight(mg)} - \text{Initial Weight(mg)}}{\text{Duration of Experiment (days)} * \text{Surface Area (cm}^2\text{)}} \quad [9]$$

$$\text{Surface Area} = \frac{\pi}{2}(D^2 - d^2) + \pi Dt + \pi dt \quad [10]$$

D = diameter of the specimen

d=diameter of the mounting hole

t=thickness

There were multiple specimens of each alloy and the subsequent graphs show the average values of the specimens for each alloy. The error bars were obtained using the values from the samples that had the least and the most weight gain rate for a specific alloy. The scatter in the data from the different samples may be attributed to extremely small weight gains, the potential for reaction with small quantities of oxygen/water vapor present in the gas stream, inhomogeneous corrosion behavior, and surface defects.

The equipment uncertainty associated with equation 9 for the LA1 and LA3 experiments (XS105 Dual Range Scale had an accuracy of ±.02 mg, the micrometer had an accuracy of ±0.005 cm, and the calipers had an accuracy of ±0.0001 cm) was calculated to be roughly $8x10^{-4}$ mg/cm^2*day using standard error propagation formulas (46). The uncertainty associated with the LA2 experiment was $6.0x10^{-3}$ mg/cm^2*day, the difference between the two uncertainties can be attributed to the large difference in surface area, as the LA2 samples were roughly 10 times smaller. The calculation uncertainty was not incorporated into the error bars in the graphs.

It is also important to determine if contaminants in the SCO_2 could be responsible for the observed weight gain. CO_2 gas with a certified purity of 99.9999% was utilized, so a concentration of 0.0001% oxygen was assumed when calculating the concentration of impurities as it would provide the maximum amount of contaminants in the system. The total number of moles of gas in the system was determined using the real gas law (equation 11), which consequently allowed the concentration of impurities to be determined.

$$n = \frac{PV}{zRT} \qquad [11]$$

The following parameters were used in the calculation: pressure 20 MPa, temperature 714°C, volume 80L (the total volume of CO_2 that flowed through the system during a 250 hour period) and a compressibility factor 1.05 (47). These were the parameters obtained from the experiment which utilized the highest CO_2 flowrate and thus, producing the highest amount of contaminants. This calculation showed that there would be a maximum of 6 mg of impurities in the system. The LA1 and LA3 samples had a much larger total weight gain than 6 mg, shown in Appendix A, therefore the weight gain could not be attributed to contaminants alone. Additionally, the surface area of the autoclave is much greater than the surface area of the samples, therefore the contaminants are more likely to react with the autoclave itself.

Figure 30 - Figure 37 show the results of the experimental program and the following trend was observed: AUSS 316L had the highest weight gain rate, more than an order of magnitude higher than the nickel based alloys. This was expected as the combination of nickel and chromium forms a higher integrity and more stable passive film than iron and chromium. Additionally, nickel had a lower oxygen affinity than iron and therefore the migration of cations into the scale was lower. The chromium content for the AUSS 316L was also the lowest, which contributed to the high oxidation rates.

5.1.1 LA1 (T= 714 °C, P=20 MPa, large sample)

Figure 31 shows the results for the LA1 experiment and illustrates that Inconel 693, 740, and 740+ outperformed the Inconel 690,718, and 725. This may have been due to high iron content in Inconel 690, 718, and 725 (The EG under Inconel 718 and 725 denotes that the samples were cut parallel to the rolling direction, which was discussed in section 3.3). Additionally, Alloy 690, the nickel alloy with the highest weight gain, had a negligible aluminum content, which could explain the high weight gain, as aluminum can form an underlying protective oxide layer. The exceptional performance of alloys 740 and 740+ could be attributed to a higher silicon content, which would potentially aid in the formation of a continuous protective oxide layer as discussed in Section 2.2.3. Alloy 693 had the lowest corrosion rate that could be explained by the fact that it had the highest aluminum content, which may have aided in the formation of a continuous protective film. The energy dispersive x-ray spectroscopy (EDX) spectrums shown in Figure 56, Figure 82, and Figure 89 further supported this hypothesis as the surface film for Inconel 693 was shown to be enriched with aluminum and the surface film for 740 and 740+ appeared to be enriched with both silicon and aluminum.

Figure 30 also shows that the initial rate of weight gain for all alloys was elevated and then leveled off after the first time point. This was expected because within the first 250 hours a continuous protective film, most likely composed of chromium, nickel, or iron, was formed preventing the inward diffusion of carbon dioxide and other corrodents, and the outward diffusion of metal ions.

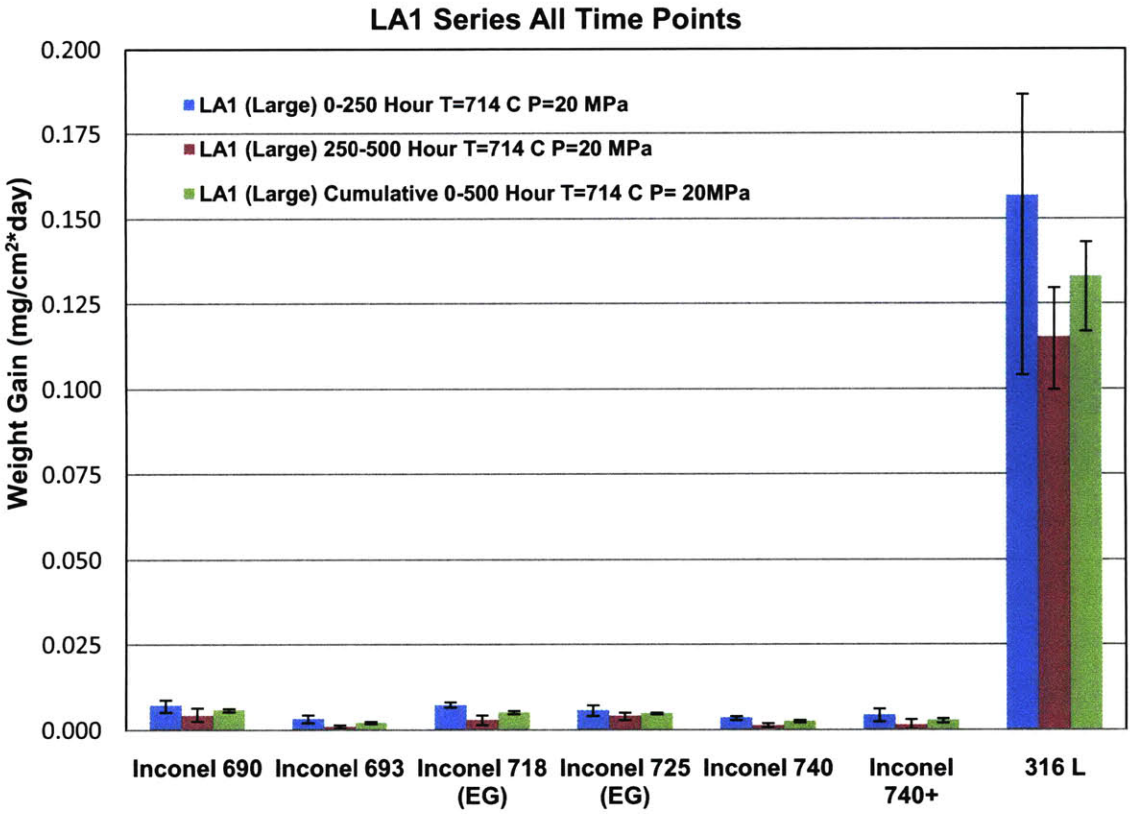

Figure 30: Total Weight Gain Rate Data for LA1 (T= 714 ºC P=20 MPa)

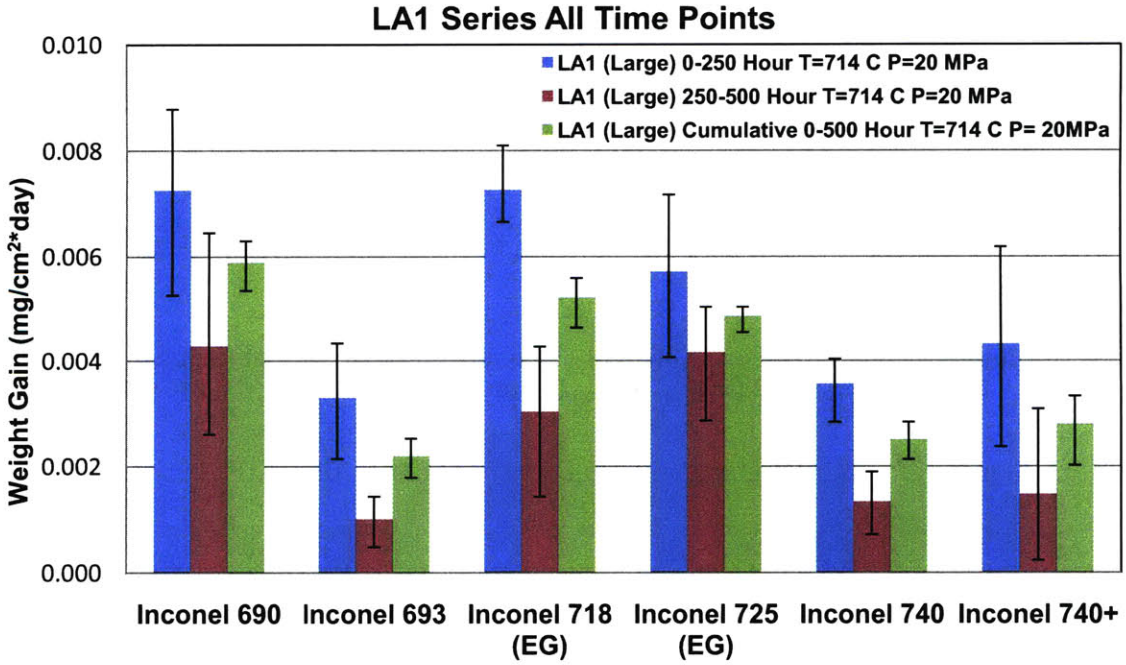

Figure 31: Total Weight Gain Rate Data for the Nickel Based Alloys on LA1 (T= 714 ºC P=20 MPa)

5.1.2 LA2 (T=650 °C, P=12.5 MPa, small sample)

The LA2 series showed a similar trend which is illustrated in Figure 32: the AUSS 316L had the highest weight gain and the nickel based alloys the lowest due to the high iron content and low chromium content in the AUSS 316L. Also, alloy 690 performed the worst out of the nickel based alloys similar to the LA1 series. This may have been due to the relatively high iron content and negligible aluminum content. Again, each alloy showed a high initial weight gain which then decreased as exposure time increased, analogous to the LA1 series. However, unlike the LA1 (T=714 °C, P=20 MPa, large sample) and LA3 (T=750 °C, P=12.5 MPa, large sample) series, the LA2 series samples had a very small surface area, roughly 0.48 cm^2 compared to 4 cm^2, which resulted in a smaller overall weight gain.

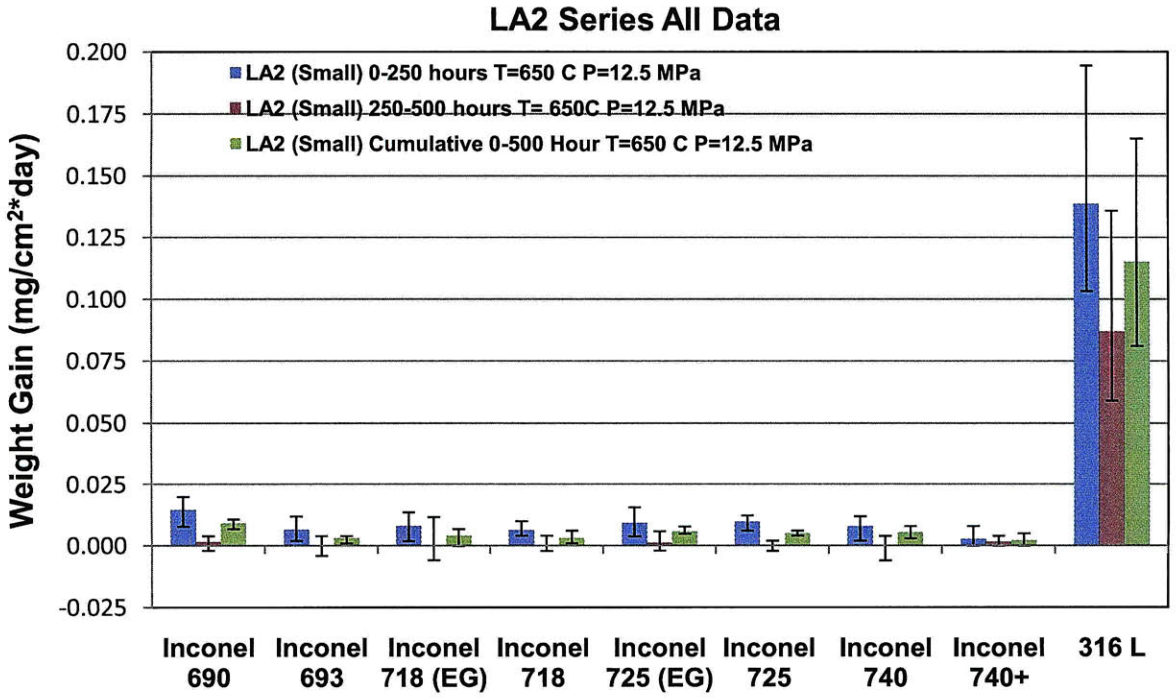

Figure 32: Total Weight Gain Rate Data for LA2 (T= 650 °C P=12.5 MPa)

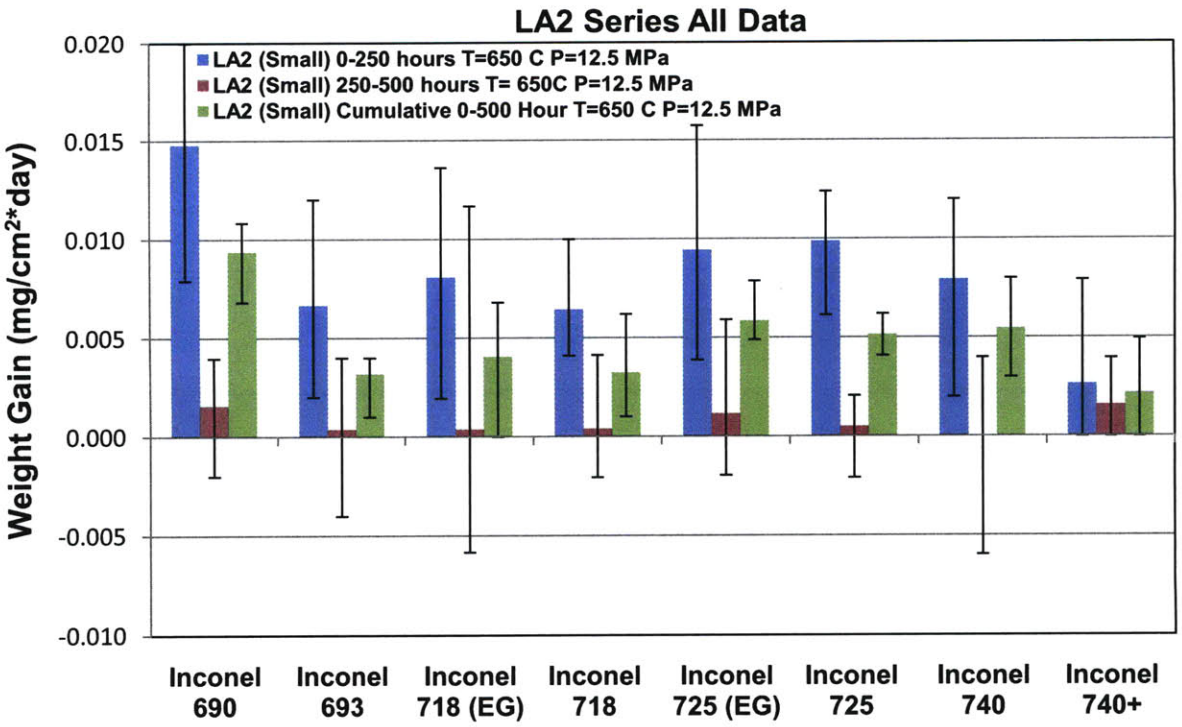

Figure 33: Total Weight Gain Rate Data for the Nickel Based Alloys on LA2 (T= 650 °C P=12.5 MPa)

Based on the data presented in Table 9 the average weight gain was between 0 and 0.07 mg for the nickel alloys and as high as 0.69 mg for the AUSS 316L. For the nickel alloys this small weight gain was on the order of the uncertainty associated with the XS105 Dual Range Scale, ±.02 mg. Additionally, the error that was propagated from the weight gain calculation (the subtraction of two weights from different time points) had to be accounted for by summing up the individual uncertainties in quadrature (46). This calculation generated a total uncertainty value of ±0.03 mg associated with the weight gain calculation. Judging from the data in Table 9 the majority of the weight gain had values comparable to the uncertainty, thus making the magnitude of the LA2 graphs not representative of the true weight gain, but more likely and upper bound. In the LA2 series, the AUSS 316L was the only alloy in which the results were quantitatively useful as it had a weight gain that was greater than the uncertainty value by an order of magnitude. The weight gains for the LA1 and LA3 series (large samples) were significantly greater than the uncertainty in most cases. The raw data can be found in Appendix A.

Specimen	Avg Weight (mg) 0 hr	Avg Weight (mg) 250 hr	Avg Weight gain (mg) 0-250 hr	Avg Weight (mg) 500 hr	Avg Weight gain (mg) 250-500 hr	Total Weight Gain (mg)
Inconel 690	26.04	26.11	0.07	26.12	0.01	0.08
Inconel 693	30.59	30.62	0.03	30.62	0	0.03
Inconel 718 (EG)	35.60	35.64	0.04	35.64	0	0.04
Inconel 718	19.84	19.87	0.03	19.87	0	0.03
Inconel 725 (EG)	33.34	33.39	0.05	33.40	0.01	0.06
Inconel 725	15.92	15.97	0.05	15.97	0	0.05
Inconel 740	26.53	26.57	0.04	26.57	0	0.04
Inconel 740+	34.54	34.56	0.02	34.56	0.01	0.03
AUSS 316 L	17.28	17.97	0.69	18.66	0.42	1.11

Table 9: Weight Gain Data for LA2 (T= 650 °C P=12.5 MPa)

5.1.3 LA3 (T= 750 °C, P=12.5 MPa, large sample)

The LA3 experiment showed the same trend as the other experiments: the nickel based alloys had a lower weight gain than the AUSS 316L. There was not much of a statistical difference in the performance of each nickel based alloy, except alloy725, which had the highest weight gain as Figure 34 demonstrates. This may be attributed to alloy 725 having one of the lowest Al and Si contents of the nickel based alloys, which can help to form a continuous oxide, and having a high iron content, which has a higher affinity for oxygen.

Alloys 718 and 725 samples were cut both parallel and perpendicular to the rolling direction. The samples cut parallel to the rolling direction (denoted with (EG)) were expected to have a higher corrosion rate than the samples cut perpendicular to the rolling direction due to the exposed endgrains and grain boundaries causing a higher concentration of stress and an easier diffusion path. However, this was not the case and both sets of samples showed analogous weight gain as illustrated by Figure 35. All of the nickel based alloys exhibited the same high initial weight gain until a continuous protective film formed (within the first 250 hours). The weight gain then tapered off in subsequent time points once the base metal was isolated from the environment via the scale. However, AUSS 316L was an anomaly: the weight gain rate continued to increase over time. This could be explained by the initial formation of a continuous thin dense layer of chromium rich oxide, due to the high diffusion rate of chromium caused by the high temperature. Once the chromium layer was formed, iron cations slowly diffused through the surface scale forming an iron rich oxide external to the chromium layer, which increased the weight gain over time. The photographs in Section 5.2.7 support this as the

external iron oxide content increased as exposure time increased, contrary to the other alloys which had a continuous film formed after the first time point.

Again, for Figure 34 and Figure 35 the error bars were obtained from the sample that had the least and most amount of weight gain for a specific alloy. For the cumulative weight gain and the 750-1000 hour data point only one sample of each alloy was left in the autoclave (the other samples were removed as an archival record) and therefore no error bar was generated.

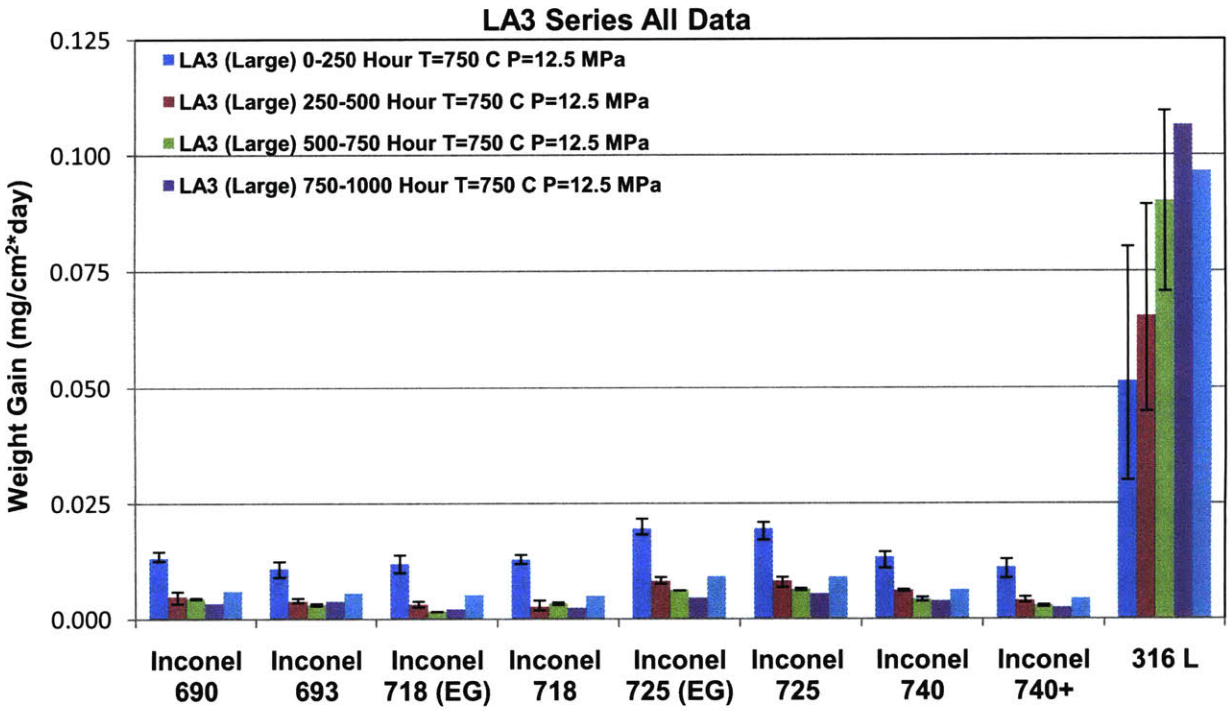

Figure 34: Total Weight Gain Rate Data for LA3 (T= 750 °C P=12.5 MPa)

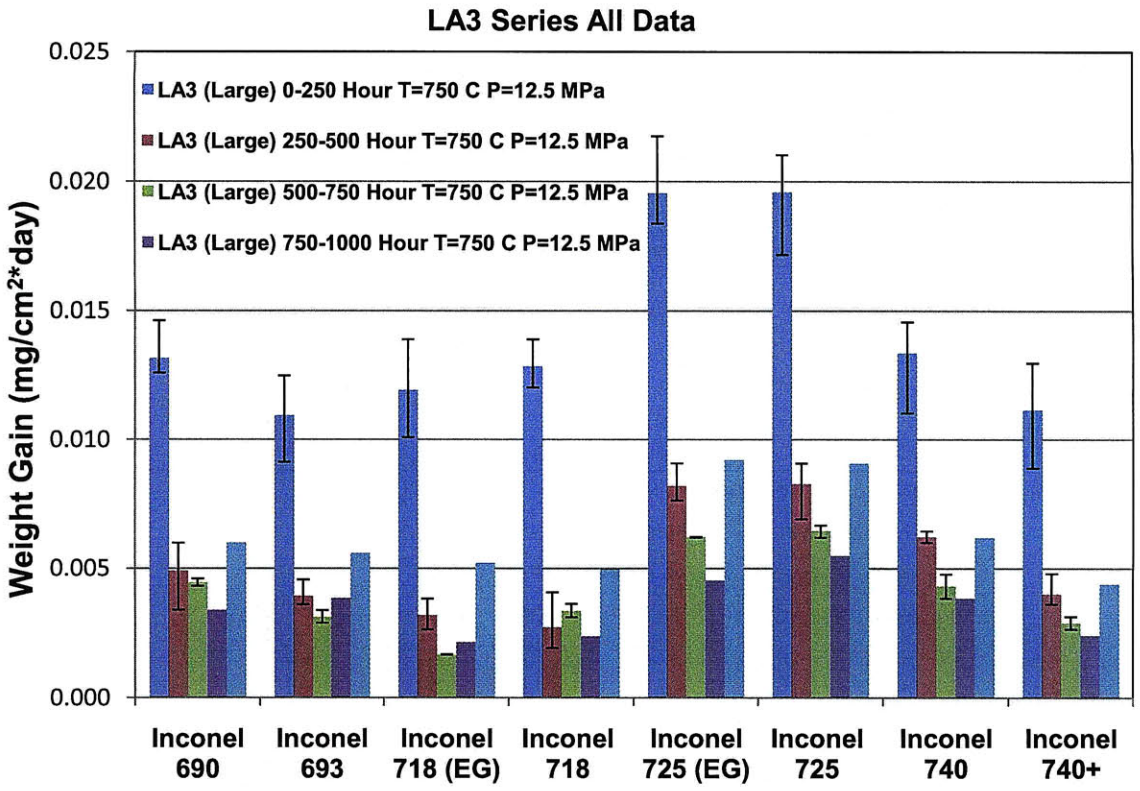

Figure 35: Total Weight Gain Rate Data for the Nickel Based Alloys on LA3 (T= 750 °C P=12.5 MPa)

5.1.4 Comparison of LA1, LA2, and LA3

Based on the comparison of all the experiments at 500 hours, shown in Figure 36, it is clear that the temperature at which the experiment was run had a significant effect on the oxidation rate. The effect of pressure appeared negligible compared to the effect of temperature, as a 43% reduction in pressure but only a 5% increase in temperature produced significantly higher corrosion rates. However, more experiments are needed comparing two different pressures at the same temperature to confirm this. The experiment performed at 750 °C and 12.5 MPa (LA3) had the highest nickel alloy oxidation rate. This was expected as the corrosion rate should follow an Arrhenius trend and for an increase in temperature of 15°C the corrosion rate should increase roughly by a factor of 2. However, AUSS 316L showed an opposite trend then what was expected.

The AUSS 316L behaved counter-intuitively, the corrosion rate declined as the temperature increased from 714 °C (LA1) to 750 °C (LA3) and increased from 650 °C (LA2) to 750°C (LA1). However, there are many variables in play when comparing LA2 with LA1 and

LA3 including: the LA2 specimen's surface area being 10 times smaller than the LA1 or LA3 series. Such a small surface area could have introduced a large number of inhomogeneities including added stress, which could increase the corrosion rate. Additionally, the 316L sample in the LA2 experiment had the largest error bars, as a small weight gain (on the order of the scale's accuracy) would lead to a large weight gain rate due to the small surface area.

One possible reason for the AUSS 316L sample having the lowest corrosion at 750 °C could be that the increase in temperature resulted in an increase in the diffusion rate in the alloy, which most likely facilitated a faster growth rate of an inner "healing" layer of chromium rich oxide, that restricted the outward diffusion of cations. Some studies support this theory as the corrosion rate of AUSS at 650 °C was less than at 600 °C and at 550 °C (32). Additionally, photographs of the LA3 AUSS 316L sample as a function of exposure time located in Section 5.2.7 further supports this theory. These photographs demonstrate that a thin chromium rich oxide layer initially formed on the surface and over time iron cations diffused through the surface scale forming an iron oxide external to the chromium oxide. Each photograph, which represented a 250 hour exposure interval, demonstrated a thicker iron oxide on the sample than the previous exposure interval. This signifies more iron cations diffused through the chromium oxide, which explains the continued increase of weight gain over time for the AUSS 316L in the LA3 series. The LA1 and LA2 series showed a continuous layer of iron oxide on the surface after 250 hours, which explained why the weight gain leveled off, and did not grow linearly like the LA3 series as shown in Figure 30 and Figure 32.

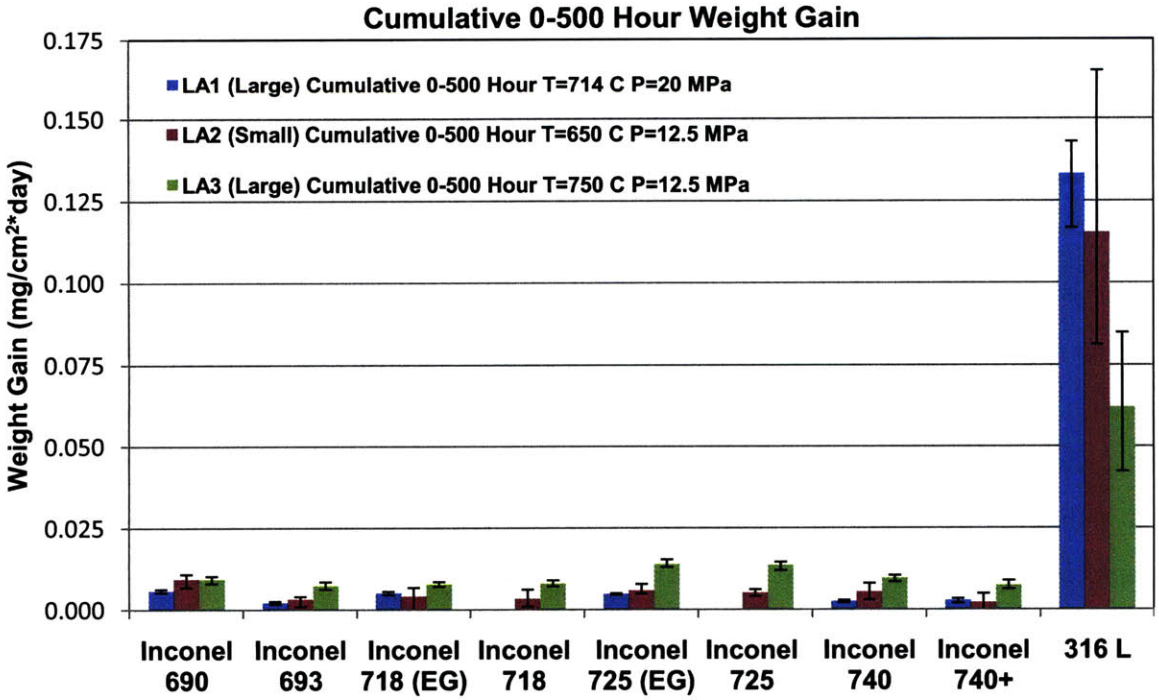

Figure 36: Cumulative Weight Gain Rate at 500 hours for all Experiments

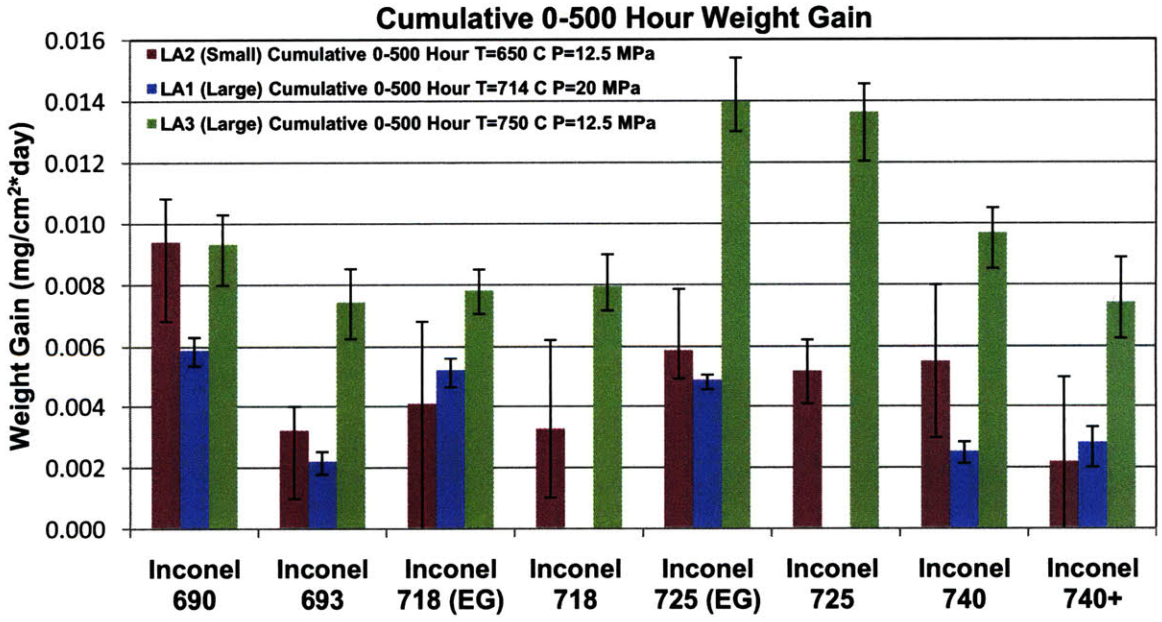

Figure 37: Cumulative Weight Gain Rate Comparison on Nickel Alloy at 500 hours for all Experiments

5.1.5 Comparison of AUSS 316L in LA1 and LA2 to Similar Experiments

Similar experiments involving AUSS 316L subjected to SCO_2 were conducted at the University of Wisconsin (WIS) and previously at the Massachusetts Institute of Technology (MIT) (29) (30). These tests exposed AUSS 316L to temperatures and pressures of 650 °C and 20 MPa and 600 °C and 20 MPa respectively. The sample geometry for both the MIT and WIS samples were the same as the large samples used in the LA1 (T= 714 °C, P=20 MPa, large sample) and LA3(T= 750 °C, P=12.5 MPa, large sample) series for this testing regime. Based on the experiments run in this testing regime, it would be useful to compare the data collected from MIT and WIS to the LA1 (T= 714 °C, P=20 MPa, large sample) and LA2 (T= 650°C, P=12.5MPa, small sample) data, which were conducted at either the same pressure or temperature.

After 500 hours WIS obtained a cumulative weight gain rate of 0.0023 mg/cm^2*day, while MIT had a cumulative weight gain rate of 0.0016 mg/cm^2*day for the AUSS 316L. The LA2 experiment, which was run at the same temperature but different pressure, had a weight gain rate that was roughly 75 times larger. This large variance most likely cannot be attributed to the difference in pressure alone as there were other inconsistencies with the experiments, including: a smaller surface area with LA2 that could have introduced a large number of inhomogeneities including added stress, different heats of AUSS 316L which would change the sample composition, sample preparation and gas purity, and differences in data acquisition. In the MIT and WIS experiments data was recorded every 500 hours, while data was recorded every 250 hours for the results reported here. The extra data points added thermal stress into the sample as the system temperature and pressure was cycled an extra time.

The WIS data showed a low initial weight gain from 0-500 hours then an increase by almost a factor of 10 in the weight gain rate between 500-1000 hours, which indicates that a continuous protective film did not form within the first data point. This result was contrary to the data collected in both the LA1 and LA2 experiments and the one conducted at MIT, which showed a high initial weight gain rate that tailed off after the first time point. This suggests that a protective film formed within the first time point on the MIT, LA1, and LA2 experiments, which limited the transport of atmospheric species and metal ions across the film.

The LA1 experiment was run at the same pressure, but at a higher temperature, 714°C compared to 650°C used in the WIS and MIT experiments. The LA1 experiment had a weight gain rate of 0.13mg/cm^2*day while WIS and MIT had weight gain rates of 0.0023 mg/cm^2*day and 0.0016 mg/cm^2*day respectively. The LA1 experiment was expected to have a higher corrosion rate due to the higher temperature. If the Arrhenius equation is assumed to be an accurate representation of the corrosion rate then the predicted weight gain rate at 714°C, for WIS and MIT would be 0.044 mg/cm^2*day and 0.31 mg/cm^2*day respectively. As one can see there is a large discrepancy between the three trials, which indicates that the Arrhenius equation may not be an accurate representation of predicted weight gain for the AUSS 316L. Figure 36 also supports this as the highest temperature trial showed the least amount of weight gain for AUSS 316L.

5.2 Oxidation Kinetics

The oxidation kinetics were also important to examine in order to understand the scale growth rate. LA3 (T= 750°C P=12.5MPa) was the only experiment that contained enough data points in which information about the oxidation kinetics could be garnered. The weight gain associated with the oxidation growth in the AUSS 316L exhibited roughly linear kinetics of the following form:

$$w = kt \qquad [12]$$

w = Cumulative Weight Gain (mg/cm^2)
k = is a constant dependent on gas composition, operating temperature, pressure, moisture content, or alloy composition
t = Elapsed Time (hours)

The linear relationship was expected as a continuous outer layer of iron oxide was still forming on the specimen as Figure 38 illustrates. Once a continuous layer was formed, the kinetics were expected to shift to a parabolic shape of the form similar to the kinetics shown in the nickel based alloys:

$$w=at^b \qquad [13]$$

w = Cumulative Weight Gain (mg/cm^2)
a = Parabolic Rate Constant
t= Elapsed Time (hours)
b= Exponential Factor

All of the nickel based alloys showed parabolic kinetics with the exponential factor ranging from 0.587 to 0.565. As more time points are collected the exponential value is expected to decrease, because the first data point was abnormally large compared to subsequent data points due to the formation of the protective film. Once a continuous protective layer was formed the weight gain rate decreased as diffusion across the scale was limited by the dense oxide that formed. The parabolic kinetics suggested that the diffusion through the protective oxide was the rate-limiting step.

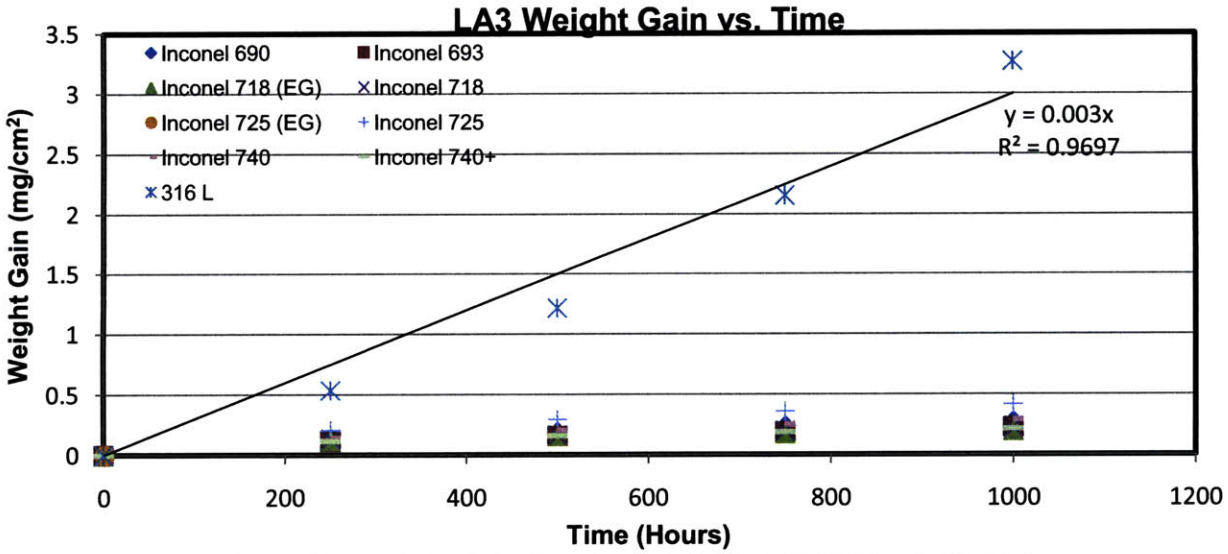

Figure 38: Weight Gain Data for LA3 (T= 750 °C P=12.5 MPa)

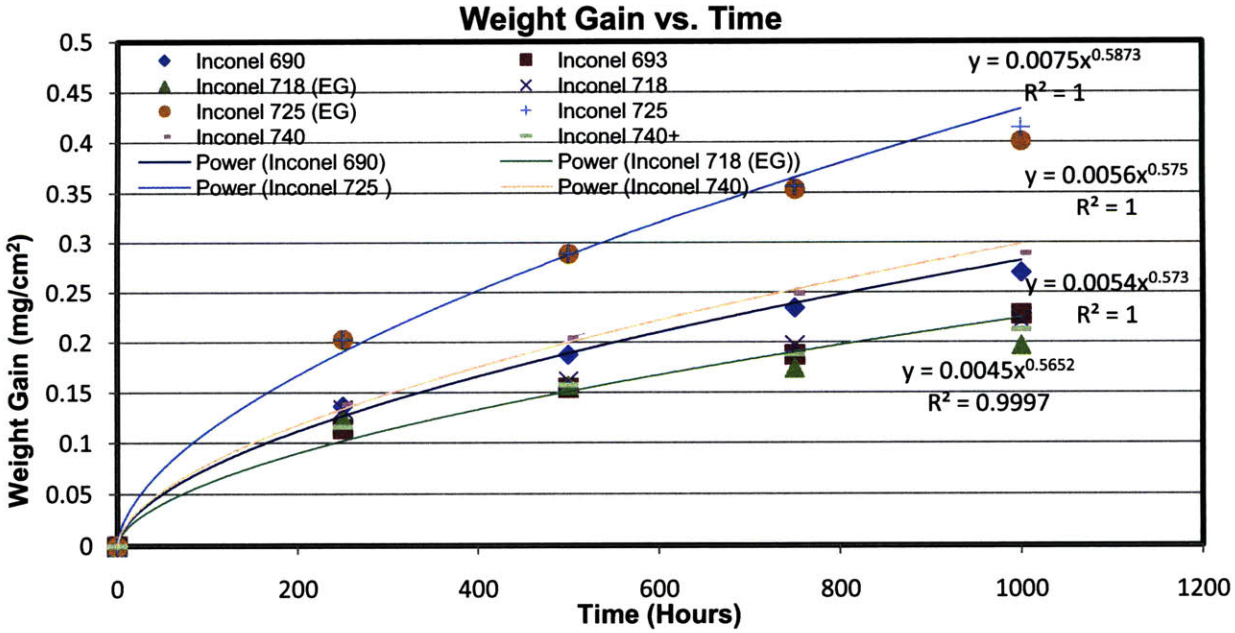

Figure 39: Weight Gain Data for the Nickel Based Alloys on LA3 (T= 750 °C P=12.5 MPa)

5.3 Oxygen Partial Pressure

Three pure metal samples of Au, Cu, and Fe were exposed to the conditions of the LA3 experiment (750 ºC and 12.5 MPa), which was done in order to determine the partial pressure of oxygen in the large autoclave at these conditions. As discussed in Section 2.3, the partial pressure of oxygen can be determined from the Ellingham diagram if both the temperature and oxide is known. Under these conditions the iron oxidized to form Fe_3O_4, while the gold and copper did not oxidize. Therefore according to the Ellingham diagram the partial pressure of oxygen at these conditions was somewhere between 10^{-10} atm (iron oxidation reaction) and 10^{-20} atm (the copper oxidation reaction). This is important as it demonstrates that any oxidation reaction which has a lower Gibbs free energy than the iron oxidation reaction is thermodynamically possible and any oxidation reaction that has greater than or the same amount of Gibbs free energy than the copper oxidation reaction is not possible. Additionally, as the oxygen partial pressure in the autoclave increases oxide stability decreases (7).

5.4 Surface Morphology and EDX

The surface morphology of the 500 hour samples were analyzed using the Scanning Electron Microscope (SEM) (the brightness and contrast on some images have been artificially altered to provide a crisper picture. However, no other adjustments of the images were made.) and Electron Dispersive X-ray Spectroscopy (EDX). As only the 500 hour samples were analyzed due to time constraints, more surface analysis is needed on other time points in order to determine the effect that time spent in the autoclave had on surface characteristics. Additionally, if one assumes that all of the weight gain was generated from the formation of a 50% nickel, 50% chromium oxide film, which was generally the case, the film thickness would be less than 1 micron. However, the EDX detects X-rays emitted beneath the first few microns of the specimen surface, therefore the detector will pick up signal not only from the film, but also the bulk matrix as well.

5.4.1 Inconel 690

Inconel 690 is an austenitic solid-solution hardened nickel based alloy, that has a low solubility for carbon, and its microstructure normally contains carbides. The major carbide present in the alloy is of the $M_{23}C_6$ type; in addition to nitrides, carbides, and carbonitrides (40).

LA1-02 (Inconel 690, T=714 °C, P=20 MPa)

Figure 40 shows LA1-02 (Inconel 690, T=714 °C, P=20 MPa) formed a stable continuous oxide film, however, there was preferential corrosion around the mounting hole. This continuous oxide explains the low weight gains as it prevented oxygen, carbon, and metal ion transport across the scale. EDX spectrums shown in Figure 41 and Figure 42 showed that the external scale likely consisted of a chromium-nickel spinel, with a few "islands" composed of chromium oxide, most likely Cr_2O_3. Due to the proximity in energy level between the x-rays emitted from the oxygen K electron shell and the Ti, Cr, Mn, Ni, and Fe L electron shells it was difficult to distinguish quantitatively between the EDX peaks. The surface characteristics support the fact that in nickel-chromium alloys, NiO is the first oxide to form. Then, over time the chromium metal diffuses, mostly through the grain boundaries, to the metal scale interface to form a complete chromia scale underneath the NiO as discussed in Section 2.2.1. This could explain why only a few "islands" of chromium oxide were formed, perhaps the surface NiO scale flaked off, or there were underlying inhomogeneities which favored chromium oxide formation.

Additionally, titanium precipitates were found throughout the surface of the sample, penetrating the protective film. Although there was no titanium listed from the manufacturer, Special Metals, for Inconel 690 trace amounts were probably present in the bulk matrix which formed the precipitate. The precipitates were square and blocky which indicates that they were most likely carbides or carbonitrides, however it was impossible to determine quantitatively with the EDX due to its poor sensitivity to light elements, carbon/nitrogen in particular. The composition of the precipitates was supported by the product manual, which states that alloy 690 was solution-hardened with γ' precipitates, which normally contains carbides of the $M_{26}C_6$ type (48). The Gibbs free energy associated with forming both carbides and nitrides is negative, which supports that this reaction is theoretically possible. The carbides and nitrides could have formed when titanium in the bulk matrix reacted with the SCO_2 to form the precipitate. The resulting reaction products occupy more space than the reactants, causing the precipitates to

expand and protrude out of the film. These precipitates may have deleterious effects on fatigue as they would make excellent crack initiation sites. Also the location of the precipitates and the localized chromium enriched areas may be a result of close proximity to grain boundaries where diffusion is much faster. Additionally, the LA2-02(T= 650 °C, P=12.5 MPa, small sample) specimen had a similar morphology containing an external Ni-Cr spinel film. Ti precipitates were also found scattered on the surface and the SEM images and EDX are located in Appendix C.

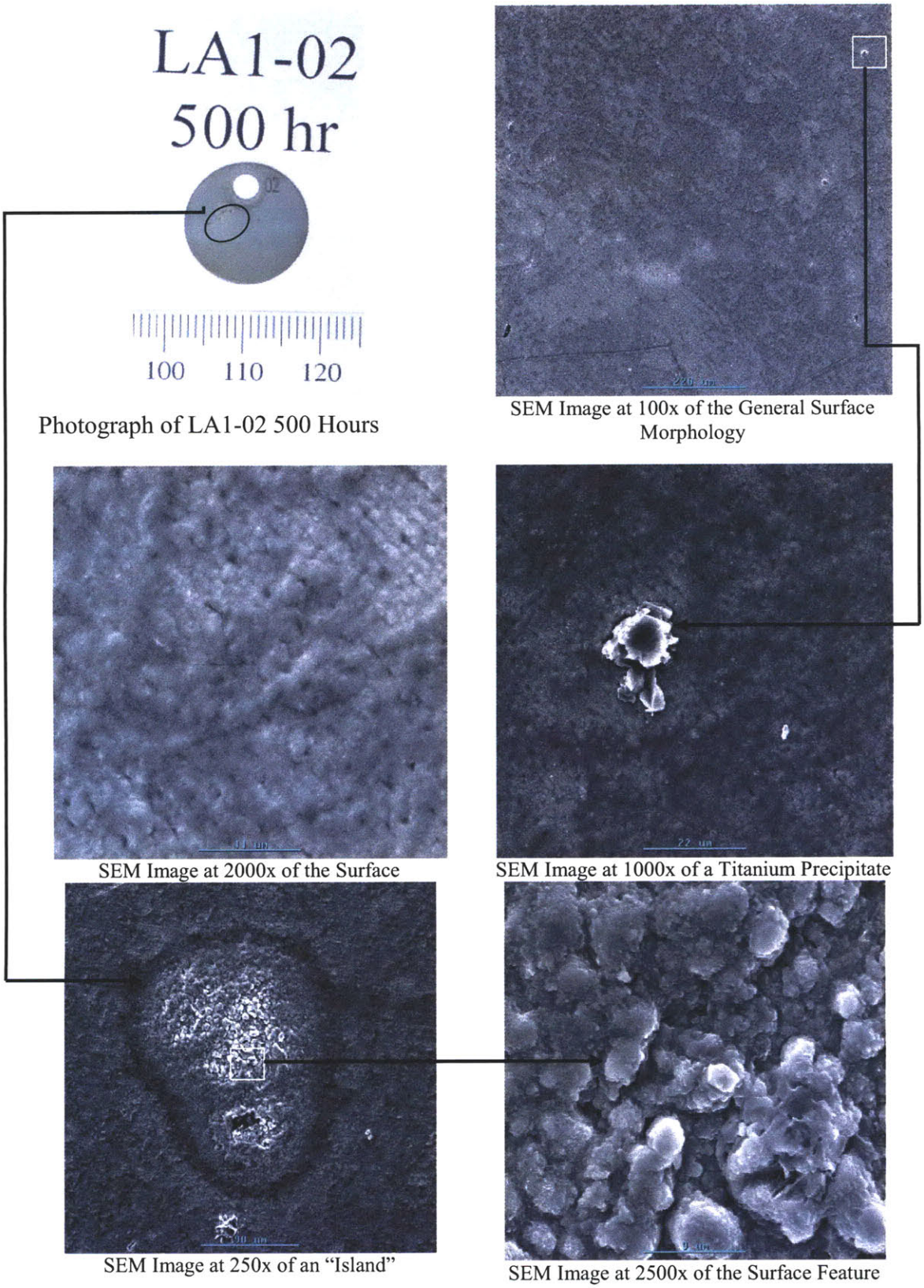

Photograph of LA1-02 500 Hours

SEM Image at 100x of the General Surface Morphology

SEM Image at 2000x of the Surface

SEM Image at 1000x of a Titanium Precipitate

SEM Image at 250x of an "Island"

SEM Image at 2500x of the Surface Feature

Figure 40: Surface Morphology for LA1-02 (Inconel 690 T=714 °C P=20 MPa) After 500 Hours of Exposure

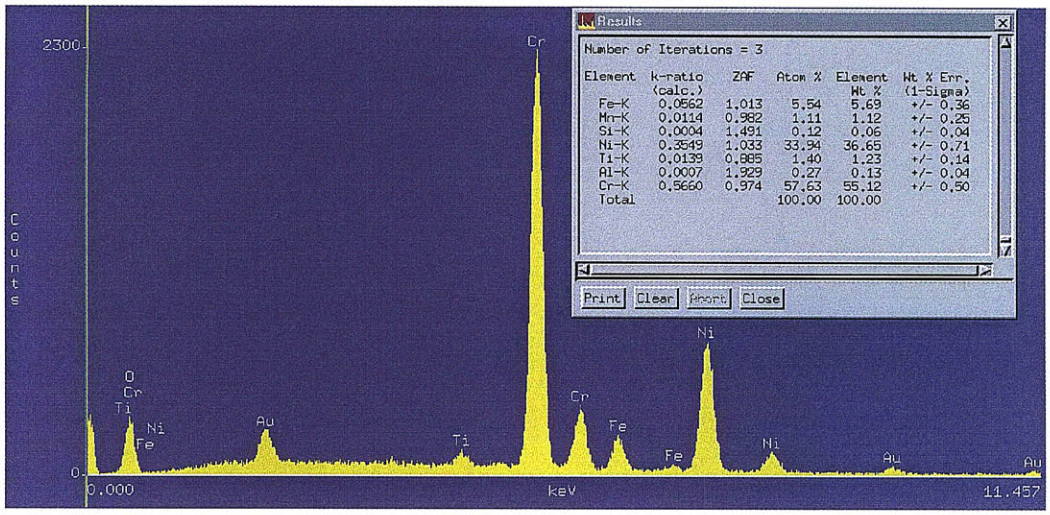

Figure 41: EDX at 10000x of the Surface Layer for LA1-02

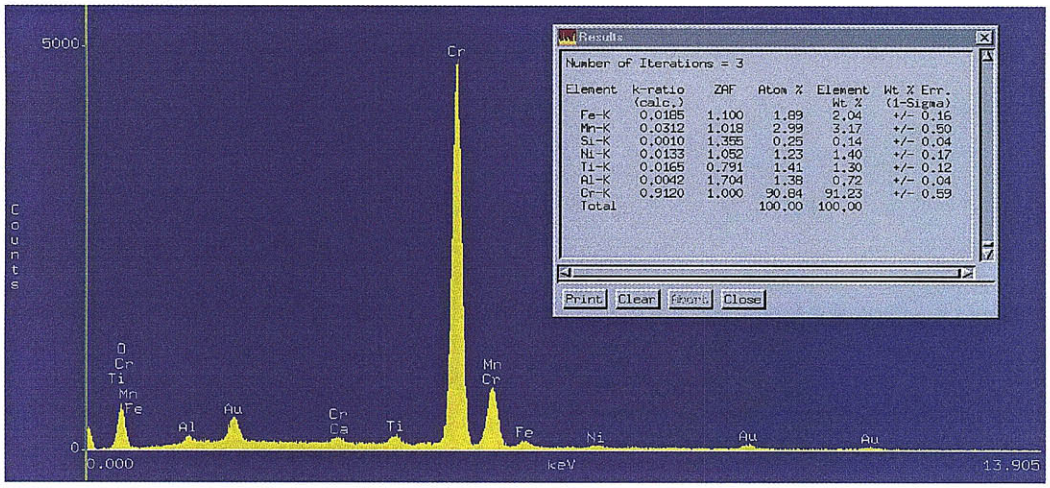

Figure 42: EDX at 2500x of the "Island" for LA1-02

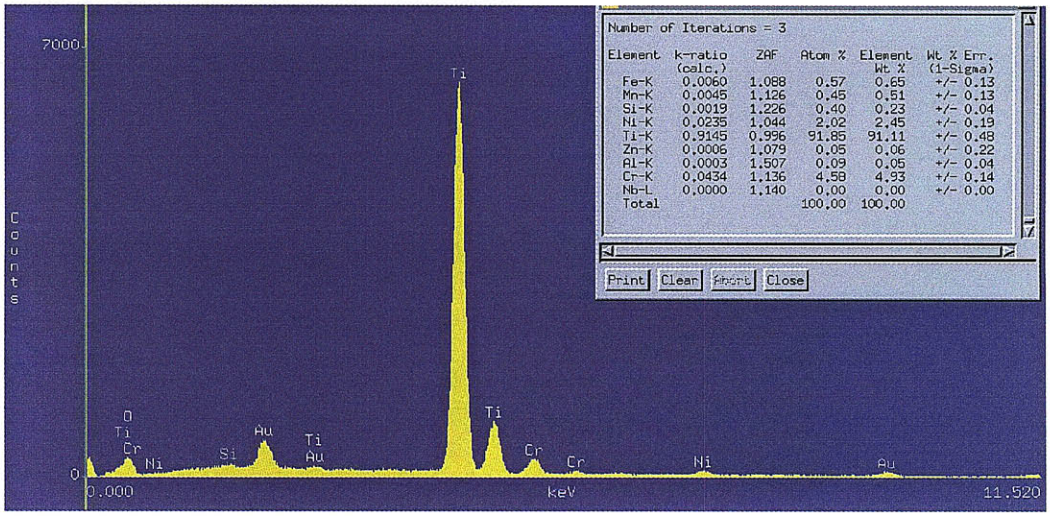

Figure 43: EDX at 75000x of the Titanium Precipitate for LA1-02

LA3-02 (Inconel 690, T=750 °C, P=12.5 MPa)

LA3-02 (Inconel 690, T=750 °C, P=12.5 MPa) showed a different surface morphology compared to the other Inconel 690 specimens. Figure 44 shows clear grain boundaries on the surface of the alloy. This indicates that the higher temperature exposure may have caused the alloy to suffer localized chromium depletion (sensitization). Sensitization occurs when chromium reacts with carbon forming insoluble chromium carbides ($Cr_{23}C_6$ or Cr_7C_3) that precipitate out at the grain boundary. However, if there is an adequate amount of either niobium or titanium present in the alloy they will preferentially react with carbon, generally preventing sensitization. The chemical composition of Inconel 690, showed little to no titanium or niobium in the alloy, which indicated sensitization may have occurred. EDX shown in Figure 46 reveals that chromium, most likely carbides, formed on the grain boundaries. EDX spectra of the film revealed the same nickel-chromium spinel which was present on the other Inconel 690 samples.

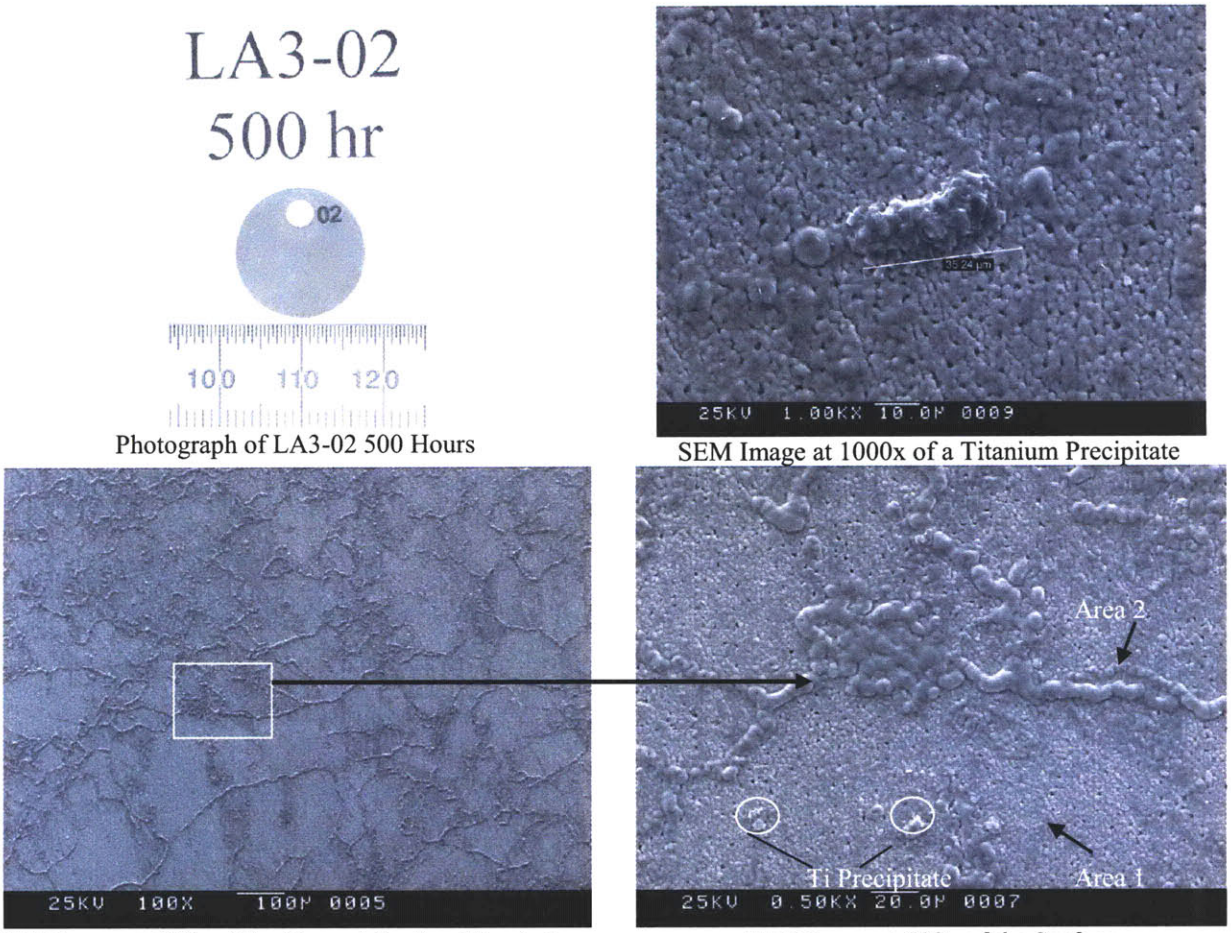

Photograph of LA3-02 500 Hours

SEM Image at 1000x of a Titanium Precipitate

SEM Image at 100x of the General Surface Morphology

SEM Image at 500x of the Surface

Figure 44: Surface Morphology for LA3-02 (Inconel 690 T=750 °C P=12.5 MPa) After 500 Hours of Exposure

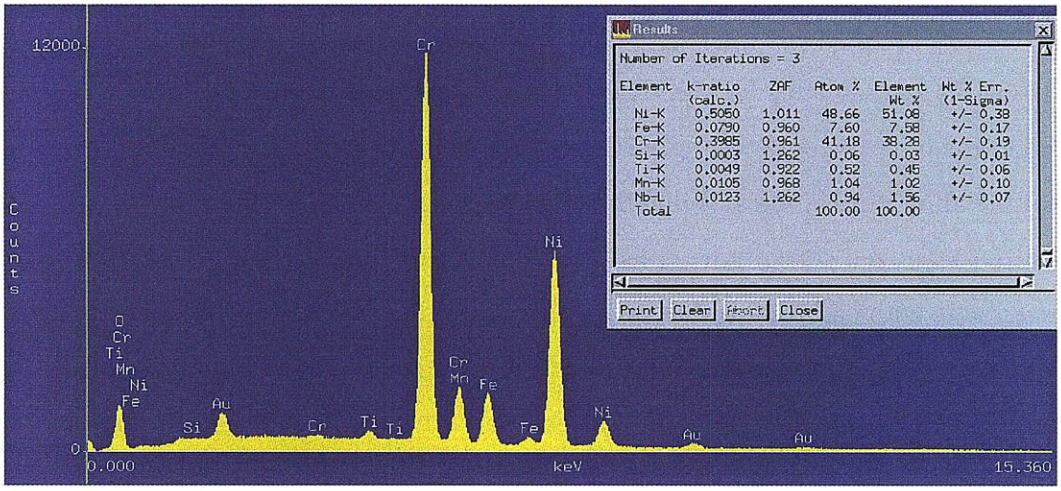

Figure 45: EDX at 7000x of Area 1 for LA3-02

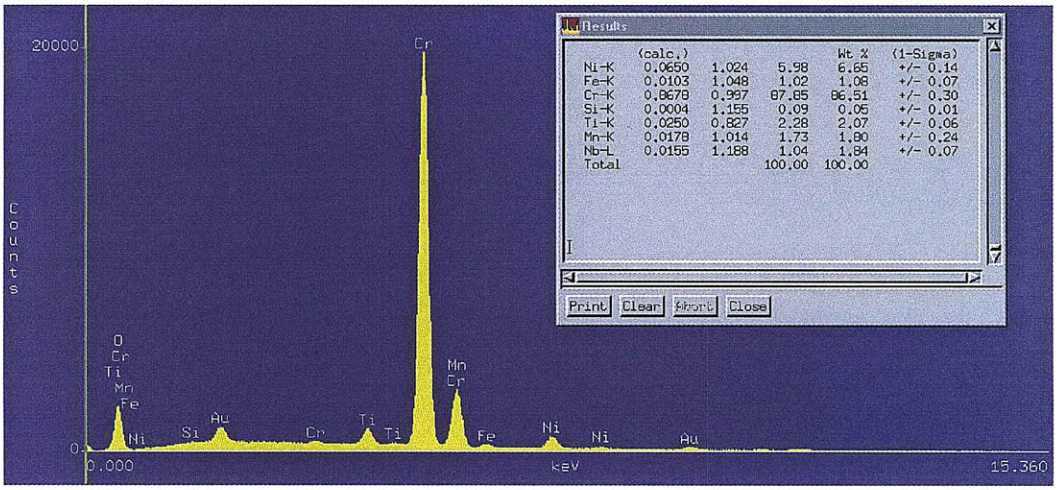

Figure 46: EDX at 10000x of Area 2 for LA3-02

5.4.2 Inconel 693

Inconel 693 is a solid-solution hardened, single-phase nickel based alloy and was supplied in the annealed condition and can precipitate second phases when exposed to intermediate temperatures (538° to 760°C). The major carbide present in the alloy is of the $M_{23}C_6$ type; in addition to titanium, niobium, aluminum, nitrides, carbides, and carbonitrides (40).

LA1-12 (Inconel 693, T=714 °C, P=20 MPa)

Inconel 693 was one of the best performing alloys in the whole testing regime and exhibited one of the lowest weight gains. The SEM images of LA1-12 (Inconel 693, T=714 °C, P=20 MPa) shown in Figure 47 demonstrate that both a light and dark oxide layer formed. The

light oxide layer appeared to have formed with the same orientation as the polishing direction. The oxide may have preferentially formed on the scratches caused by the silicon-carbide paper. The EDX spectrums shown in Figure 48 and Figure 49 demonstrate that the two oxides have very similar composition which indicates that the two oxide colors may be an artifact of the different thicknesses in the oxide.

The composition of the oxide was very similar to that found on alloy 690; however the oxide on alloy 693 had an aluminum peak, which may have aided in the formation of an underlying protective scale. This could explain why alloy 693 outperformed alloy 690. The protective film on alloy 693 was most likely thinner than that on 690 which would explain a smaller weight gain. This is supported by Figure 47 which shows a bluish tint on LA1-62 that indicates the film thickness was less than the wave length of blue light, 475 nm. Due to the small thickness of the film, the EDX analysis of the surface most likely received a strong signal from the underlying bulk matrix.

Ti, Nb, and Zr precipitates were also found throughout the surface, which is consistent with the composition of 693. These precipitates were most likely carbides, nitrides or carbonitrides, as group IV and V transition metals are very strong carbide and nitride formers (50).

Photograph of LA1-12 500 Hours

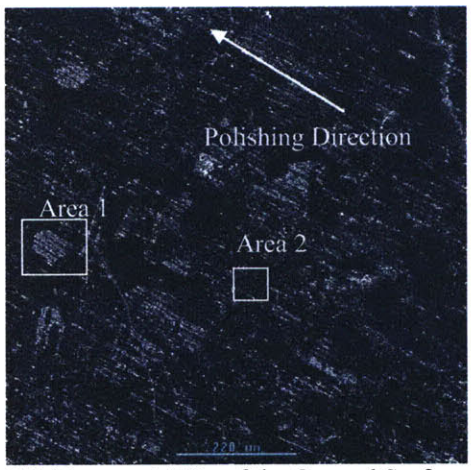

SEM Image at 100x of the General Surface Morphology

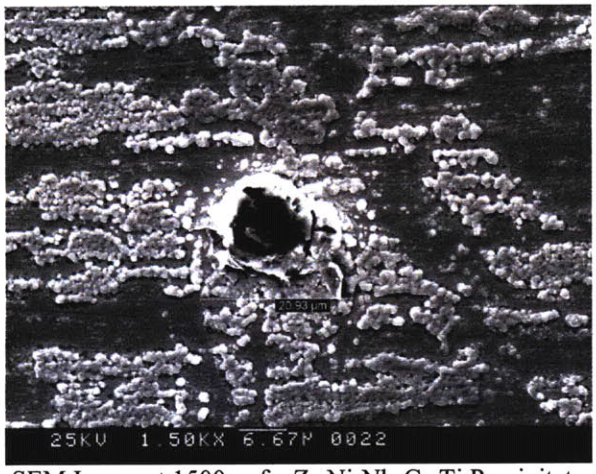

SEM Image at 1500x of a Zr-Ni-Nb-Cr-Ti Precipitate

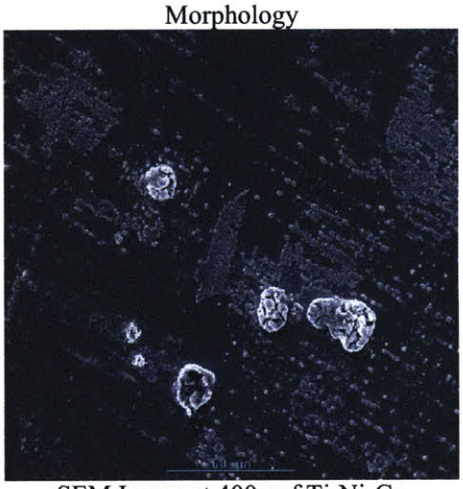
SEM Image at 400x of Ti-Ni-Cr Precipitates

Figure 47: Surface Morphology for LA1-12 (Inconel 693 T=714 °C P=20 MPa) After 500 Hours of Exposure

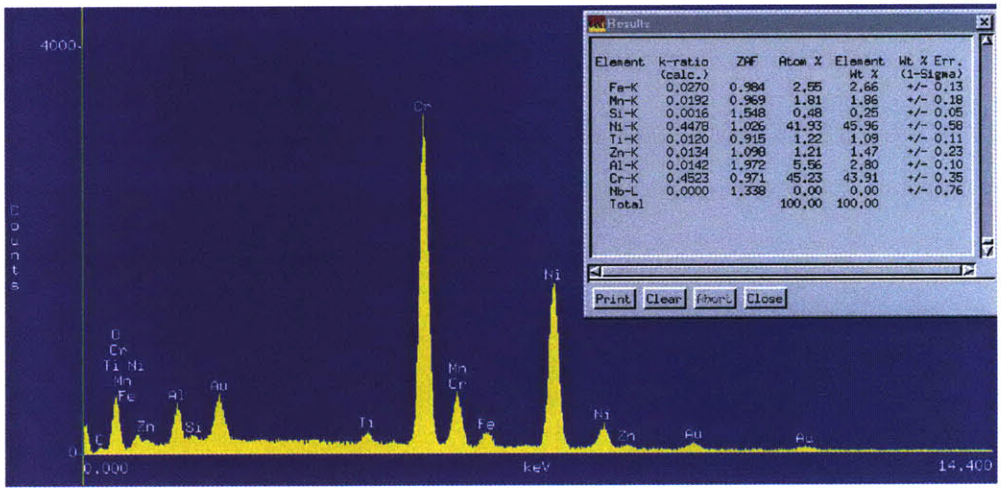

Figure 48: EDX at 100000x of Area 1 for LA1-12

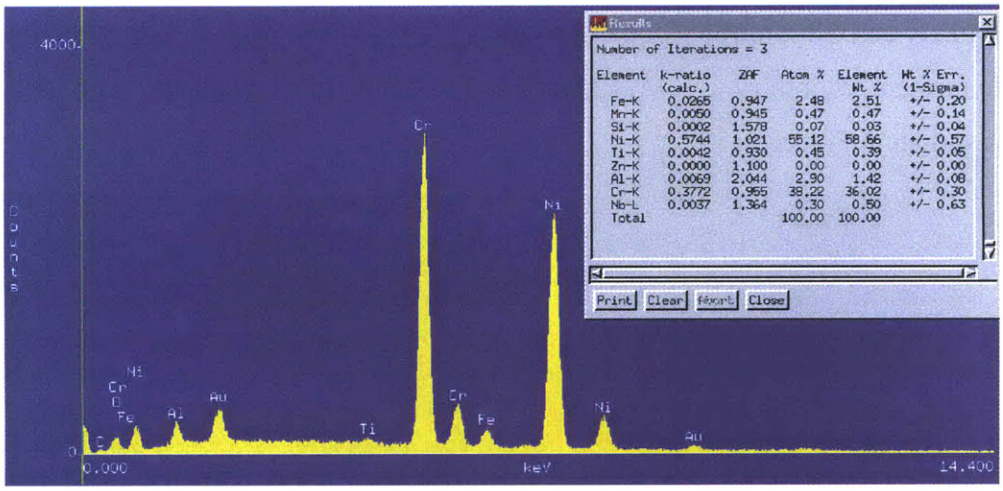

Figure 49: EDX at 100000x of Area 2 for LA1-12

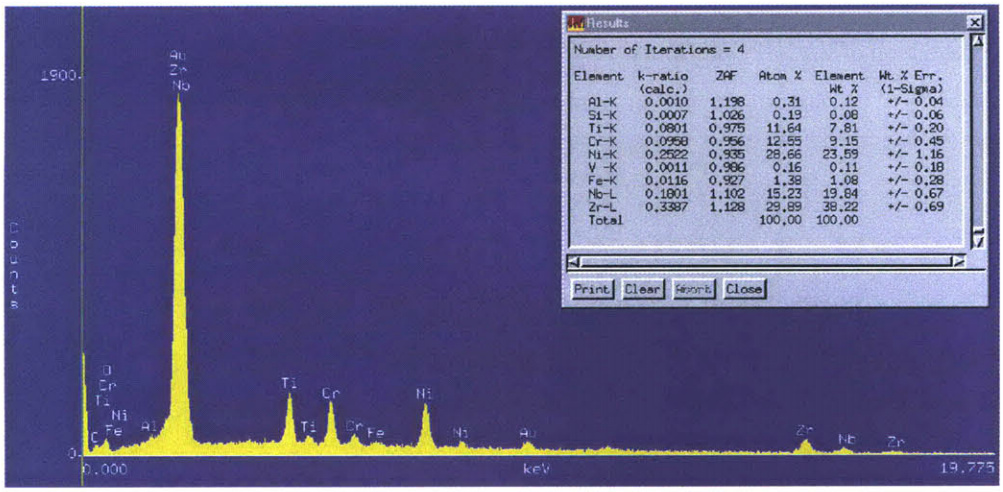

Figure 50: EDX at 40000x of the Zr-Ni-Nb-Cr-Ti Precipitate for LA1-12

LA2-12 (Inconel 693, T=650 ºC, P=12.5 MPa)

LA2-12 (Inconel 693, T=650 ºC, P=12.5 MPa) demonstrated a continuous oxide that was just in the initial stages formation. This was supported by the EDX spectrums shown in Figure 52 and Figure 53, which demonstrates that the oxide had a higher nickel content compared to the sample exposed to 750 ºC and 20 MPa. Additionally, the composition of the external scale was analogous to the composition of the bulk matrix. This was expected because the diffusion of the chromium would be smaller at a lower temperature. There seemed to be no difference in composition between the light and dark oxides, which indicates that they were just different thicknesses. Additionally, Ti, Nb, and Zr precipitates were found throughout the surface and

were most likely carbides, nitrides or carbonitrides, as group IV and V metals are strong carbide and nitride formers. Contrary to LA1-12 the Ni-Cr-Zr precipitates seemed to have grown in clusters as shown in Figure 51.

Photograph of LA2-12 500 Hours

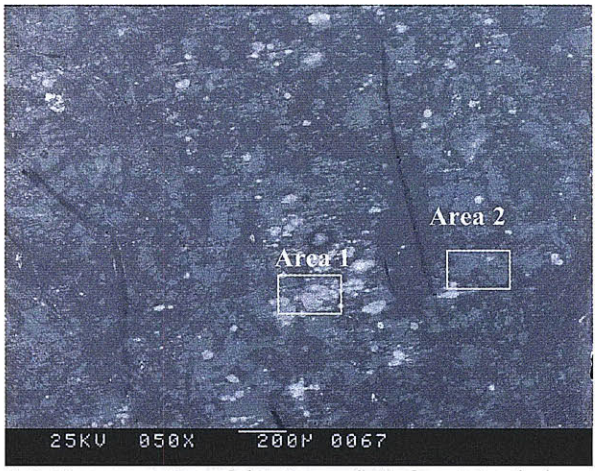

SEM Image at 50x of the General Surface Morphology

SEM Image at 1000x of a Ni-Cr-Zr Precipitate

SEM Image at 1500x of the Surface

SEM Image at 2500x of a cluster of Ni-Cr-Zr Precipitates

Figure 51 Surface Morphology for LA2-12 (Inconel 693 T=650 °C P=12.5 MPa) After 500 Hours of Exposure

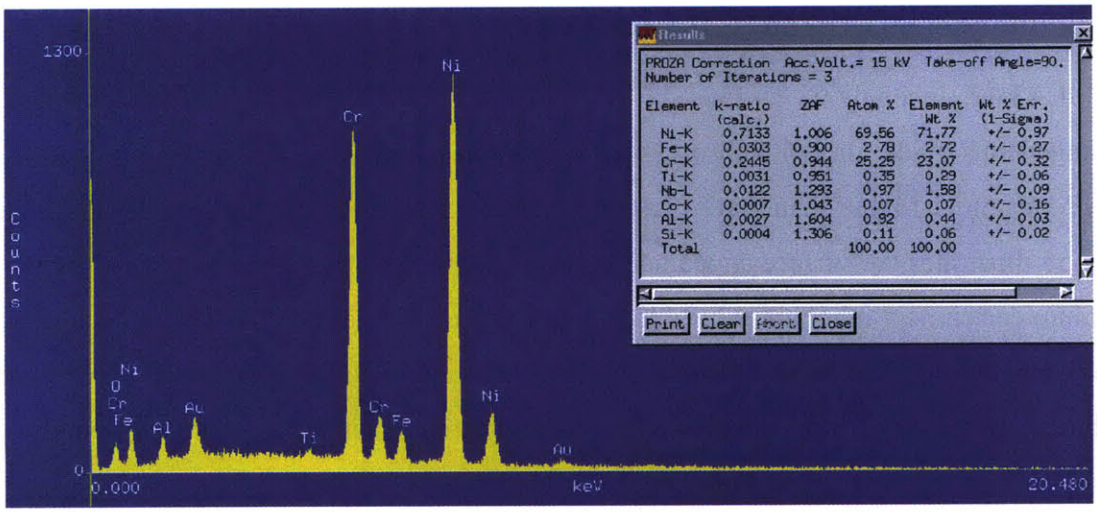

Figure 52: EDX at 150000x of Area 1 for LA2-12

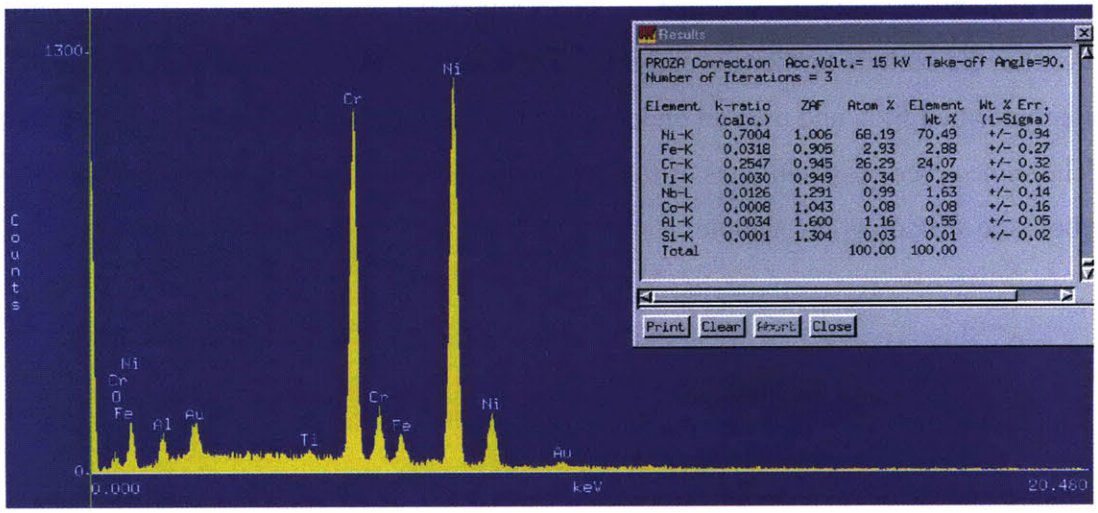

Figure 53: EDX at 150000x of Area 2 for LA2-12

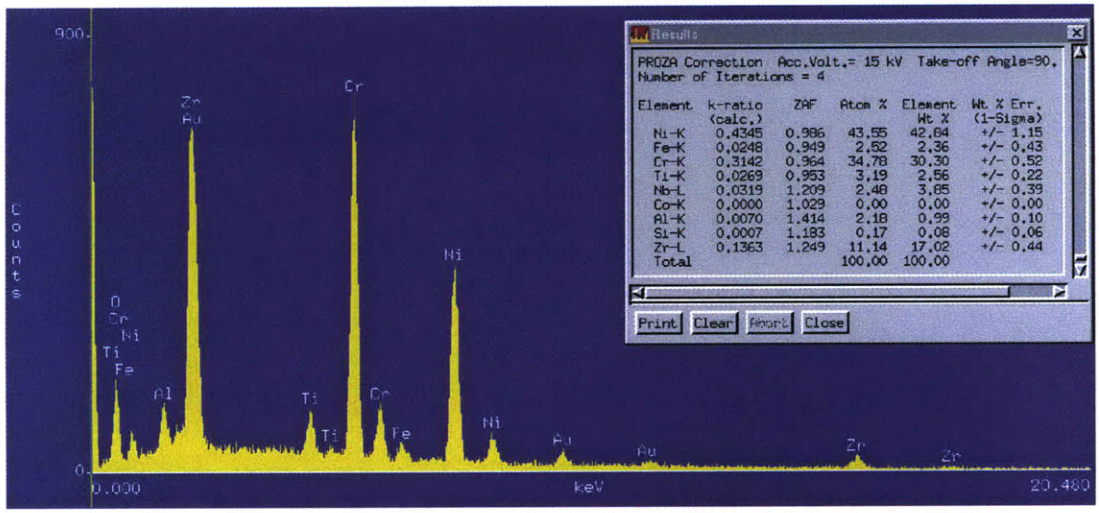

Figure 54: EDX at 150000x of a cluster of Ni-Cr-Zr precipitates for LA2-12

LA3-12 (Inconel 693 T=750 °C P=12.5 MPa)

LA3-12 (Inconel 693 T=750 °C P=12.5 MPa) showed a much more developed, but inhomogeneous oxide film with chromium enriched areas as high as 65%. The Cr content in LA3-12 was much higher than that of LA1 and LA2 which contained less than 45% Cr. As Figure 55 illustrates the surface appears to be very inhomogeneous, some areas have high chromium enrichment other areas have low chromium enrichment. Most likely the areas with higher chromium enrichment have a more developed scale. Additionally, these areas could have a higher degree of cold work, which would add dislocations increasing the surface energy causing preferential corrosion. These regions of localized enrichment could also be just above or very near a grain boundary that would act as an easy diffusion path for chromium ions from the matrix. The photograph of the specimen shows a bluish tint within the gray oxide, which indicates that the scale is further developed then alloy 693 from LA1. Furthermore, a NiO scale most likely formed first, and then an underlying chromium rich scale formed similar to alloy 690. The same types of precipitates as the other alloy 693 samples were found scattered throughout the surface of the sample.

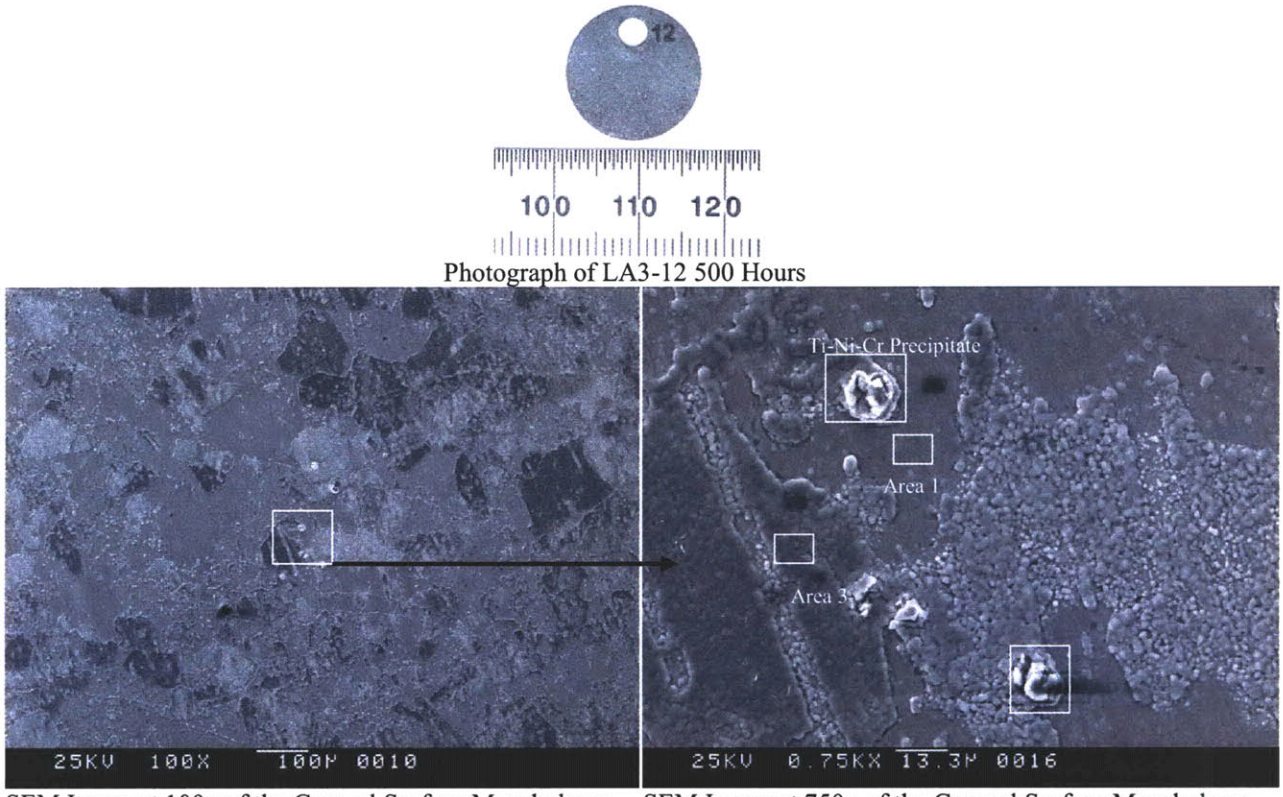

Photograph of LA3-12 500 Hours

SEM Image at 100x of the General Surface Morphology

SEM Image at 750x of the General Surface Morphology

Figure 55: Surface Morphology for LA3-12 (Inconel 693 T=750 ºC P=12.5 MPa) After 500 Hours of Exposure

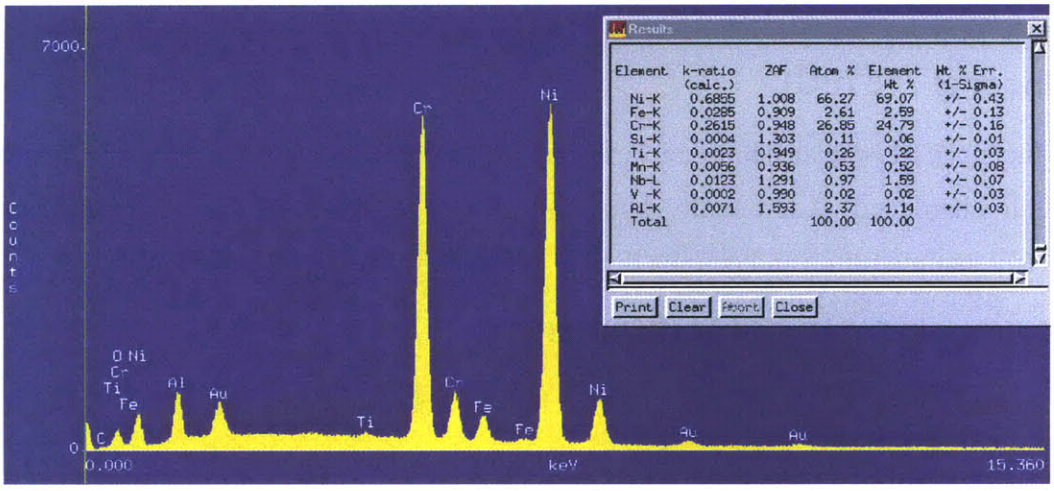

Figure 56: EDX at 20000x of Area 1 on LA3-12

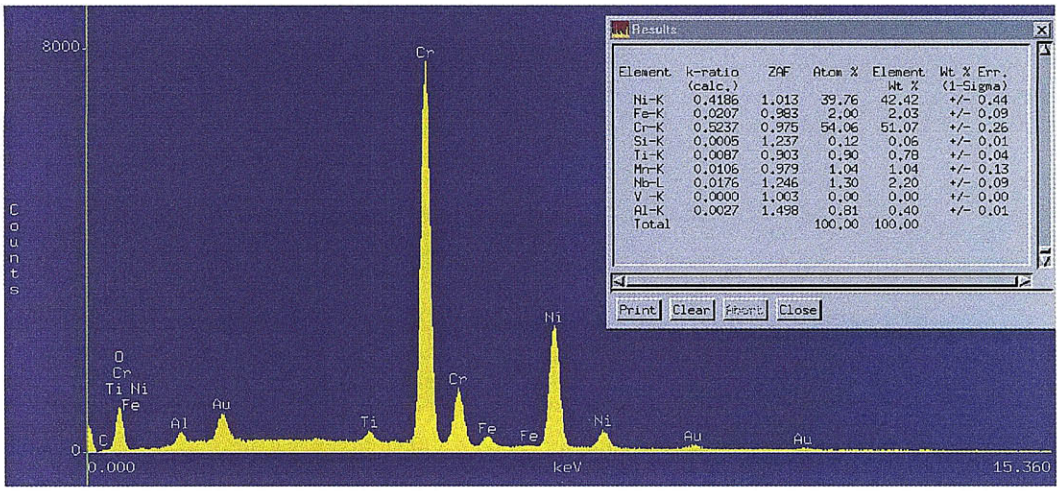

Figure 57: EDX at 15000x of Area 2 on LA3-12

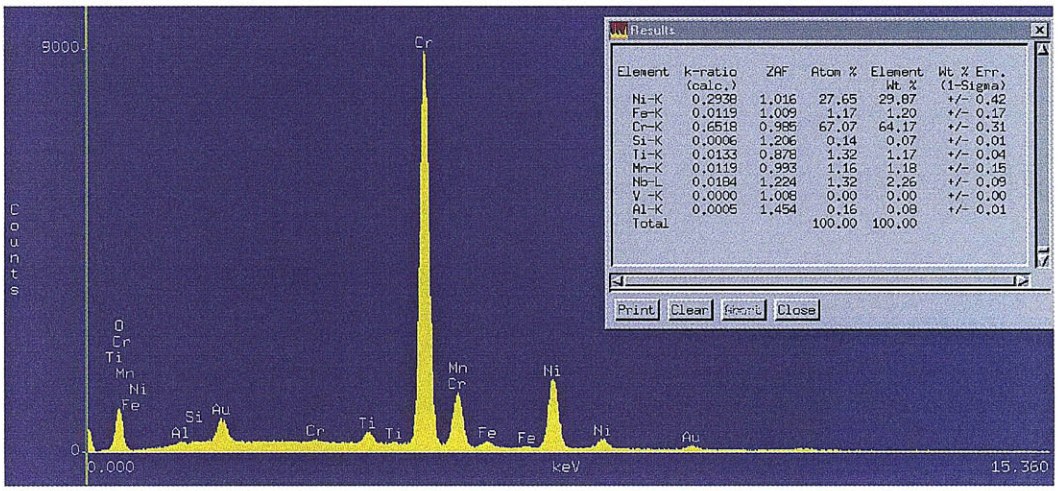

Figure 58: EDX at 15000x of Area 3 on LA3-12

5.4.3 Inconel 718 (EG)

Inconel 718 is an austenitic nickel-iron based alloy which has been solution annealed and precipitation hardened. Additionally, alloy 718 is hardened by the precipitation of secondary phases (e.g. gamma prime and gamma double-prime) into the metal matrix (40).

LA1-22 (Inconel 718, T=714 °C, P=20 MPa)

Inconel 718 was the alloy that had the highest concentration of precipitates on the surface. These precipitates consisted of Zr, Nb, and Ti, which was consistent with the alloy's composition. The brass colored film that formed on LA1-22 (Inconel 718, T=714 °C, P=20

MPa), which is shown in Figure 59, was not very well developed as the composition of the oxide was analogous to the composition of the underlying bulk matrix as shown in Figure 60.

Alloy 718 contained the highest iron content, which explains why there was a large Fe signal from the EDX. Therefore it came as no surprise that 718 had one of the highest weight gains for a nickel alloy in this experiment as iron has a high affinity for oxygen and thus the migration of cations into the scale is higher. Additionally, there appeared to be very little Si and Al content in the film, which can form a protective inner layer of oxide. The chromium content of the surface film was only 25%, which was significantly less than alloy 690 and 693 under the same conditions. The weight gain was high in alloy 718 compared to the other nickel alloys which indicated that the film should be thicker, and the low chromium content displayed in the EDX was most likely not just from the bulk matrix.

Photograph of LA1-22 500 Hours

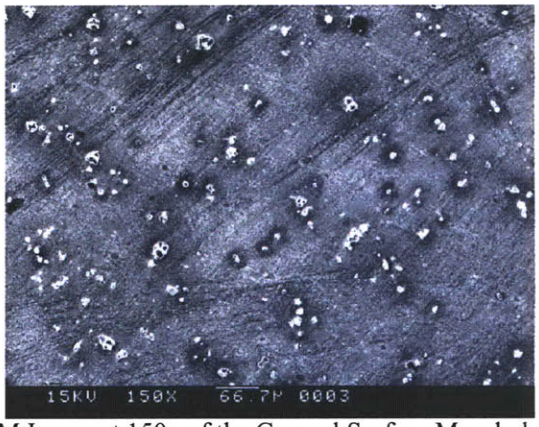

SEM Image at 150x of the General Surface Morphology

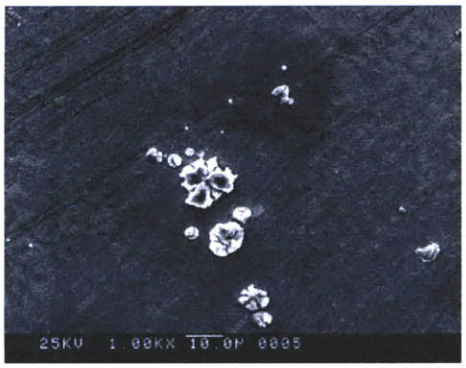

SEM Image at 1000x of Precipitates

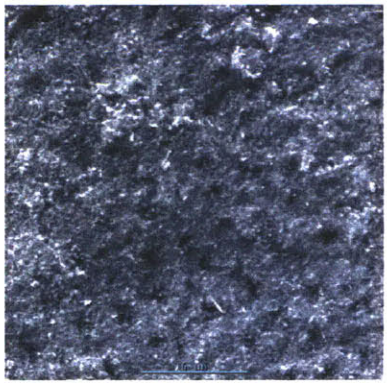

SEM Image at 4000x of the Surface

Figure 59: Surface Morphology for LA1-22 (Inconel 718 T=714 °C P=20 MPa) After 500 Hours of Exposure

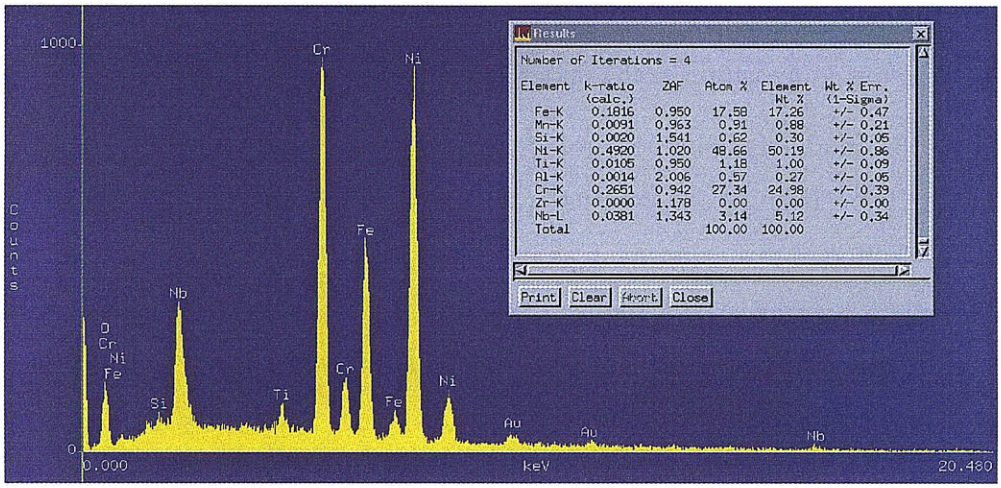

Figure 60: EDX at 30000x of the Surface on LA1-22

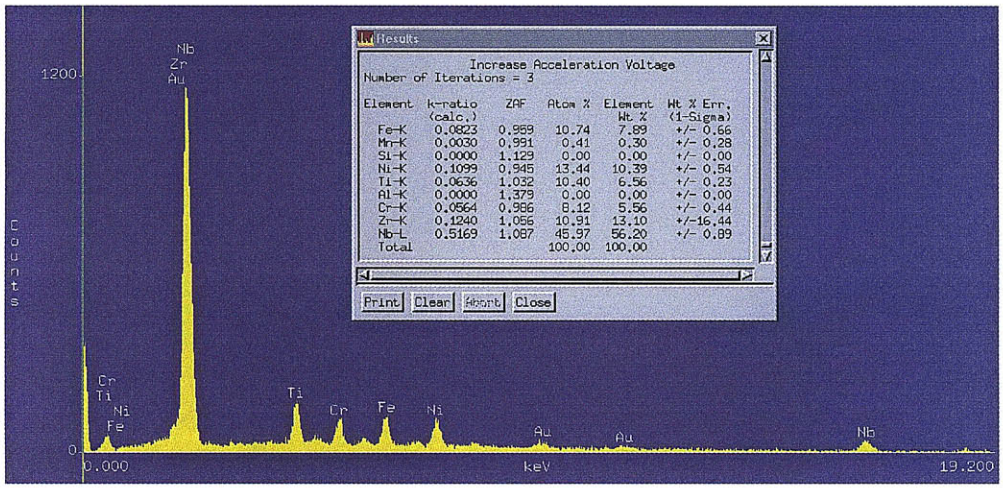

Figure 61: EDX at 50000x of the Precipitates on LA1-22

LA2-22 (Inconel 718, 650 ºC, and 12.5 MPa)

LA2-22 (Inconel 718, 650 ºC, and 12.5 MPa) showed a less continuous scale than LA1-22, with areas of localized corrosion. These areas had an iron enrichment that was greater than the composition in the bulk matrix which suggests that a Fe-Ni-Cr spinel formed. Additionally, the general oxide that formed consisted of only 20% chromium, which is roughly the amount contained in the bulk matrix. This shows that the diffusion rate of chromium through the matrix was low, and the external scale consisted mainly of nickel oxide. The uniform lines shown in Figure 62 are most likely scratch marks caused by the polishing process. Again LA2-22 formed the same types of precipitates as LA1-22 and the EDX spectrums can be found in Appendix C.

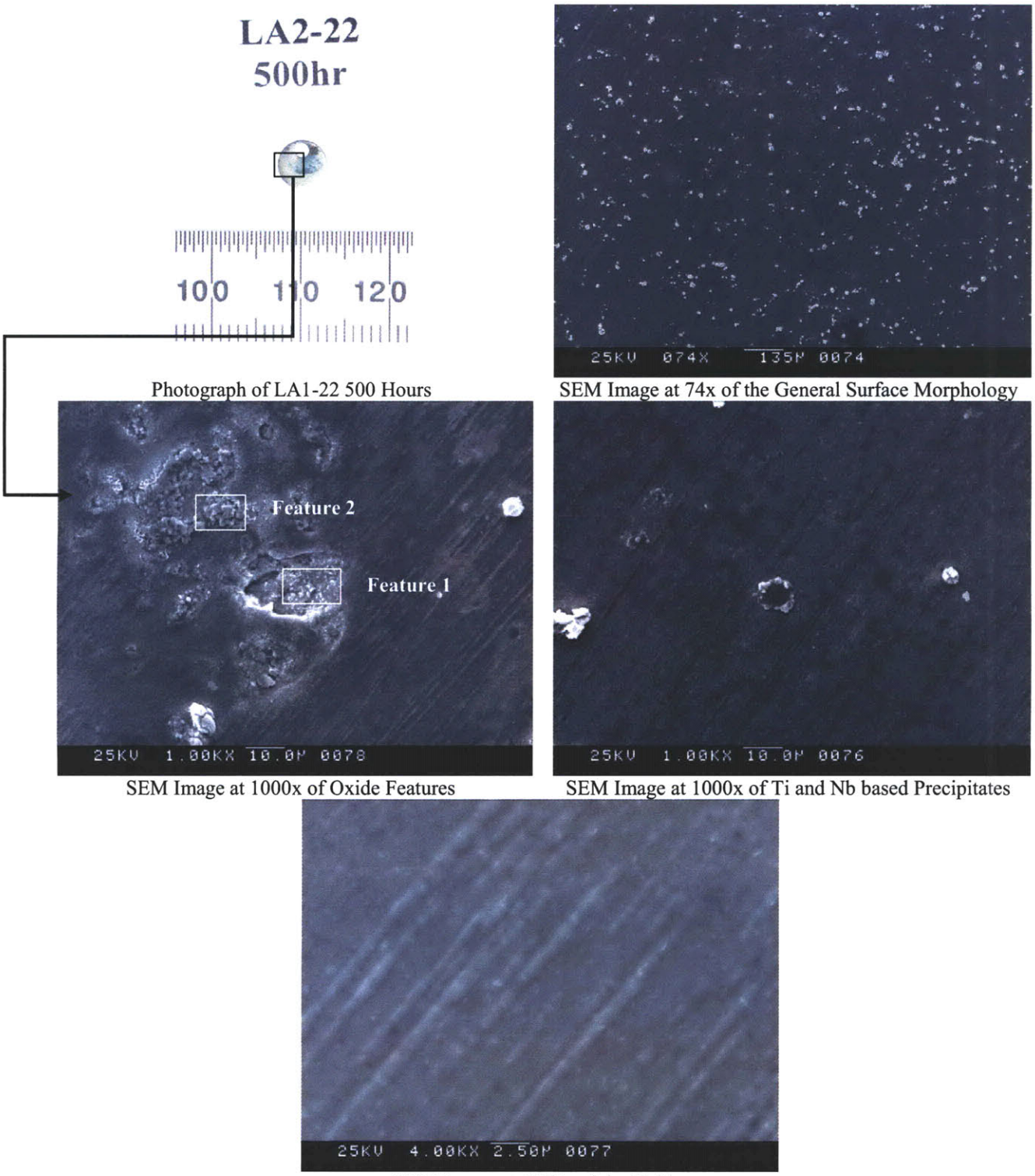

Photograph of LA1-22 500 Hours

SEM Image at 74x of the General Surface Morphology

SEM Image at 1000x of Oxide Features

SEM Image at 1000x of Ti and Nb based Precipitates

SEM Image at 4000x of the Oxide

Figure 62: Surface Morphology for LA2-22 (Inconel 718 T=650 ºC P=12.5 MPa) After 500 Hours of Exposure

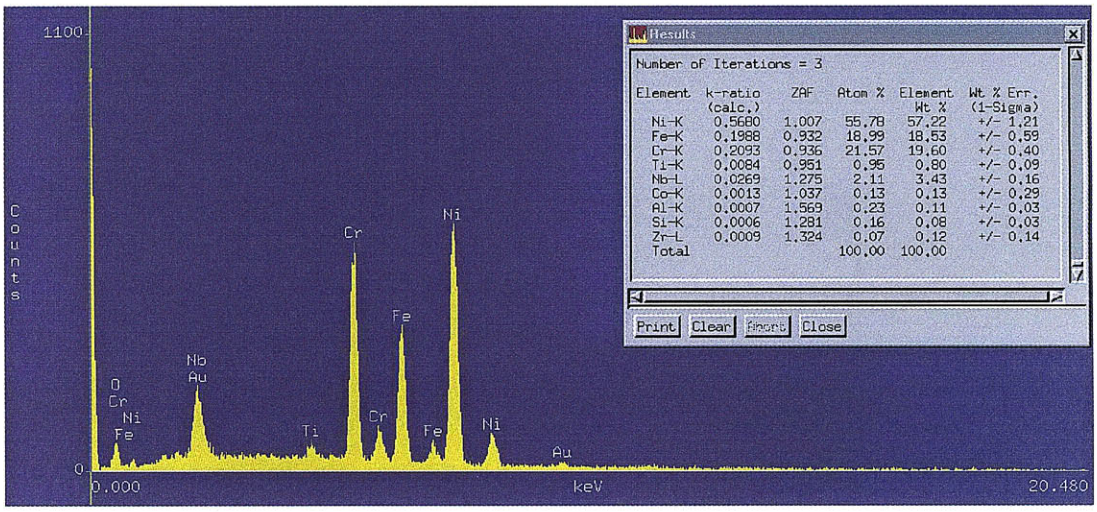

Figure 63: EDX at 100000x of the oxide on LA1-22

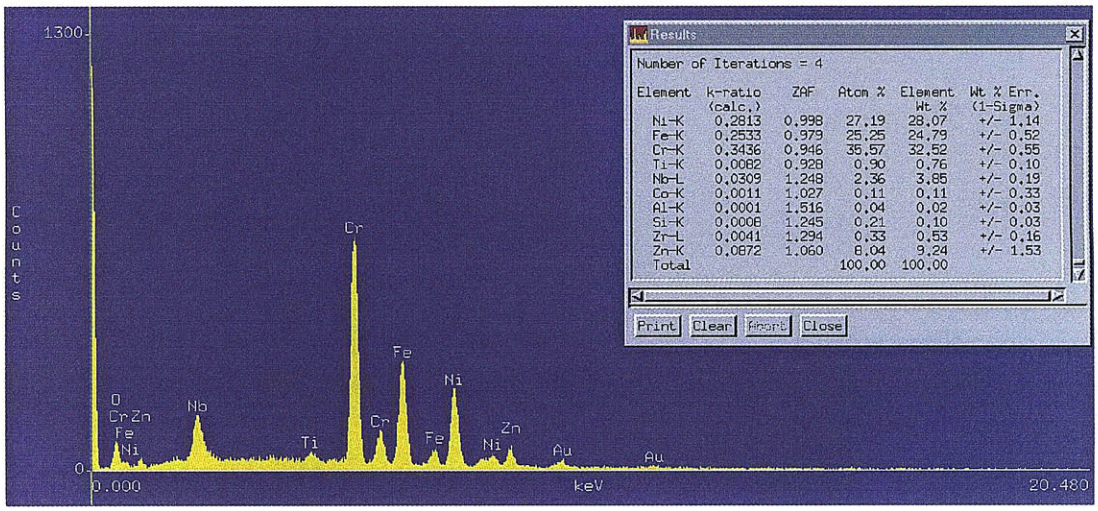

Figure 64: EDX at 100000x of Feature 1 on LA1-22

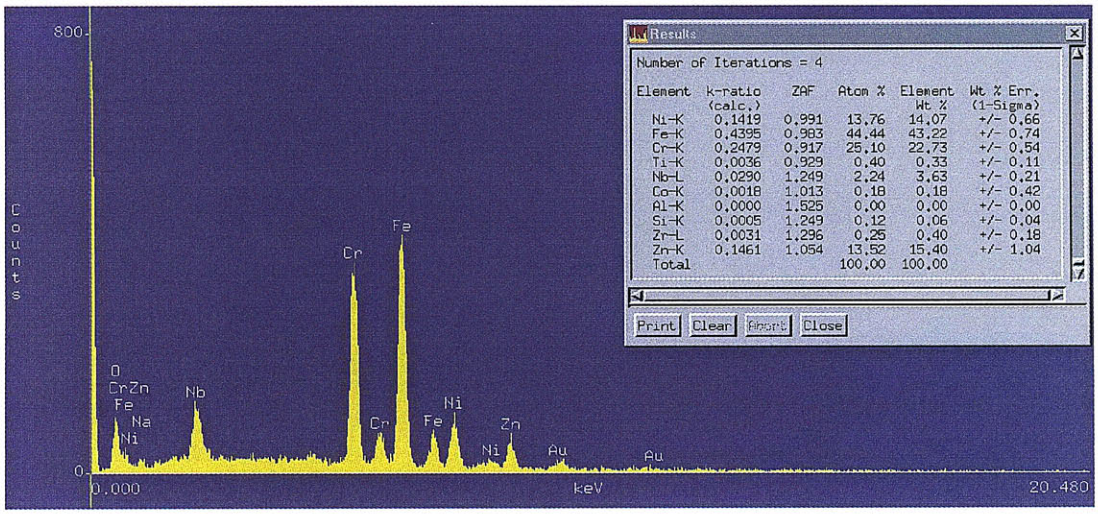

Figure 65: EDX at 100000x of Feature 2 on LA1-22

LA3-22 (Inconel 718, T=750°C, P=12.5MPa)

LA3-22 (Inconel 718, T=750 °C, P=12.5 MPa) demonstrated the most developed oxide layer compared to the other alloy 718 samples as seen in Figure 74. The oxide had the highest chromium content, 60% compared to less than 30% for the other alloy718 samples, and about half as much iron. This suggests that the external scale most likely consisted of a Cr-Ni spinel. The specimen also contained two different types of precipitates that formed on the surface, large and small ones. The large precipitates consisted mostly of Ti and Nb, the EDX spectrums can be viewed in Appendix C. The small precipitates consisted mainly of chromium and were only found near the edge of the sample, where preferential corrosion is likely to occur due to the higher concentration of stress. Additionally, the 718 samples that were cut perpendicular to the rolling direction had a very similar surface morphology as the samples cut parallel to the rolling direction; the SEM images and the EDX spectra for the samples cut perpendicular to the rolling direction can be found in Appendix C. The similar surface morphologies were expected as both sets of samples had analogous corrosion rates.

Photograph of LA3-22 500 Hours

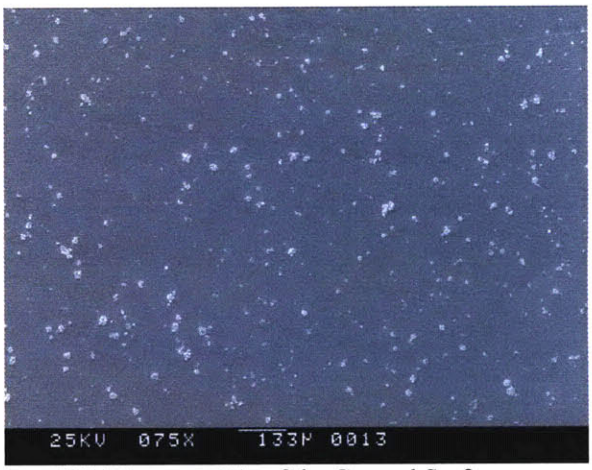

SEM Image at 75x of the General Surface Morphology

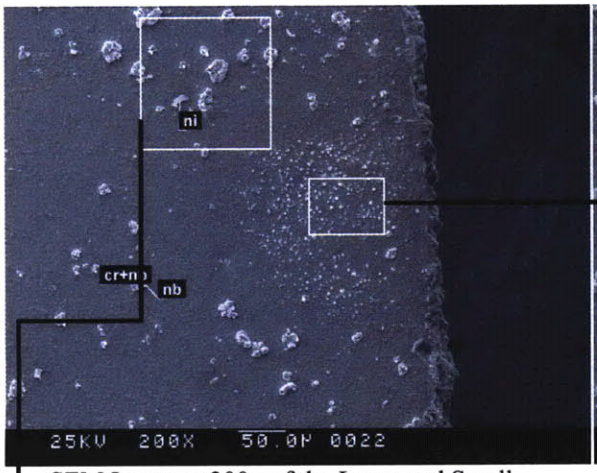

SEM Image at 200x of the Large and Small Precipitates

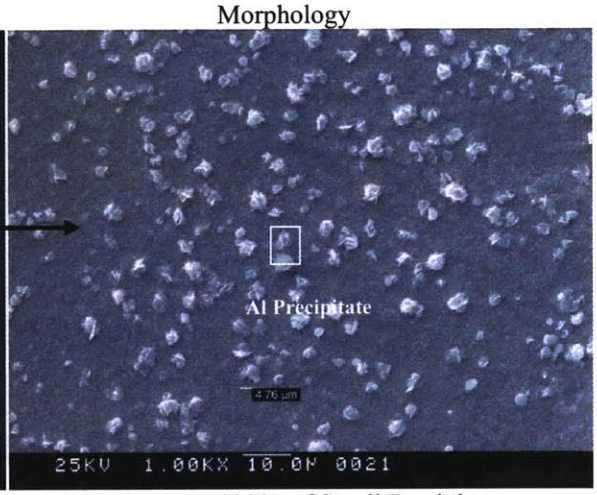

SEM Image at 1000x of Small Precipitates

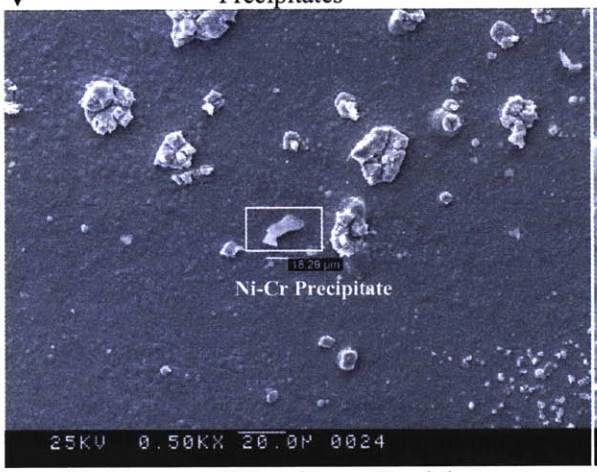

SEM Image at 500x of Large Precipitates

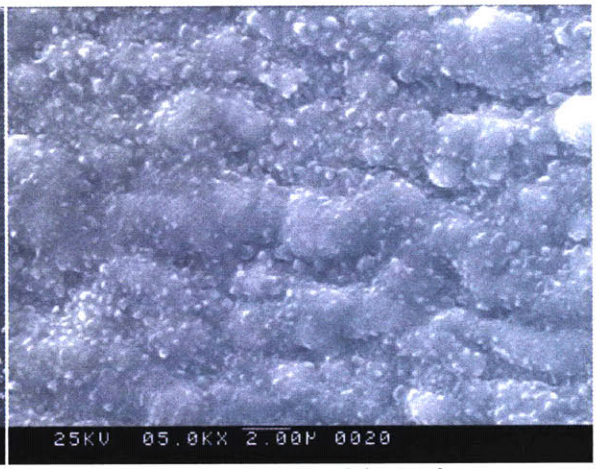

SEM Image at 5000x of the Surface

Figure 66: Surface Morphology for LA3-22 (Inconel 718 T=750 °C P=12.5 MPa) After 500 Hours of Exposure

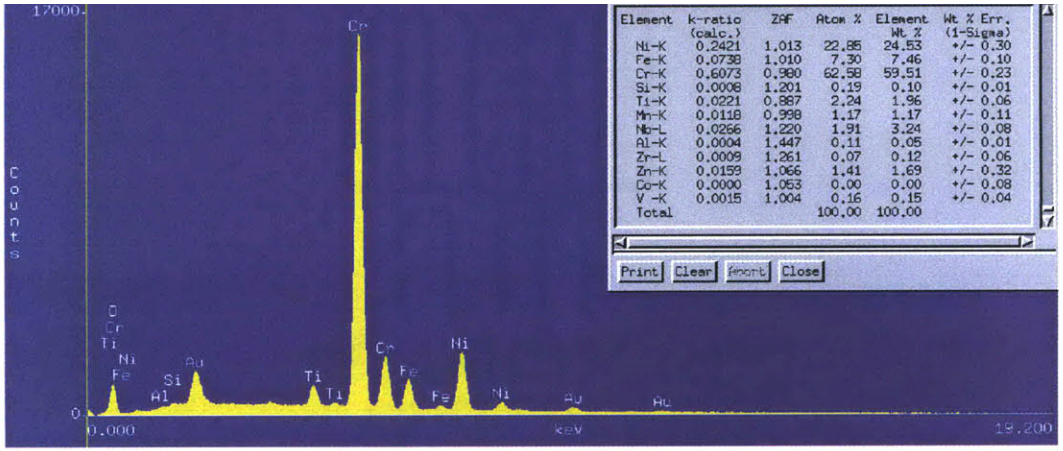

Figure 67: EDX at 30000x of the Surface on LA3-22

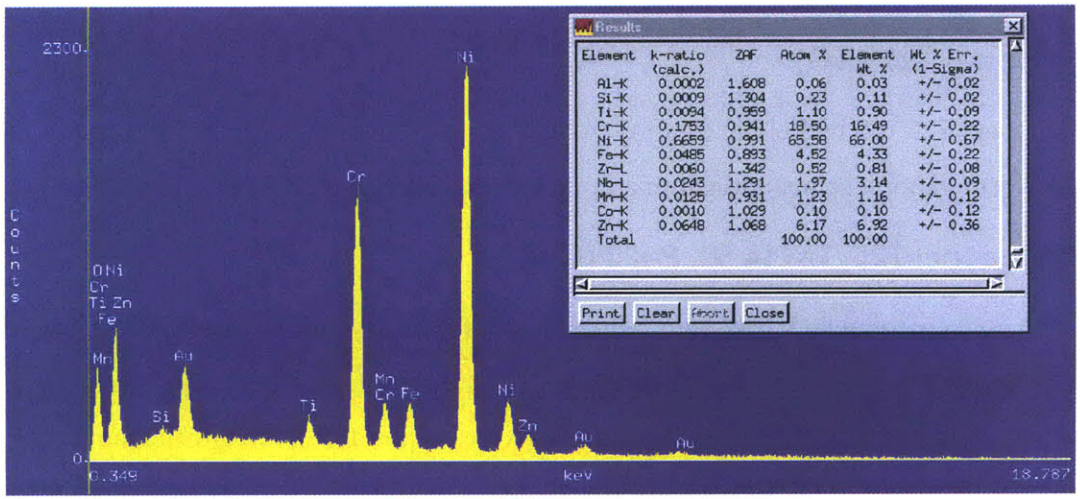

Figure 68: EDX at 100000x of Ni-Cr Precipitate on LA3-22

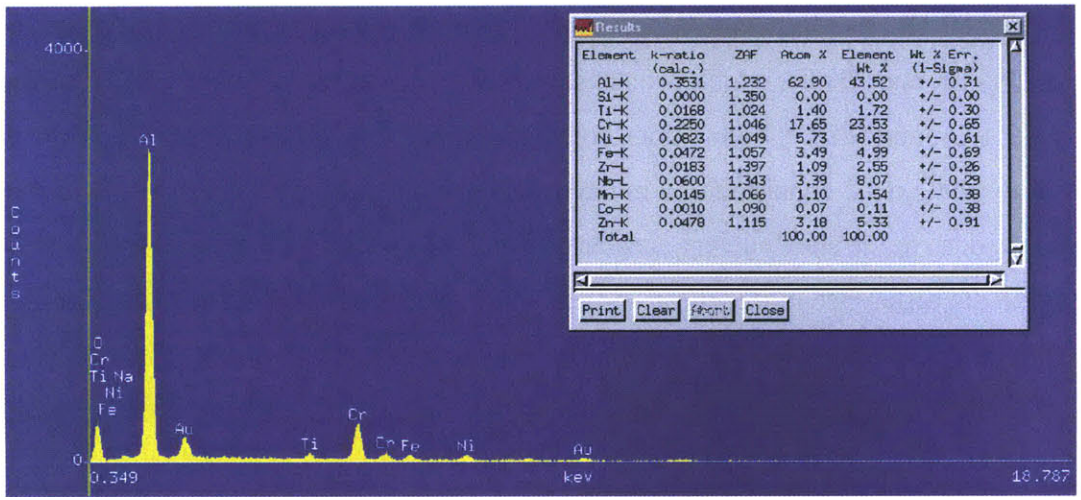

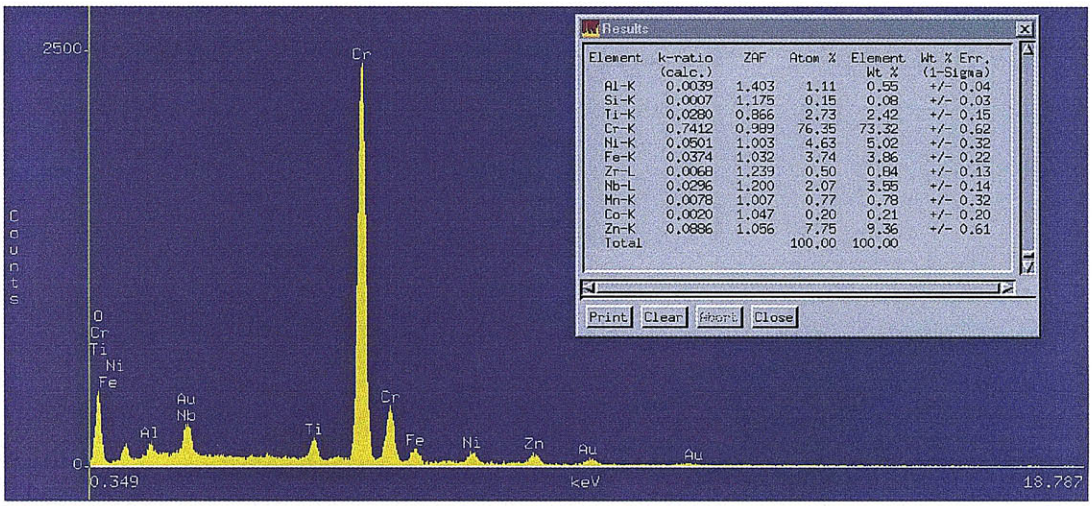

Figure 70: EDX at 150000x of the Small Precipitates on LA3-22

5.4.4 Inconel 725 (EG)

Inconel 725 is a nickel based alloy, which is precipitation hardened that contain Ti, Nb, and Al to form gamma prime and gamma double prime precipitates for strength (40).

LA1-32 (Inconel 725, T=714 °C, P=20 MPa)

LA1-32 (Inconel 725, T=714 °C, P=20 MPa) formed a continuous protective scale, that showed little to no signs of localized corrosion. The images in Figure 71 show that the external scale was gray and consisted of a light and dark oxide. Upon further magnification it can be seen that the surface consisted of two types of oxides: the first (denoted as area 1) a very uniform scale, while the second (denoted as area 2) consisted of spherical nodules roughly 1 micron in diameter. The EDX spectrums in Figure 72 and Figure 73 show that area 1 was composed of 65% Ni, 23% Cr, and 7% Fe, which is consistent with the bulk matrix, while area 2 consisted of 43% Ni, 45% Cr, and 5% Fe; both oxides contained minor amounts of Nb and Ti. This demonstrates that area 2 consisted of a much more developed and thicker scale. Additionally, the light and dark oxide showed very similar composition and the contrast can most likely be attributed to the difference in thickness. Ti and Nb based precipitates were found throughout the surface and the EDX spectrums can be found in Appendix C. Additionally, LA2-32 had a very similar surface morphology, however more localized corrosion was observed on the surface near the mounting hole and the SEM images and EDX spectrums can be found in Appendix C.

Photograph of LA1-32 500 Hours

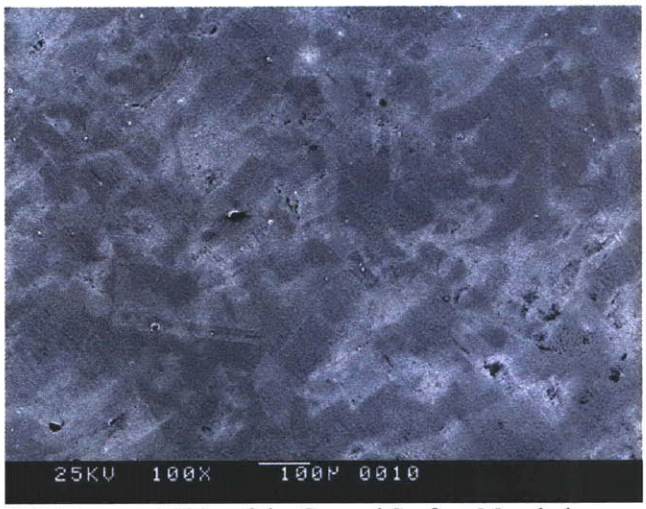

SEM Image at 100x of the General Surface Morphology

SEM Image at 2500x of Titanium Precipitate

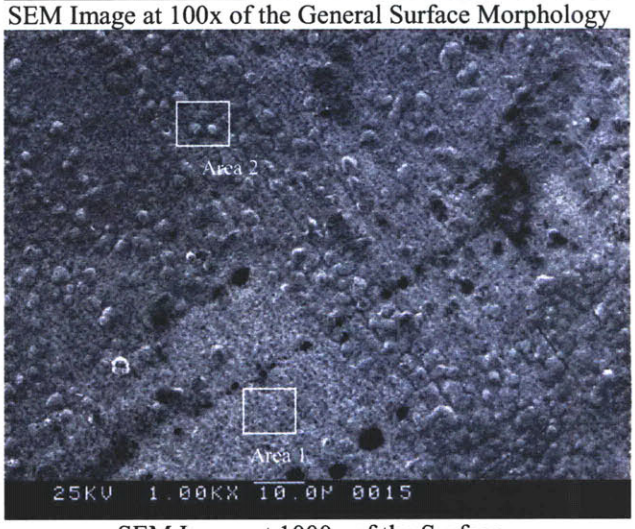

SEM Image at 1000x of the Surface

Figure 71: Surface Morphology for LA1-32 (Inconel 725 (EG) T=714 °C P=20 MPa) After 500 Hours of Exposure

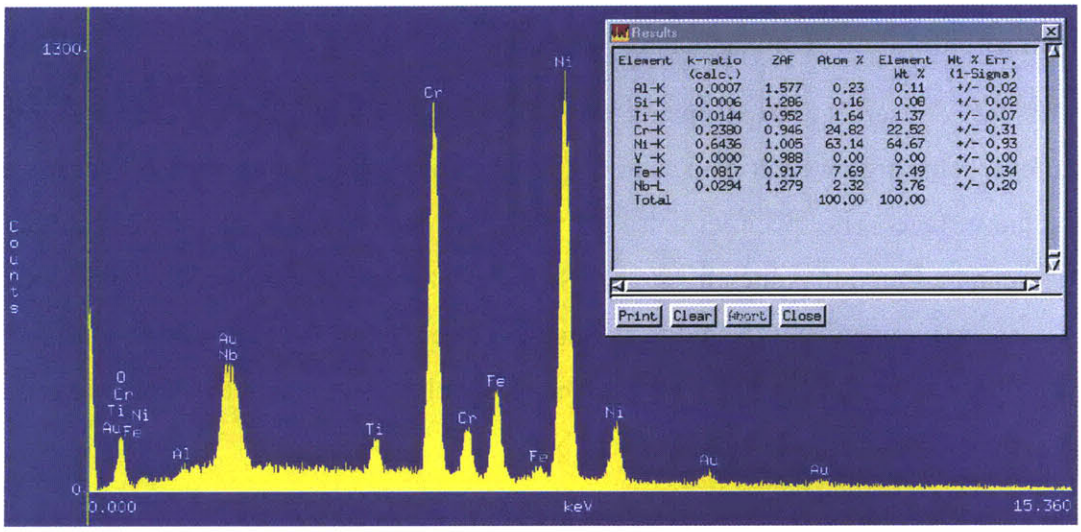

Figure 72: EDX at 25000x of Area 1 on LA1-32

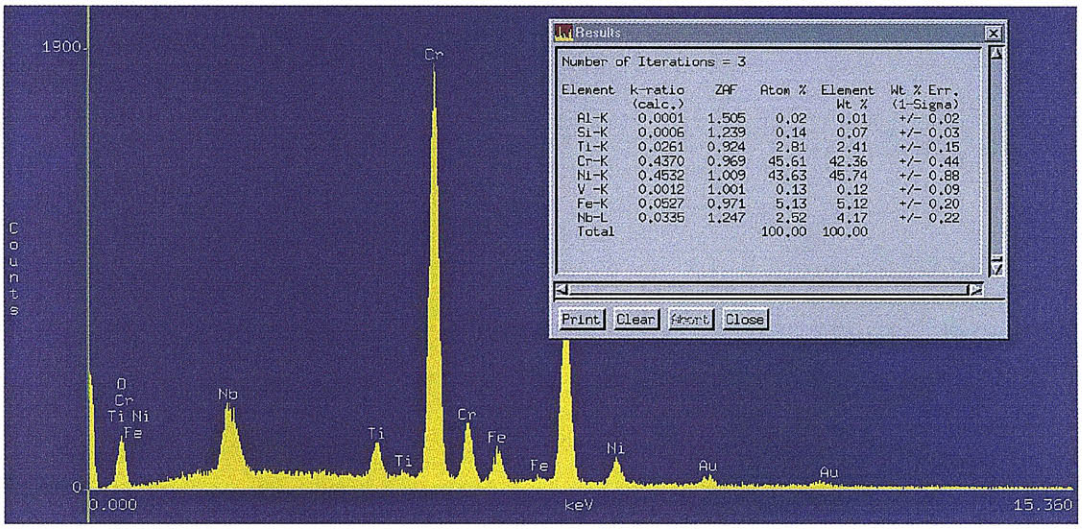

Figure 73: EDX at 3000x of Area 2 on LA1-32

LA3-32 (Inconel 725, T=750 °C, P=12.5 MPa)

LA3-32 (Inconel 725, T=750 °C, P=12.5 MPa) showed a much more developed continuous oxide film compared to the samples exposed to lower temperatures. Similar to LA1-32 two types of oxides formed on LA3-32. The first oxide consisted of an agglomeration of the nodules seen in LA1-32; the EDX spectrum in Figure 72 shows a very similar chemistry as well. The second oxide consisted of a larger blocky more continuous oxide that was speckled with white flakes of chromium as Figure 71 illustrates. The second oxide contained almost 90% chromium which indicates that it is most likely chromia, Cr_2O_3. The white flakes have a very similar composition as the second oxide and the EDX can be found in Appendix C. Additionally, grains can be seen throughout the surface of the specimen, and it appears as if chromium carbides formed on the boundaries.

In the LA3 series of experiments, alloy 725 showed the greatest weight gain for the nickel alloys. This high weight gain can be attributed to the formation of a thick dense chromia oxide on the surface. The specimens also contained Nb and Ti based precipitates and the EDX spectrums can be found in Appendix C. LA3-82 was the same base alloy as LA3-32, except LA3-82 was cut perpendicular from the rolling direction while LA3-32 was cut parallel. They displayed very similar weight gains and surface morphologies and both the SEM images and EDX spectrums can also be found in Appendix C.

Photograph of LA3-32 500 Hours

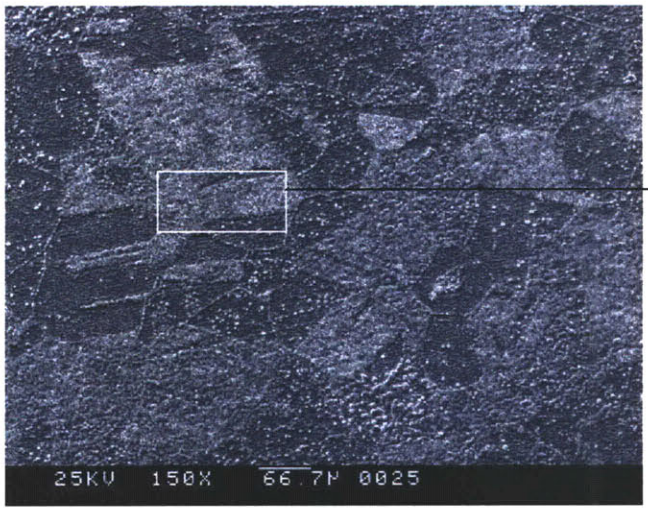

SEM Image at 150x of the General Surface Morphology

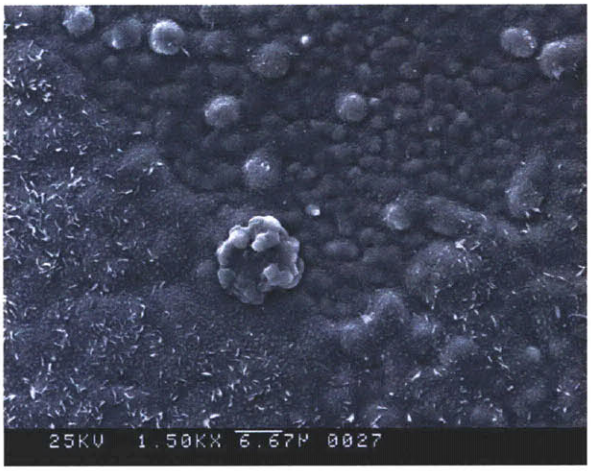

SEM Image at 1500x of Titanium Precipitate

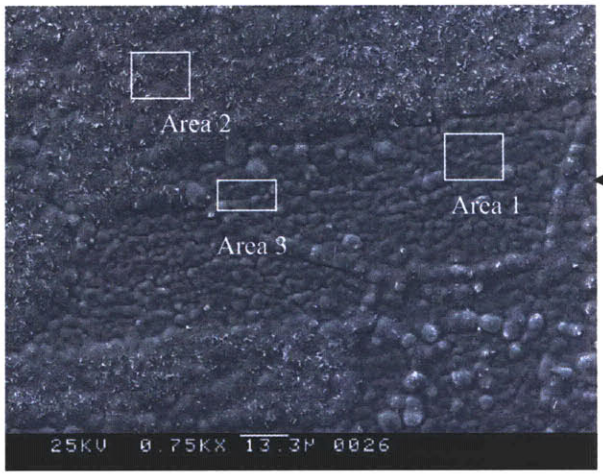

SEM Image at 750x of the Surface

Figure 74: Surface Morphology for LA3-32 (Inconel 725 (EG) T=750 °C P=12.5 MPa) After 500 Hours of Exposure

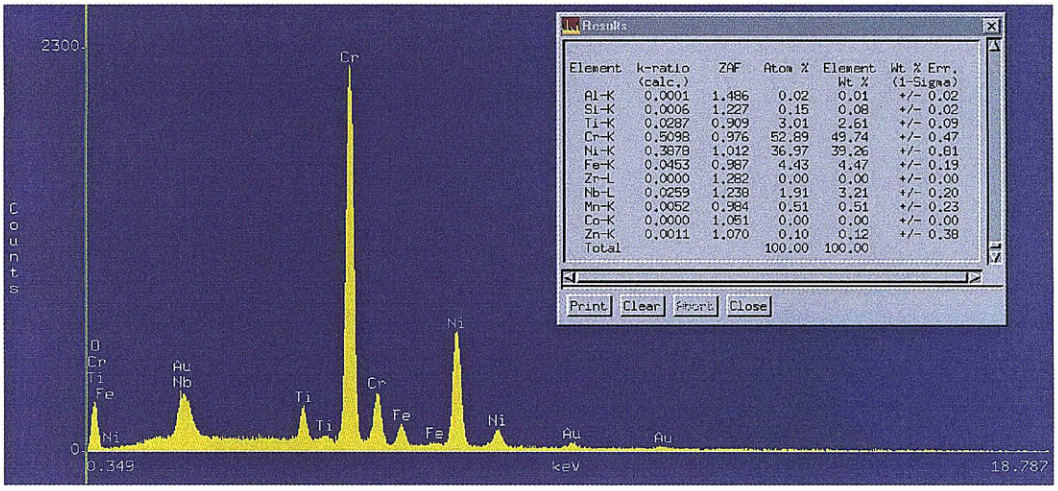

Figure 75: EDX at 20000x of the Area 1 on LA3-32

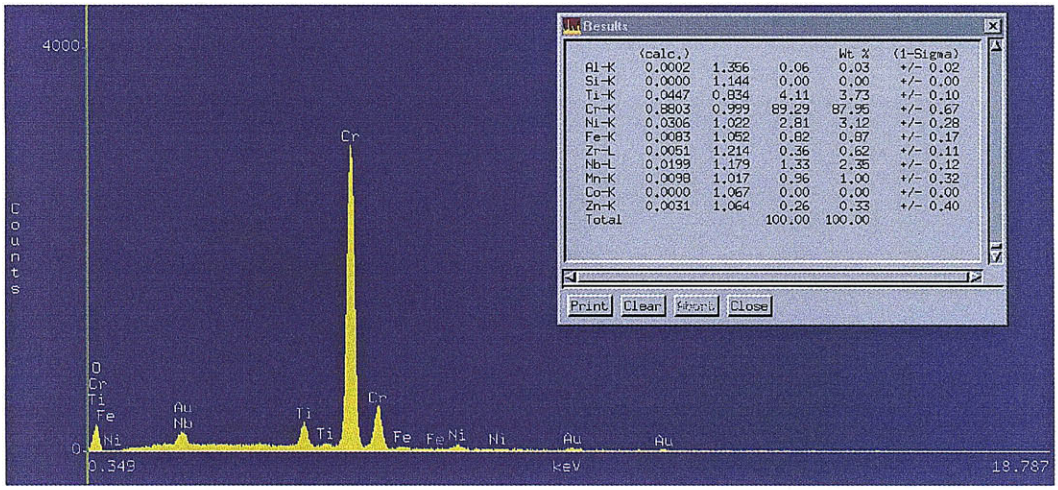

Figure 76: EDX at 25000x of the Area 2 and Area 3 on LA3-32

5.4.5 Inconel 740

Inconel 740 is a nickel-chromium-cobalt alloy that is age hardenable by the precipitation of a secondary gamma prime phase. The gamma prime precipitates consist of niobium, aluminum, and titanium, which is required for strengthening. Additionally, the alloy is solid-solution strengthened by the high content of cobalt (40).

LA1-42 (Inconel 740, T=714 °C, P=20 MPa)

LA1-42 (Inconel 740, T=714 °C, P=20 MPa) showed a thin homogenous continuous oxide film, with some localized corrosion around the mounting hole as Figure 77 shows. The light and dark colored oxide had very similar chemical compositions, which is shown in Figure 78 and Figure 79 and the differences in contrast can be attributed to the different thicknesses in the oxide. The EDX of the surface film showed the composition to be roughly 52% Ni, 22%Cr, and 20% Co. These values are very similar to the composition of the bulk matrix. This indicates that the film is probably very thin and the EDX is picking up the majority of the signal from the underlying bulk matrix, which suggests very little oxidation has occurred.

From the SEM images the rolling and polishing direction can be ascertained. The precipitates formed straight lines, which illustrate the rolling direction and the polishing direction can be determined by the orientation in which the oxide developed. Again the EDX of the precipitates for all the samples consisted of Nb and Ti and can be found in Appendix C. LA2-42 had a very similar morphology and compositional analysis as LA1-42 and the SEM images and EDX spectrums can be found in Appendix C.

Photograph of LA1-42 500 Hours

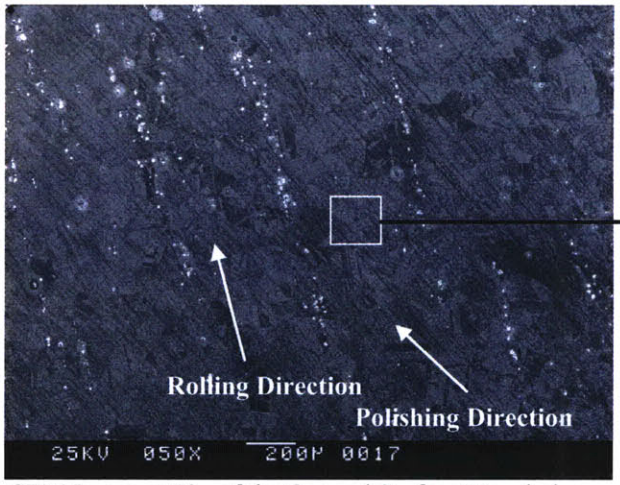

SEM Image at 50x of the General Surface Morphology

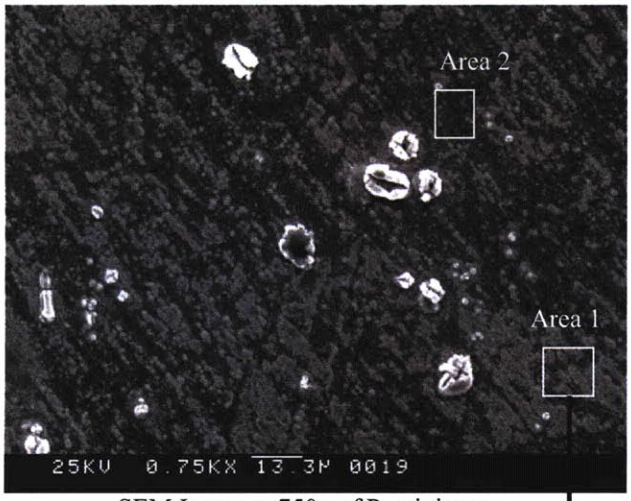

SEM Image at 750x of Precipitates

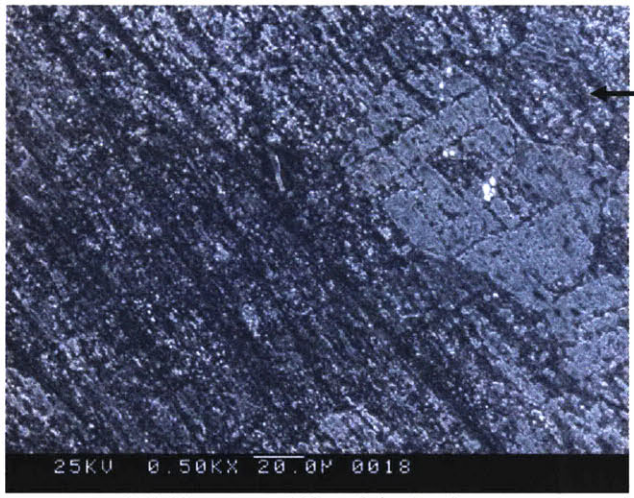

SEM Image at 500x of the Surface

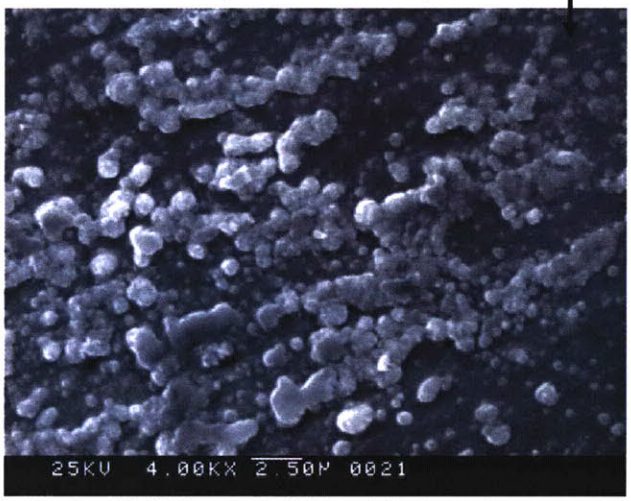

SEM Image at 4000x of the Area 1

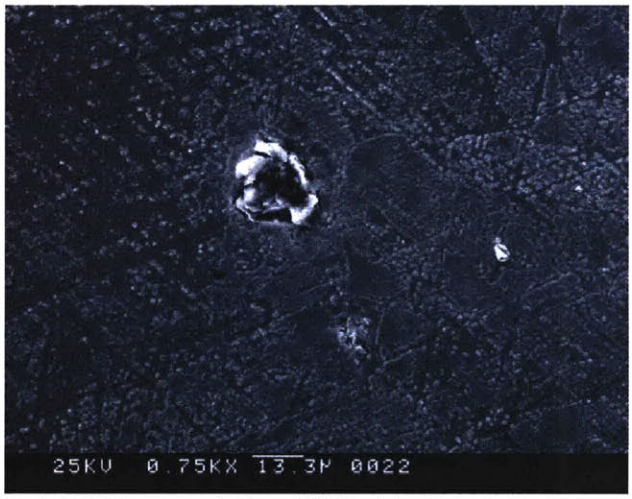

SEM Image at 750x of Si Enriched Precipitate

Figure 77: Surface Morphology for LA1-42 (Inconel 740 T=714 °C P=20 MPa) After 500 Hours of Exposure

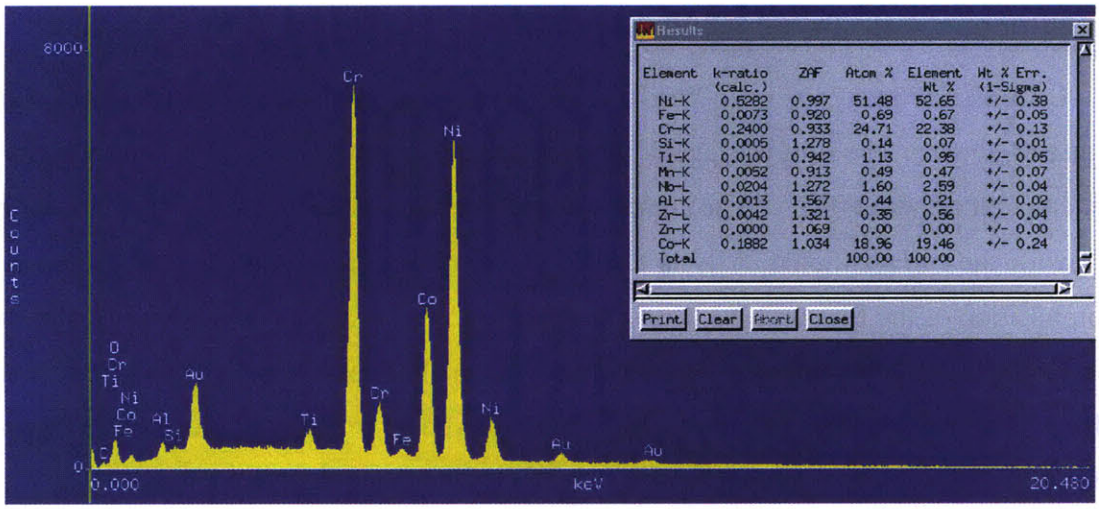

Figure 78: EDX at 10000x of Area 1 on LA1-42

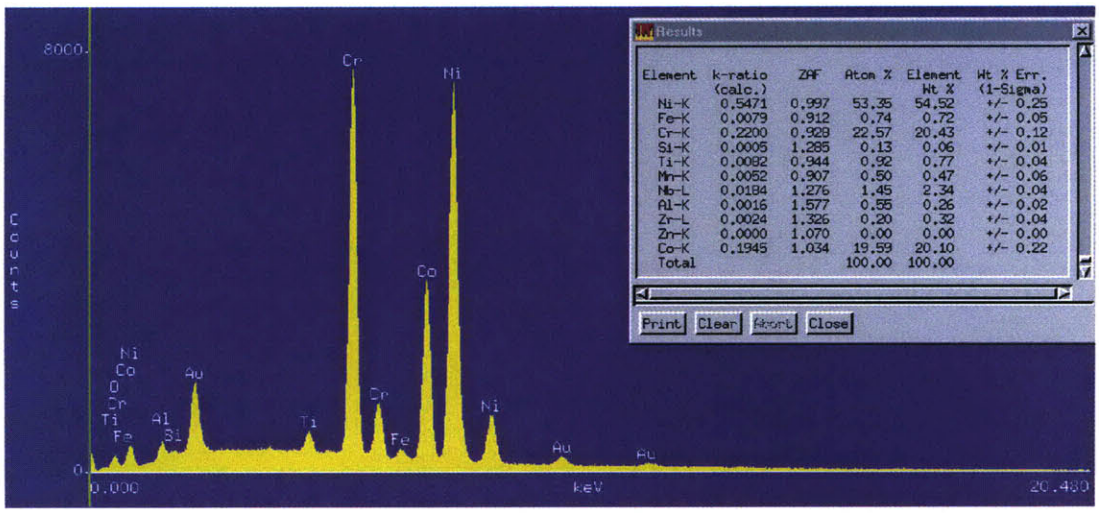

Figure 79: EDX at 20000x of Area 2 on LA1-42

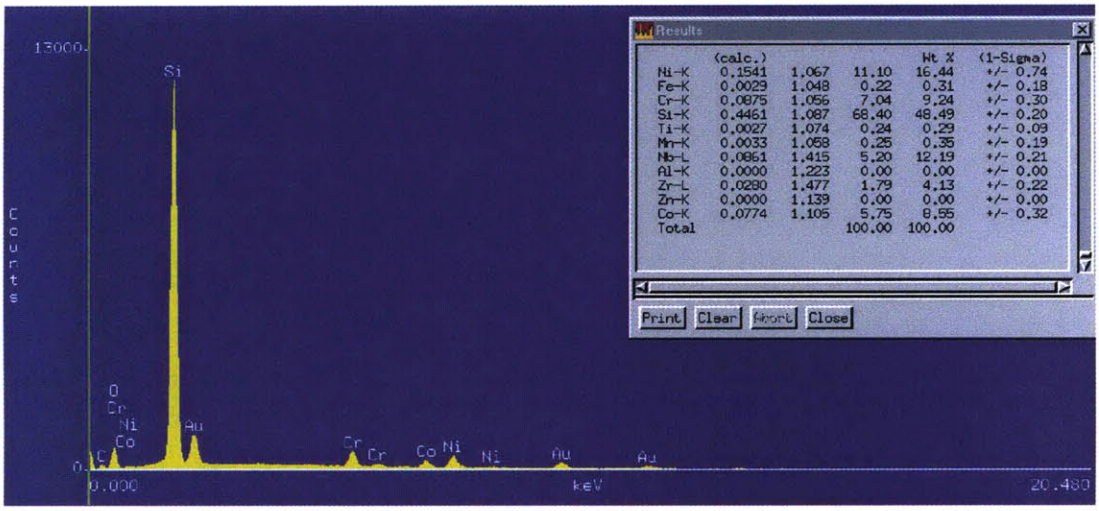

Figure 80: EDX at 150000x of the Si Enriched Precipitate

LA3-42 (Inconel 740, T=750 °C, P=12.5 MPa)

LA3-42 (Inconel 740, T=750°C, P=12.5MPa) had a continuous film form on the surface as Figure 81 shows. The film was again, more developed than the LA1-42, which was expected as the temperature was higher. The composition of the film on LA1was analogous to the base metal, while the compositional analysis for LA3 was Cr enriched. As Figure 82 demonstrates, the composition of the film on LA3 consisted of 63% Cr, 23% Ni, and 8% Co. This shows that the film most likely contained a Ni-Cr spinel. Additionally, the oxide had a few surface features which were long and blotchy, however, EDX analysis shown in Figure 83 revealed a similar composition to the oxide. This indicates that the surface feature was probably an artifact of the SEM imaging process. Additionally, detailed compositional analysis on the surface precipitates revealed a composition containing varying concentrations of Ti, Nb, Ni, and Cr, which can be found in Appendix C.

Photograph of LA3-42 500 Hours

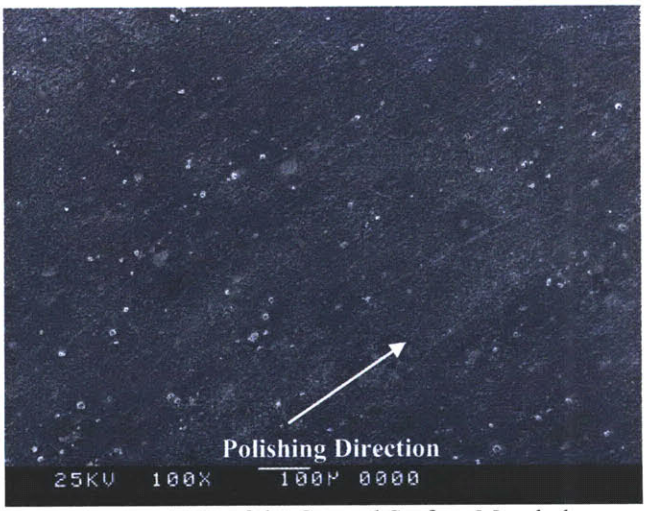

SEM Image at 100x of the General Surface Morphology

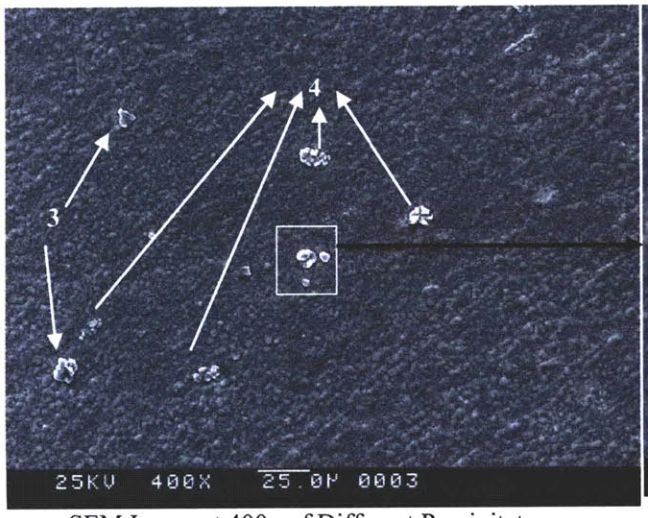

SEM Image at 400x of Different Precipitates

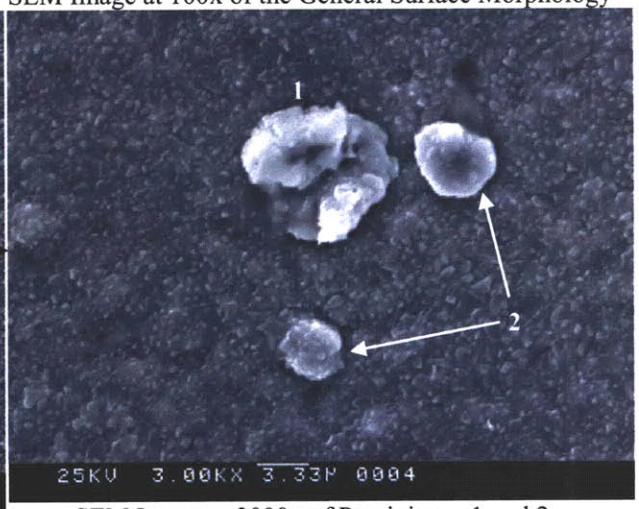

SEM Image at 3000x of Precipitates 1 and 2

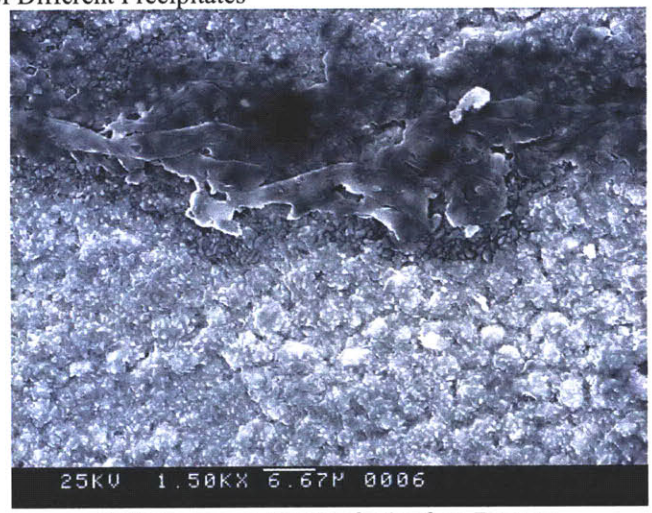

SEM Image at 1500x of a Surface Feature

Figure 81: Surface Morphology for LA3-42 (Inconel 740 T=750 ºC P=12.5 MPa) After 500 Hours of Exposure

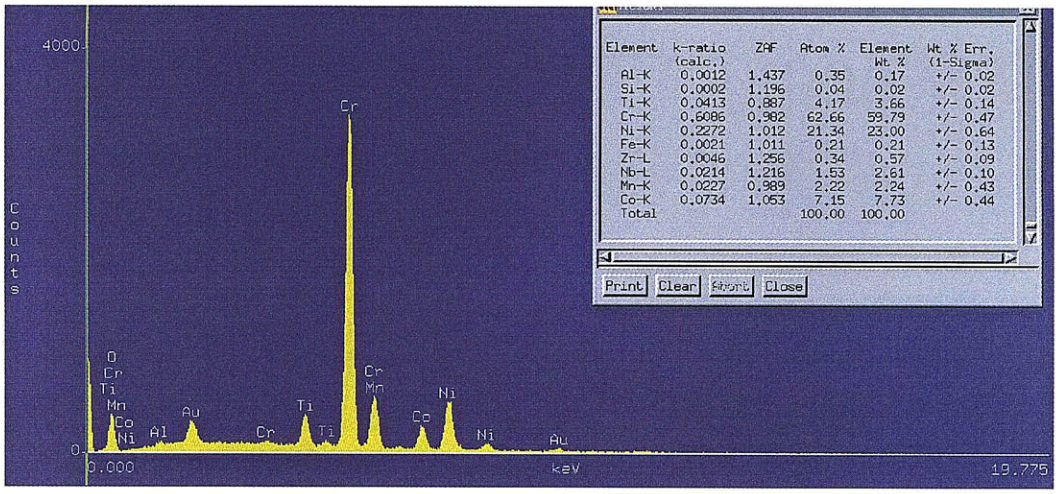

Figure 82: EDX at 4000x of the Surface on LA3-42

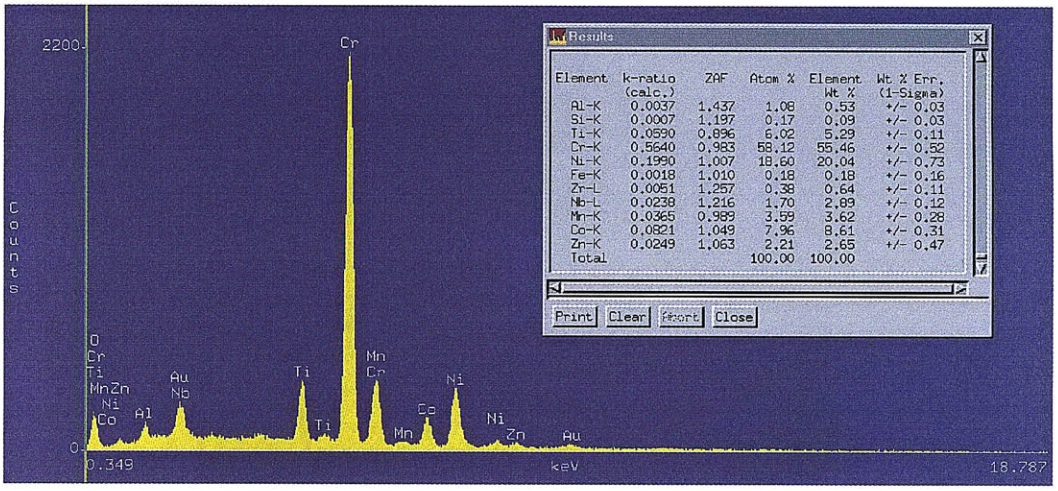

Figure 83: EDX at 4000x of the Surface Feature on LA3-42

5.4.6 Inconel 740+

The Inconel 740+ is a modified version of Inconel 740, which promotes structural stability at temperatures up to 760°C. Additionally, alloy 740+ has a higher Zr, Mo, and Si content (40).

LA1-52 (Inconel 740+, T=714 °C, P=20 MPa)

The LA1-52 (Inconel 740+, T=714 °C, P=20 MPa) and LA2-52 (Inconel 740+, T=650 °C, P=12.5 MPa) showed very similar surface morphologies and compositions as that in LA1-42. This was expected, as both alloys had very similar chemical compositions. The surface film on LA1-52 had a chemical composition similar to that of the bulk matrix as Figure 85 shows. This indicated that the film was likely very thin, and the majority of the signal was from the bulk matrix. Additionally, surface inhomogeneities riddled the sample, similar to LA3-42, however they had very similar compositions as the surface film and may be an artifact of the SEM imaging process. Area 2 in Figure 85 looks like a break in the oxide film.

Figure 90 shows that this break was chromium depleted, which supports this. Additionally, numerous Nb and Ti precipitates were found throughout the surface and the EDX spectrums can be found in Appendix C.

Photograph of LA1-52 500 Hours

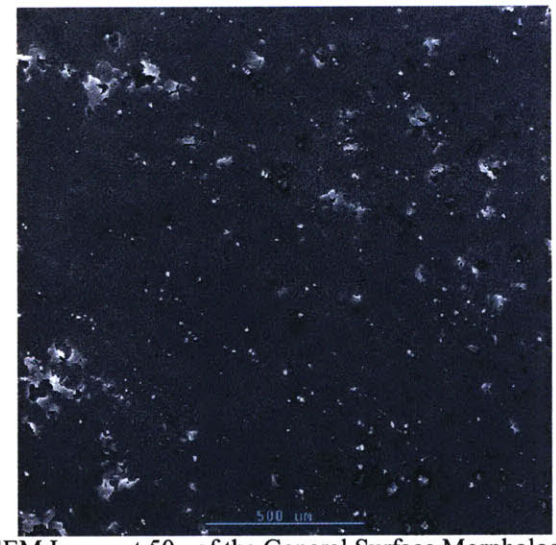

SEM Image at 50x of the General Surface Morphology

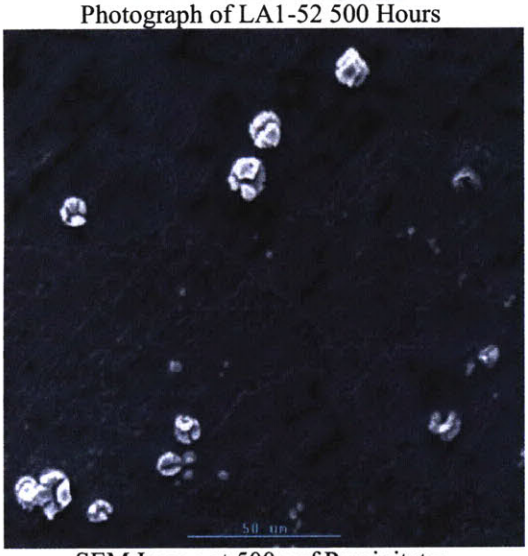

SEM Image at 500x of Precipitates

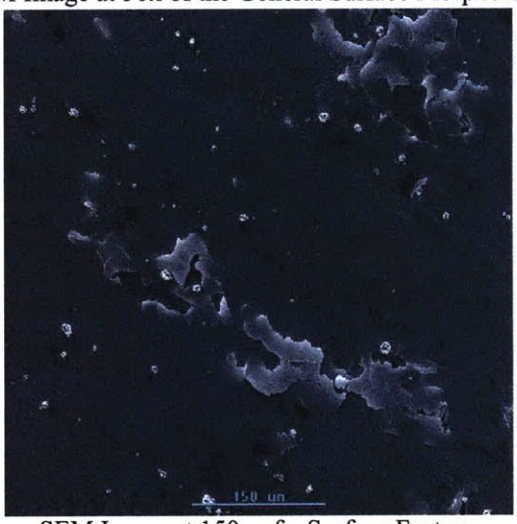

SEM Image at 150x of a Surface Feature

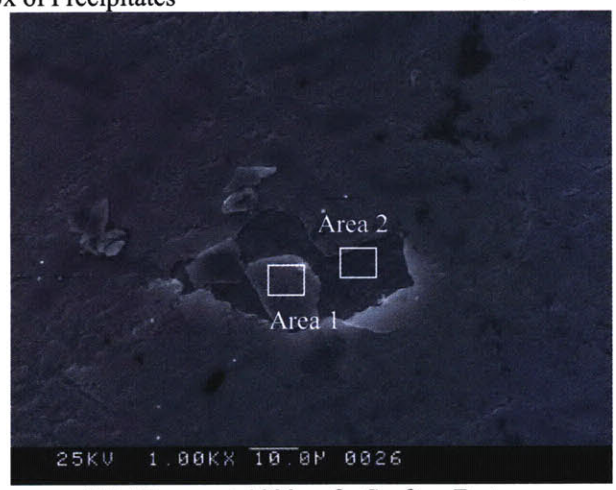

SEM Image at 1000x of a Surface Feature

Figure 84: Surface Morphology for LA1-52 (Inconel 740+ T=714 °C P=20 MPa) After 500 Hours of Exposure

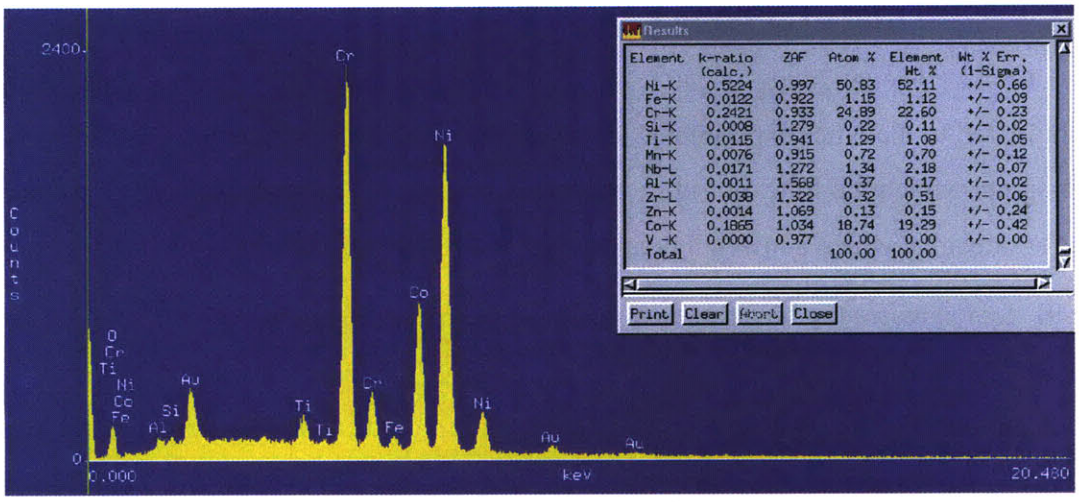

Figure 85: EDX at 100000x of the Surface on LA1-52

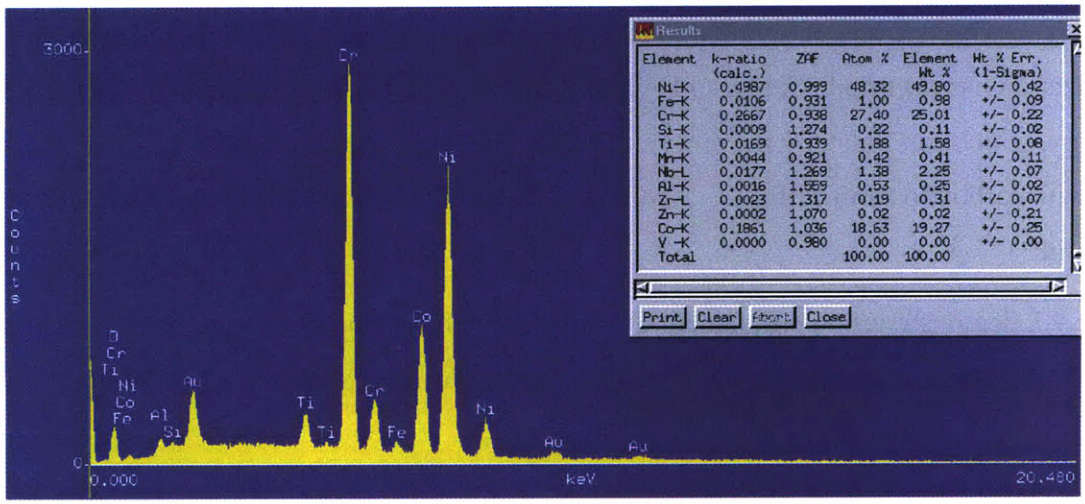

Figure 86: EDX at 100000x of Area 1 on LA1-52

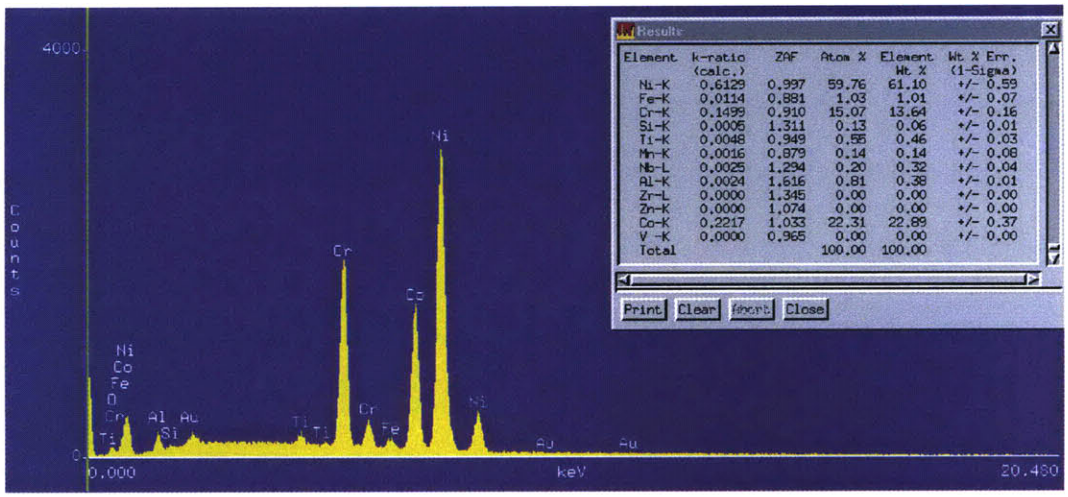

Figure 87: EDX at 75000x of Area 2 on LA1-52

LA3-52 (Inconel 740+, T=750 °C, P=12.5 MPa)

LA3-52 (Inconel 740+, T=750 °C, P=12.5 MPa) had a much more developed surface scale compared to the other experiments involving Inconel 740+. The external scale consisted of a Ni-Cr spinel, which the EDX in Figure 89 and 90 support. The scale was relatively uniform except for one area, which showed a break in the oxide. EDX analysis shown in

Figure 91 demonstrates the break in the oxide had a composition similar to that of the base metal. The scale also had a lower chromium content then alloy 740 under the same conditions. This may indicate the presence of a less developed chromium oxide film. Additionally, the weight gain for the 740+ experiments was significantly less than the 740 experiments, which signifies a thinner film.

The presence of clear grain boundaries are shown in Figure 88. This may indicate that sensitization has occurred, similar to LA3-02. However, there is a total of 3% of Nb and Ti in the alloy, which can typically prevent sensitization from happening as they will preferentially form with carbon to form carbides. Additionally, the EDX spectrum of the grain boundaries, shown in

Figure 90, demonstrates an enrichment of chromium 60%, compared to the surface oxide 42%, but not to the extent seen in LA3-02 which showed a chromium enrichment of 90%.

Photograph of LA3-52 500 Hours

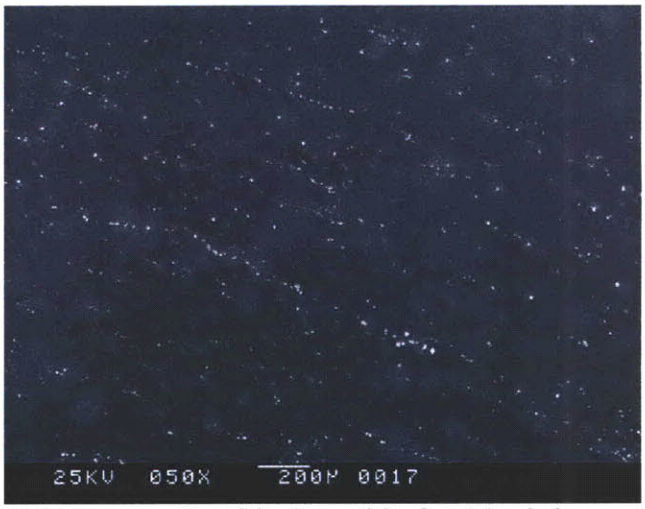

SEM Image at 50x at the General Surface Morphology

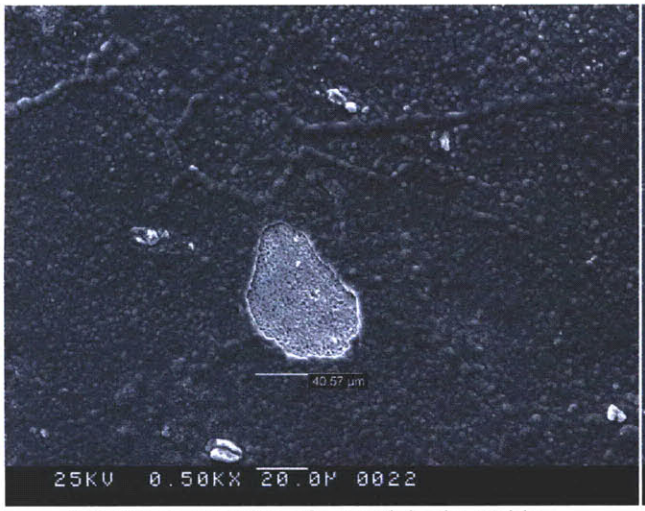

SEM Image at 500x of a Break in the Oxide

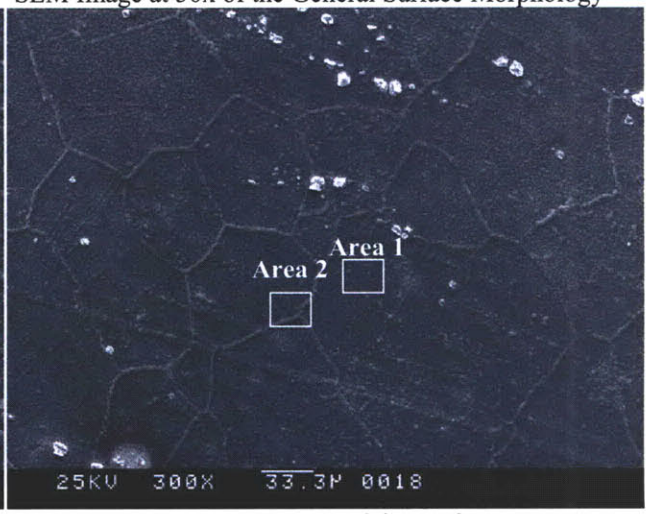

SEM Image at 300x of the Surface

SEM Image at 1000x of the Precipitates

Figure 88: Surface Morphology for LA3-52 (Inconel 740+ T=750 ºC P=12.5 MPa) After 500 Hours of Exposure

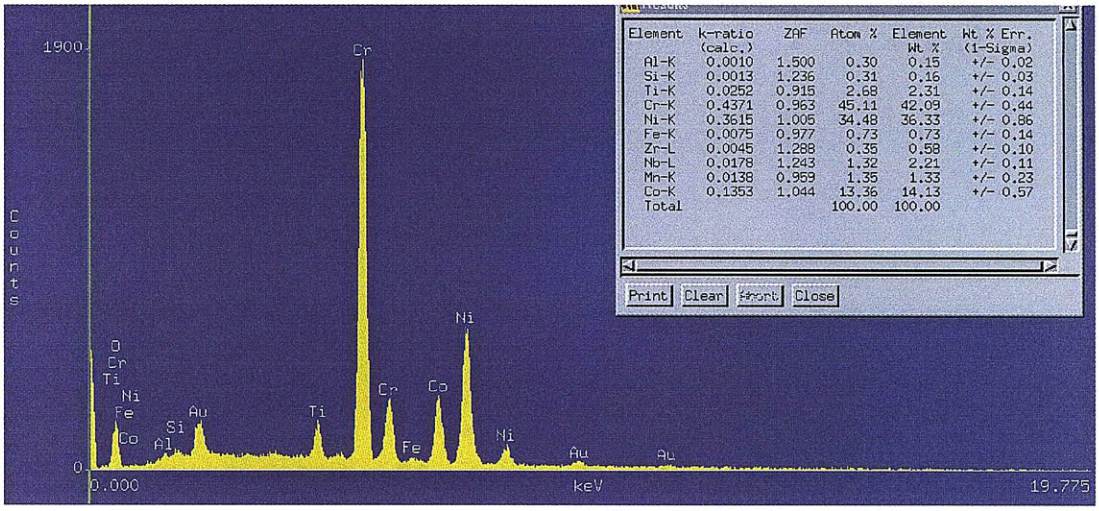

Figure 89: EDX at 50000x of Area 1 on LA3-52

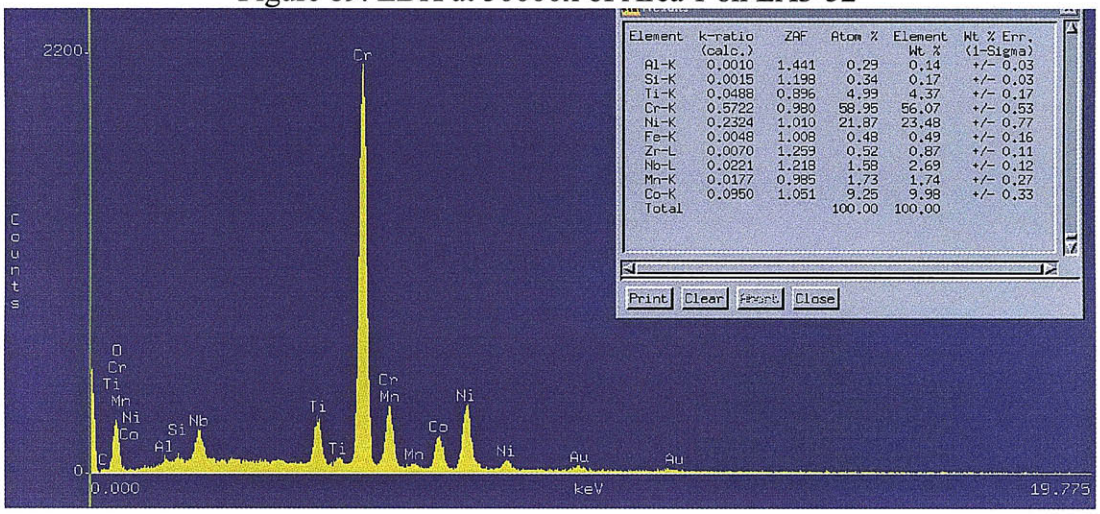

Figure 90: EDX at 100000x of Area 2 on LA3-52

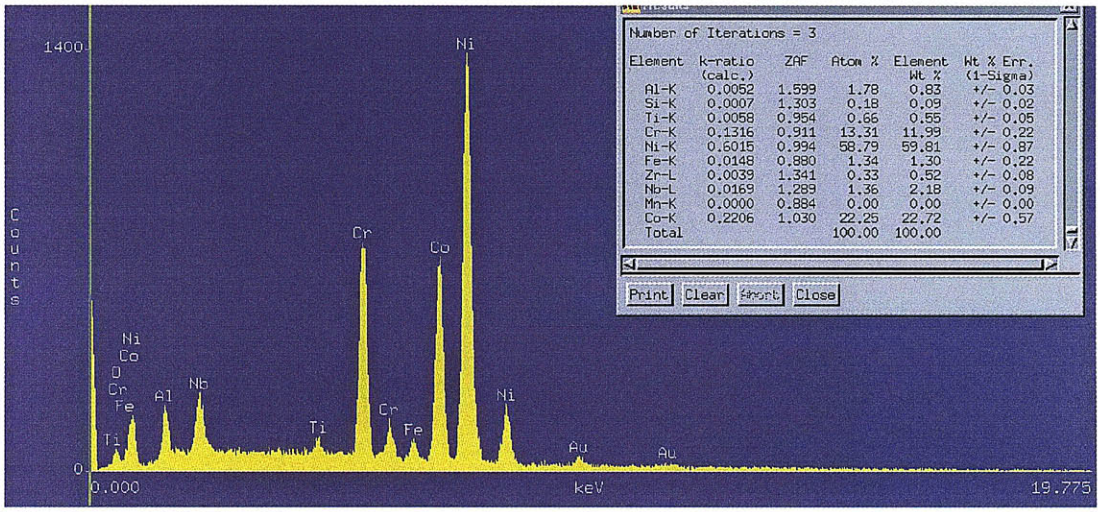

Figure 91: EDX at 7500x of a Break in the Oxide on LA3-52

5.4.7 Overall Surface Morphology Observations for the Nickel Based Alloys

Many of the nickel based alloy specimens had regions of chromium enrichment. These regions of localized corrosion most likely were above or very near a grain boundary, which would act as an easy diffusion path from the matrix. Precipitates, most likely oxidized metal carbides, nitrides, or carbonitrides, were observed on the surface of all of the specimens as well. Again, these precipitates may have been in close proximity to grain boundaries where diffusion was much faster. The precipitates also appeared to have little to no effect on film stability as no additional localized corrosion was found near the precipitate initiation sites and the overall weight gain on the nickel based alloys were very low. However, longer duration experiments are needed to confirm this.

The LA3 series of experiments (T=750 °C, P=12.5 MPa) formed the most developed oxide layers. The signal going to the EDX was most likely dominated by the actual oxide. While the LA1 (T=714 °C, P= 20MPa) and LA2 (T=650 °C, P= 12.5 MPa) showed a less developed oxide layer and the signal going to the EDX may be attributed to the underlying bulk matrix. This was supported by the strong similarity between the film composition and the composition of the bulk matrix.

5.4.8 AUSS 316L

AUSS 316L is an austenitic iron based alloy, which has low carbon content. The main advantage AUSS alloys have over nickel based alloys is the price.

LA1-62 (AUSS 316L at 714 °C and 20 MPa)

As demonstrated in section 5.1 the AUSS 316L had the highest corrosion rate; which was expected due to the lower chromium content and higher iron content compared to the nickel alloys. Figure 92 shows that a thick blackish grey iron oxide, most likely magnetite, formed on the surface of LA1-62. At higher magnifications, breaks in the iron oxide can be observed. No evidence of spallation was ever observed in the bottom of the sample trains. Surface EDX in Figure 93and Figure 94 show that the external oxide was all iron based and the breaks in the oxide had a composition which was analogous to the base alloys composition. LA2-62 had a similar surface morphology and composition and the SEM images and EDX spectrums can be found in Appendix C.

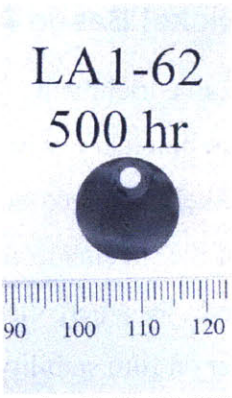

Photograph of LA1-62 500 Hours

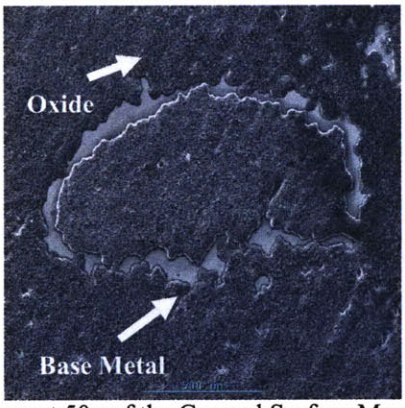

SEM Image at 50x of the General Surface Morphology

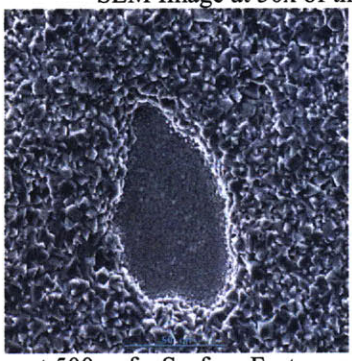

SEM Image at 500x of a Surface Feature on LA1-62

Figure 92: Surface Morphology for LA1-62 (AUSS 316L T=714 °C and P= 20MPa) After 500 Hours of Exposure

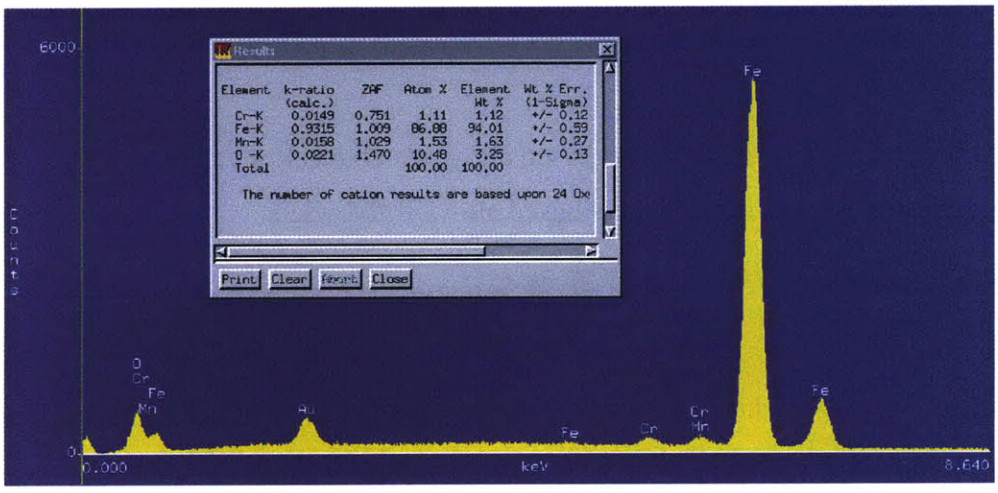

Figure 93: EDX at 1000x of the Oxide on LA1-62

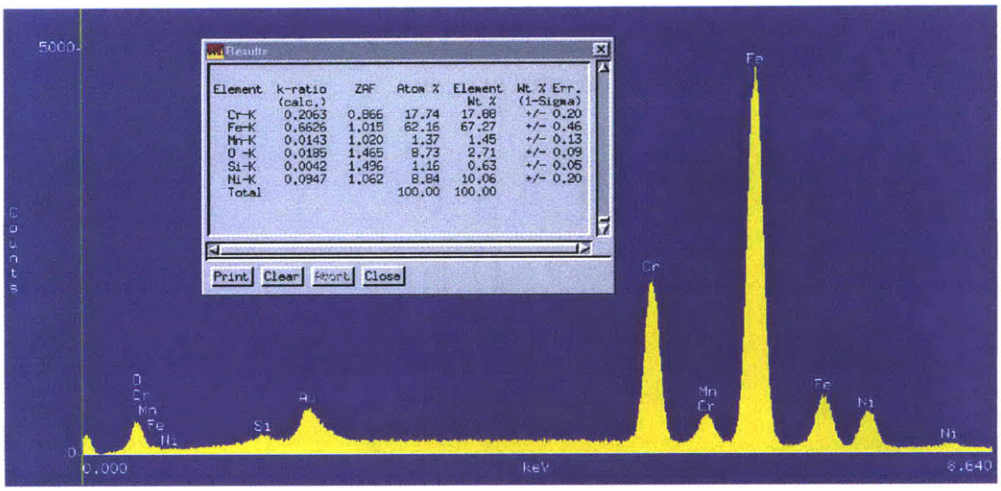

Figure 94: EDX at 2000x of a Surface Feature on LA1-62

LA3-62 (AUSS 316L at 750 ºC and 12.5 MPa)

LA3-62 (AUSS 316L at 750 ºC and 12.5 MPa) had a vastly different surface morphology compared to the LA1-62 (AUSS 316L at 650 °C and 12.5 MPa) and LA2-62 (AUSS 316L at 750 °C and 20 MPa). Figure 95 demonstrates a continuous iron oxide layer did not form on the surface even after 1000 hours; contrary to LA1-62 and LA2-62, which showed a continuous iron oxide layer after 250 hours. The EDX spectrums shown in Figure 97 and Figure 98 demonstrate that the thick grey oxide was iron oxide, most likely magnetite, and the thin bronze colored film was chromium enriched. However, it should be noted that the chromium enriched film is probably very thin and the electron beam could be penetrating through the film and picking up additional signal from the bulk matrix.

Figure 34 shows that LA3-62 was the only alloy in the whole testing regime that the weight gain rate increased with increasing exposure time. Also, LA3-62 had the least amount of weight gain out of all the AUSS 316L samples, which Figure 36 shows. This indicates that the LA3-62 sample most likely formed a chromium enriched protective layer first, then iron cations diffused through the chromia scale to form a thick iron oxide on top. This demonstrates that the protective chromium enriched layer formed the fastest on LA3-62 compared to the other AUSS 316L samples. This is intuitive as the diffusion rate is highest in this experiment as the LA3-62 experiment was conducted at the highest temperature, 750°C. Perhaps on the lower temperature experiments a continuous chromium enriched inner oxide did not form or formed slower, which

explains the higher weight gain rate. This is also supported by Figure 94 which shows that a break in the iron oxide was not chromium enriched.

Figure 95: Photographs of LA3-64 (AUSS 316L T=750 °C and P= 12.5 MPa) at Different Exposure Times

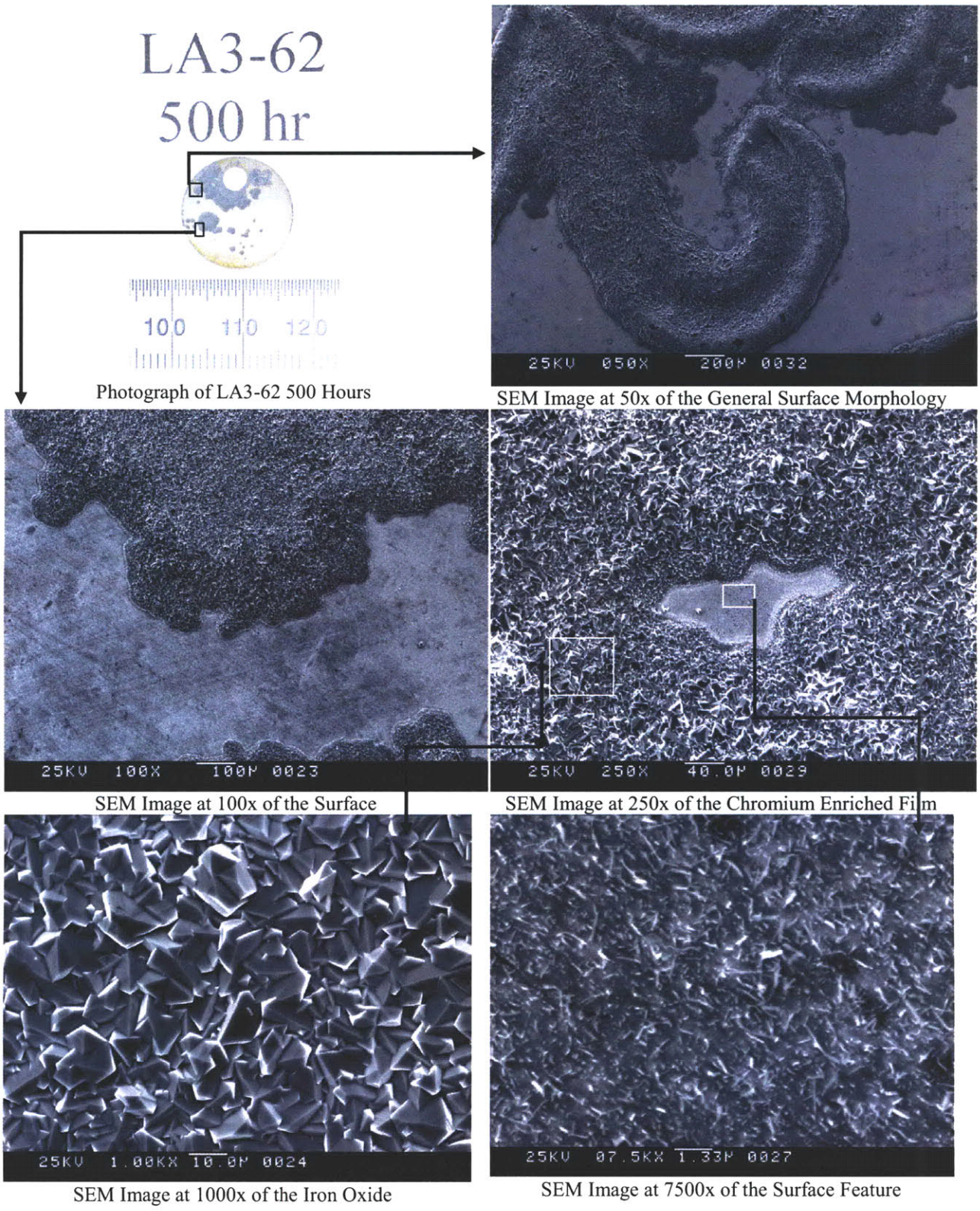

Photograph of LA3-62 500 Hours

SEM Image at 50x of the General Surface Morphology

SEM Image at 100x of the Surface

SEM Image at 250x of the Chromium Enriched Film

SEM Image at 1000x of the Iron Oxide

SEM Image at 7500x of the Surface Feature

Figure 96: Surface Morphology for LA3-62 (AUSS 316L T=750°C P=12.5MPa) After 500 Hours of Exposure

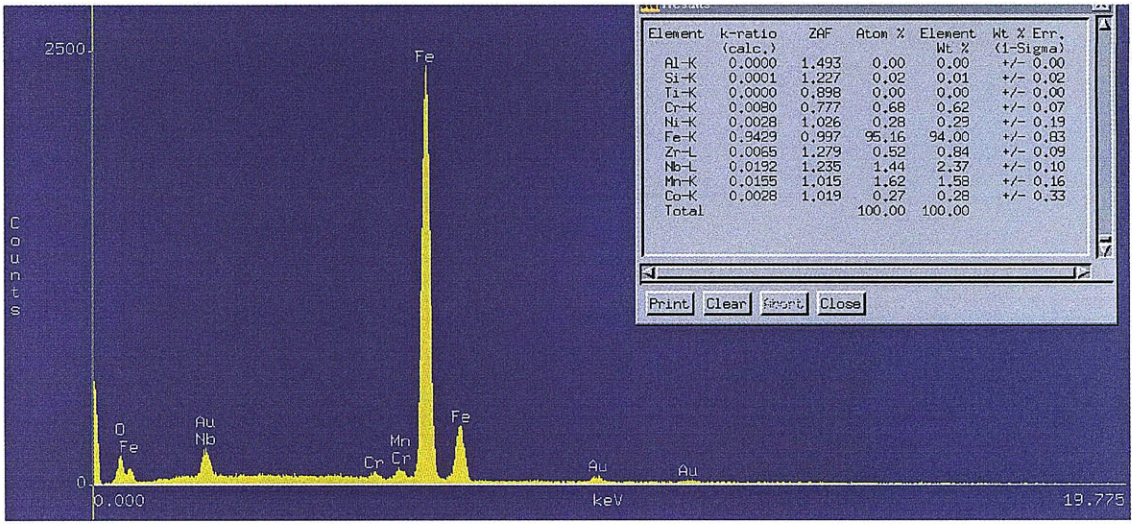

Figure 97: EDX at 10000x of the Iron Oxide on LA3-62

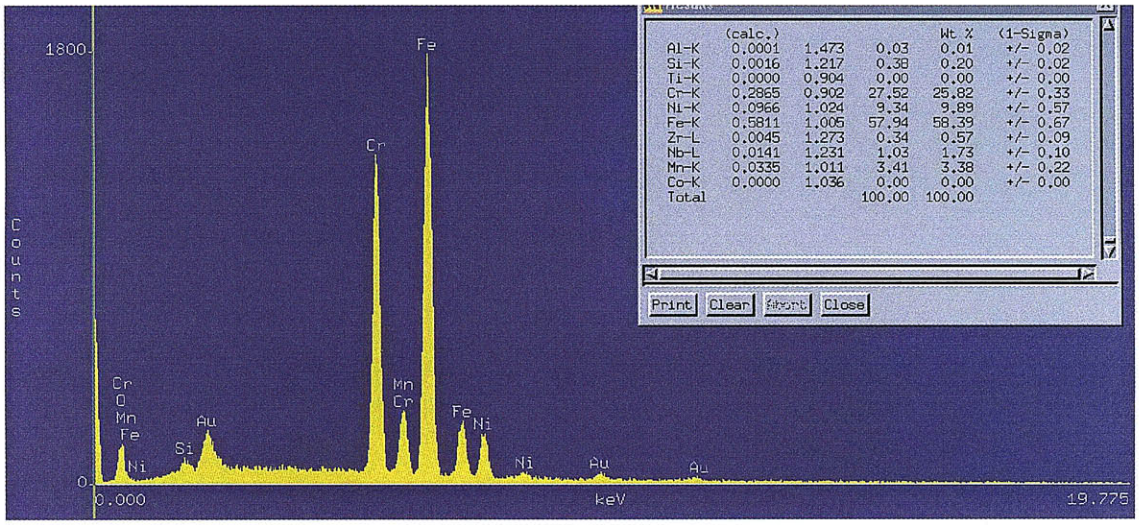

Figure 98: EDX at 10000x of the Chromium Enriched Film on LA3-62

5.5 Microstructural Analysis

Microstructural analysis was conducted on Inconel 693 in order to observe if there were any differences between the as-received material and the material exposed to high temperature and pressure SCO_2. As discussed in Section 3.8 the modified glyceregia could not etch both samples, which indicates that the exposure to SCO_2 at a temperature of 750 °C and pressure of 20 MPa had changed the microstructure of the Inconel 693.

The as-received sample appeared to be in the solution annealed condition as Figure 99 shows and evidence of twinning, prior grain boundaries that recrystallized, grains within grains,

and precipitates was observed. Additionally, the long lines of precipitates, most likely former grain boundaries, appeared to have been pinned during the processing of the material. These precipitates may have prevented the recrystallization of smaller grains during annealing. The LA1-12 (Inconel 693, T= 714 °C, P=20 MPa) sample showed intragranualar precipitates, which was not as obvious on the as received sample and may be a result of ageing at 714 °C. It also appears as if precipitates formed on the smaller recrystallized grains, which was not visible on the as-received sample.

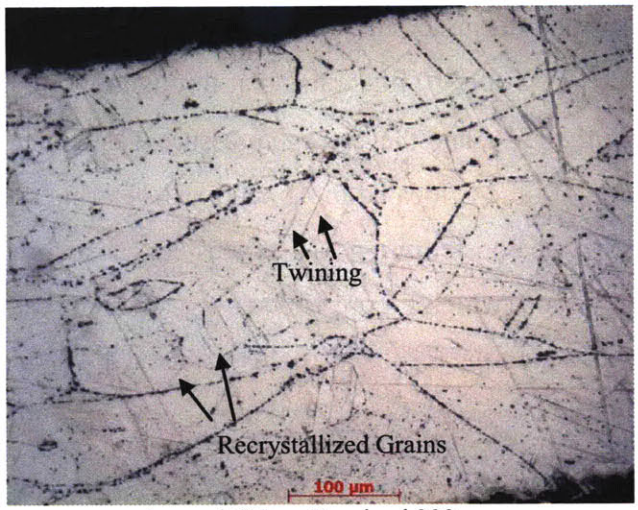

Inconel 693 as-Received 200x

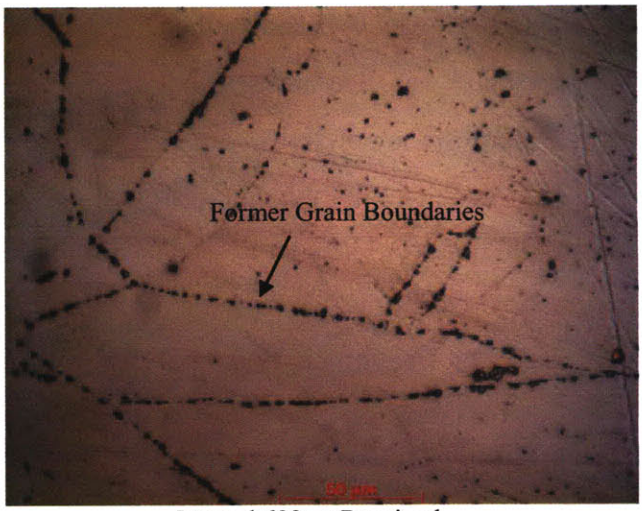

Inconel 693 as-Received

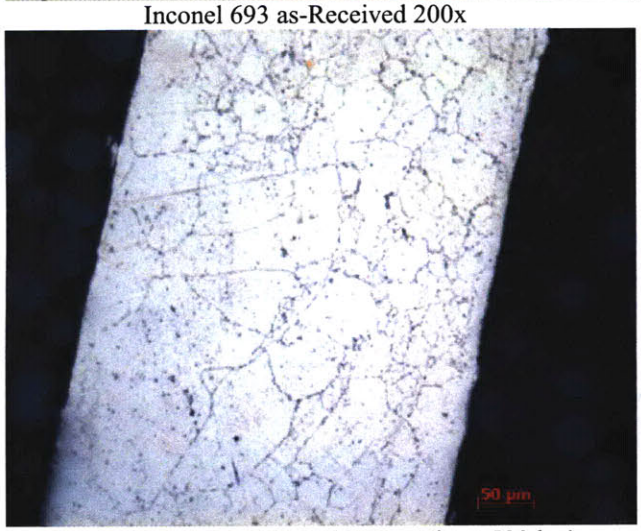

LA1-12 (693, T=750°C, P=20MPa, Time=500 hrs)

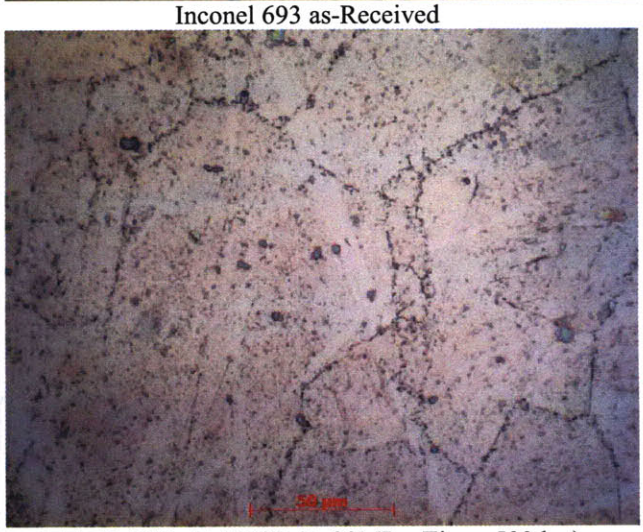

LA1-12 (693, T=750°C, P=20MPa, Time=500 hrs)

Figure 99: Inconel 693 Microstructure

5.6 Temperature and Pressure Variation During the Experiments

According to equation 7, the Arrhenius equation, the rate of oxidation increases by a factor of two for an increase in temperature of 15 °C, therefore it was imperative to accurately control and measure the internal temperature of the system.

5.6.1 LA1 Series (T=714 °C, P=20 MPa)

During the LA1 series of experiments no accurate internal temperature measurement was obtained. However, based on the temperature profiling discussed in Section 4.4.1, the internal temperature was determined to be roughly 714 ± 6 °C. Table 10 illustrates that throughout the 0-250 hour test the pressure did not change by more than 5%, and the average pressure was 20 MPa. The graph plotting the pressure as a function of time is located in Appendix B. During the 250-500 hour test the compressed air supply for the gas booster pump was exhausted, causing the pressure to decrease to 16.2 MPa over an 11 hour period, which Figure 100 shows. Overall this pressure transient probably did not have a large impact on the results as it only affected 4.4% of the total test time and the overall average pressure only decreased by 0.2 MPa.

Time (Hours)	Pressure Range (MPa)	Pressure Average (MPa)
0-250	19.3-20.4	20
250-500	16.2-20.5	19.8

Table 10: Pressure Variance for LA1 series

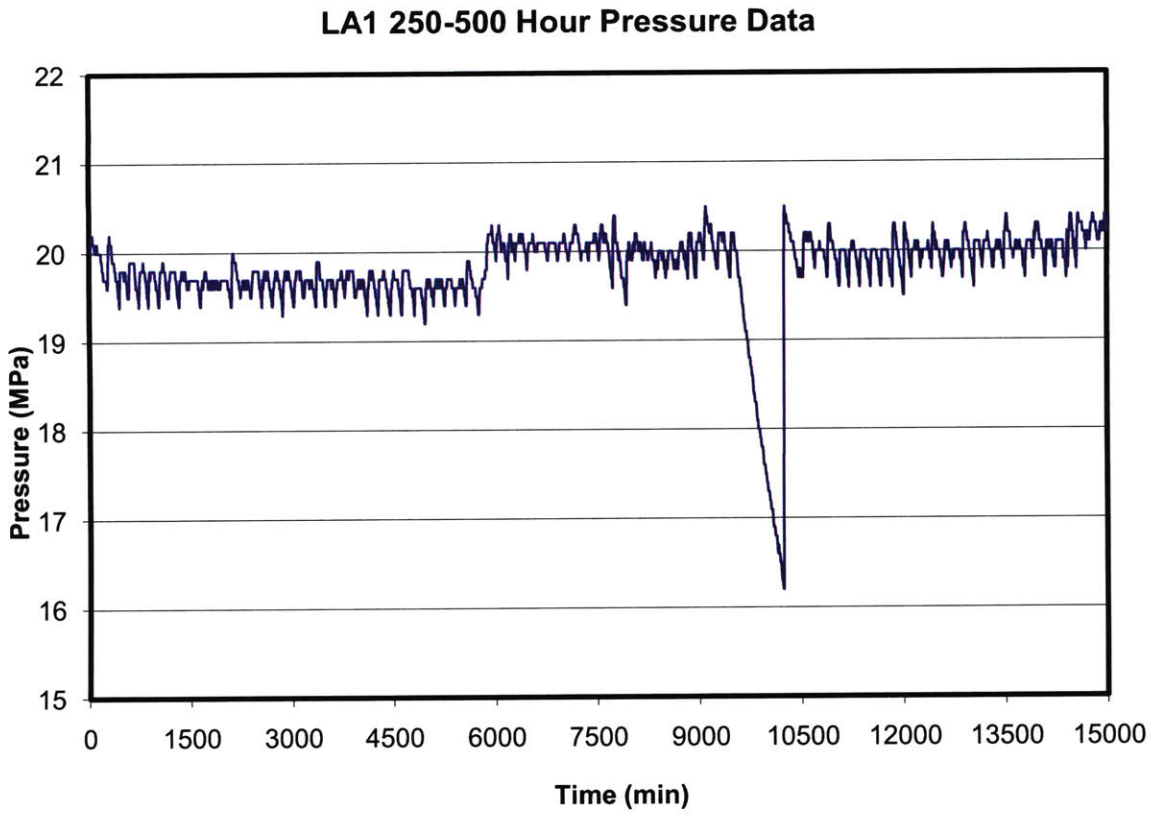

Figure 100: Pressure Variation with Time for the LA1 250-500 Hour Experiment

5.6.2 LA2 Series (T=650 ºC, P=12.5 MPa)

During the LA2 0-250 hour experiment, the gas booster pump failed to energize for roughly 11 hours during the experiment causing the pressure to drop to 3.3 MPa, and also causing the temperature to increase by 5 ºC. The duration of the transient lasted less than 5% of the total experiment time and decreased the total average pressure by only 0.3 MPa. As the transient time was small compared to the total experiment time, the overall impact that this caused was probably minimal. The 250-500 hour experiment behaved as expected, and the plot of temperature and pressure vs. time can be found in Appendix B.

The temperature measurements were conducted from the thermocouple probe that was mounted 7 cm away from the sample train inlet. The measurements obtained were within 2 ºC of the predicted temperature values based on the temperature profile trials. The variance may be attributed to the heat reflection caused by the samples on the sample train, which were not present during the profiling. Additionally, as Section 4.4.3 shows, the closer the samples were to

the midpoint of the sample train the higher the temperature was. Therefore, an average temperature uncertainty of ± 5 °C can be attributed to the lack of temperature uniformity throughout the sample train.

Time (Hours)	Pressure Range (MPa)	Pressure Average (MPA)	Measured Internal Temperature Range (°C)	Measured Internal Temperature Average (°C)	Average Temperature of Samples Based on Temp Profile (°C)
0-250	3.3-12.8	12.2	644-652	647	650 ± 5
250-500	12-12.8	12.5	643-650	645	648 ± 5

Table 11: Pressure and Temperature Variance for LA2 series

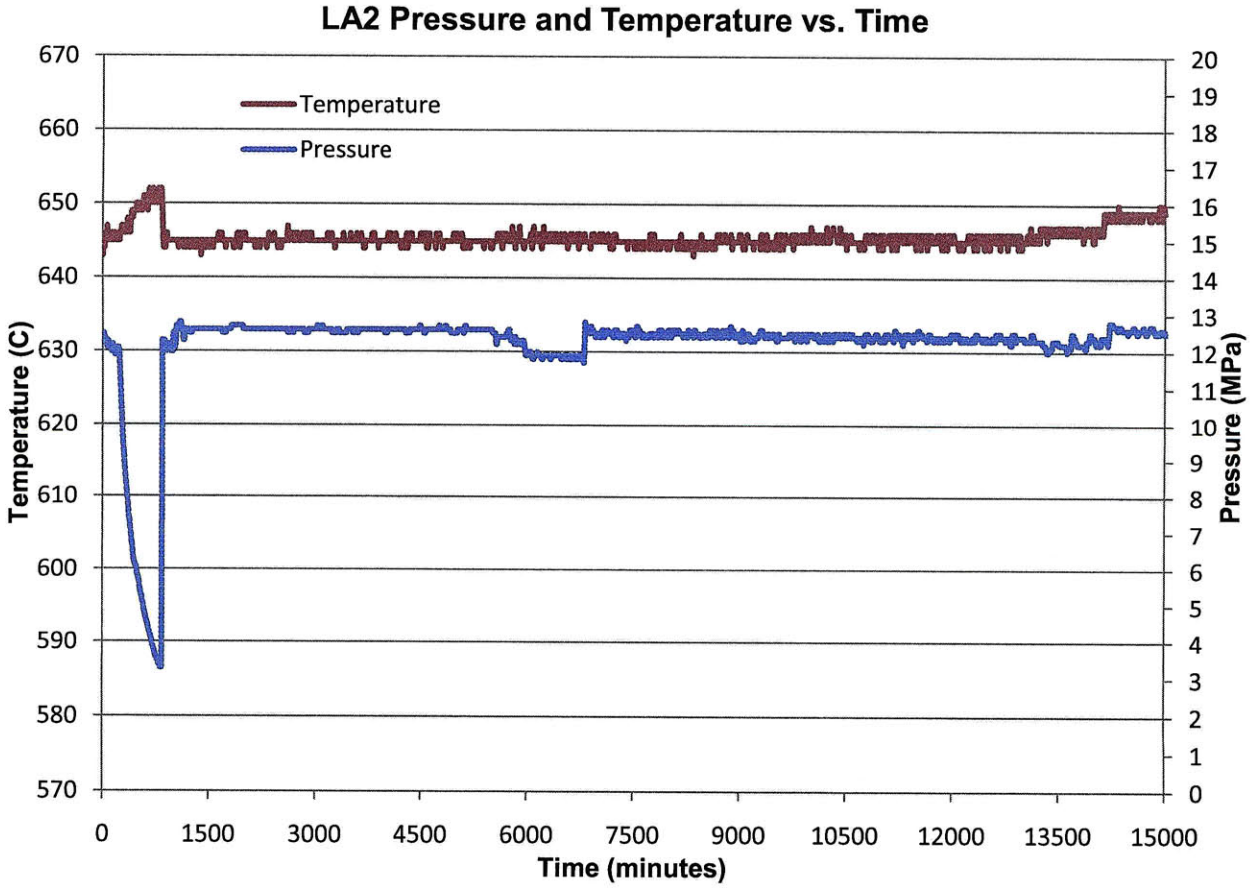

Figure 101: Pressure and Temperature Variation with Time for the LA2 0-250 Hour Experiment

5.6.3 LA3 Series (T=750 °C, P=12.5 MPa)

During the LA3 series no unexpected temperature or pressure transients occurred and the graphs plotting temperature and pressure vs. time can be found in Appendix B. Throughout the whole testing regime the pressure varied by about 4% and the temperature varied by less than 1%. Additionally, the average temperature measurements obtained during the experiment were analogous to the measurements obtained from the temperature profiling shown in Section 4.4.2. Therefore it was assumed that the temperature of the middle sample was roughly 6 °C warmer than the temperature of the instrumented dummy sample. From this an average temperature accuracy of ± 3 °C was achieved. Greater temperature accuracy was obtained for the LA3 experiments compared to the LA2 experiments because the sample train was roughly 33% shorter in the LA3 test causing less overall temperature variation.

Time (Hours)	Pressure Range (MPa)	Pressure Average (MPA)	Measured Internal Temperature Range (°C)	Measured Internal Temperature Average (°C)	Average Temperature of Samples Based on Temp Profile (°C)
0-250	12-12.9	12.6	744-748	746	749 ± 3
250-500	12-13	12.5	746-750	747	750 ± 3
500-750	12.1-13.1	12.6	745-749	747	750 ± 3
750-1000	11.9-12.9	12.5	744-750	747	750 ± 3

Table 12: Pressure and Temperature Variance for LA3 series

5.7 Residual Gas Analyzer Data

At temperatures greater than 700 °C the carbon monoxide dissociation reaction, $2C + O_2 \leftrightarrow 2CO$, becomes more thermodynamically favorable than the carbon dioxide dissociation reaction $C + O_2 \leftrightarrow CO_2$. Therefore it may be possible to see a difference in the RGA signal peaks for CO_2, C, CO, or O_2, which would support that a new oxidation reaction was taking place. However, this was not the case because the final RGA reading (at temperature and pressure) showed the same composition as the CO_2 reading directly from the bottle at room temperature and at 5 MPa (not flowing through the experimental apparatus), which Figure 103 shows. However, the data obtained from the RGA can only be used qualitatively with respect to concentration as the different molecules and atoms in the system migrated at different rates; thus the arrival rate of species to the sampling system did not necessarily correspond to their

concentrations in the autoclave. Furthermore, the RGA ionized the molecules in the autoclave causing the spectra to contain not only signal from species present in the autoclave, but also the decomposition products of these species as well. This indicates that the RGA is not a powerful enough measuring tool to either prove or disprove if a new oxidation mechanism has occurred. A more rigorous gas composition analyzer, such as a gas chromatograph, needs to be used in order to obtain quantitative gas composition information.

The RGA readings in all of the experiments showed that there were no appreciable differences in gas composition in the autoclave from the start of the test to the finish, which Figure 102 supports. The initial reading (yellow) was recorded once the autoclave was at the desired temperature and pressure for the experiment and the final reading (green) was documented the moment before scheduled shutdown. This demonstrates that none of the inner components were off-gassing causing contamination of the samples. Additional RGA data for the other experiments can be found in Appendix B.

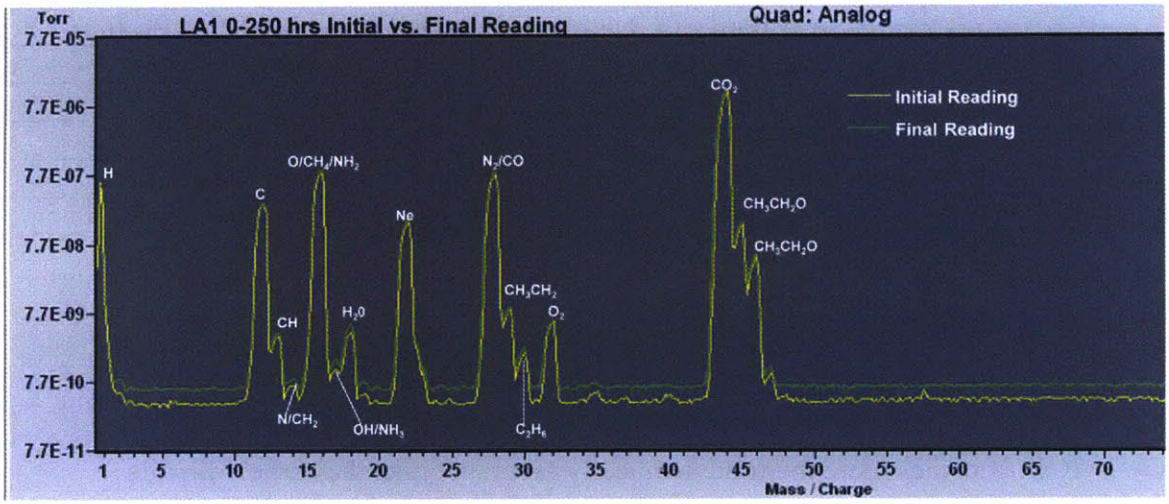

Figure 102: RGA Initial vs. Final Reading for the LA1 0-250 Hour Experiment

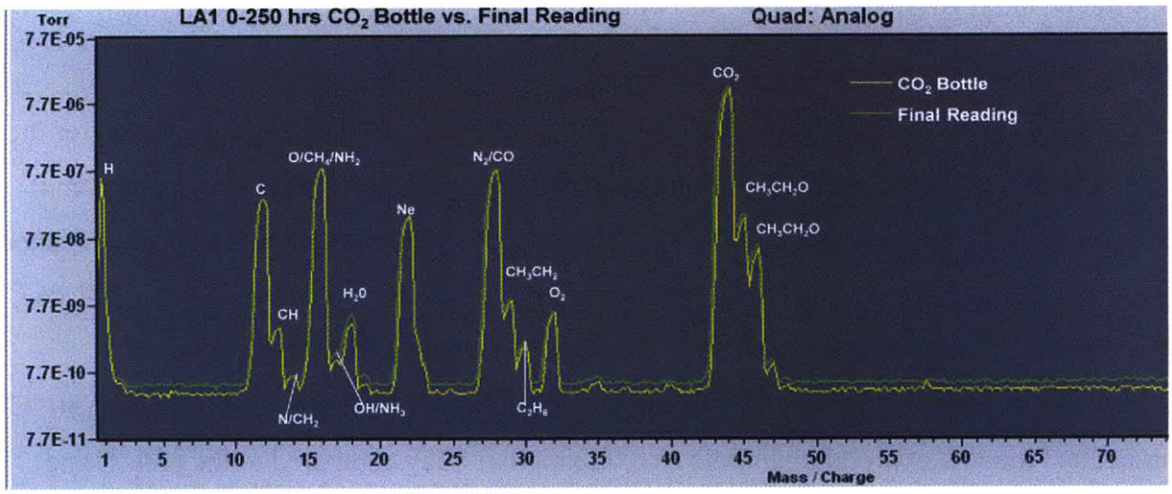

Figure 103: RGA CO_2 Bottle Reading vs. Final Reading for LA1 0-250 Hour Experiment

6. Summary and Conclusions

The goal of this thesis was to determine the effect temperature had on various alloys in a SCO_2 environment. SCO_2 is a prime coolant candidate for use in Generation IV gas cooled fast reactors as it allows for higher efficiencies, reduced pumping power, lower plant temperatures, and more compactness compared to the other gas coolants currently being examined.

A total of 7 different alloys, 6 nickel based and 1 austenitic stainless steel were used in three sets of experiments. The experiments, LA1, LA2, and LA3, exposed the specimens to SCO_2 with temperatures of 714 °C, 650 °C, and 750 °C, pressures of 20 MPa, 12.5 MPa, and 12.5 MPa, and for durations of 500 hours, 500 hours, and 1000 hours respectively. The nickel based alloys demonstrated very promising results as the weight gain rates were almost an order of magnitude lower than the stainless steel. The average nickel based sample exposed to SCO_2 at a temperature of 750 °C and a pressure of 12.5 MPa showed a weight gain rate of 0.0063 mg/cm^2*day, while the stainless steel sample had a weight gain rate of 0.096 mg/cm^2*day after a duration of 1000 hours. This was expected as the combination of nickel and chromium forms a higher integrity and more stable passive film than iron and chromium. Additionally, nickel has a lower oxygen affinity than iron and therefore the migration of cations into the scale is smaller. The chromium content for the AUSS 316L was also the lowest, which most likely contributed to the high oxidation rates. Inconel 693 and 740+ showed the lowest weight gain rates within the nickel base alloys throughout the experiments. This may be attributed to these alloys having a

low Fe content and high Si and Al contents, which promote the formation of underlying protective scales.

The tests conducted at 750 °C and 12.5 MPa showed the highest weight gain rates for the nickel based alloys. This was expected as the corrosion rate should follow an Arrhenius trend and for an increase in temperature of 15 °C the corrosion rate should increase roughly by a factor of 2. The effect of pressure seemed negligible compared to the effect of temperature as a 43% reduction in pressure and a 5% increase in temperature between experiments produced significantly higher corrosion rates. The AUSS 316L, behaved counter-intuitively as the 750 °C experiment had the lowest weight gain rate of 0.062 mg/cm^2*day compared to the 650 °C and 714 °C experiments, which had weight gain rates of 0.12 mg/cm^2*day and 0.13 mg/cm^2*day respectively. One explanation for this behavior may be that the increase in temperature caused an increase in the diffusion rate of Cr in the alloy, which facilitated a faster growth rate of an inner "healing" layer of chromium rich oxide that restricted the outward diffusion of cations and inward diffusion of anions. This was supported by the oxide morphologies of the specimens at each time point, which demonstrated that a thin chromium rich oxide layer initially formed on the surface and over time iron cations diffused through the surface scale forming an iron oxide external to the chromium oxide.

The surface morphology demonstrated that most of the nickel based alloys formed continuous protective films, generally consisting of a nickel-chromium spinel. Additionally, most of the nickel based alloys were precipitation hardened, which caused precipitates comprised mostly of Ti and Nb to form through the protective film. Longer duration tests are needed in order to determine the effect of precipitates on scale adherence. The stainless steel specimens appeared to have a thick iron oxide layer, most likely magnetite, form on the outer surface of the 650 °C and 714 °C experiment. The 750 °C experiment demonstrated a chromium rich layer formed initially, which iron cations diffused through causing the formation of an external magnetite layer over time.

It was also important to understand the effect that the carbon monoxide dissociation reaction, $2C + O2 \leftrightarrow 2CO$, had on the oxidation rate, as it becomes more thermodynamically favorable than the carbon dioxide dissociation reaction, $C + O2 \leftrightarrow CO_2$, at temperatures greater than 700°C. Understanding the carbon monoxide dissociation reaction is important as it may

introduce a new oxidation mechanism which might significantly affect the rate of weight gain. The RGA reported no appreciable differences between the CO_2 composition of the 650°C experiment and the 750°C, which indicates no new oxidation mechanism took place. However, the RGA was only a qualitative measuring tool, and a more powerful gas analyzer, such as a gas chromatograph must be used in order to definitively state if another oxidation reaction had occurred.

6.1 Future Work

This thesis was a preliminary study on the effect SCO_2 had on different alloys. More work is needed before these alloys are put into operation. Significantly longer tests, on the order of 20,000 hours, are needed in order to determine if any of the alloys will undergo the deleterious effects of breakaway corrosion. Additionally, longer duration tests are needed in order to determine the effect the surface precipitates have on both resistance to metal ion transport across the scale and scale adhesion. Surface precipitates may also be a very likely initiation site for fatigue cracking; therefore sample fatigue must be examined as well

Auger analysis should be used in order to determine if the precipitates are carbides, nitrides or carbonitrides. This analysis technique would confirm the exact composition of the thin films that formed on the surface as the penetration depth is only 1-10 nm. A conductive mounting compound should also be used with the sectioned samples in order to visibly see the different layers of oxides that form. Specimens of alloy 625, the material the autoclave was made of, should also be exposed to the same conditions as the experiments preformed in this thesis. This would show the effect the internal environment has on the autoclave. Additionally, this would show if the autoclave was scavenging all of the oxygen contaminants present in the gas.

Finally, tests that mimic the actual gas composition that will be used in an AGR need to be conducted, as the carbon dioxide will most likely contain minor concentrations of CO, water vapor, and carbohydrates (oil leakage) that the ultra pure CO_2 used in this experiment did not contain. The following properties also need to be assessed in a SCO_2 environment at temperature and pressure to determine the suitability of the different alloys: high temperature strength, creep strength, fracture toughness, swelling resistance and irradiation susceptibility.

7. References

1. **Nuclear Energy Institute.** http://www.nei.org/resourcesandstats/nuclear_statistics/worldstatistics/. [Online] August 2009.
2. **DOE, U.S.** *A Technical Roadmap for Generation IV Nuclear Energy Systems.* December 2002.
3. **Lim, J. Y., et al.** *Corrosion of Materials in Supercritical Carbon Dioxide Environments.* s.l. : Massachusetts Instituite of Technology.
4. **Madina, Virgina.** *Corrosion of Steels in Carbon Dioxide Environments: Literature Review.* June 2008.
5. **Shropshire, David, E.** *Lessons Learned from GEN 1 Carbon Dioxide Cooled Reactors.* s.l. : ICONE 12, April 25, 2004.
6. **Dostal, Vaclav, M.J., Driscoll and P., Hejzlar.** *A Supercritical Carbon Dioxide Cycle for Next Generation Nuclear Reactors.* s.l. : MIT CANES Report MIT-ANP-TR-100, March 2004.
7. **MIT.** http://web.mit.edu/2.813/www/readings/Ellingham_diagrams.pdf. [Online]
8. **Thon, Susanna.** *Selection of Materials for a Supercritical Carbon Dioxide Cooled Gas Fast Reactor.* s.l. : CANES, Aug 2002.
9. **Jones, Denny, A.** *Principles and Prevention of Corrosion.* Upper Saddle River, NJ : Prentice Hall, 1996.
10. **Holmes, D.R., Mortimer, D. and Newell, J.** *Discovery and Assessment of Accelerated Corrosion in Fe-9Cr Alloys and Steels.* s.l. : BNES International Conference on Corrosion of Steels in Carbon Dioxide, 1974.
11. **Taylor, J.W. and Trotsenberg, P.V.** *9 Cr-Mo Steels Breakaway Effects in Carbon Dioxide Coolant Media.* s.l. : BNES International Conference on Corrosion of Steels in Carbon Dioxide, 1974.
12. **Rowlands, P.C., et al.** *The Oxidation Performance of Magnox and Advanced Gas-Cooled Reactor Steels in High Pressure Carbon Dioxide.* s.l. : Nuclear Energy, 1986, Vol. 25.
13. **Smith, Gaylord.** *The Role of Protective Scales in Enhancing Oxidation Resistance.* s.l. : Corrosion , 1996. Paper number 137.
14. **Meier, G.H, Coons, W.C. and Perkings, R.A.** *Corrosion of Iron, Nickel, and Cobalt base alloys in Atmospheres Containing Carbon and Oxygen.* 3/4, s.l. : Oxidation of Metals, 1982, Vol. 17.
15. **Lobnig, R.E.** *Diffusion of cations in chromia layers grown on iron-base alloys.* 1/2, s.l. : Oxidation of Metals, 1992, Vol. 37.
16. **Stott, F.H., Wood, G.C. and Hobby, M.G.** *A Comparison of the Oxidation Behavior of Fe-Cr-Al, Ni-Cr-Al, and Co-Cr-Al Alloys.* s.l. : Oxidation of Metals, 1971, Vol. 2.
17. **Wood, G.C.** *High-Temperature Oxidation of Alloys.* 1, s.l. : Oxidation of MEtals, 1970, Vol. 2.
18. **Li, B and Gleeson, B.** *Effects of Silicon on the Oxidation Behavior of Ni-Base Chromia-Forming Alloys.* 1/2, s.l. : Oxidation of Metals, 2006, Vol. 65.
19. **Stott, F.H., Gabriel, G.J. and Wood, G.C.** *The Influence of Silicon on the High-Temperature Oxidation of Nickel.* 5, s.l. : Oxidation of Metals, 1987, Vol. 28.
20. **Kumar, A and Douglass, D.L** *Modification of the Oxidation Behavior of High-Purity Austenitic Fe-14Cr-14Ni by the Addition of Silicon..* 1, s.l. : Oxidation of Metals, 1976, Vol. 10.
21. **Evans, E, et al.** *Influence of Silicon Additions on the Oxidation Resistance of a Stainless Steel.* 1, 1983, Vol. 19.
22. **Whittle, D. P and Stringer, J.** *Improvements in High Temperature Oxidation Resistance by Additions of Reactive Elements or Oxide Dispersions.* A295, s.l. : Phil. Trans. R. Soc. London., 1980.
23. **Pint, B.A.** *Progress in Understanding the Reactive Element Effect Since the Whittle and Stringer Literature Review.* s.l. : Oak Ridge National Laboratory, 2001.
24. **Smeggil, J.G and Peterson, G. G.** *Nature of Indigenous Sulfur Segregated to the Free Metal Surface and to the Scale-Metal Interface* . 1988 : Oxidation of Metals, Vol. 1/2.
25. **Stasik, M. C., et al.** *Effects of Reactive Element Additions and Sulfur Removal on the Oxidation Behavior of FeCrAl Alloys.* 12, s.l. : Scripta Metallurgica et Materialia, 1994, Vol. 31.
26. **Cotell, C. M., et al.** *The Influence of Grain-Boundary Segregation of Y in Cr203 on the Oxidation of Cr Metal.* s.l. : Oxidation of Metals, 1990, Vol. 34.
27. **Stott, F. H., We, F.I. and Enahoro, C.A.** *Influence of Manganese on the High-Temperature Oxidation of Iron-Chromium Alloys Oxidation of Iron-Chromium Alloys.* 4, s.l. : Werkstoffe und Korrosion, 1989 , Vol. 40.
28. **Revie, Winston, R.** *Uhlig's Corrosion Handbook Second Edition.* New Jersey : Hoboken, New Jersey, 2006.
29. **Dunlevy, M., et al.** *Corrosion of Materials in a Supercritical Carbon Dioxide Environment.* Troy, NY : Supercritical Carbon Dioxide Power Cycle Symposium, 2009.
30. **Cao, G., et al.** *Corrosion of Candidate Alloys in Supercritical Carbon Dioxide.* Troy, Ny : Supercritical CO2 Power Cycle Symposium, 2009.

31. **Y., Kato.** *Overview of Supercritical Carbon Dioxide Cycle Studies at Tokyo Tech.* Cambridge, Ma : MIT-Tokyo Tech Symposium on Innovative Nuclear Energy Systems, NOv 2-4, 2005.
32. **Hejzlar, P, et al.** *Supercritical CO2 Brayton Cycle for Medium Power Applications.* s.l. : Center for Advanced Nuclear Energy Systems, April 2006.
33. **Tripathi, K.C. and Antill, J.E.** *Influence of Metallurgical Condition and Surface Finish on the High Temperature Oxidation Behaviour of Austenitic Stainless Steel in Carbon Dioxide.* s.l. : Corrosion Science, 1970, Vol. 10.
34. **Uhlig, Herbert and Winston Revie.** *Corrosion and Corrosion Control Third ed.* s.l. : John Wiley & Sons, 1985.
35. **Bowman, Randy.** *Superalloys: A Primer and History.* s.l. : The Minerals, Metals, and Materials Societcy.
36. **Reed-Hill, Robert E. and Abbaschian, Reza.** *Physical Metallurgy Principles, Third Edition.* s.l. : PWS Publishing Company, 1994.
37. **Waddington, J.S. and Jones, R.B.** *Properties of Stainless Steel Cladding for use in Advanced Gas Cooled Reactors.* Loucestershire : Physical Metallurgy of Reactor Fuel Elements Conference Proceedings, 1973.
38. **Castle, P.J. and Smallman, R.E.** *The Protective Oxidation of a 9.75% Cr-Fe Alloy in Carbon Dioxide.* 2, s.l. : Corrosion Science, 1984, Vol. 24.
39. **Ferguson, J.M., Garrett, J.C.P. and Lloyd, B.** *A Multivariable Investigation of the Kinetics of Oxidation of Mild Steels in High Temperature Carbon Dioxide.* s.l. : Corrosion of Steels in Carbon Dioxide, 1974.
40. **Special Metals.** *http://specialmetals.com/products/index.php.* [Online]
41. **Smith, Gaylord.** Personal Electronic Correspondence at Special Metals.
42. **ASTM.** *G31-72: Standard Practice for Laboratory Immersion Corrosion Testing of Materials.* 2004, ASTM.
43. **ASTM.** *Nonferrous Metals - Nickel, Cobalt, Lead, Tin, Zinc, Cadmium, Precious, Reactive, Refractory Metals and Alloys; Materials for Thermostats, Electrical Heating and Resistance Contacts, and Connectors.* 2005. Volume 02.04.
44. **Ragab, Abdel-Rahman and Bayoumi, Salah.** *Engineering Solid Mechanics.* s.l. : CRC, 1998.
45. **Omega.** *The Pressure, Strain, and Force Handbook Volume MM.* 2000.
46. **Cantrell, C.D.** *Modern Mathematical Methods for Physicists and Engineers.* s.l. : Cambridge University Press, 2000.
47. **Green, D and Perry, R.** *Perry's Chemical Engineers' Handbook, Eighth Edition* . s.l. : McGraw-Hill , 2007.
48. **Special Metals.** http://www.specialmetals.com/documents/Inconel%20alloy%20690.pdf. [Online]
49. **ZAJAC, S and JANSSON, B.** *Thermodynamics of the Fe-Nb-C-N System and the Solubility of Niobium Carbonitrides in Austenite.* s.l. : METALLURGICAL AND MATERIALS TRANSACTIONS , February, 1998, Vol. 29B.
50. **Buehler.** http://www.buehler.com/technical_information/Ni/4step/4step_nickel.htm. [Online]
51. **Bennett, M.J, Desport, J.A. and Labun, P.A.** *Analytical Electron Microscopy of a Selective Oxide formed on 20% Cr-25%Ni-Nb Stainless Steel.* 5/6, s.l. : Oxidation of Metals, 1984, Vol. 22.

Appendix A: Raw Weight Gain Data

Alloy	Specimen	0 hr Weight (g)	250 hr Wt (g)	0-250 hr Wt gain (mg)	0-250 hr Wt gain (mg/cm^2 day)	250 hr Avg Wt gain (mg/cm ^2day)	500 Hr Wt (g)	250-500 hr Wt gain (mg)	250-500hr Wt gain (mg/cm^ 2 day)	500 hr Avg Wt gain (mg/cm^ 2*day)	0-500 hr Cumulative Wt Gain mg/cm^2* day)	Surface Area (cm^2)
Inconel 690	LA1-01	0.58019	0.58044	0.25	0.0059	0.0073						4.042
Inconel 690	LA1-02	0.55601	0.55638	0.37	0.0088		0.55653	0.15	0.0035	0.0042	0.0061	4.041
Inconel 690	LA1-03	0.63915	0.63949	0.34	0.0081		0.63960	0.11	0.0026		0.0053	4.042
Inconel 690	LA1-04	0.65410	0.65446	0.36	0.0086		0.65463	0.17	0.0040		0.0063	4.038
Inconel 690	LA1-05	0.58602	0.58631	0.29	0.0069		0.58651	0.20	0.0047		0.0058	4.045
Inconel 690	LA1-06	0.63824	0.63846	0.22	0.0053		0.63873	0.27	0.0064		0.0058	4.018
Inconel 693	LA1-11	0.63940	0.63952	0.12	0.0029							4.029
Inconel 693	LA1-12	0.54814	0.54832	0.18	0.0043	0.0033	0.54835	0.03	0.00072	0.0010	0.0025	3.979
Inconel 693	LA1-13	0.62248	0.62263	0.15	0.0036		0.62265	0.02	0.00048		0.0020	4.020
Inconel 693	LA1-14	0.63065	0.63079	0.14	0.0033		0.63084	0.05	0.0011		0.0022	4.022
Inconel 693	LA1-15	0.61699	0.61708	0.09	0.0021		0.61714	0.06	0.0014		0.0017	4.022
Inconel 693	LA1-16	0.62467	0.62482	0.15	0.0036		0.62487	0.05	0.0011		0.0023	4.022
Inconel 718	LA1-21	0.67393	0.67421	0.28	0.0067	0.0073						4.029
Inconel 718	LA1-22	0.67545	0.67579	0.34	0.0081		0.67588	0.09	0.0021	0.0030	0.0051	4.029
Inconel 718	LA1-23	0.68592	0.68625	0.33	0.0079		0.68631	0.06	0.0014		0.0046	4.034
Inconel 718	LA1-24	0.68855	0.68886	0.31	0.0074		0.68901	0.15	0.0035		0.0054	4.040
Inconel 718	LA1-25	0.69368	0.69397	0.29	0.0069		0.69415	0.18	0.0042		0.0055	4.040
Inconel 718	LA1-26	0.69098	0.69126	0.28	0.0067		0.69142	0.16	0.0038		0.0052	4.040
Inconel 725	LA1-31	0.68539	0.68566	0.27	0.0065	0.0057						4.011
Inconel 725	LA1-32	0.68517	0.68546	0.29	0.0069		0.68559	0.13	0.0031	0.0041	0.0050	4.007
Inconel 725	LA1-33	0.70080	0.70110	0.30	0.0072		0.70122	0.12	0.0028		0.0050	4.017
Inconel 725	LA1-34	0.67433	0.67452	0.19	0.0046		0.67472	0.20	0.0047		0.0046	4.007
Inconel 725	LA1-35	0.68583	0.68604	0.21	0.0050		0.68625	0.21	0.0050		0.0050	4.007
Inconel 725	LA1-36	0.68994	0.69011	0.17	0.0041		0.69032	0.21	0.0050		0.0045	4.007
Inconel 740	LA1-41	0.61793	0.61805	0.12	0.0028	0.0036						4.049
Inconel 740	LA1-42	0.65253	0.65267	0.14	0.0033		0.65271	0.04	0.00095	0.0013	0.0021	4.039
Inconel 740	LA1-43	0.65415	0.65431	0.16	0.0038		0.65437	0.06	0.0014		0.0026	4.044
Inconel 740	LA1-44	0.68283	0.68300	0.17	0.0040		0.68307	0.07	0.0016		0.0028	4.049
Inconel 740	LA1-45	0.64878	0.64892	0.14	0.0033		0.64900	0.08	0.0019		0.0026	4.043
Inconel 740	LA1-46	0.68675	0.68692	0.17	0.0040		0.68695	0.03	0.00071		0.0023	4.043

Alloy	Specimen	0 hr Weight (g)	250 hr Wt (g)	0-250 hr Wt gain (mg)	0-250 hr Wt gain (mg/cm^2 day)	250 hr Avg Wt gain (mg/cm ^2day)	500 Hr Wt (g)	250-500 hr Wt gain (mg)	250-500hr Wt gain (mg/cm^ 2 day)	500 hr Avg Wt gain (mg/cm^ 2*day)	0-500 hr Cumulative Wt Gain mg/cm^2* day)	Surface Area (cm^2)
Inconel 740+	LA1-51	0.66123	0.66145	0.22	0.0052	0.00432						4.036
Inconel 740+	LA1-52	0.69570	0.69596	0.26	0.0061		0.69598	0.02	0.00048	0.00147	0.0033	4.036
Inconel 740+	LA1-53	0.58489	0.58511	0.22	0.0052		0.58512	0.01	0.00024		0.0027	4.036
Inconel 740+	LA1-54	0.67498	0.67516	0.18	0.0042		0.67524	0.08	0.0019		0.0030	4.039
Inconel 740+	LA1-55	0.63851	0.63862	0.11	0.002		0.63875	0.13	0.0030		0.0028	4.036
Inconel 740+	LA1-56	0.68832	0.68842	0.10	0.00238		0.68849	0.07	0.0016		0.0020	4.039
AUSS 316L	LA1-61	0.66811	0.67593	7.82	0.18	0.15680						4.031
AUSS 316L	LA1-62	0.66337	0.67120	7.83	0.18		0.67539	4.19	0.10	0.12	0.14	4.031
AUSS 316L	LA1-63	0.66160	0.66890	7.30	0.17		0.67356	4.66	0.11		0.14	4.033
AUSS 316L	LA1-64	0.66662	0.67308	6.46	0.15		0.67776	4.68	0.11		0.13	4.031
AUSS 316L	LA1-65	0.66715	0.67288	5.73	0.13		0.67813	5.25	0.12		0.13	4.033
AUSS 316L	LA1-66	0.64899	0.65335	4.36	0.10		0.65878	5.43	0.13		0.12	4.022

Table A.1 Raw Data for the LA1 (T=714°C P=20 MPa) Experiment

Alloy	Specimen	0 hr Weight (g)	250 hr Wt (g)	0-250 hr Wt gain (mg)	0-250 hr Wt gain (mg/cm^2 day)	250 hr Avg Wt gain (mg/cm^2 day)	500 Hr Wt (g)	250-500 hr Wt gain (mg)	250-500hr Wt gain (mg/cm^2 day)	500 hr Avg Wt gain (mg/cm^2 day)	0-500 hr Cumulative Wt Gain mg/cm^2 day)	Surface Area (cm^2)
Inconel 690	LA2-01	0.03065	0.03071	0.06	0.011	0.014				0.0015		0.492
Inconel 690	LA2-02	0.02370	0.02374	0.04	0.0079		0.02375	0.01	0.0019		0.0049	0.486
Inconel 690	LA2-03	0.03189	0.03196	0.07	0.013		0.03196	0.00	0.00000		0.0068	0.492
Inconel 690	LA2-04	0.02819	0.02828	0.09	0.017		0.02830	0.02	0.0039		0.0108	0.487
Inconel 690	LA2-05	0.02454	0.02463	0.09	0.017		0.02465	0.02	0.0039		0.0109	0.482
Inconel 690	LA2-06	0.02186	0.02196	0.10	0.020		0.02195	-0.01	-0.0020		0.0090	0.480
Inconel 693	LA2-11	0.02379	0.02384	0.05	0.010	0.0067				0.00040		0.471
Inconel 693	LA2-12	0.03085	0.03087	0.02	0.0040		0.03089	0.02	0.0040		0.0040	0.479
Inconel 693	LA2-13	0.03125	0.03131	0.06	0.012		0.03129	-0.02	-0.0040		0.0040	0.479
Inconel 693	LA2-14	0.03002	0.03003	0.01	0.0020		0.03003	0.00	0.00000		0.0010	0.479
Inconel 693	LA2-15	0.03147	0.03150	0.03	0.0060		0.03151	0.01	0.0020		0.0040	0.479
Inconel 693	LA2-16	0.02936	0.02939	0.03	0.0060		0.02939	0.00	0.00000		0.0030	0.480
Inconel 718 (EG)	LA2-21	0.03556	0.03561	0.05	0.0097	0.0081				0.00039		0.494
Inconel 718 (EG)	LA2-22	0.03549	0.03550	0.01	0.0019		0.03556	0.06	0.011		0.0068	0.493
Inconel 718 (EG)	LA2-23	0.03596	0.03603	0.07	0.013		0.03600	-0.03	-0.0058		0.0038	0.493
Inconel 718 (EG)	LA2-24	0.03594	0.03597	0.03	0.0058		0.03594	-0.03	-0.0058		0.00000	0.494
Inconel 718 (EG)	LA2-25	0.03548	0.03552	0.04	0.0077		0.03553	0.01	0.0019		0.0048	0.494
Inconel 718 (EG)	LA2-26	0.03512	0.03517	0.05	0.0097		0.03517	0.00	0.00000		0.0048	0.493
Inconel 718	LA2-71	0.01802	0.01806	0.04	0.0082	0.0064				0.00042		0.463
Inconel 718	LA2-72	0.01858	0.01860	0.02	0.0040		0.01860	0.00	0.00000		0.0020	0.469
Inconel 718	LA2-73	0.02193	0.02195	0.02	0.0040		0.02195	0.00	0.00000		0.0020	0.469
Inconel 718	LA2-74	0.01593	0.01597	0.04	0.0082		0.01599	0.02	0.0041		0.0062	0.464
Inconel 718	LA2-75	0.02712	0.02717	0.05	0.0100		0.02717	0.00	0.00000		0.0050	0.480
Inconel 718	LA2-76	0.01565	0.01567	0.02	0.0041		0.01566	-0.01	-0.00205		0.0010	0.468
Inconel 725 (EG)	LA2-31	0.03591	0.03593	0.02	0.0038	0.0094				0.0011		0.494
Inconel 725 (EG)	LA2-32	0.03086	0.03088	0.02	0.0039		0.03091	0.03	0.0059		0.0049	0.487
Inconel 725 (EG)	LA2-33	0.03249	0.03255	0.06	0.011		0.03254	-0.01	-0.0019		0.0049	0.489
Inconel 725 (EG)	LA2-34	0.03553	0.03559	0.06	0.011		0.03560	0.01	0.0019		0.0068	0.494
Inconel 725 (EG)	LA2-35	0.03475	0.03480	0.05	0.0098		0.03480	0.00	0.00000		0.0049	0.489
Inconel 725 (EG)	LA2-36	0.03306	0.03314	0.08	0.015		0.03314	0.00	0.00000		0.0078	0.488

Alloy	Specimen	0 hr Weight (g)	250 hr Wt (g)	0-250 hr Wt gain (mg)	0-250 hr Wt gain (mg/cm^2 day)	250 hr Avg Wt gain (mg/cm^2 day)	500 Hr Wt (g)	250-500 hr Wt gain (mg)	250-500hr Wt gain (mg/cm^2 day)	500 hr Avg Wt gain (mg/cm^2 day)	0-500 hr Cumulative Wt Gain mg/cm^2 day)	Surface Area (cm^2)
Inconel 725	LA2-81	0.01773	0.01778	0.05	0.010	0.0099				0.00051		0.469
Inconel 725	LA2-82	0.01507	0.01513	0.06	0.012		0.01513	0.00	0.00000		0.0062	0.464
Inconel 725	LA2-83	0.01151	0.01156	0.05	0.010		0.01155	-0.01	-0.0020		0.0041	0.461
Inconel 725	LA2-84	0.01976	0.01981	0.05	0.010		0.01982	0.01	0.0020		0.0061	0.466
Inconel 725	LA2-85	0.01735	0.01738	0.03	0.0061		0.01739	0.01	0.0020		0.0040	0.469
Inconel 725	LA2-86	xxxx	xxxxx	xxxx	xxxx	xxxx	xxxx	xxxx	xxxx		xxxx	0.478
Inconel 740	LA2-41	0.02674	0.02675	0.01	0.0020	0.0079				0.00000		0.478
Inconel 740	LA2-42	0.02416	0.02422	0.06	0.012		0.02424	0.02	0.0040		0.0080	0.480
Inconel 740	LA2-43	0.03110	0.03114	0.04	0.0078		0.03115	0.01	0.0019		0.0049	0.487
Inconel 740	LA2-44	0.02487	0.02488	0.01	0.0019		xxxxx	xxxxx	xxxxx		xxxxx	0.483
Inconel 740	LA2-45	0.03075	0.03081	0.06	0.011		0.03078	-0.03	-0.0059		0.0029	0.482
Inconel 740	LA2-46	0.02632	0.02638	0.06	0.011		0.02638	0.00	0.00000		0.0059	0.481
Inconel 740+	LA2-51	0.03408	0.03409	0.01	0.0019	0.0026				0.0015		0.484
Inconel 740+	LA2-52	0.03480	0.03481	0.01	0.0019		0.03481	0.00	0.00000		0.00099	0.487
Inconel 740+	LA2-53	0.03382	0.03386	0.04	0.0079		0.03387	0.01	0.0019		0.0049	0.485
Inconel 740+	LA2-54	0.03396	0.03398	0.02	0.0039		0.03399	0.01	0.0019		0.0029	0.485
Inconel 740+	LA2-55	0.03476	0.03476	0.00	0.00000		0.03478	0.02	0.0039		0.0019	0.484
Inconel 740+	LA2-56	0.03538	0.03538	0.00	0.00000		0.03538	0.00	0.00000		0.00000	0.469
AUSS 316L	LA2-61	0.02161	0.02217	0.56	0.11	0.13				0.08		0.455
AUSS 316L	LA2-62	0.00984	0.01033	0.49	0.10		0.01061	0.28	0.059		0.081	0.472
AUSS 316L	LA2-63	0.02265	0.02327	0.62	0.12		0.02358	0.31	0.063		0.094	0.471
AUSS 316L	LA2-64	0.02520	0.02585	0.65	0.13		0.02624	0.39	0.079		0.10	0.463
AUSS 316L	LA2-65	0.01476	0.01554	0.78	0.16		0.01601	0.47	0.097		0.12	0.459
AUSS 316L	LA2-66	0.01394	0.01487	0.93	0.19		0.01552	0.65	0.13		0.16	0.492

Table A.2 Raw Data for the LA2 (T=650°C P=12.5 MPa) Experiment

Alloy	Specimen	0 hr Weight (g)	250 hr Wt (g)	0-250 hr Wt gain (mg)	0-250 hr Wt gain (mg/cm^2 day)	250 hr Avg Wt gain (mg/cm^2 day)	500 Hr Wt (g)	250-500 hr Wt gain (mg)	250-500hr Wt gain (mg/cm^2 day)	500 hr Avg Wt gain (mg/cm^2 day)	0-500 hr Cumulative Wt Gain mg/cm^2 day)	Surface Area (cm^2)
Inconel 690	LA3-01	0.33249	0.33301	0.52	0.012	0.013				0.0049		3.897
Inconel 690	LA3-02	0.46749	0.46807	0.52	0.012		0.46829	0.22	0.0053		0.0097	3.954
Inconel 690	LA3-03	0.59915	0.59976	0.61	0.014		0.60001	0.25	0.0059		0.0103	4.004
Inconel 690	LA3-04	0.48340	0.48392	0.52	0.012		0.48406	0.14	0.0034		0.0080	3.958
Inconel 693	LA3-11	0.55515	0.55558	0.44	0.010	0.010				0.0039		3.996
Inconel 693	LA3-12	0.55662	0.55714	0.52	0.012		0.55733	0.19	0.0045		0.0085	3.996
Inconel 693	LA3-13	0.55761	0.55798	0.38	0.0091		0.55813	0.15	0.0036		0.0062	3.995
Inconel 693	LA3-14	0.52428	0.52476	0.48	0.011		0.52491	0.15	0.0036		0.0076	3.981
Inconel 718 (EG)	LA3-21	0.56163	0.56205	0.42	0.010	0.011				0.0031		3.996
Inconel 718 (EG)	LA3-22	0.58660	0.58708	0.48	0.011		0.58719	0.11	0.0026		0.0070	4.007
Inconel 718 (EG)	LA3-23	0.58273	0.58323	0.51	0.012		0.58339	0.16	0.0038		0.0079	4.012
Inconel 718 (EG)	LA3-24	0.58671	0.58729	0.58	0.013		0.58742	0.13	0.0031		0.0085	4.004
Inconel 718	LA3-71	0.54174	0.54224	0.50	0.012	0.012				0.0027		3.987
Inconel 718	LA3-72	0.57346	0.57404	0.58	0.013		0.57421	0.17	0.0040		0.0090	4.002
Inconel 718	LA3-73	0.55085	0.55141	0.55	0.013		0.55149	0.08	0.0019		0.0077	3.976
Inconel 718	LA3-74	0.61786	0.61837	0.51	0.012		0.61846	0.09	0.0021		0.0071	4.019
Inconel 725 (EG)	LA3-31	0.62725	0.62804	0.79	0.018	0.019				0.0082		4.018
Inconel 725 (EG)	LA3-32	0.63615	0.63706	0.91	0.021		0.63744	0.38	0.0090		0.015	4.018
Inconel 725 (EG)	LA3-33	0.62775	0.62855	0.80	0.019		0.62888	0.33	0.0079		0.013	4.010
Inconel 725 (EG)	LA3-34	0.65315	0.65392	0.77	0.018		0.65424	0.32	0.0076		0.013	4.020
Inconel 725	LA3-81	0.61116	0.61203	0.88	0.021	0.019				0.0082		4.019
Inconel 725	LA3-82	0.63278	0.63363	0.85	0.020		0.63400	0.37	0.0088		0.014	4.024
Inconel 725	LA3-83	0.61865	0.61947	0.83	0.019		0.61985	0.38	0.0090		0.014	4.019
Inconel 725	LA3-84	0.62127	0.62199	0.72	0.017		0.62228	0.29	0.0069		0.012	4.024
Inconel 740	LA3-41	0.58913	0.58971	0.58	0.013	0.013				0.0062		3.992
Inconel 740	LA3-42	0.61614	0.61675	0.61	0.014		0.61702	0.27	0.0064		0.010	4.018
Inconel 740	LA3-43	0.59857	0.59915	0.58	0.013		0.59941	0.26	0.0062		0.010	4.012
Inconel 740	LA3-44	0.56855	0.56901	0.46	0.011		0.56926	0.25	0.0060		0.0080	3.996
Inconel 740+	LA3-51	0.49964	0.50014	0.50	0.012	0.011				0.0040		3.975
Inconel 740+	LA3-52	0.53645	0.53699	0.54	0.012		0.53719	0.20	0.0048		0.0089	3.991
Inconel 740+	LA3-53	0.53011	0.53055	0.44	0.010		0.53070	0.15	0.0036		0.0071	3.988
Inconel 740+	LA3-54	0.55741	0.55778	0.37	0.0088		0.55793	0.15	0.0036		0.0062	3.995

Alloy	Specimen	0 hr Weight (g)	250 hr Wt (g)	0-250 hr Wt gain (mg)	0-250 hr Wt gain (mg/cm^2 day)	250 hr Avg Wt gain (mg/cm^2 day)	500 Hr Wt (g)	250-500 hr Wt gain (mg)	250-500hr Wt gain (mg/cm^2 day)	500 hr Avg Wt gain (mg/cm^2 day)	0-500 hr Cumulative Wt Gain mg/cm^2 day)	Surface Area (cm^2)
AUSS 316L	LA3-61	0.56950	0.57074	1.25	0.030	0.051				0.065		3.992
AUSS 316L	LA3-62	0.57106	0.57337	2.31	0.055		0.57594	2.57	0.061		0.058	3.992
AUSS 316L	LA3-63	0.57514	0.57679	1.65	0.039		0.57866	1.87	0.044		0.042	3.992
AUSS 316L	LA3-64	0.59026	0.59360	3.34	0.080		0.59732	3.72	0.089		0.084	3.994

Table A.3 Raw Data for the LA3 (T=750°C P=12.5 MPa) Experiment 0-500 Hours

Alloy	Specimen	750 hr Weight (g)	500-750 hr Wt gain (mg)	500-750 hr Wt gain (mg/cm^2 day)	500-750 hr Avg Wt gain (mg/cm^2day)	1000 hr Weight (g)	750-1000 hr Wt gain (mg)	Cumulative 0-1000 hr Wt gain (mg/cm^2 day)
Inconel 690	LA3-01				0.0044			
Inconel 690	LA3-02							
Inconel 690	LA3-03	0.60019	0.18000	0.0043				
Inconel 690	LA3-04	0.48425	0.19000	0.0046		0.48439	0.14	0.0034
Inconel 693	LA3-11				0.0031			
Inconel 693	LA3-12							
Inconel 693	LA3-13	0.55825	0.12000	0.0028				
Inconel 693	LA3-14	0.52505	0.14000	0.0033		0.52521	0.16	0.0038
Inconel 718 (EG)	LA3-21				0.0016			
Inconel 718 (EG)	LA3-22							
Inconel 718 (EG)	LA3-23	0.58346	0.07000	0.0016				
Inconel 718 (EG)	LA3-24	0.58749	0.07000	0.0016		0.58758	0.090	0.0021
Inconel 718	LA3-71				0.0033			
Inconel 718	LA3-72							
Inconel 718	LA3-73	0.55164	0.15000	0.0036				
Inconel 718	LA3-74	0.61859	0.13000	0.0031		0.61869	0.10	0.0023
Inconel 725 (EG)	LA3-31				0.0062			
Inconel 725 (EG)	LA3-32							
Inconel 725 (EG)	LA3-33	0.62914	0.26000	0.0062				
Inconel 725 (EG)	LA3-34	0.65450	0.26000	0.0062		0.65469	0.19	0.0045

Alloy	Specimen	750 hr Weight (g)	500-750 hr Wt gain (mg)	500-750 hr Wt gain (mg/cm^2 day)	500-750 hr Avg Wt gain (mg/cm^2day)	1000 hr Weight (g)	750-1000 hr Wt gain (mg)	Cumulative 0-1000 hr Wt gain (mg/cm^2 day)
Inconel 725	LA3-81				0.0064			
Inconel 725	LA3-82							
Inconel 725	LA3-83	0.62011	0.26	0.0062				
Inconel 725	LA3-84	0.62256	0.28	0.0066		0.62279	0.23	0.0054
Inconel 740	LA3-41				0.0043			
Inconel 740	LA3-42							
Inconel 740	LA3-43	0.59961	0.20	0.0047				
Inconel 740	LA3-44	0.56942	0.16	0.0038		0.56958	0.16	0.0038
Inconel 740+	LA3-51				0.0028			
Inconel 740+	LA3-52							
Inconel 740+	LA3-53	0.53083	0.13	0.0031				
Inconel 740+	LA3-54	0.55804	0.11	0.0026		0.55814	0.10	0.0024
AUSS 316L	LA3-61				0.0901			
AUSS 316L	LA3-62							
AUSS 316L	LA3-63	0.58160	2.94	0.070				
AUSS 316L	LA3-64	0.60188	4.56	0.10		0.60631	4.43	0.10

Table A.4 Raw Data for the LA4 (T=750°C P=12.5 MPa) Experiment 500-1000 Hours

Appendix B: Temperature, Pressure, and RGA Variation During Experiments

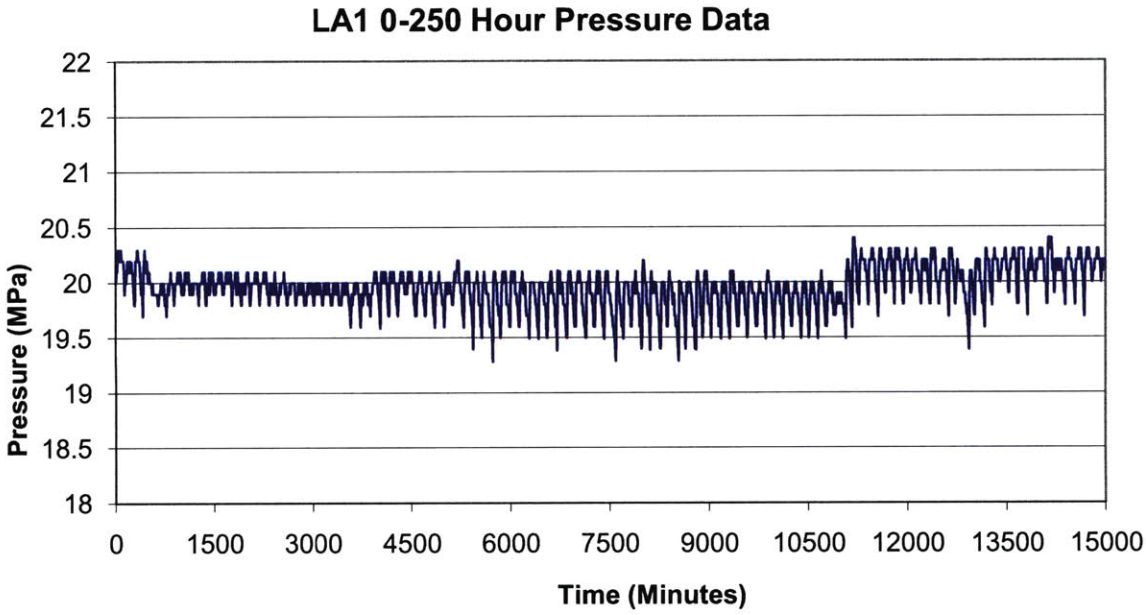

Figure B.1: Pressure Variation for the LA1 0-250 Hour Experiment

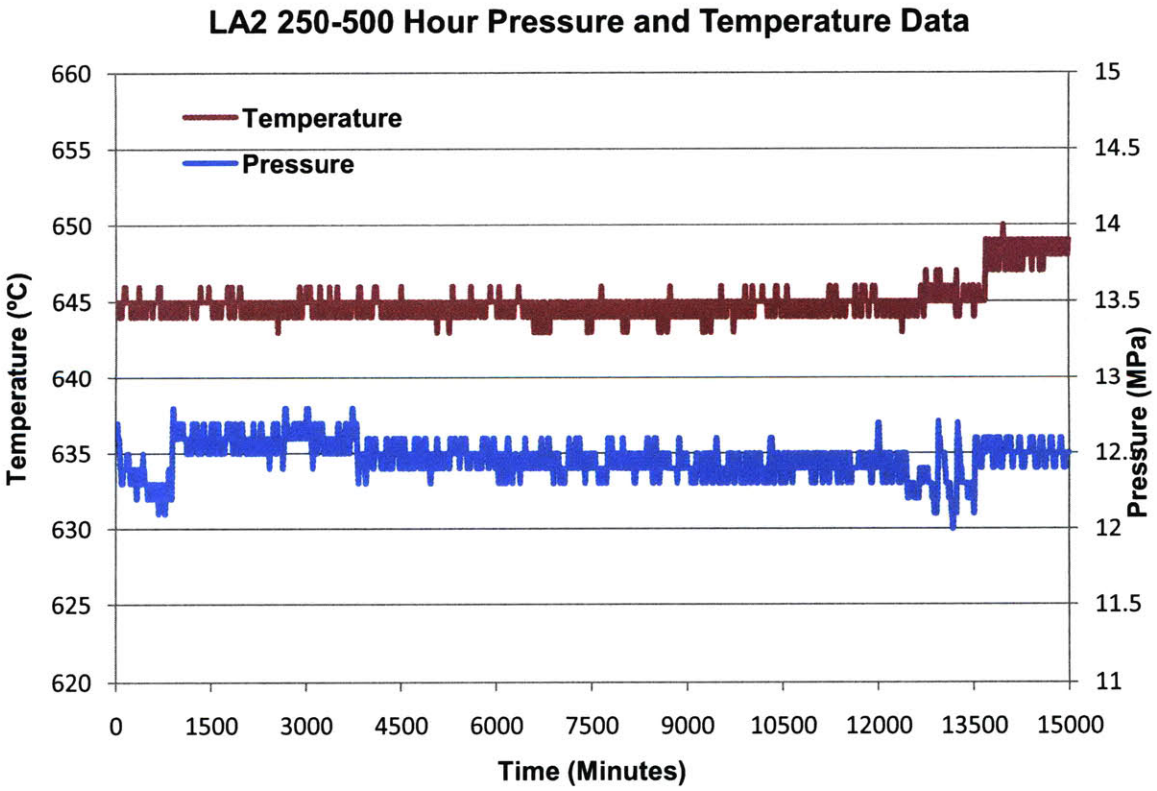

Figure B.2: Pressure Variation for the LA1 250-500 Hour Experiment

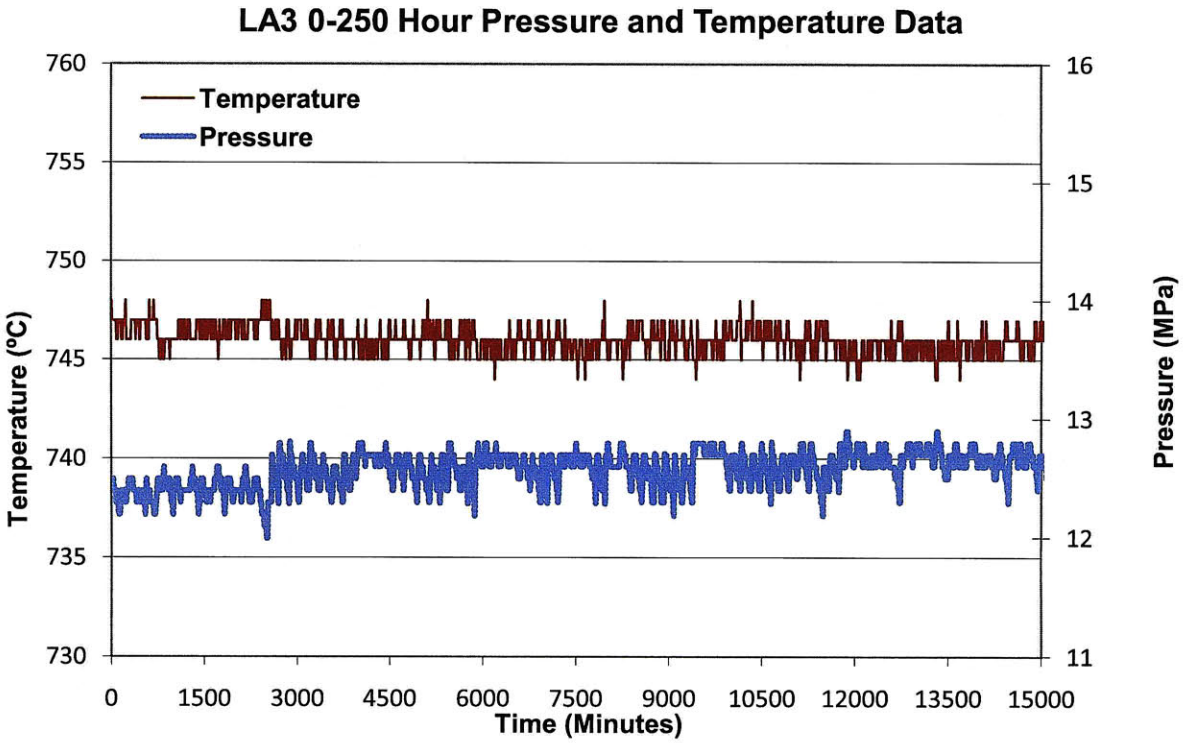

Figure B.3: Pressure and Temperature Variation for the LA3 0-250 Hour Experiment

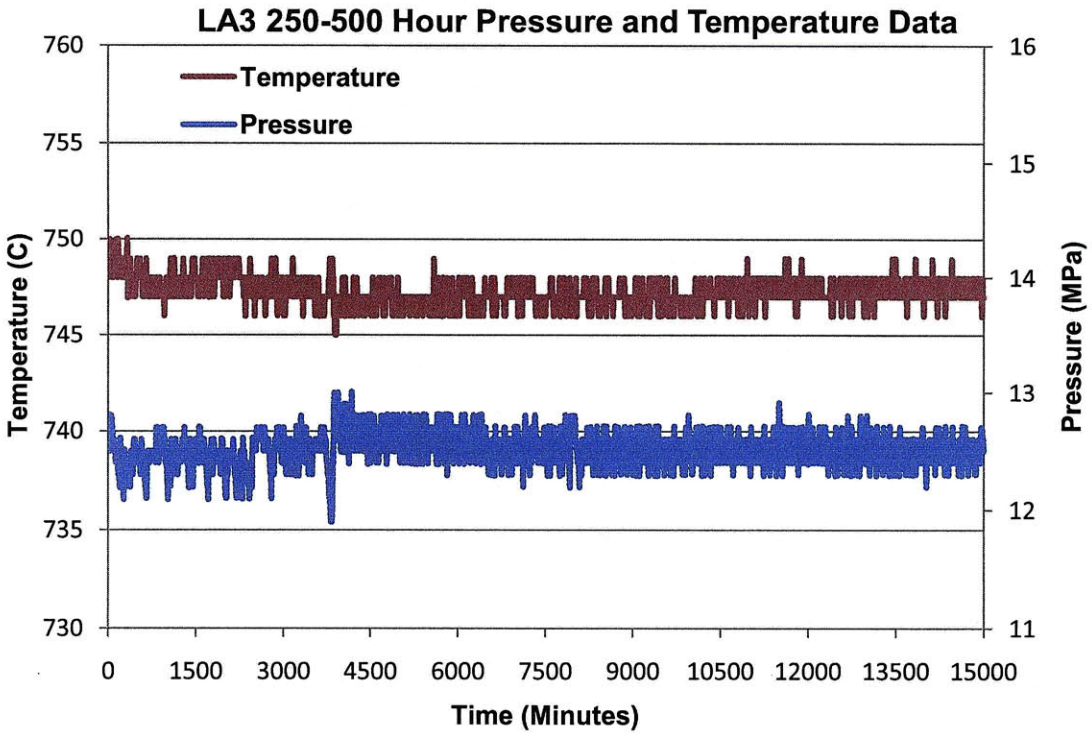

Figure B.4: Pressure and Temperature Variation for the LA3 250-500 Hour Experiment

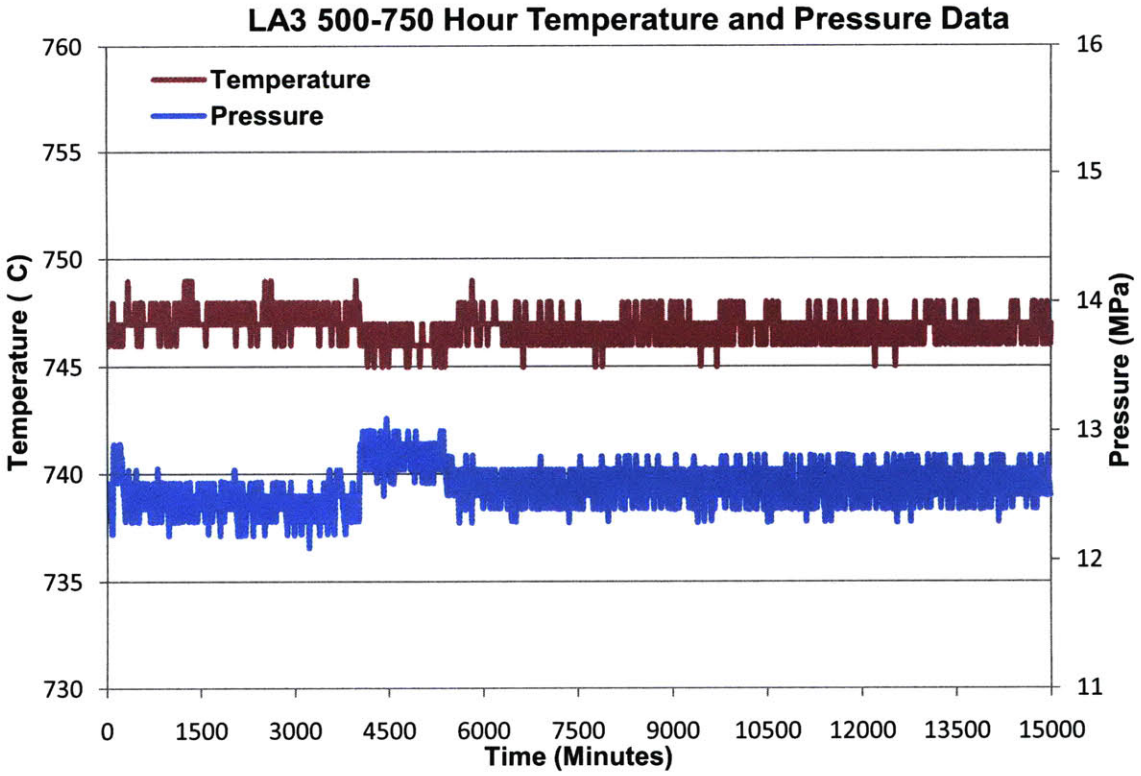

Figure B.5: Pressure and Temperature Variation for the LA3 500-750 Hour Experiment

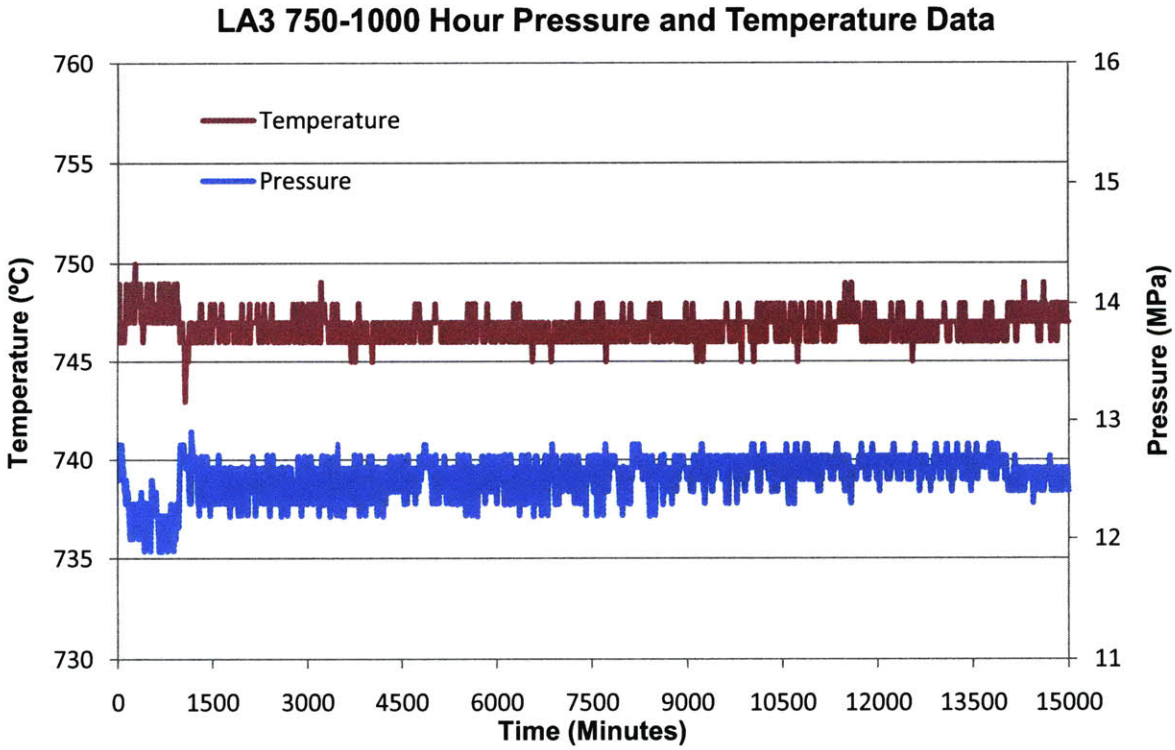

Figure B.6: Pressure and Temperature Variation for the LA3 750-1000 Hour Experiment

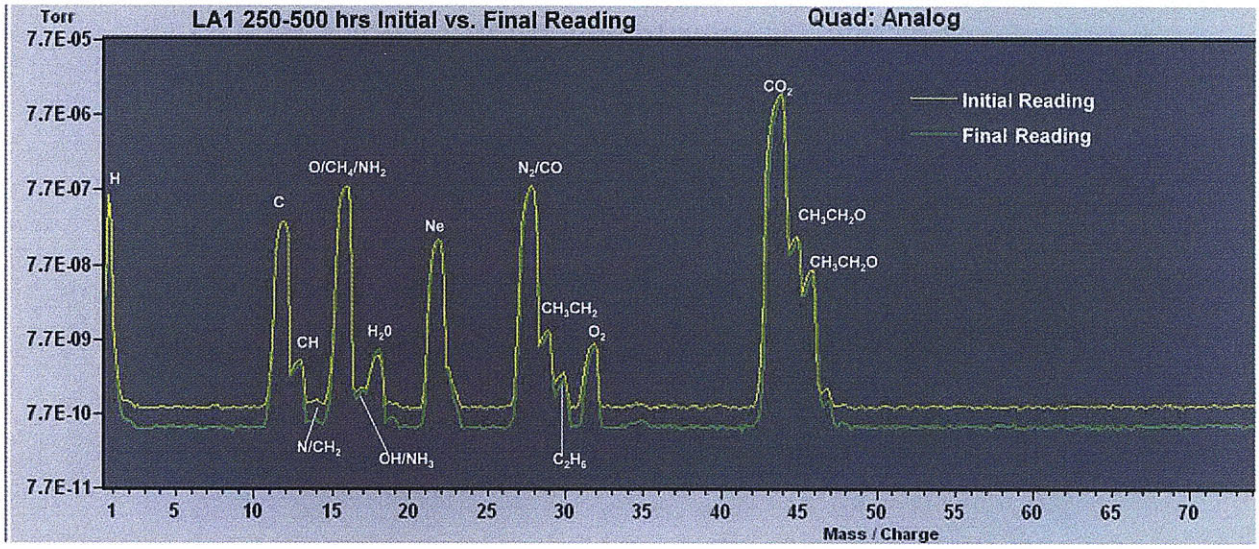

Figure B.7: RGA Initial vs. Final Reading for the LA1 250-500 Hour Experiment

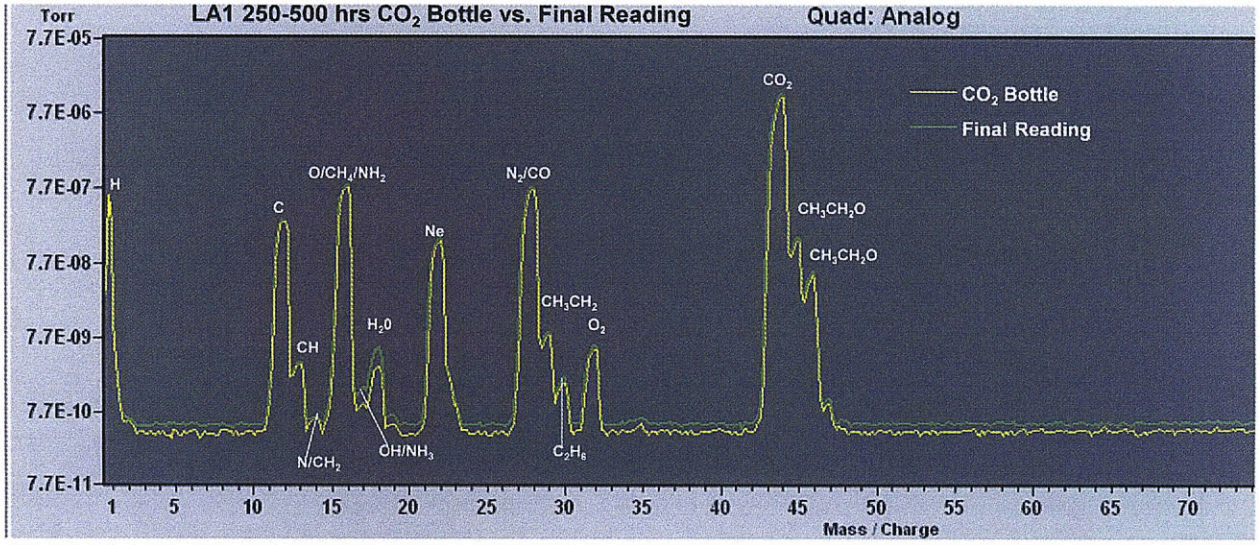

Figure B.8: RGA CO_2 Bottle Reading vs. Final Reading for LA1 250-500 Hour Experiment

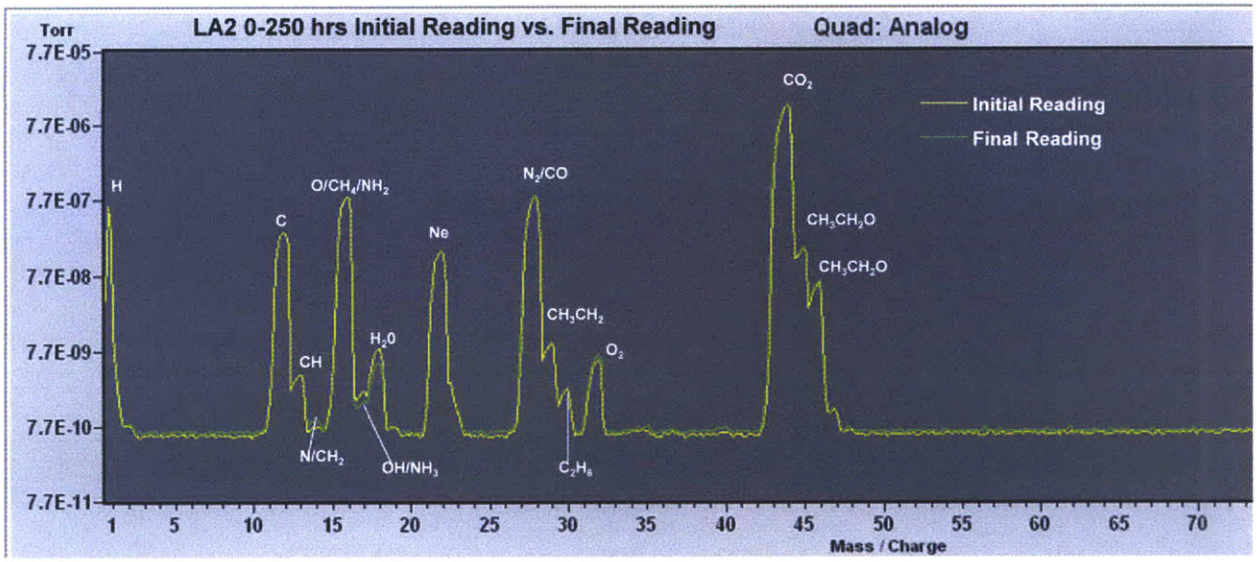

Figure B.9: RGA Initial vs. Final Reading for the LA2 0-250 Hour Experiment

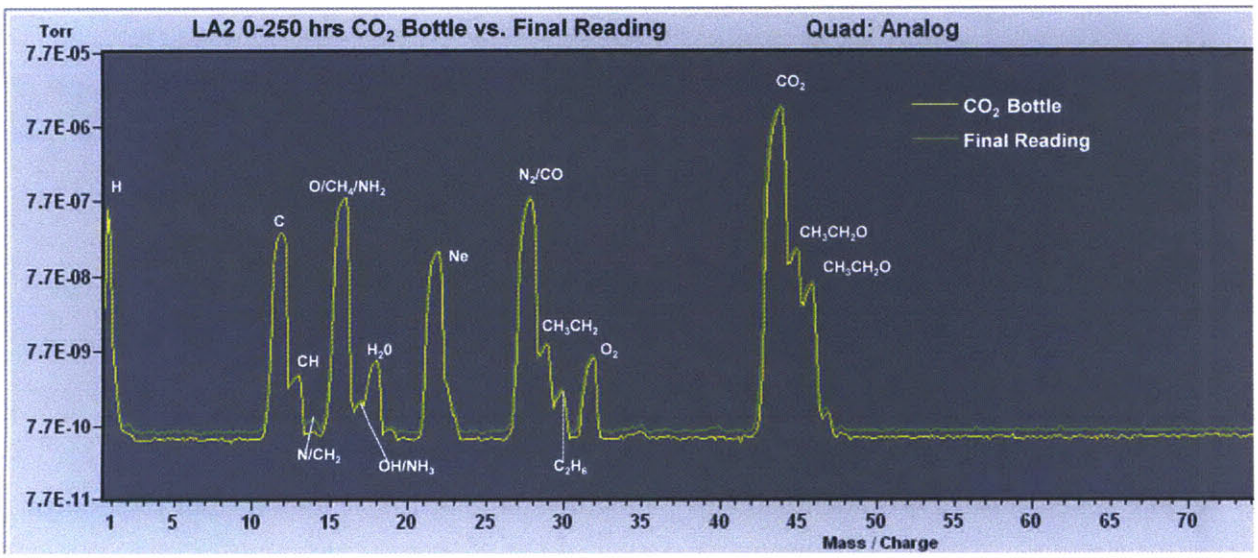

Figure B.10: RGA CO_2 Bottle Reading vs. Final Reading for LA2 0-250 Hour Experiment

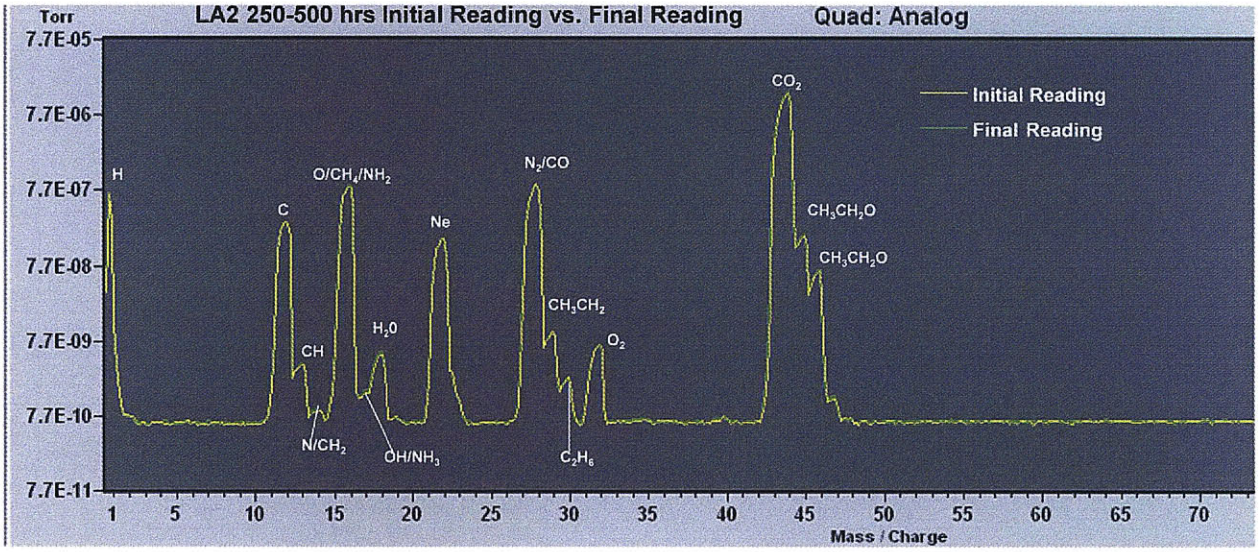

Figure B.11: RGA Initial vs. Final Reading for the LA2 250-500 Hour Experiment

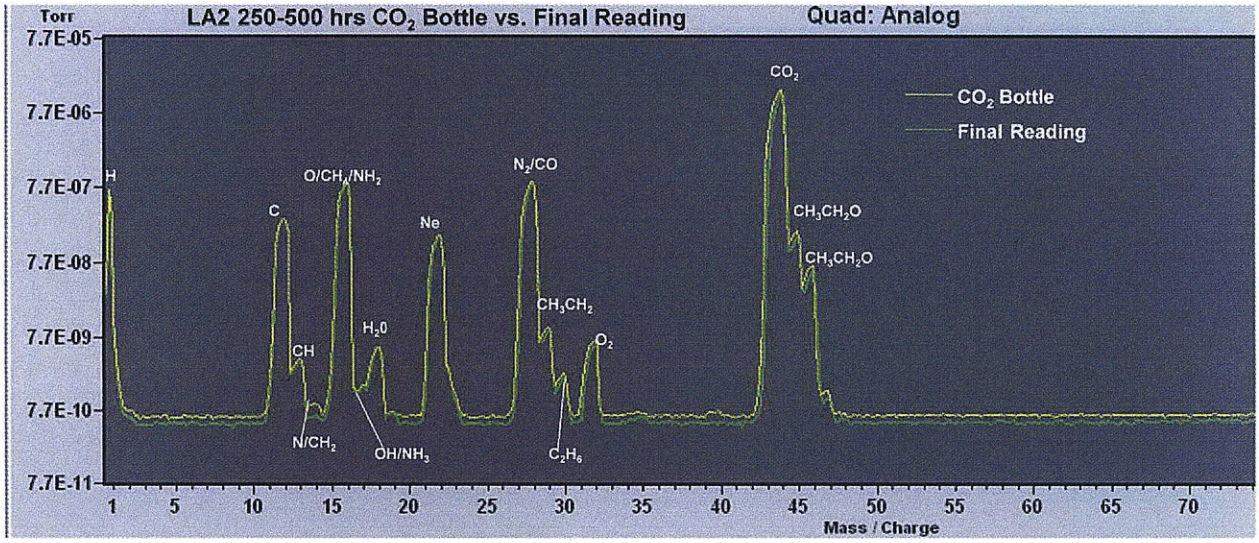

Figure B.12: RGA CO_2 Bottle Reading vs. Final Reading for LA2 250-500 Hour Experiment

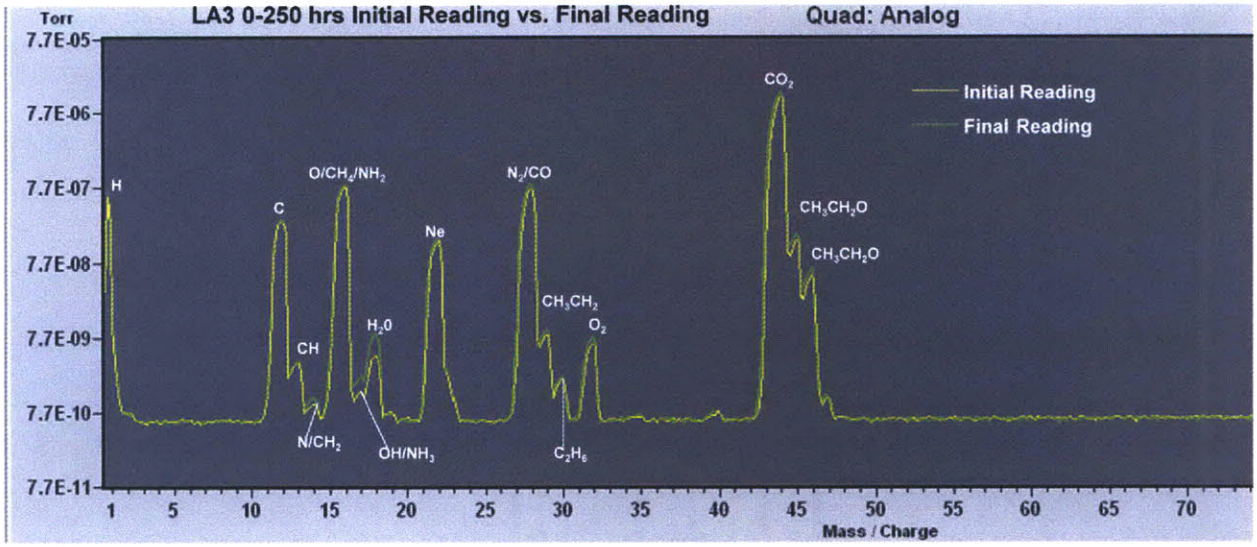

Figure B.13: RGA Initial vs. Final Reading for the LA3 0-250 Hour Experiment

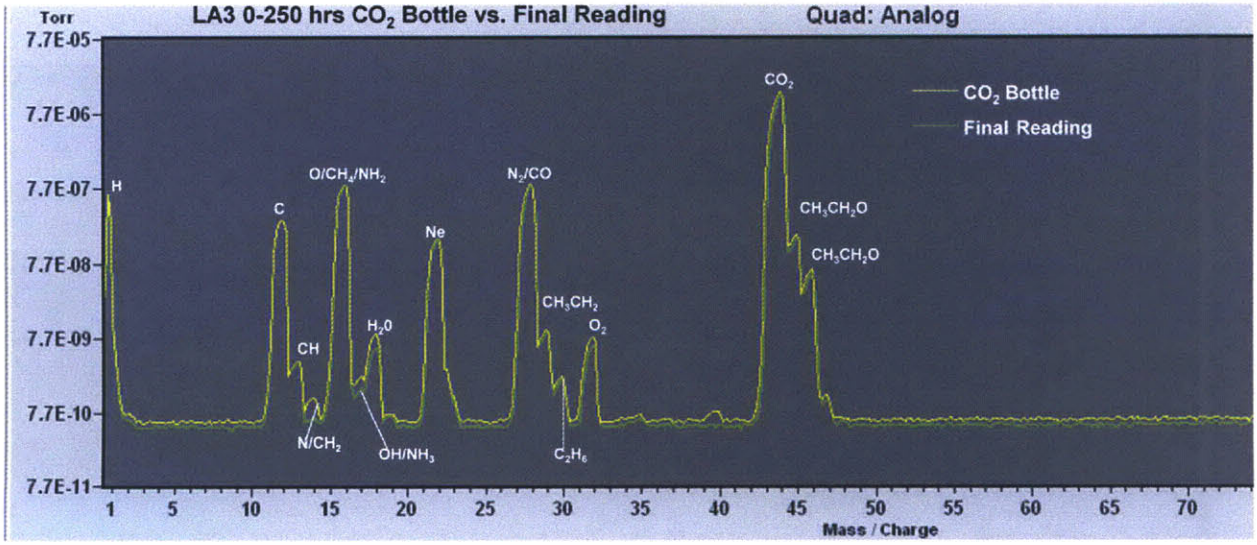

Figure B.14: RGA CO_2 Bottle Reading vs. Final Reading for LA3 0-250Hour Experiment

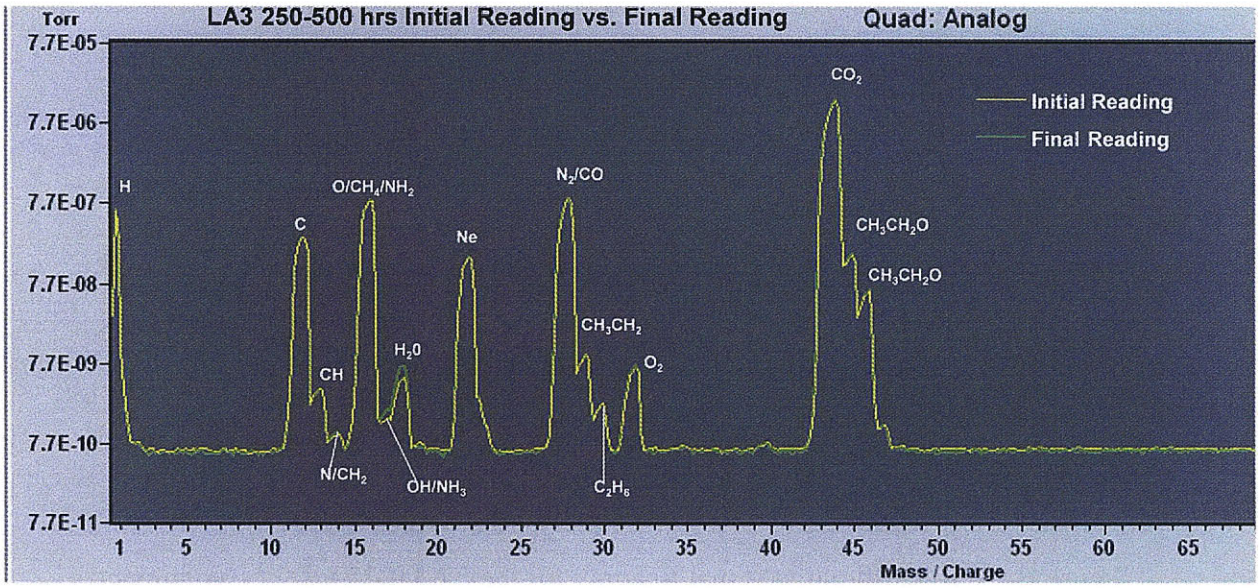

Figure B.15: RGA Initial vs. Final Reading for the LA3 250-500 Hour Experiment

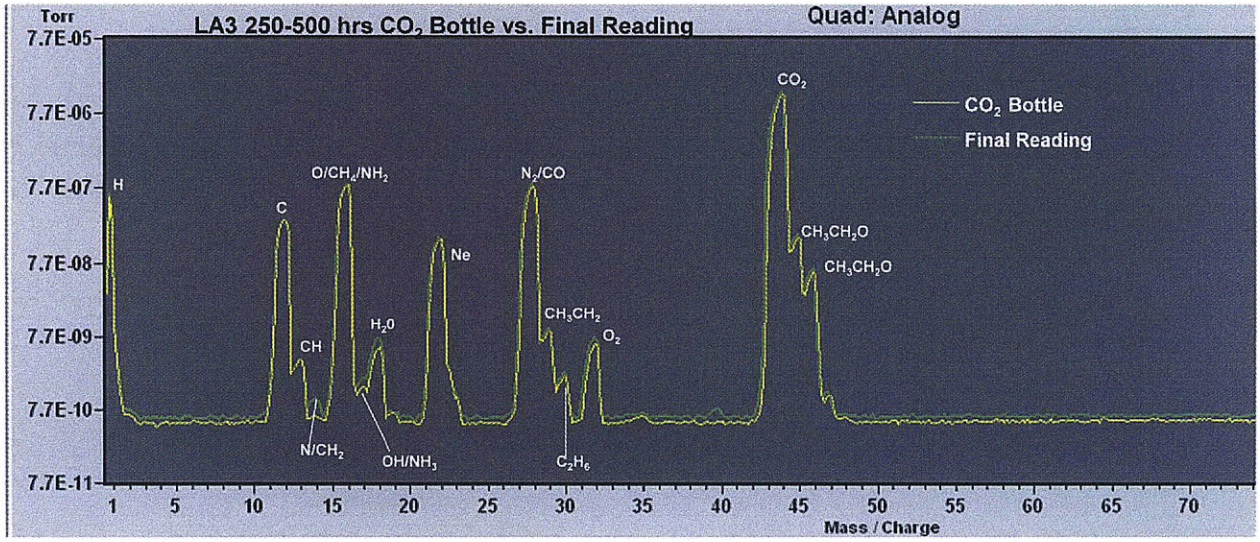

Figure B.16: RGA CO_2 Bottle Reading vs. Final Reading for LA3 250-500 Hour Experiment

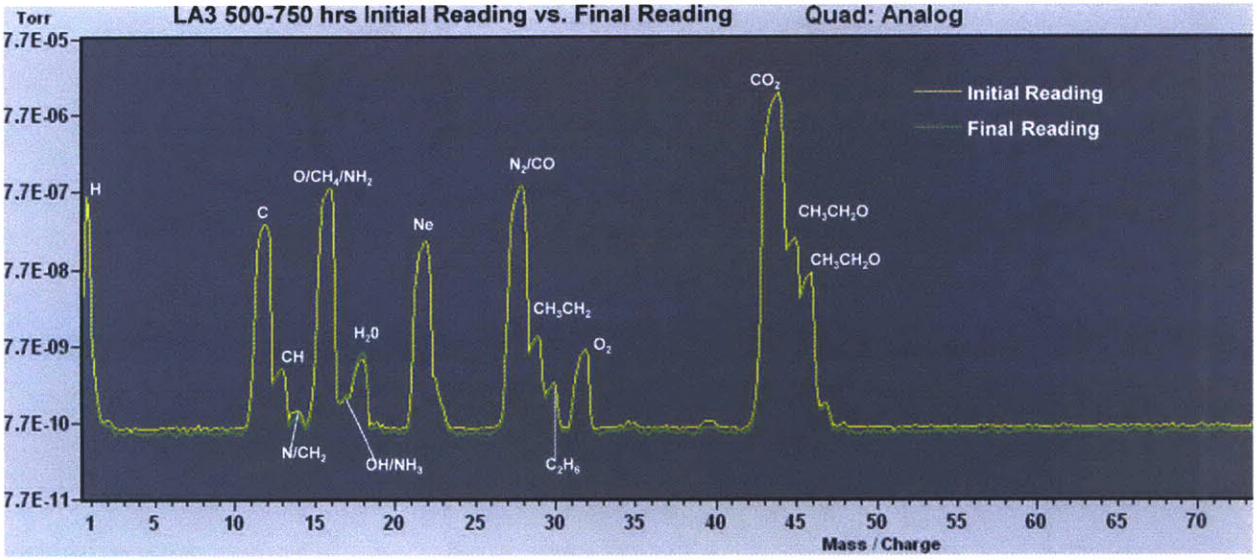

Figure B.17: RGA Initial vs. Final Reading for the LA3 500-750 Hour Experiment

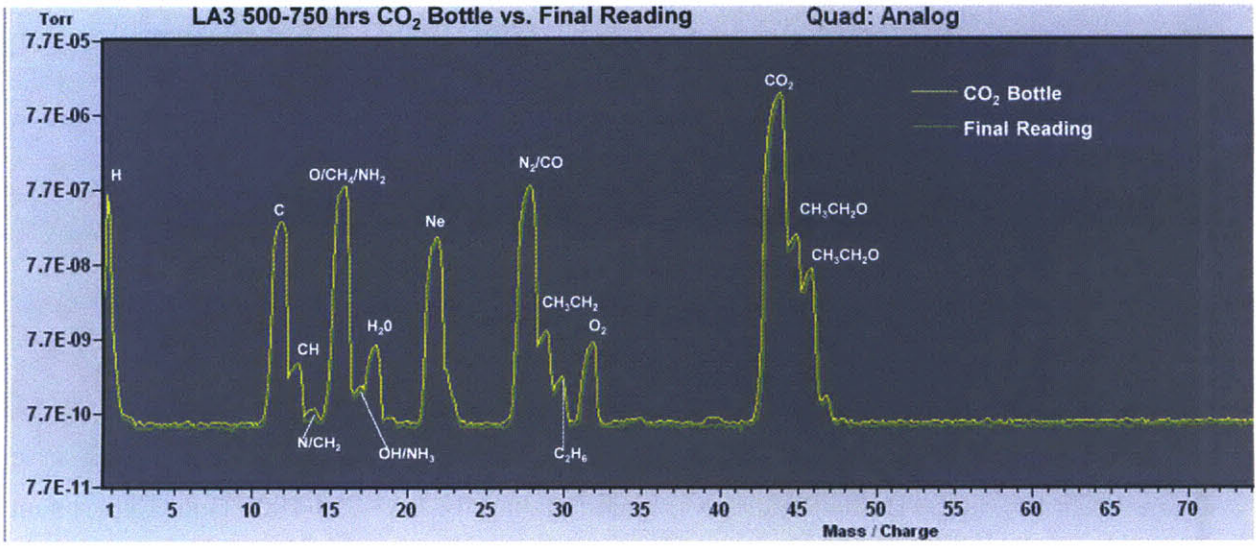

Figure B.18: RGA CO_2 Bottle Reading vs. Final Reading for LA3 500-750 Hour Experiment

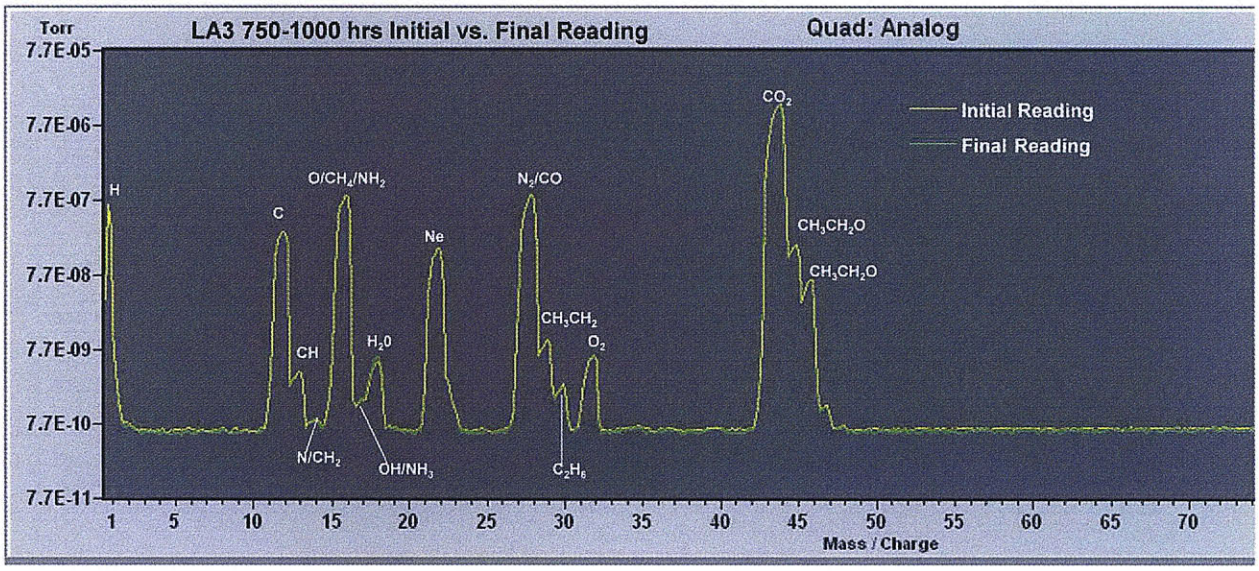

Figure B.19: RGA Initial vs. Final Reading for the LA3 750-1000 Hour Experiment

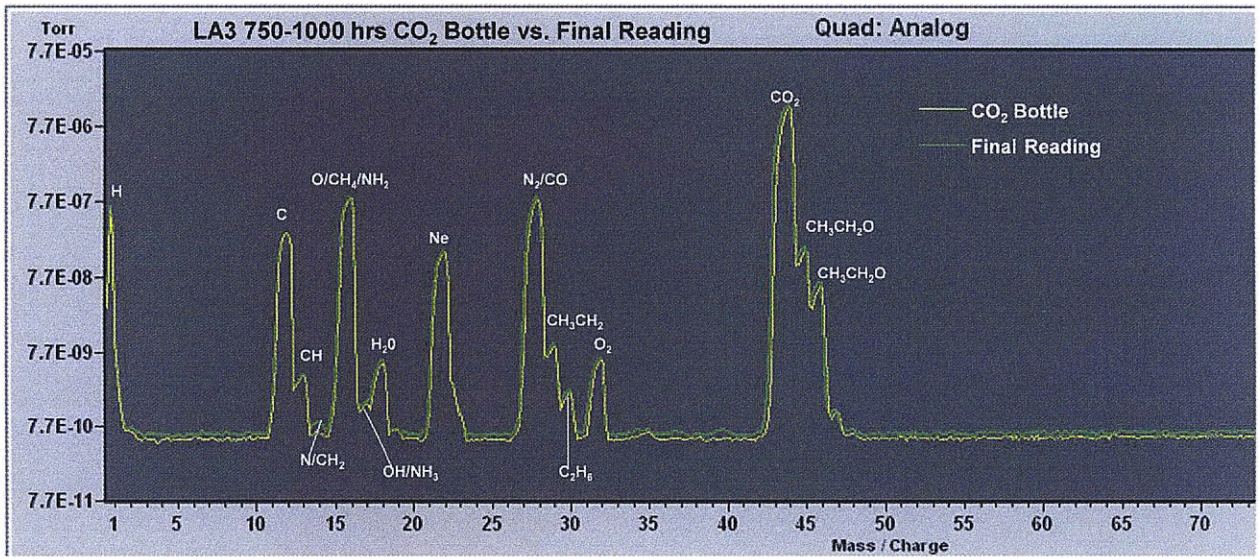

Figure B.20: RGA CO_2 Bottle Reading vs. Final Reading for LA3 750-1000 Hour Experiment

Appendix C: Supplementary EDX and SEM Pictures

LA2-02 (Inconel 690, T=650 °C, P=12.5 MPa)

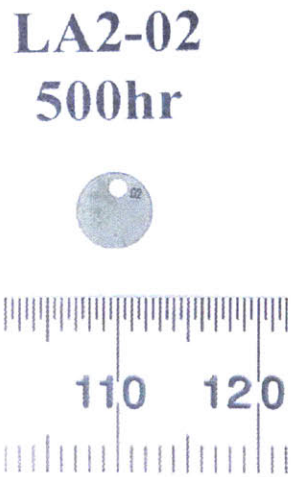

Photograph of LA1-02 500 Hours

SEM Image at 100x of the General Surface Morphology

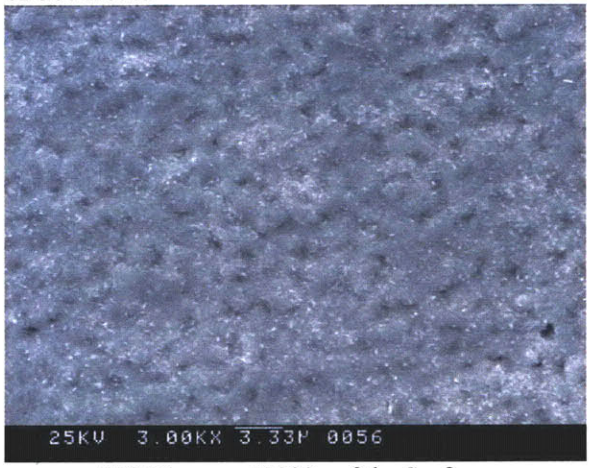

SEM Image at 3000x of the Surface

Figure C.1: Surface Morphology for LA2-02 (Inconel 690 T=650 °C P=12.5 MPa) After 500 Hours of Exposure

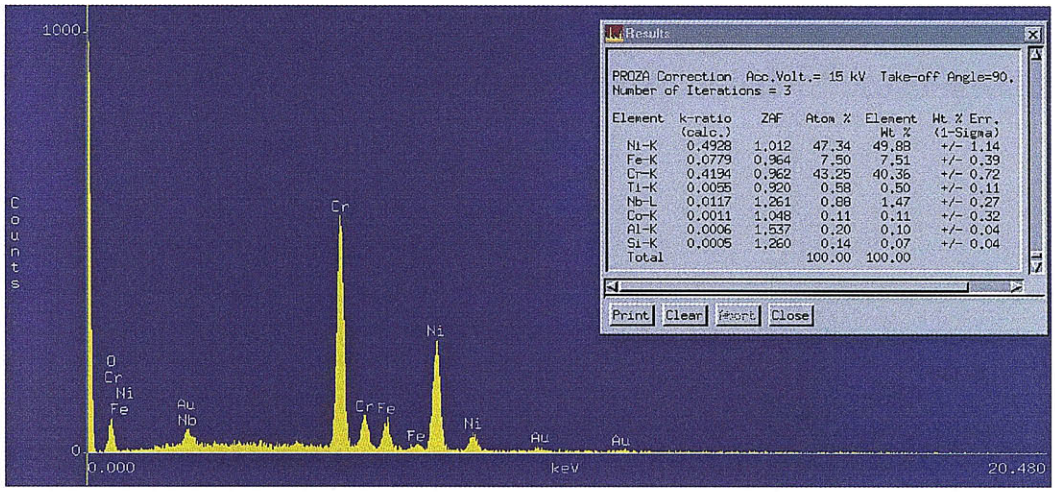

Figure C.2: EDX at 75000x of the Surface Layer for LA2-02

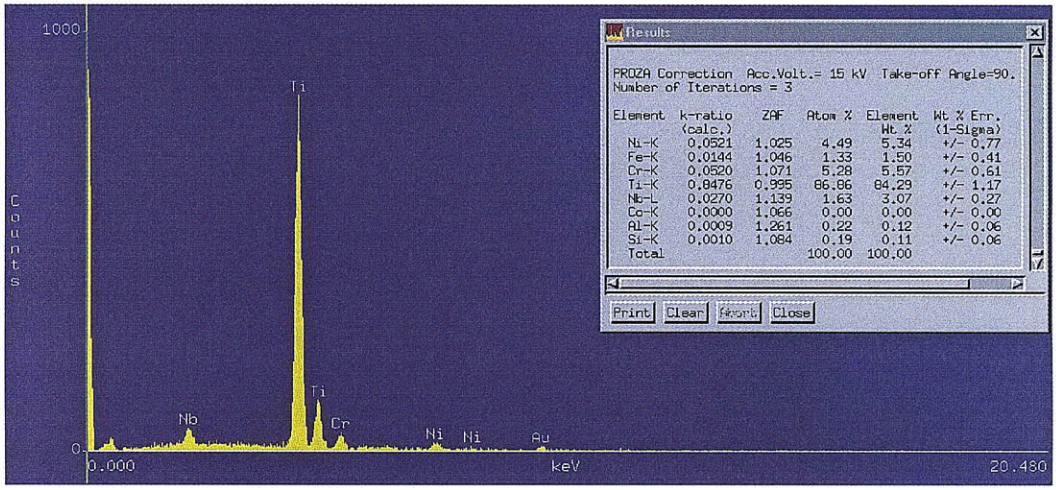

Figure C.3: EDX at 150000x of the Ti Precipitate for LA2-02

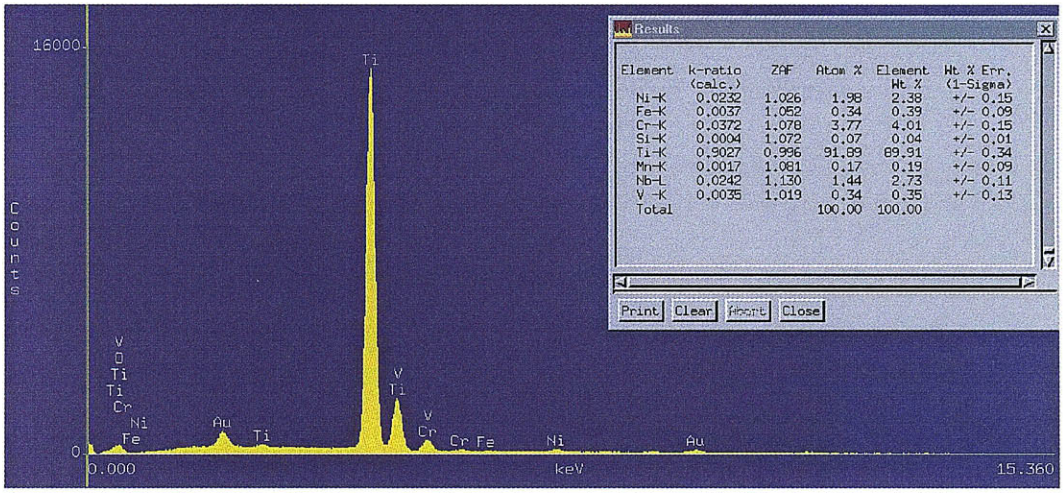

Figure C.4: EDX at 100000x of the Titanium Precipitate for LA3-02

LA1-12 (Inconel 693, T= 714 °C, P=20MPa)

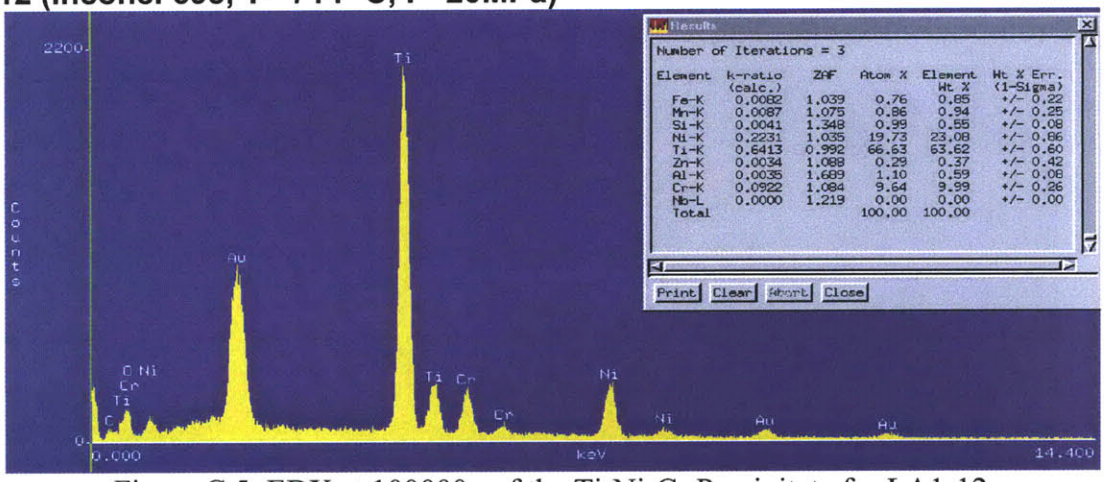

Figure C.5: EDX at 100000x of the Ti-Ni-Cr Precipitate for LA1-12

LA3-12 (Inconel 693, T=750 °C, P=12.5 MPa)

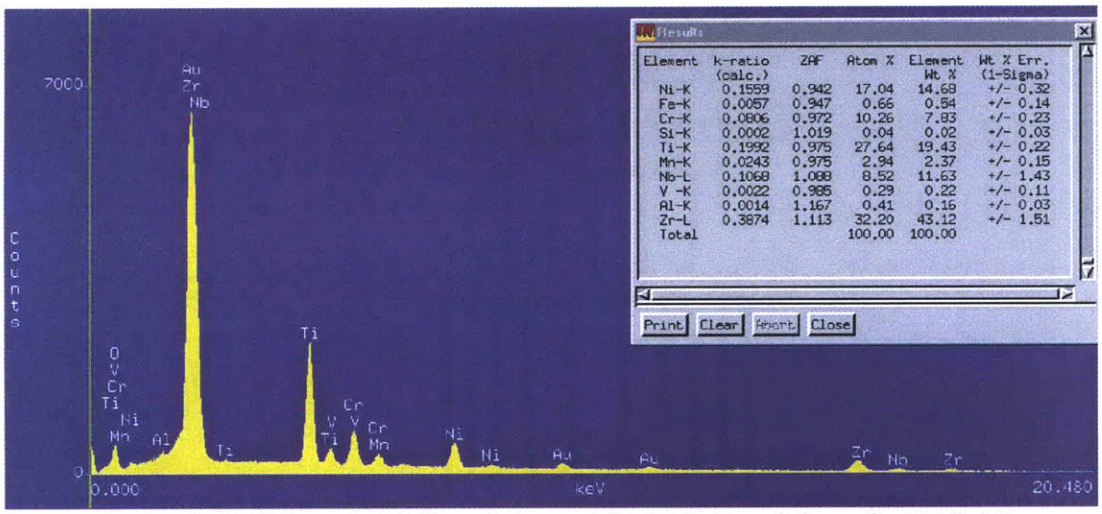

Figure C.6: EDX at 150000x of the Zr-Ti-Ni-Nb Precipitate for LA3-12

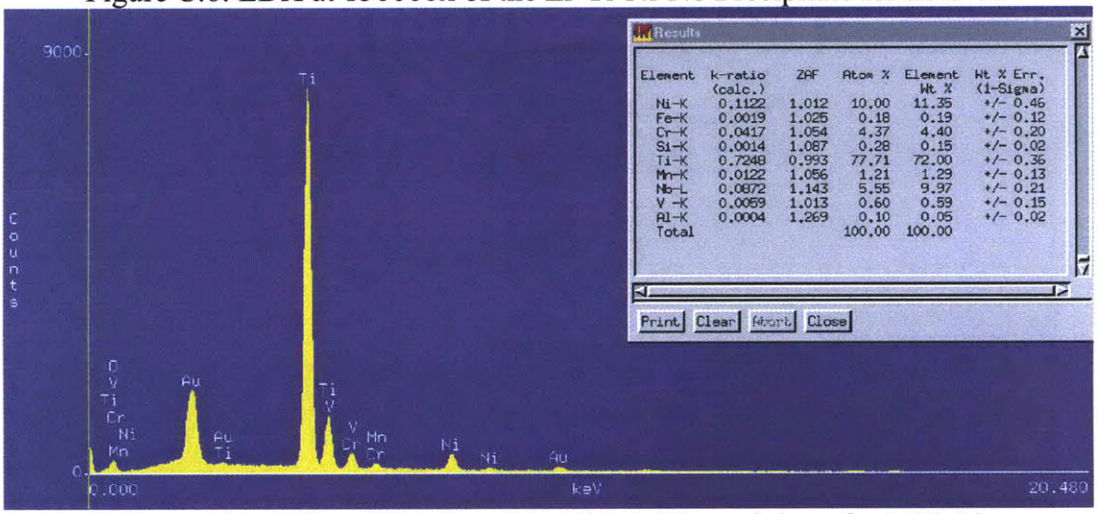

Figure C.7: EDX at 100000x of the Ti-Nb-Ni precipitate for LA3-12

LA2-22 (Inconel 718 (EG), T=650 ºC, P=12.5 MPa)

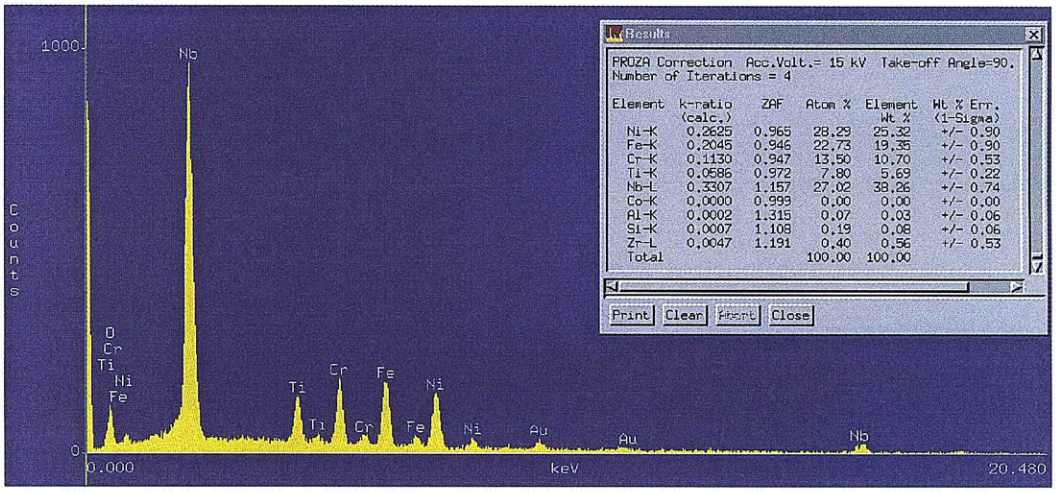

Figure C.8: EDX at 100000x of the Nb-Ni-Fe-Cr precipitate for LA2-22

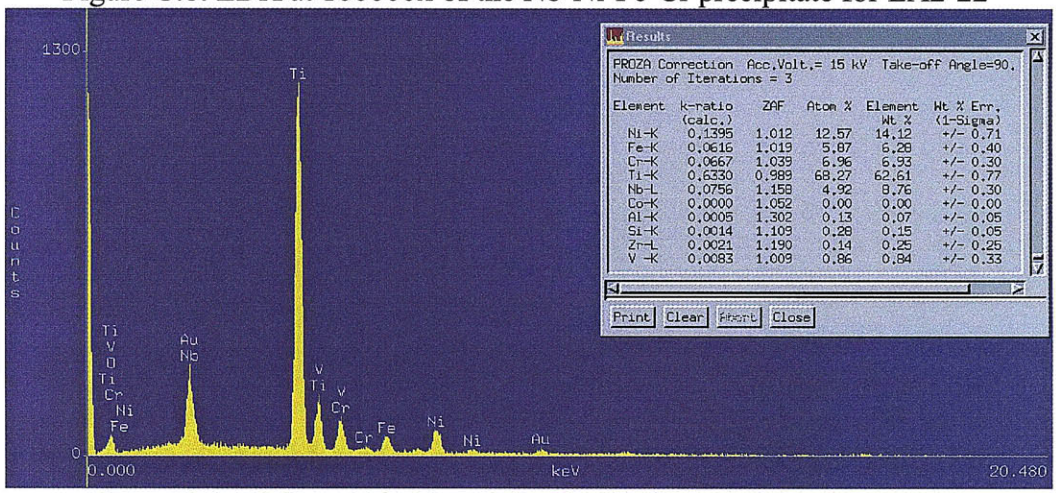

Figure C.9: EDX at 100000x of the Ti-Ni-Nb precipitate for LA2-22

LA3-22 (Inconel 718 (EG), T=750 ºC, P=12.5 MPa)

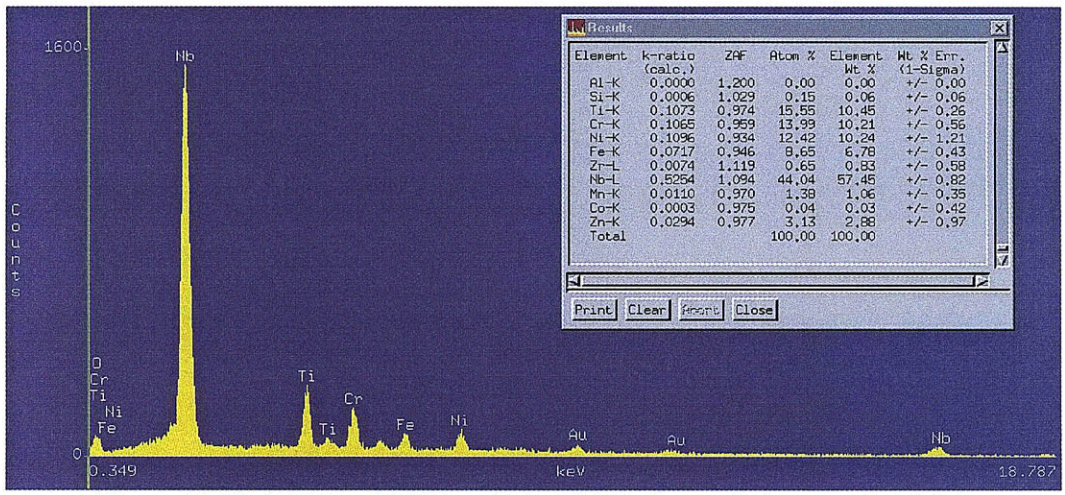

Figure C.10: EDX at 30000x of Nb-Ti-Ni-Cr precipitate on LA3-22

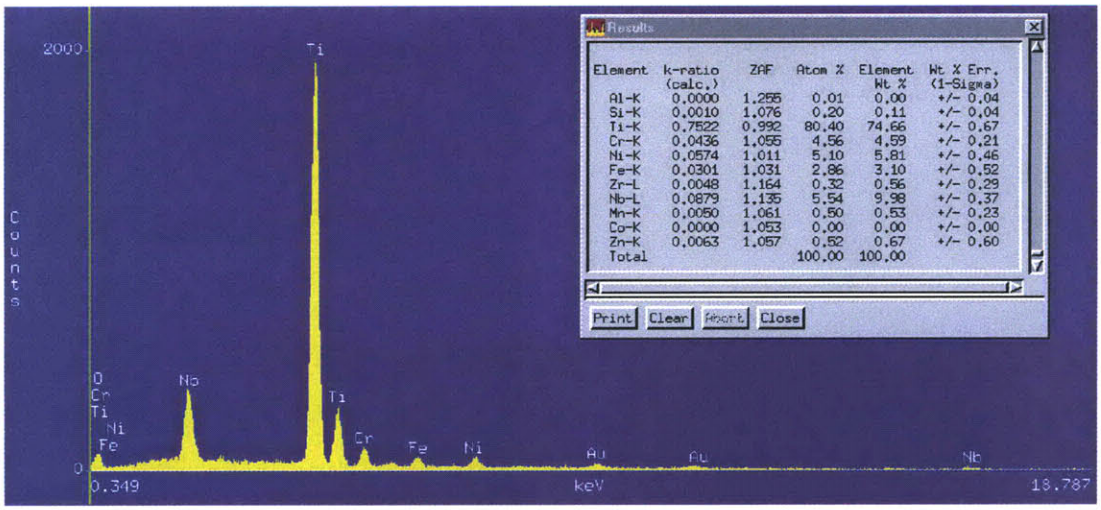

Figure C.11: EDX at 30000x of Ti-Nb precipitate on LA3-22

LA1-32 (Inconel 725 (EG), T=714 ºC, P=20 MPa)

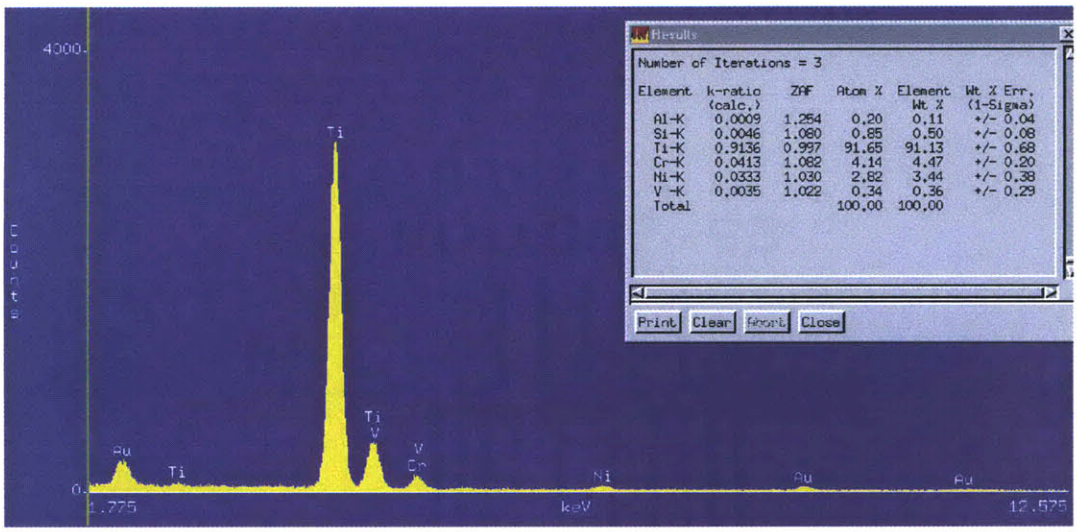

Figure C.12: EDX at 40000x of Ti Precipitate on LA1-32

LA2-32 (Inconel 725 (EG), T=650 °C, P=12.5 MPa)

Photograph of LA2-32 500 Hours

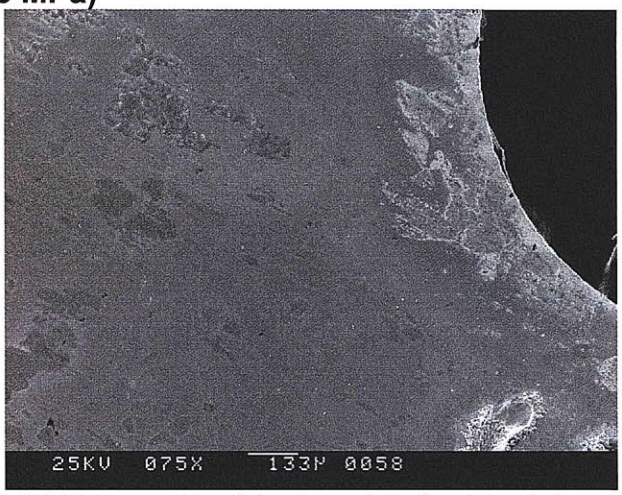

SEM Image at 75x of the General Surface Morphology

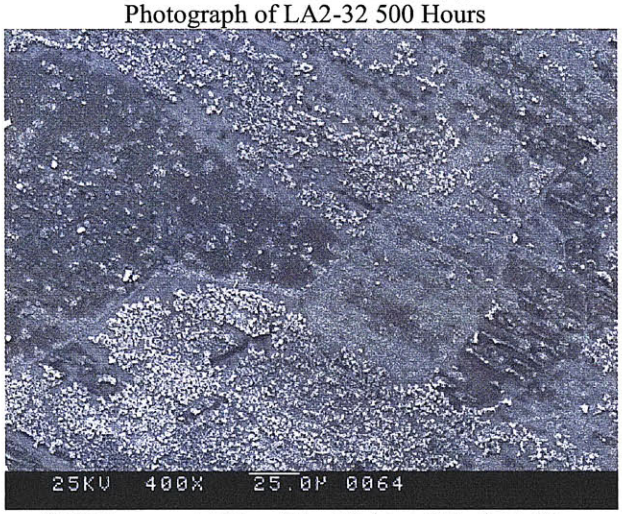

SEM Image at 400x of the Light and Dark Oxide

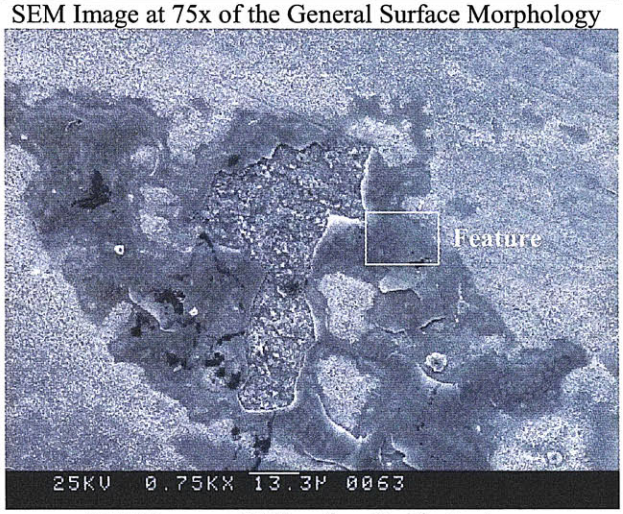

SEM Image at 750x of an Oxide Feature

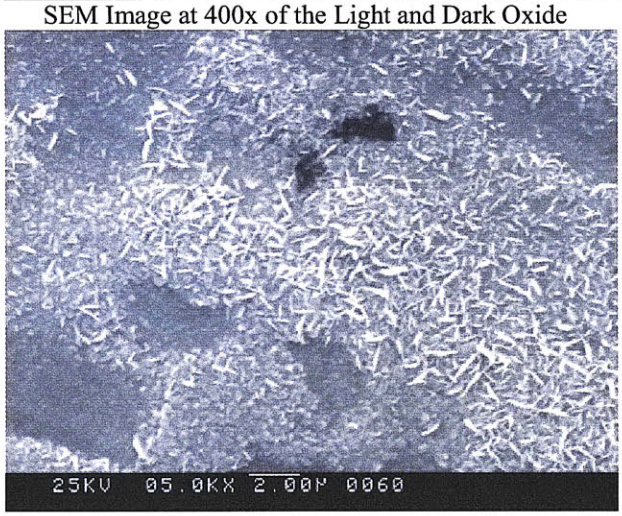

SEM Image at 5000x of the Light Oxide

SEM Image at 3000x of an Al-Ni-Cr Precipitate

Figure C.13: Surface Morphology for LA2-32 After 500 Hours of Exposure

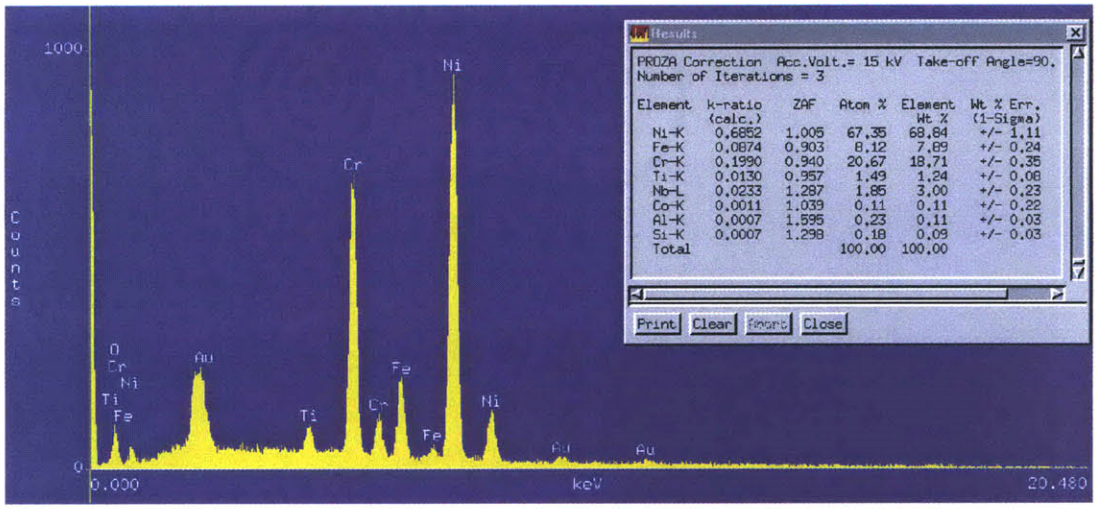

Figure C.14: EDX at 100000x of the Light Oxide on LA2-32

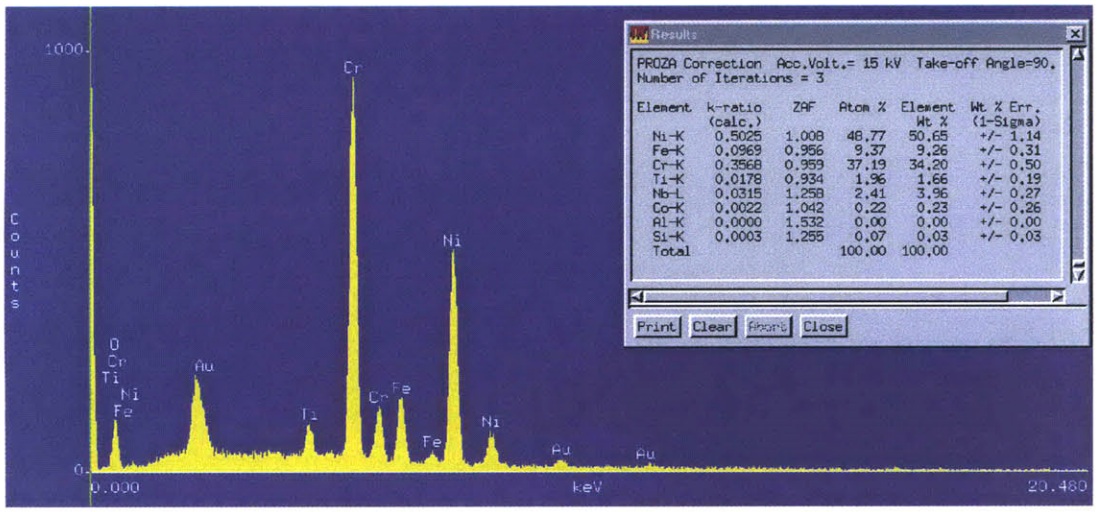

Figure C.15: EDX at 75000x of the Dark Oxide on LA2-32

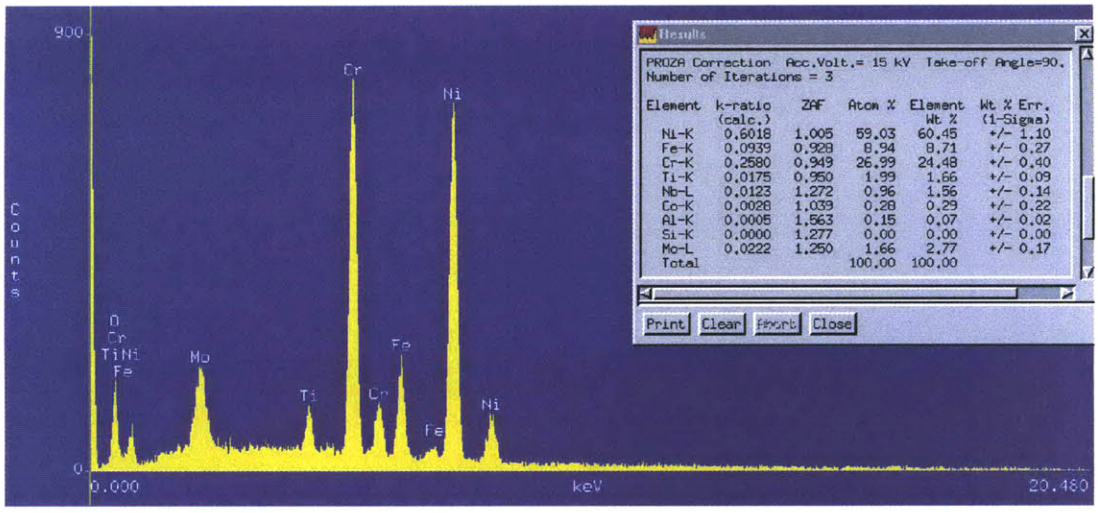

Figure C.16: EDX at 40000x of the Oxide Feature on LA2-32

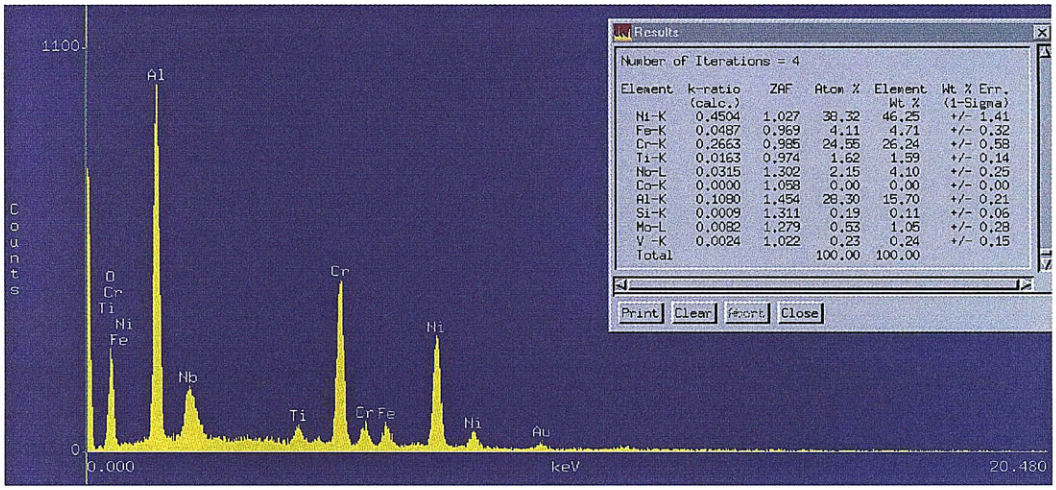

Figure C.17: EDX at 75000x of the Ni-Cr-Al Precipitate on LA2-32

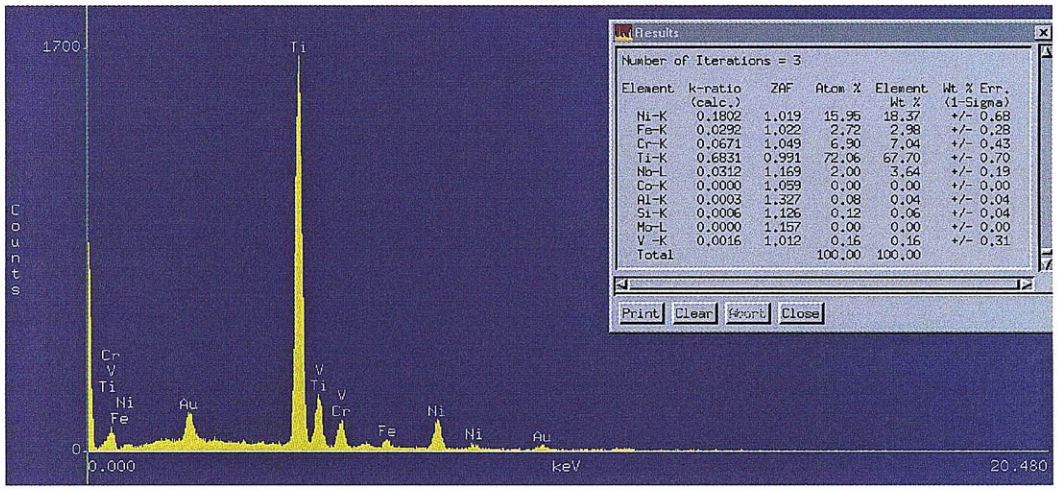

Figure C.18: EDX at 75000x of Ti Precipitate on LA2-32

LA3-32 (Inconel 725 (EG), T=750 ºC, P=12.5 MPa)

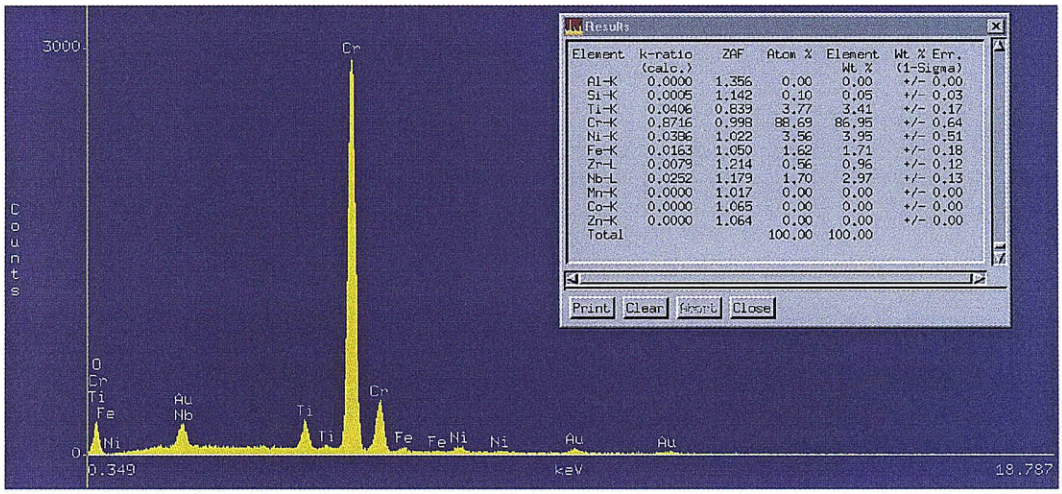

Figure C.19: EDX at 150000x of the White Flakes in the Light Oxide on LA3-32

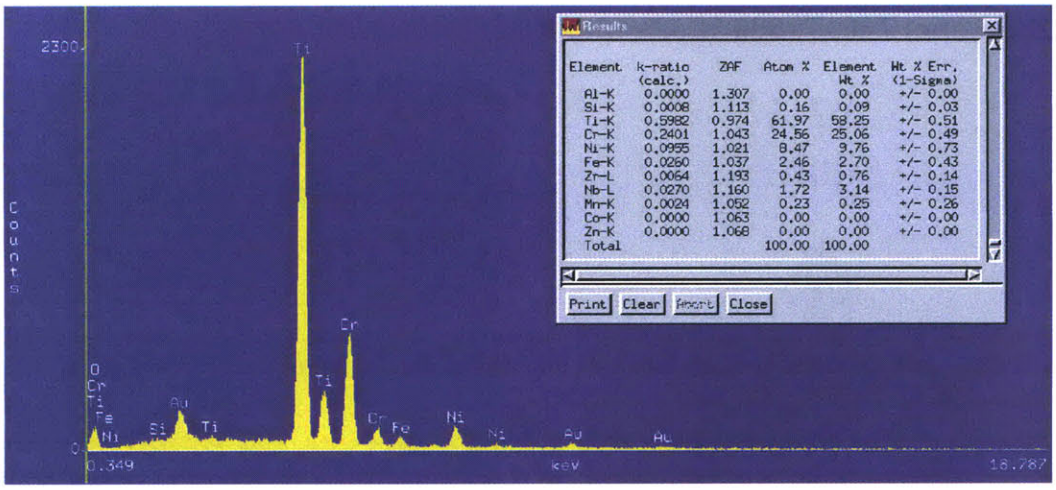

C.20: EDX at 50000x of the Ti Precipitate on LA3-32

LA1-42 (Inconel 740, T=714 ºC, P=20 MPa)

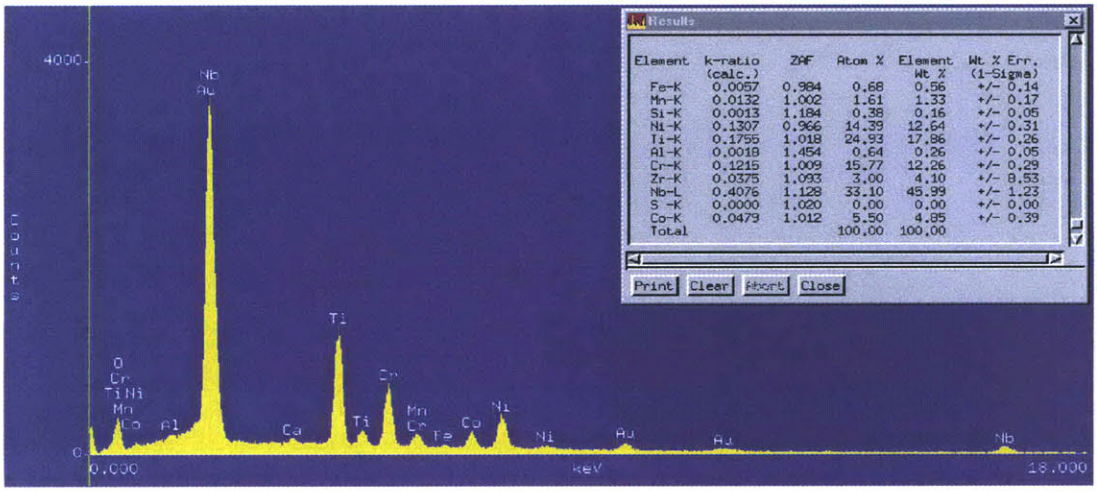

Figure C.21: EDX at 25000x of the Nb-Ti-Cr-Ni Precipitates on LA1-42

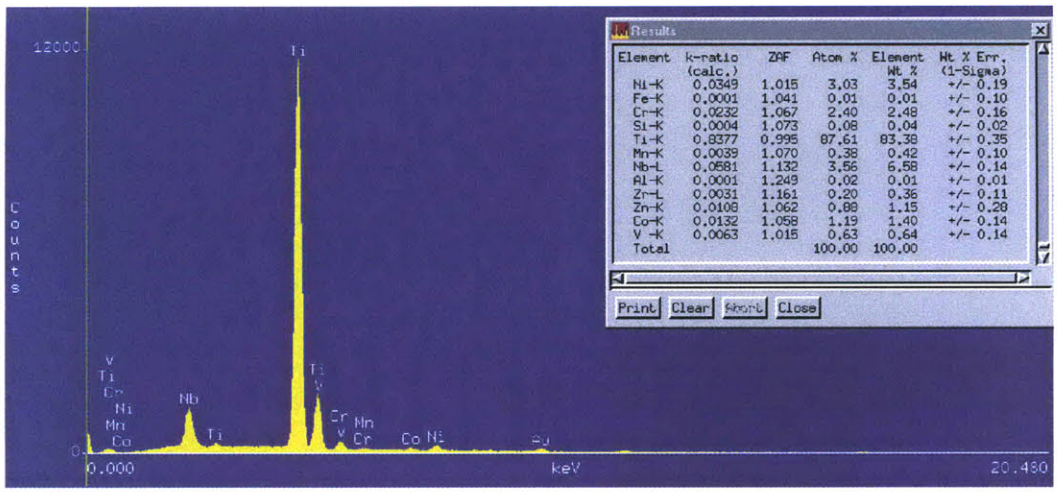

Figure C.22: EDX at 4000x of the Ti-Cr-Ni Precipitates on LA1-42

LA2-42 (Inconel 740, T=650 °C, P=12.5 MPa)

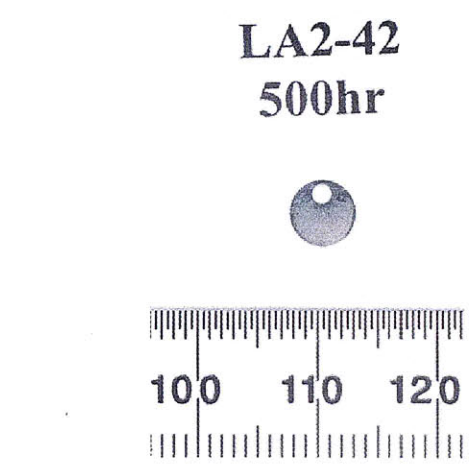

Photograph of LA2-42 500 Hours

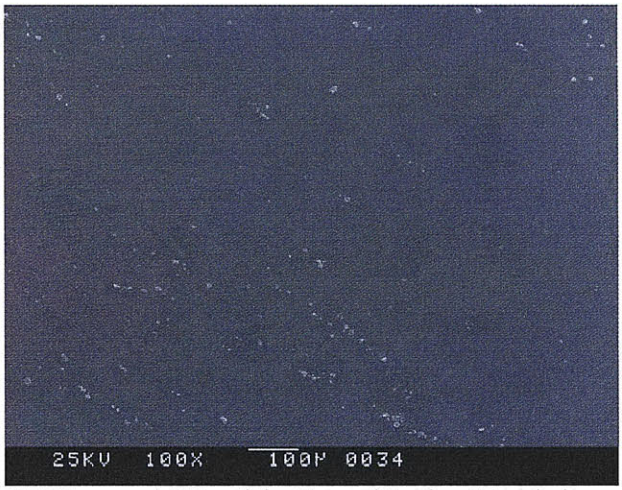

SEM Image at 100x of the General Surface Morphology

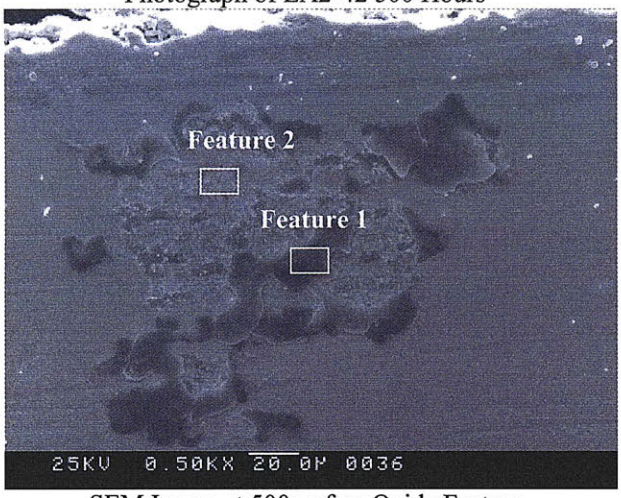

SEM Image at 500x of an Oxide Feature

SEM Image at 1500x of the Oxide

Figure 23: Surface Morphology for LA2-42 After 500 Hours of Exposure

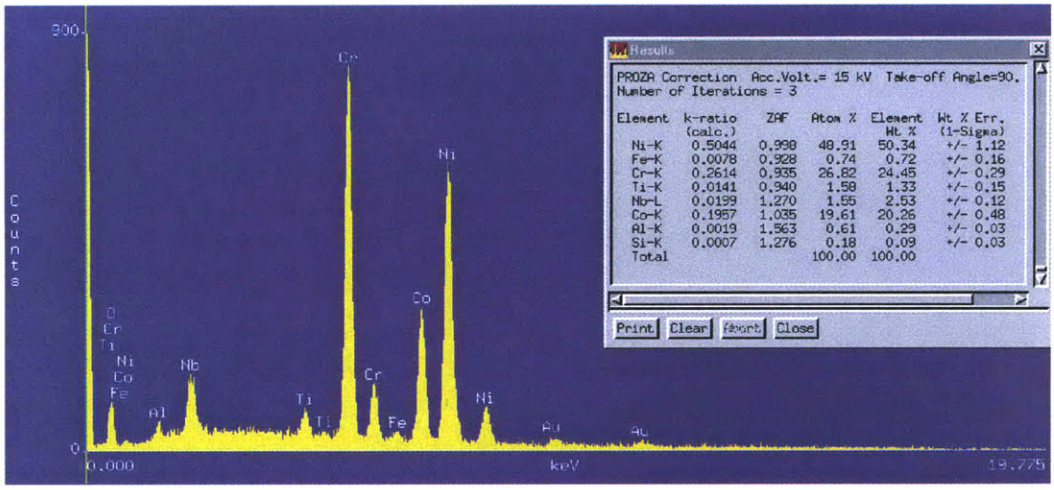

Figure C.24: EDX at 150000x of the Light Oxide on LA2-42

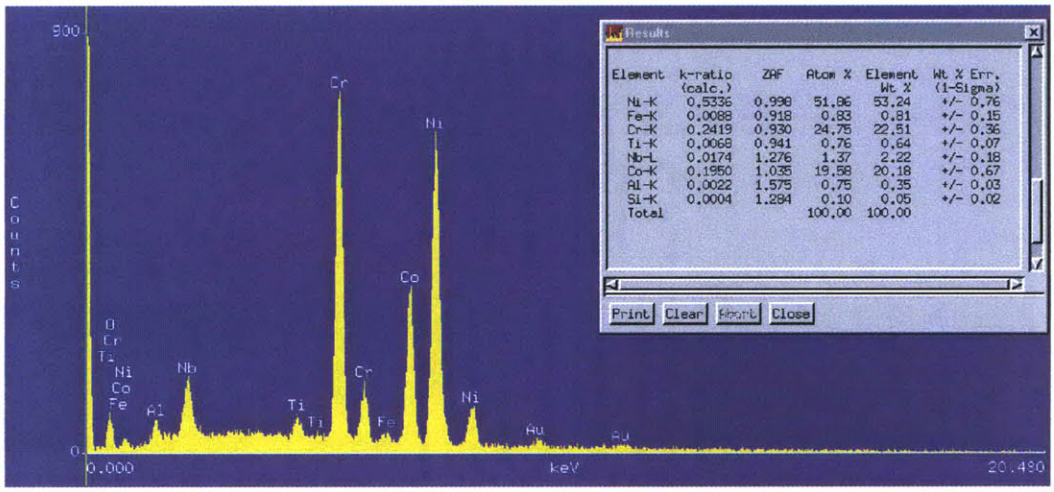

Figure C.25: EDX at 150000x of the Dark Oxide on LA2-42

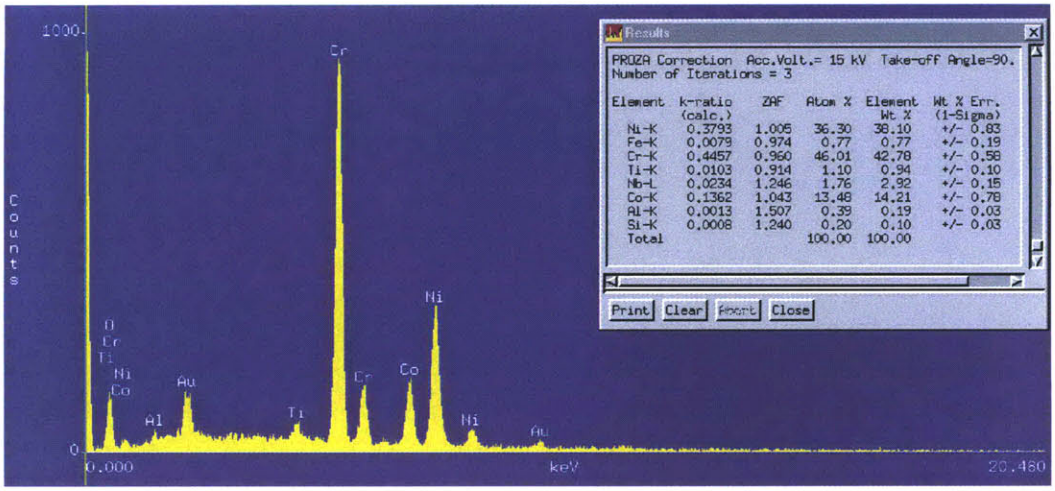

Figure C.26: EDX at 150000x of Feature 1 on LA2-42

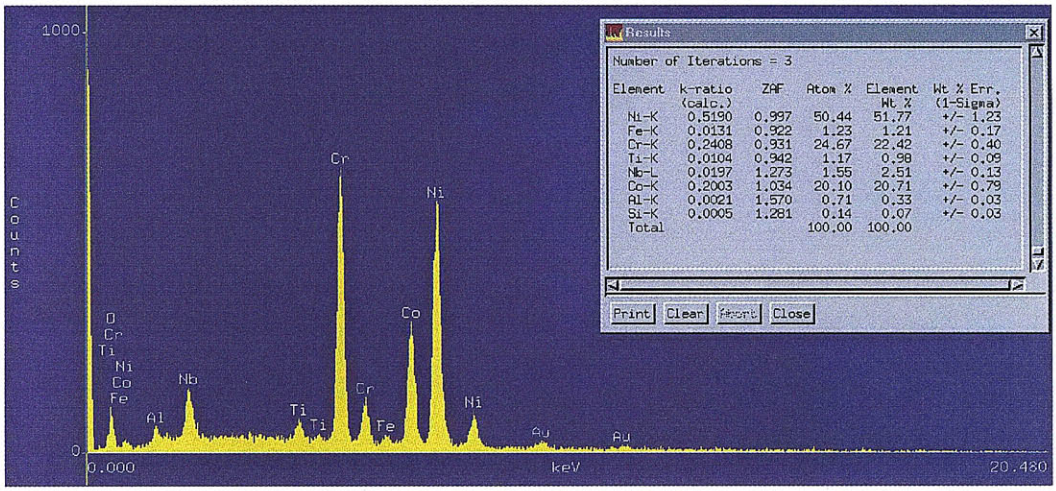

Figure C.27: EDX at 150000x of Feature 2 on LA2-42

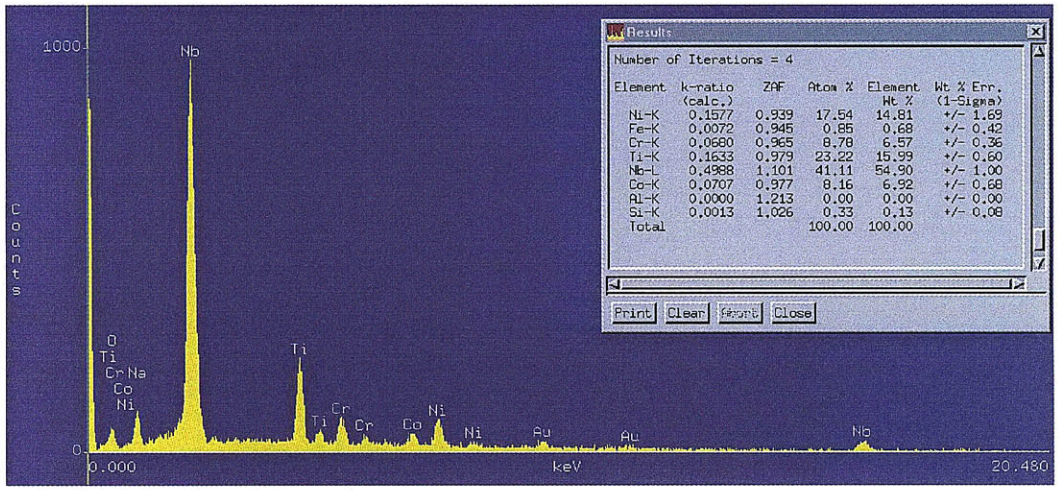

Figure C.28: EDX at 150000x of the Nb-Ti-Ni Precipitates on LA2-42

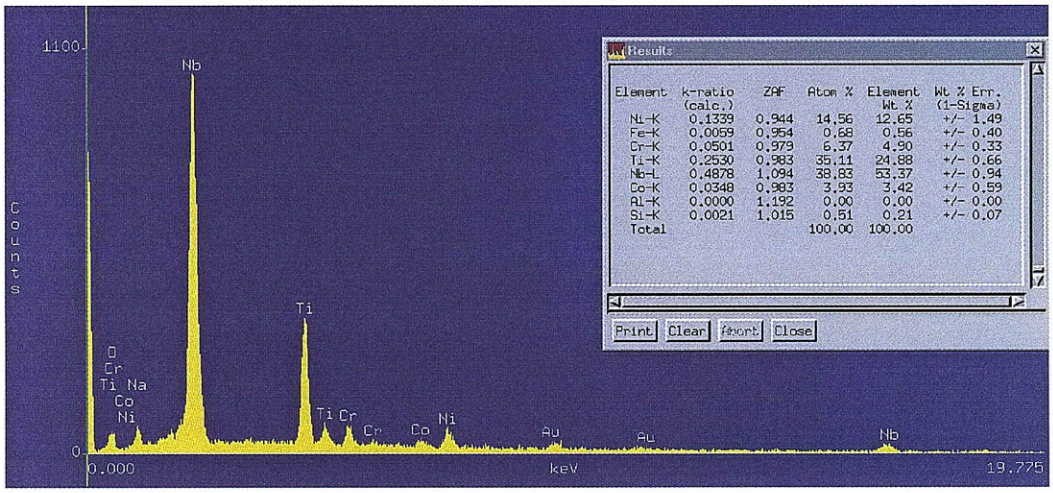

Figure C.29: EDX at 100000x of the Nb-Ti-Ni Precipitates on LA2-42

LA3-42 (Inconel 740, T=750 ºC, P=12.5 MPa)

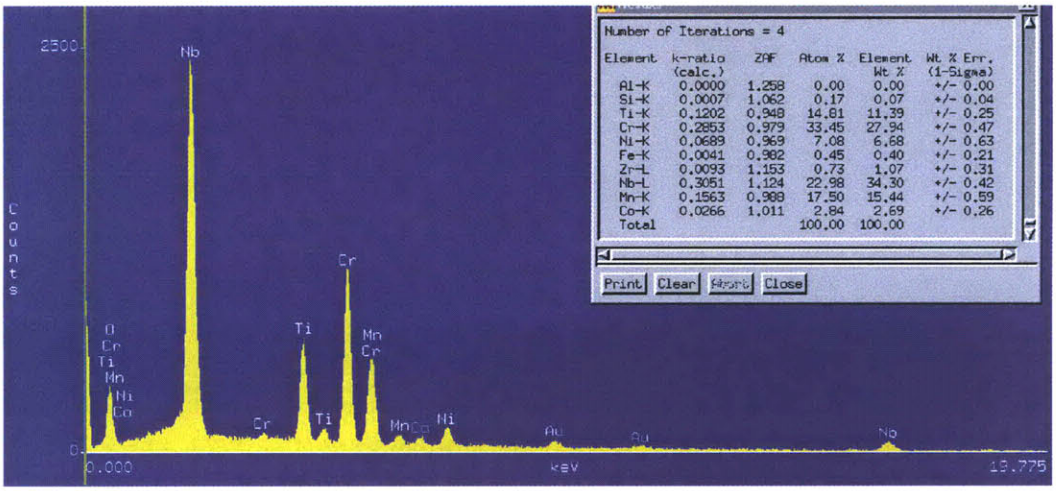

Figure C.30: EDX at 100000x of Precipitate 1 on LA3-42

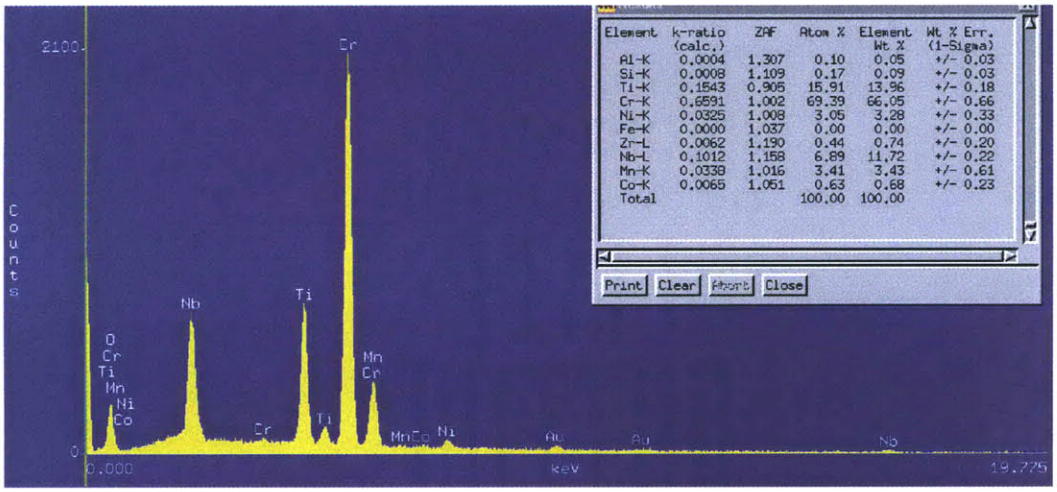

Figure C.31: EDX at 75000x of Precipitate 2 on LA3-42

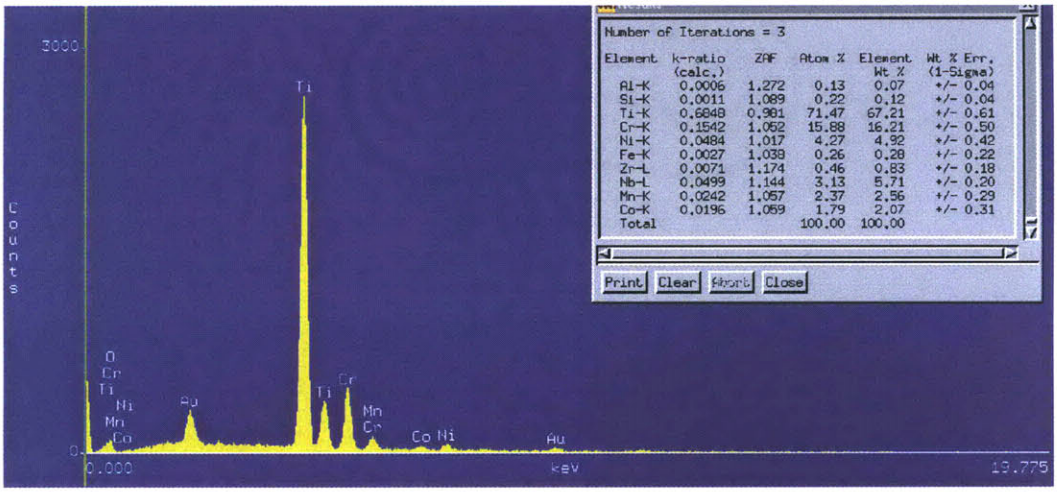

Figure C.32: EDX at 50000x of Precipitate 3 on LA3-42

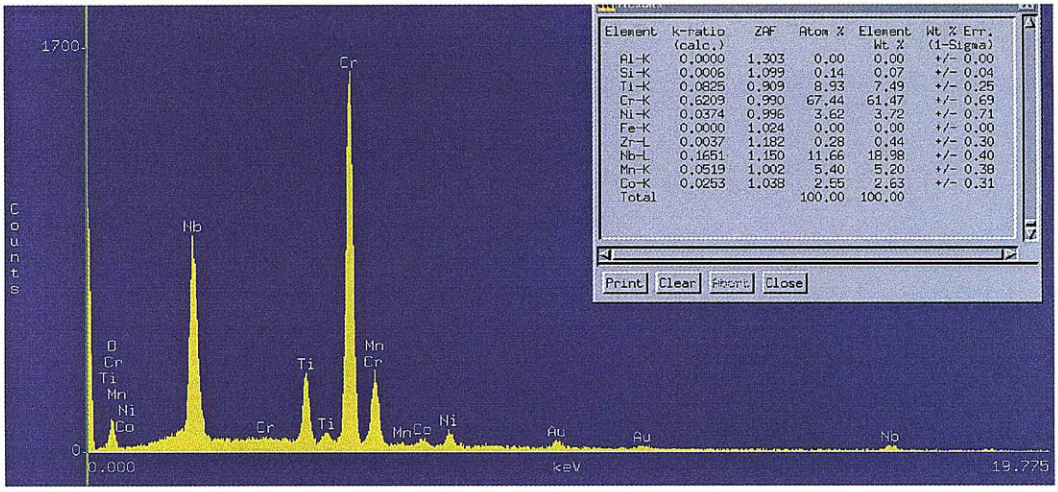

Figure C.33: EDX at 100000x of Precipitate 4 on LA3-42

LA1-52 (Inconel 740+, T=714 °C, P=20 MPa)

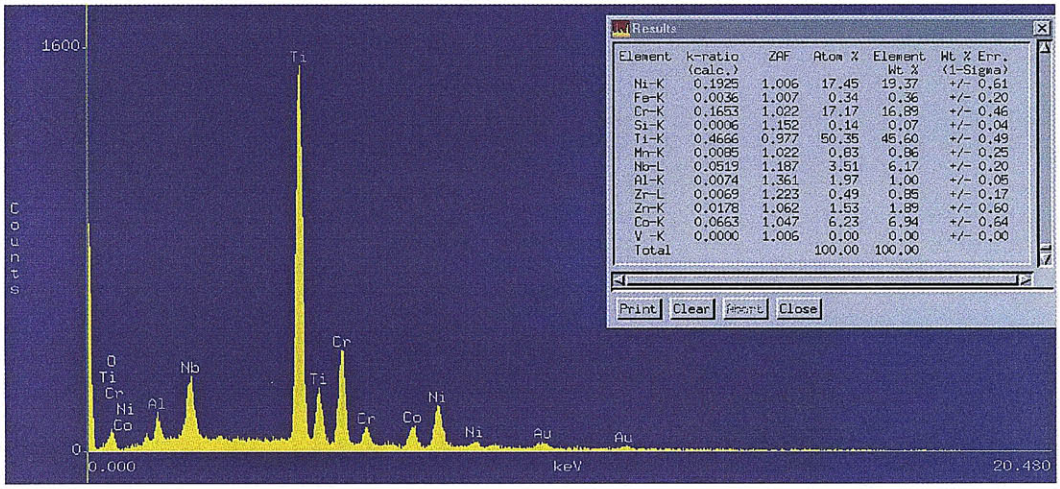

Figure C.34: EDX at 100000x of the Ti-Ni-Cr Precipitates on LA1-52

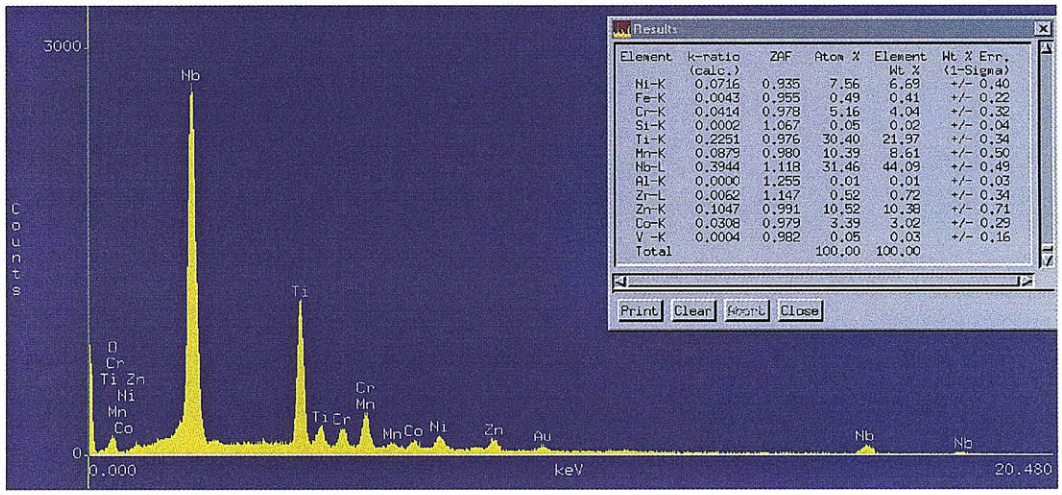

Figure C.35: EDX at 40000x of the Nb-Ti-Zn-Mn Precipitates on LA1-52

LA2-52 (Inconel 740+, T=650 ºC, P=12.5 MPa)

Photograph of LA2-52 500 Hours

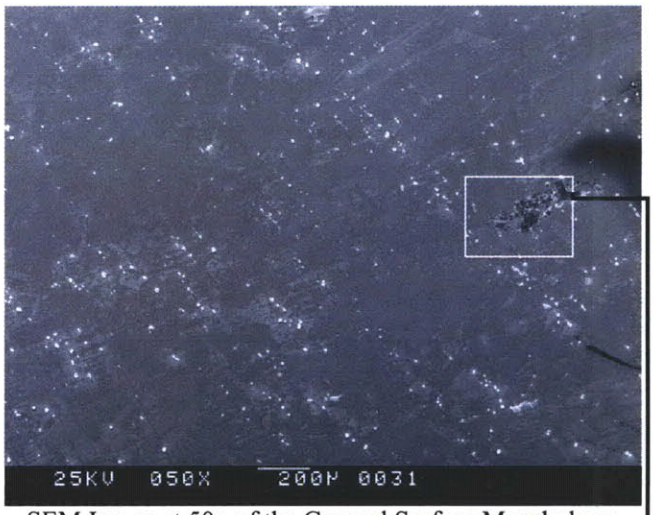

SEM Image at 50x of the General Surface Morphology

SEM Image at 1000x of Precipitates

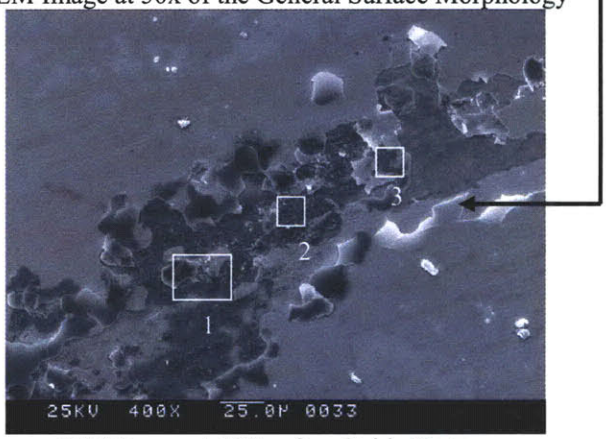

SEM Image at 400x of an Oxide Feature

Figure C.36: Surface Morphology for LA2-52 (Inconel 740+ T=714 ºC P=20 MPa) After 500 Hours of Exposure

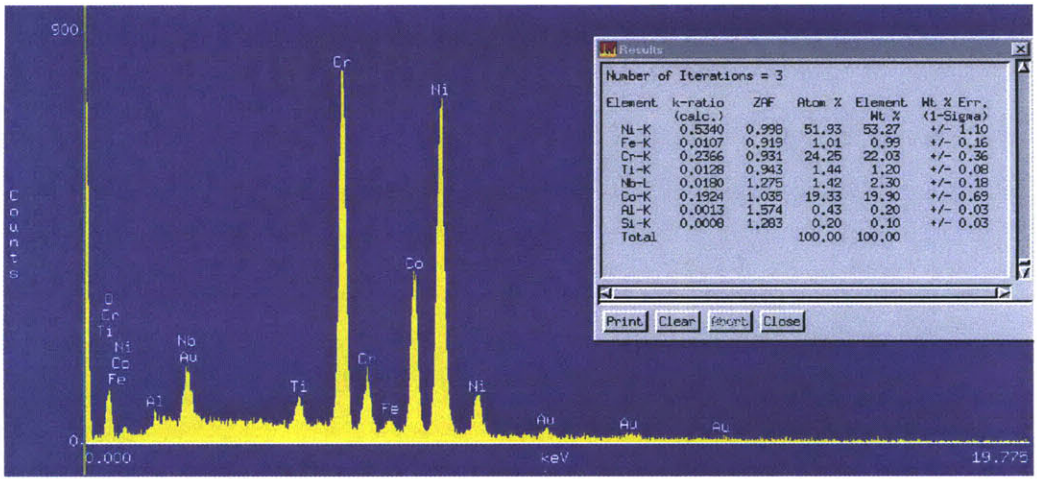

Figure C.37: EDX at 100000x of the Oxide on LA2-52

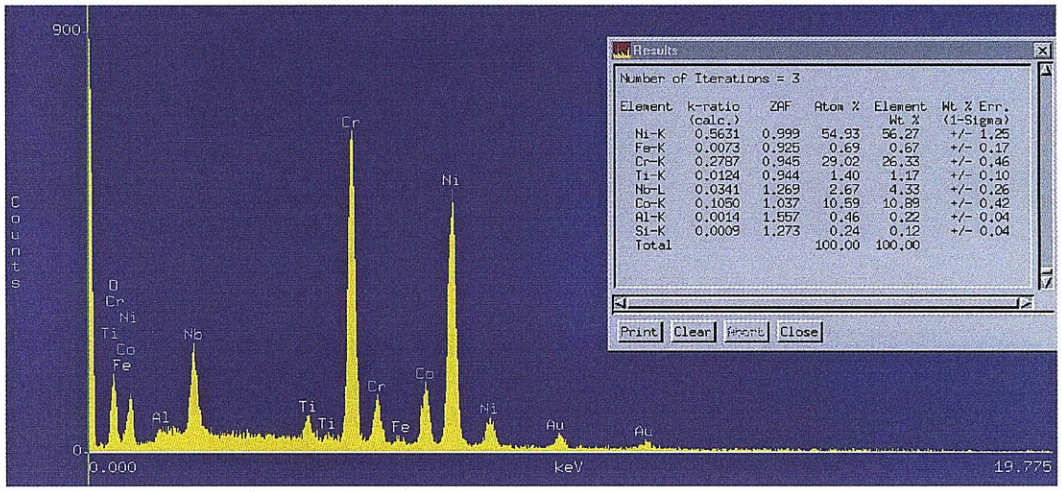

Figure C.38: EDX at 100000x of Feature 1 on LA2-52

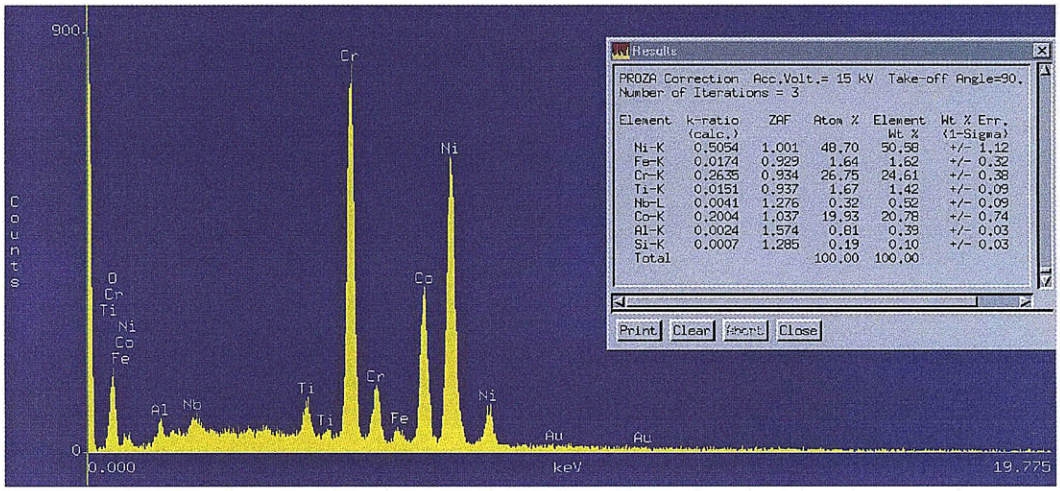

Figure C.39: EDX at 75000x of Feature 2 on LA2-52

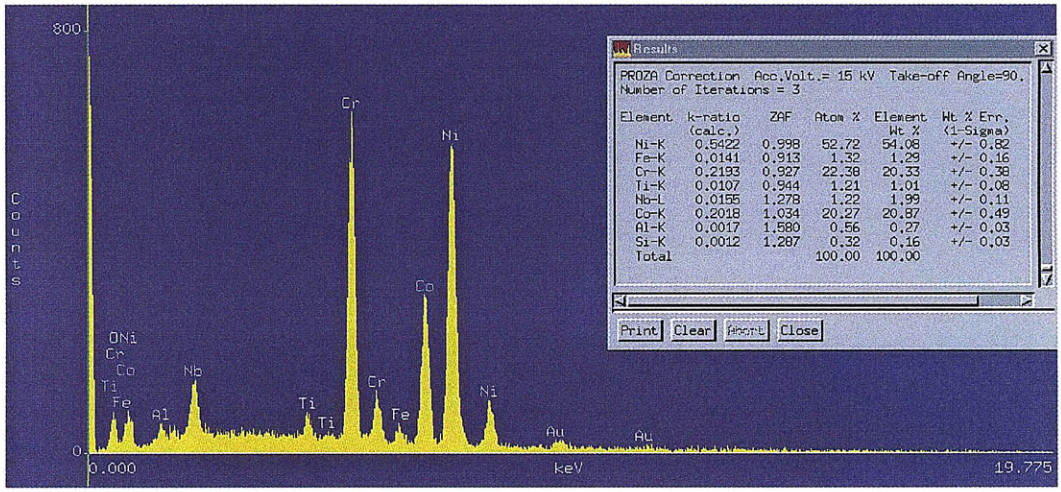

Figure C.40: EDX at 100000x of Feature 3 on LA2-52

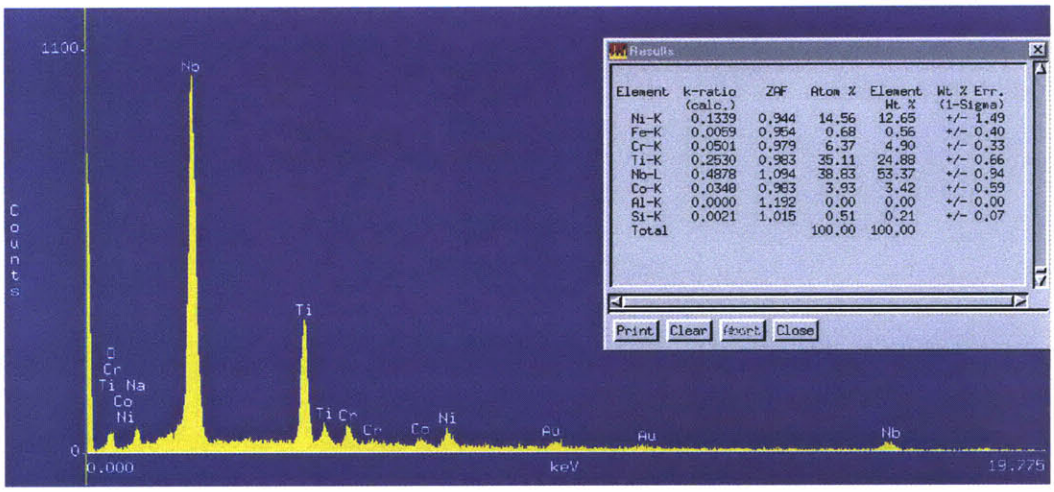

Figure C.41: EDX at 100000x of the Nb-Ti-Ni Precipitates on LA2-52

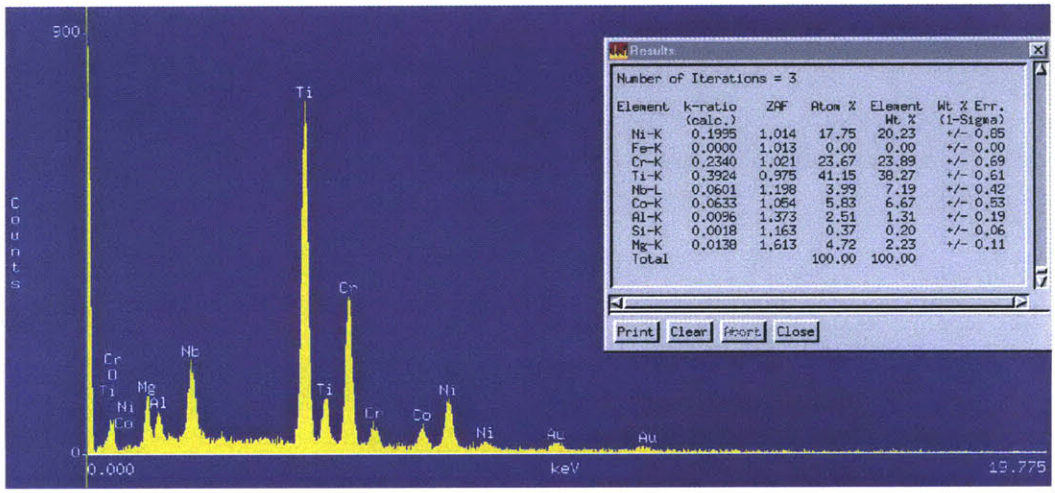

Figure C.42: EDX at 150000x of the Ti-Cr-Ni Precipitates on LA2-52

LA3-52 (Inconel 740+, T=750 °C, P=12.5 MPa)

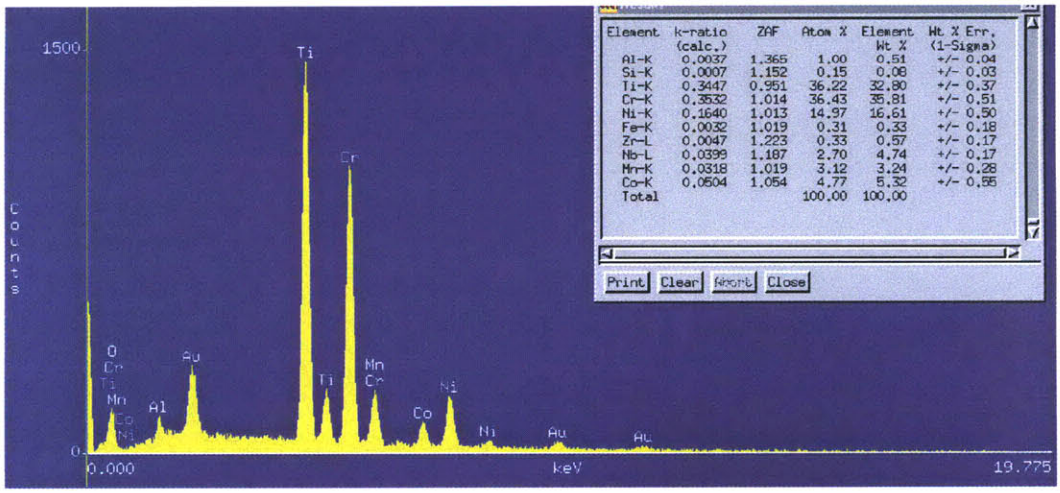

Figure C.43: EDX at 150000x of the Ti-Cr-Ni Precipitates on LA3-52

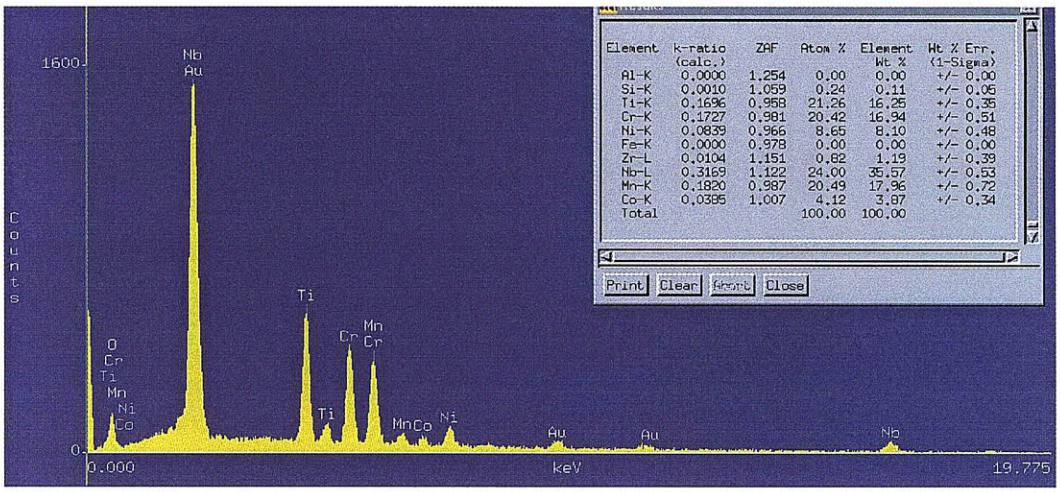

Figure C.44: EDX at 150000x of the Nb-Mn-Ti-Cr-Ni Precipitates on LA3-52

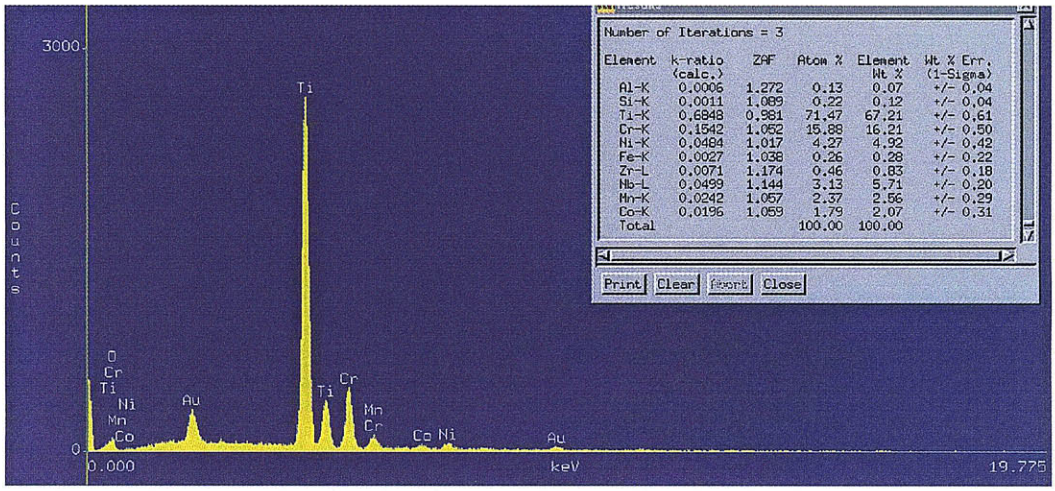

Figure C.45: EDX at 50000x of the Ti-Cr Precipitates on LA3-52

LA2-62 (AUSS 316L, T=650 °C, P=12.5 MPa)

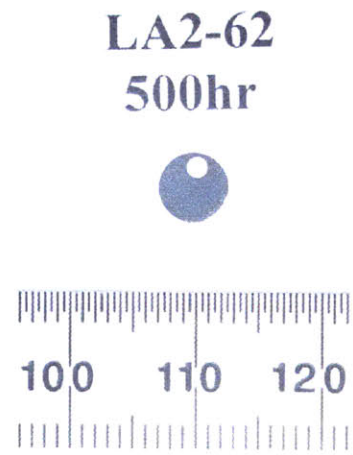

Photograph of LA2-62 500 Hours

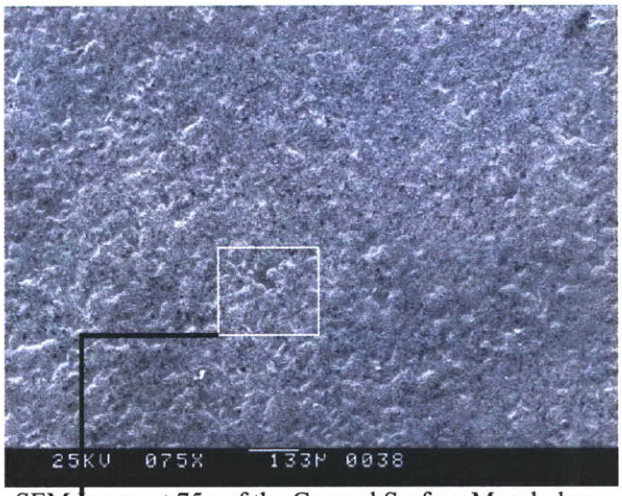

SEM Image at 75x of the General Surface Morphology

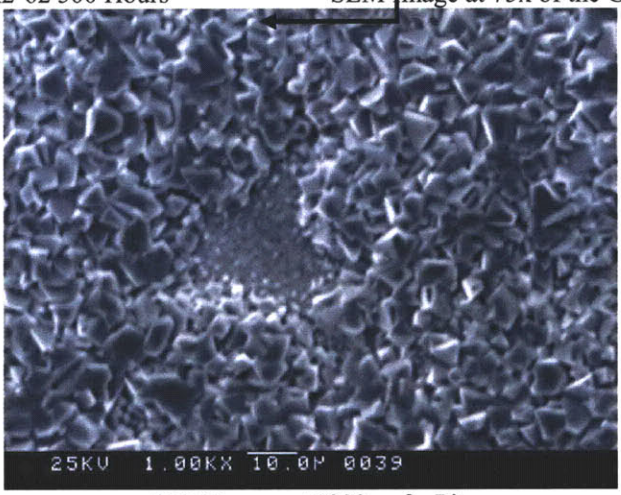

SEM Image at 1000x of a Pit

Figure C.46104: Surface Morphology for LA2-62 After 500 Hours of Exposure

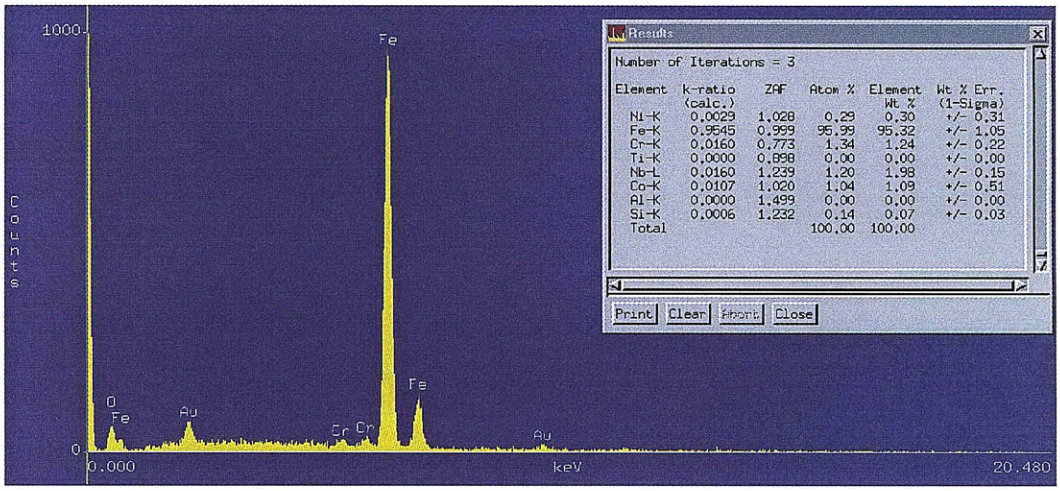

Figure C.47: EDX at 50000x of the Oxide on LA2-62

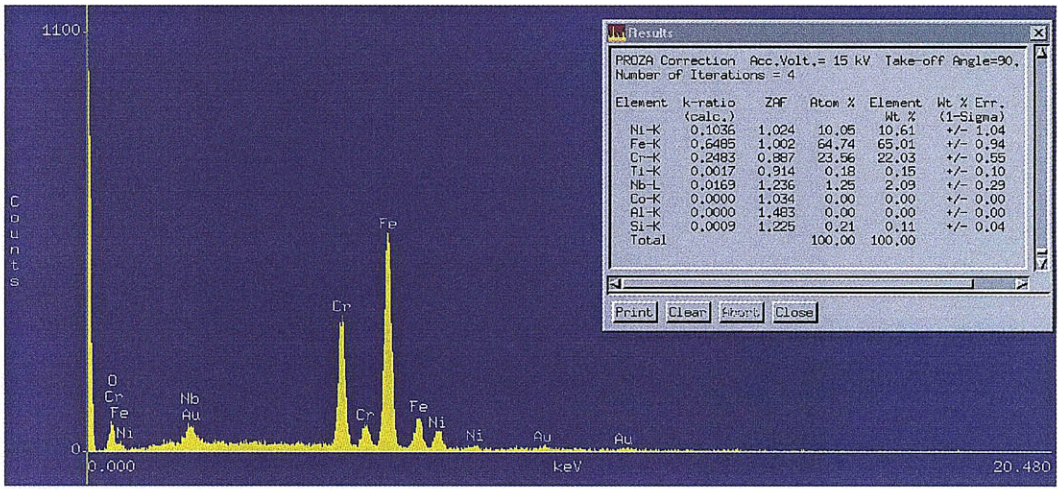

Figure C.48: EDX at 70000x of the Pit on LA2-62

LA2-72 (Inconel 718, T=650 ºC, P=12.5 MPa)

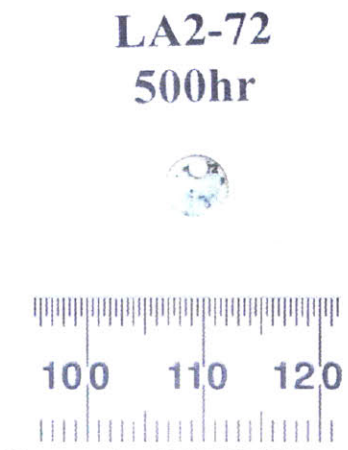

Photograph of LA2-72 500 Hours

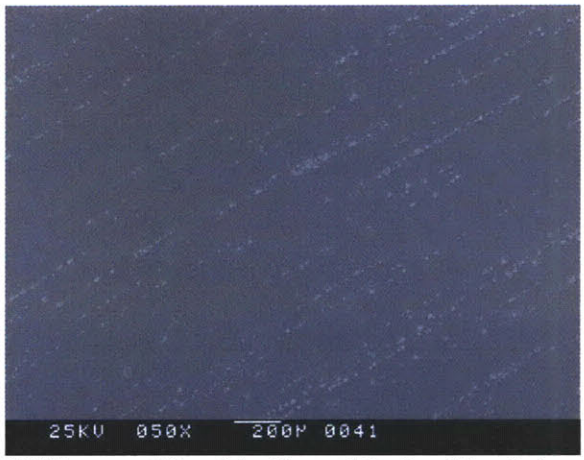

SEM Image at 50x of the General Surface Morphology

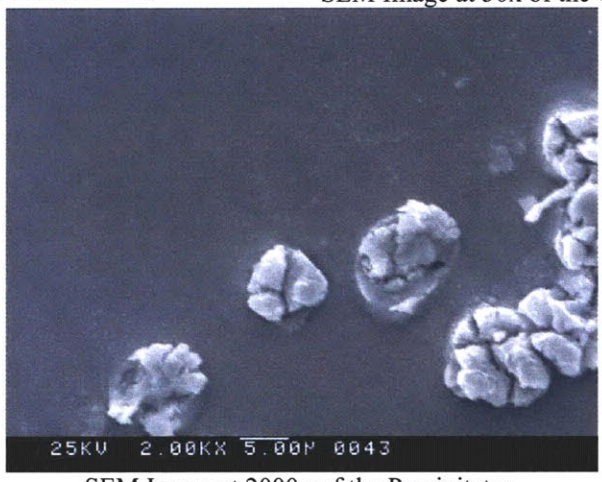

SEM Image at 2000x of the Precipitates

Figure C.49: Surface Morphology for LA2-72 After 500 Hours of Exposure

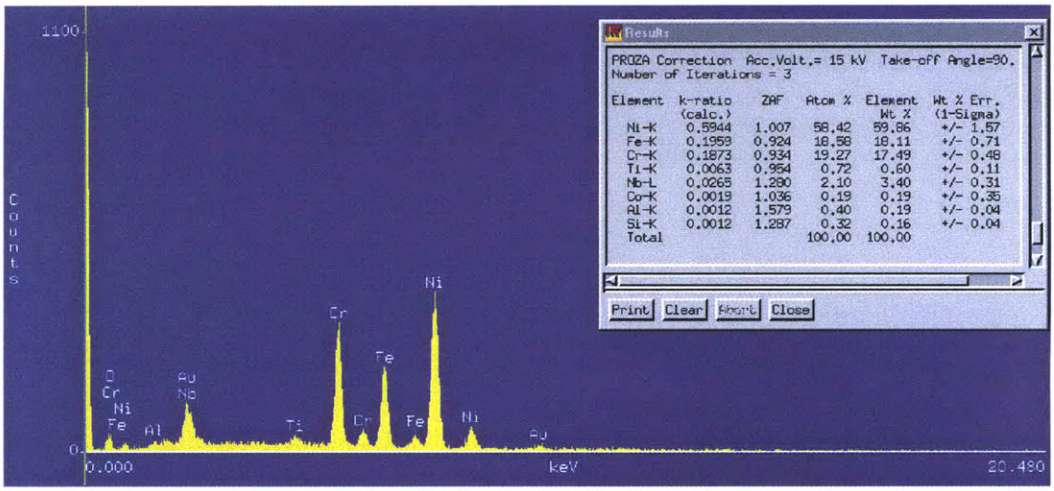

Figure C.50: EDX at 100000x of the Oxide on LA2-72

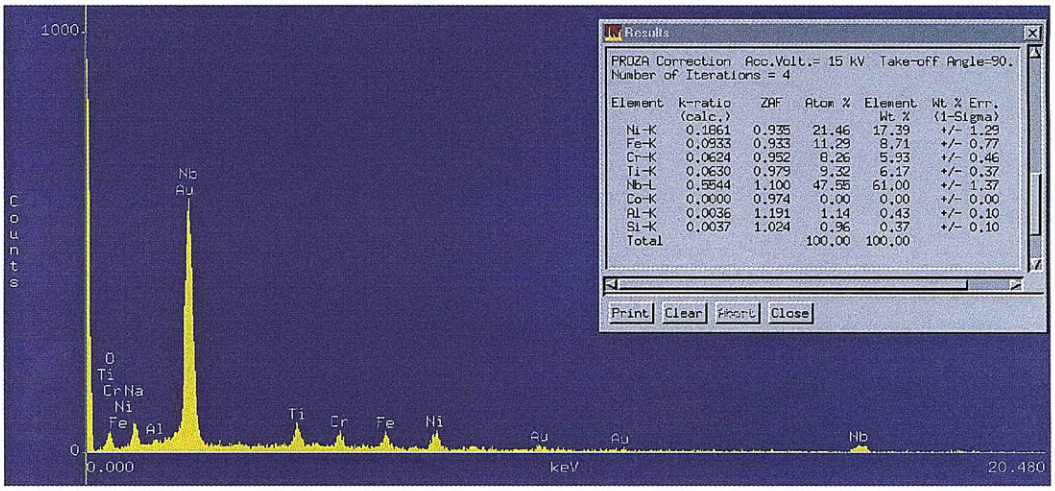

Figure C.51: EDX at 100000x a Nb-Ni Precipitate on LA2-72

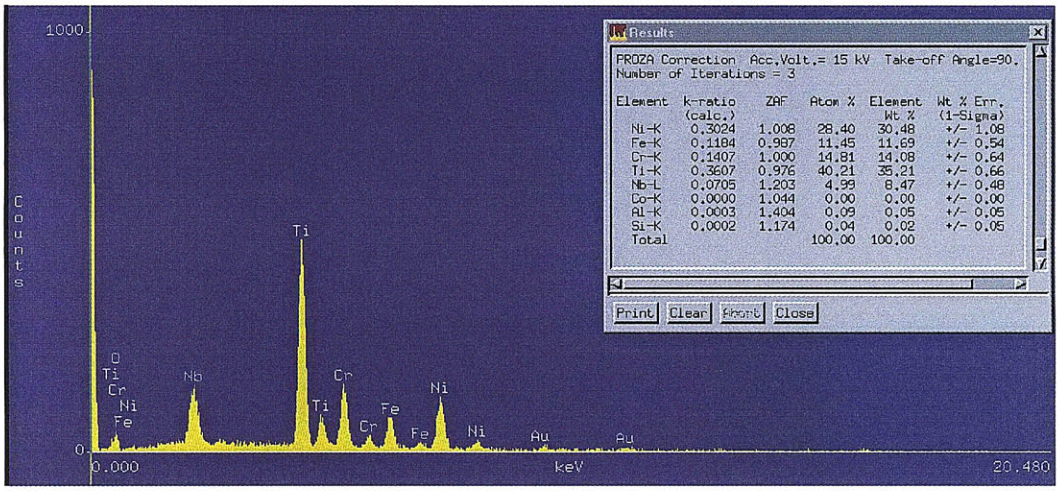

Figure C.52: EDX at 100000x a Ti-Ni-Cr-Fe Precipitate on LA2-72

LA3-72 (Inconel 718, T=750 °C, P=12.5 MPa)

Photograph of LA3-72 500 Hours

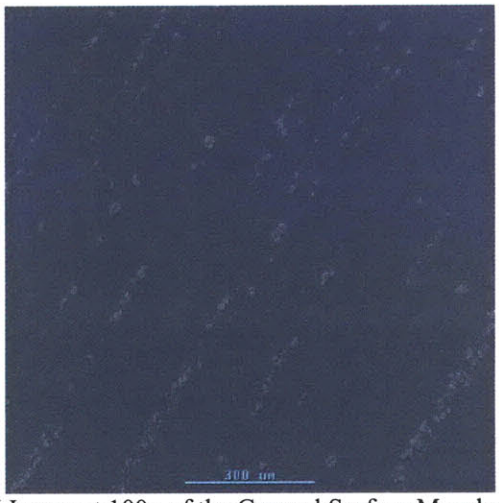

SEM Image at 100x of the General Surface Morphology

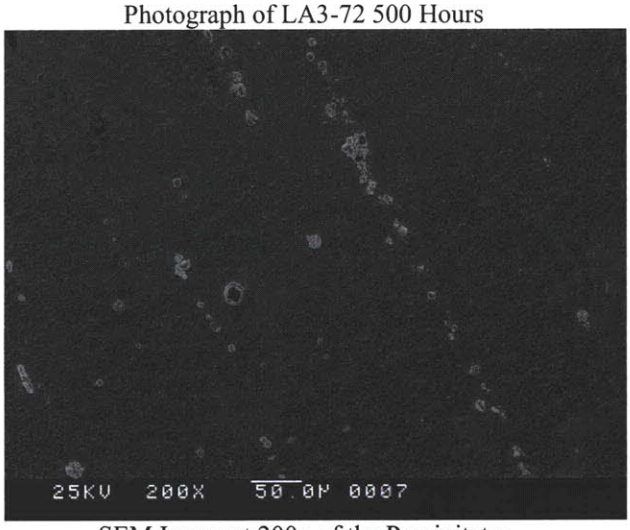

SEM Image at 200x of the Precipitates

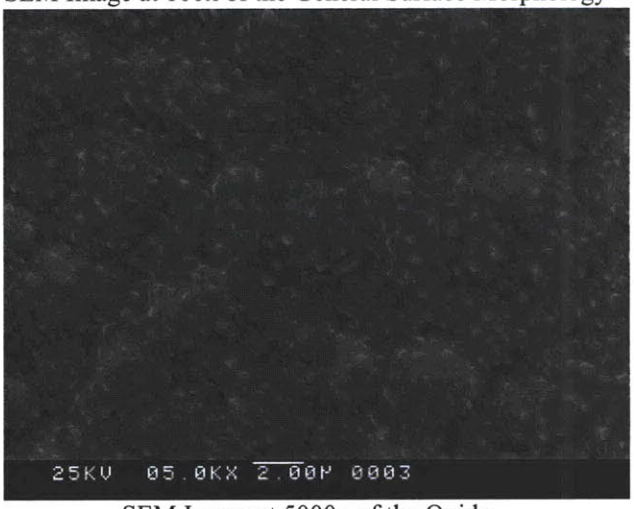

SEM Image at 5000x of the Oxide

SEM Image at 1000x of a Feature on the Oxide

Figure C.53: Surface Morphology for LA3-72 After 500 Hours of Exposure

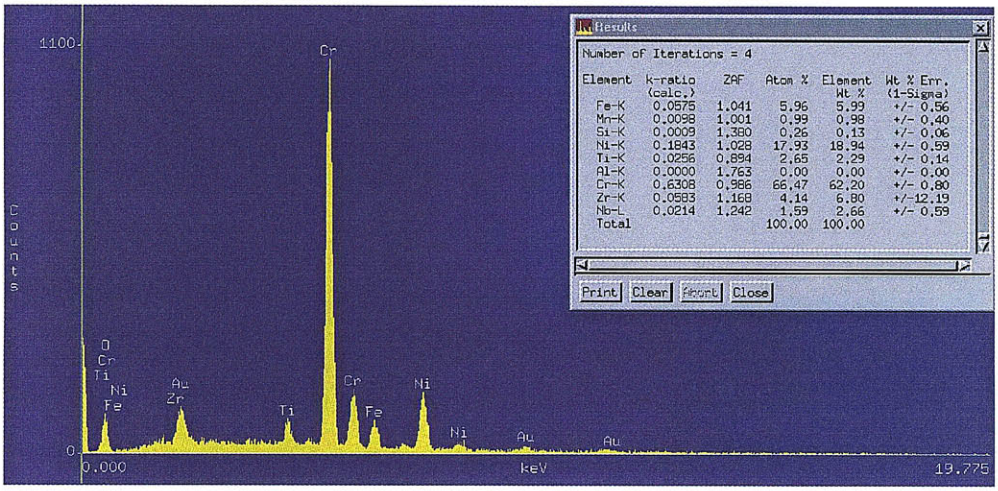

Figure C.54: EDX at 30000x of the Oxide on LA3-72

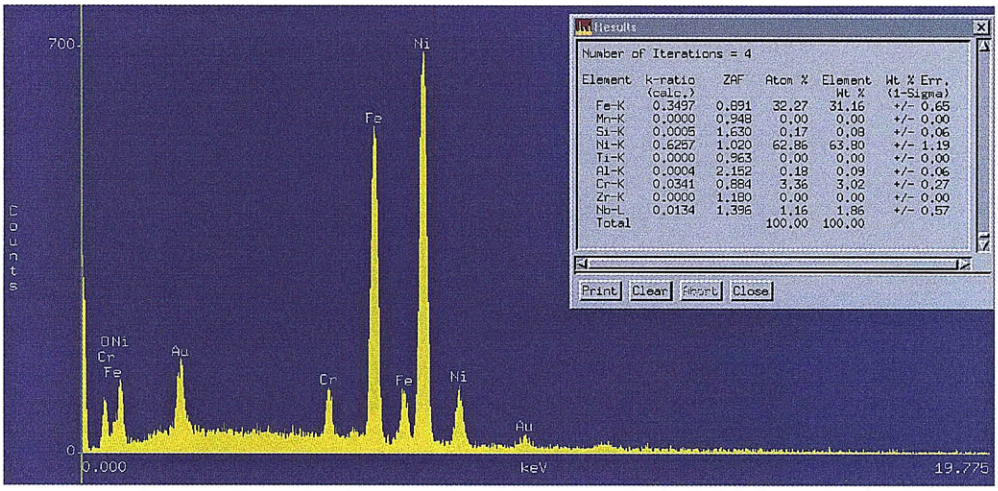

Figure C.55: EDX at 100000x of the Feature of a Feature on the Oxide on LA3-72

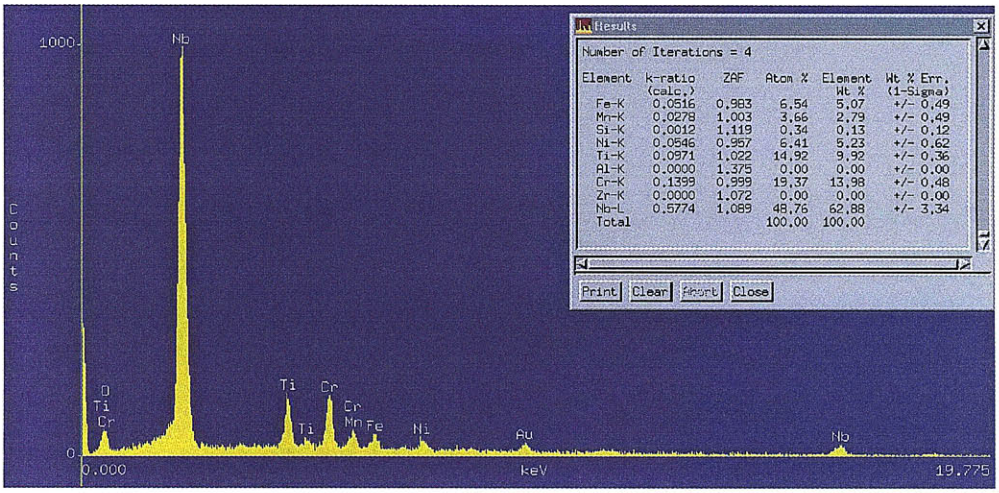

Figure C.56: EDX at 50000x of a Precipitate on LA3-72

LA3-82 (Inconel 725 (EG), T=650 °C, P=12.5 MPa)

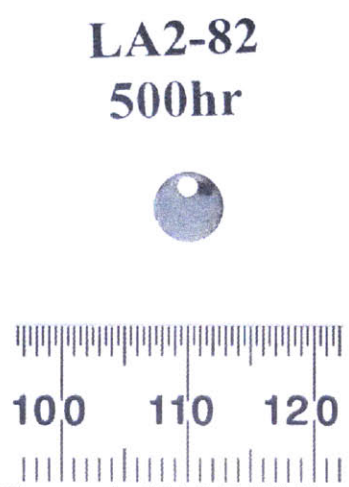

Photograph of LA2-82 500 Hours

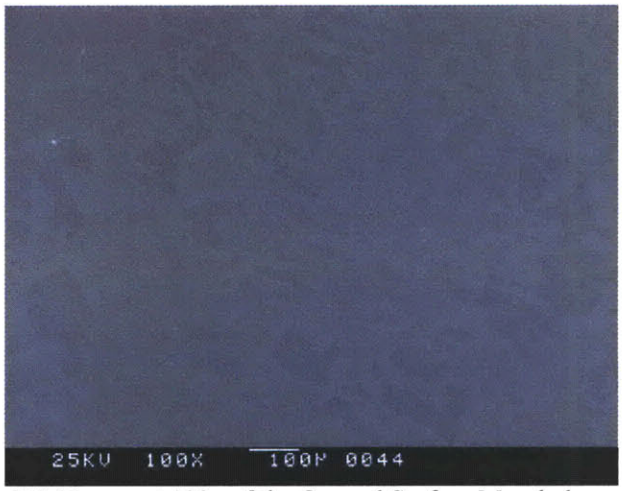

SEM Image at 100x of the General Surface Morphology

SEM Image at 1000x of the Oxide

Figure C.57: Surface Morphology for LA3-82 After 500 Hours of Exposure

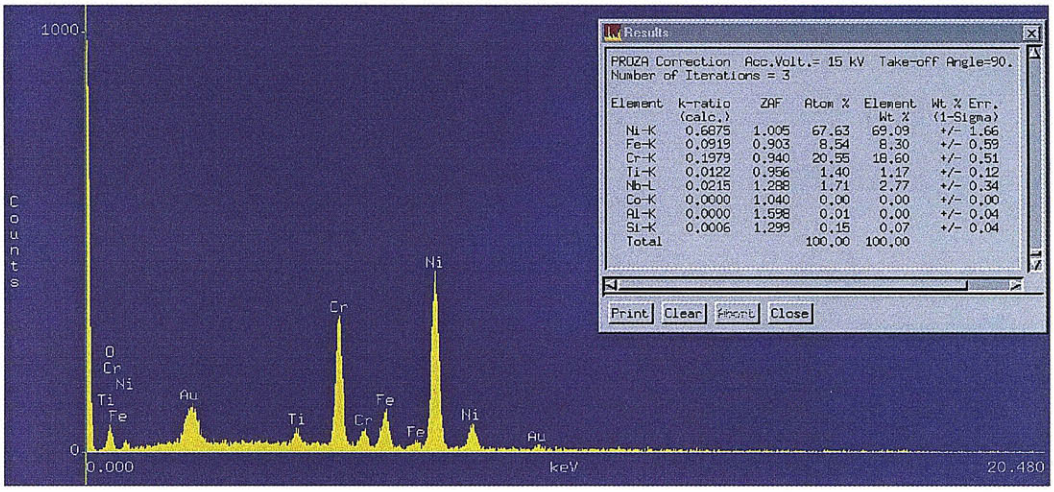

Figure C.58: EDX at 100000x of the Light Oxide on LA2-82

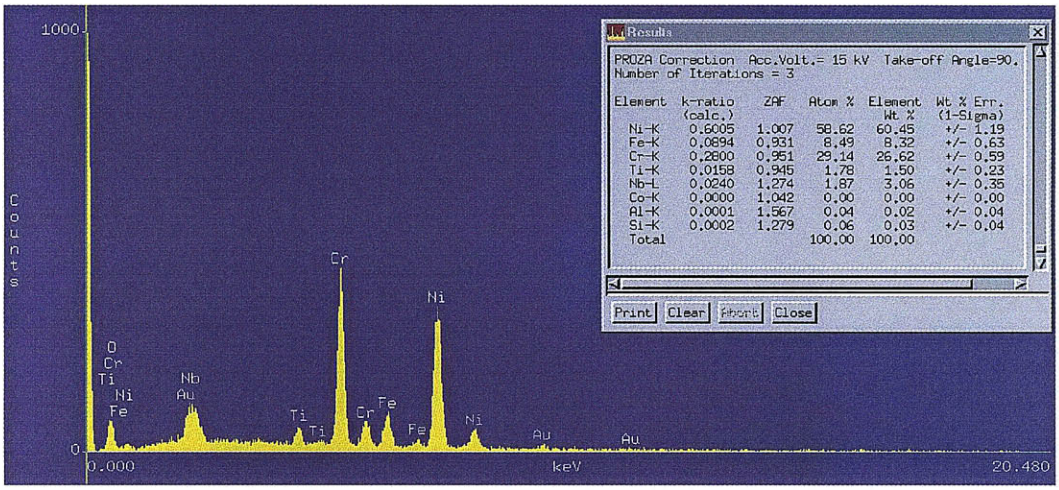

Figure C.59: EDX at 100000x of the Dark Oxide on LA2-82

LA3-82 (Inconel 725, T=750 °C, P=12.5 MPa)

Photograph of LA3-82 500 Hours

SEM Image at 100x of the General Surface Morphology

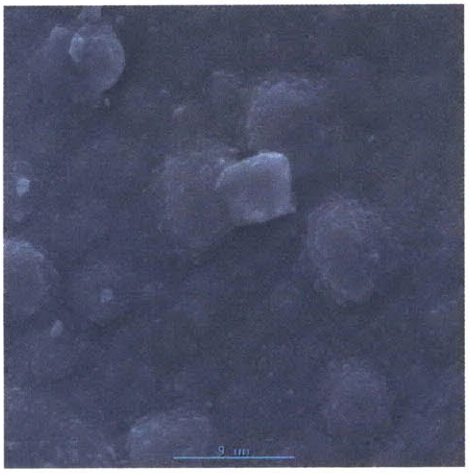

SEM Image at 4000x of a Ti-Cr Precipitate

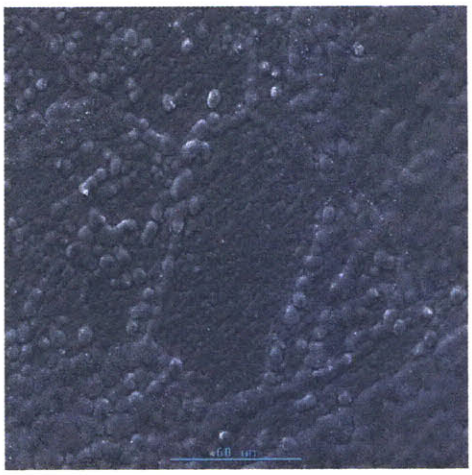

SEM Image at 400x of the Cr Enriched Grain Boundary

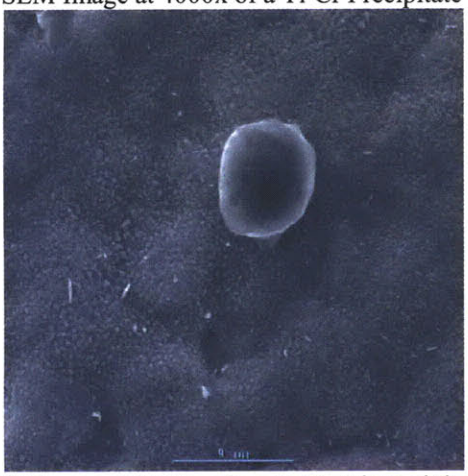

SEM Image at 2500x of an Fe-Cr-Ni Precipitate

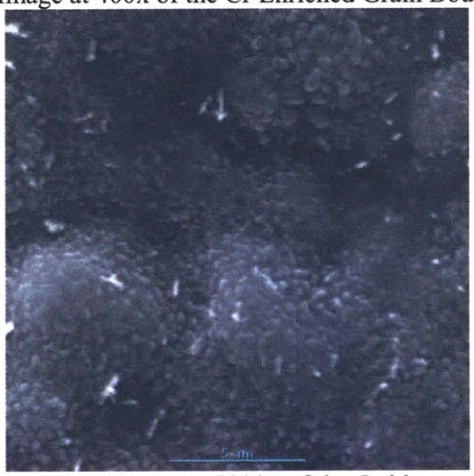

SEM Image at 5000x of the Oxide

Figure C.60: Surface Morphology for LA3-82 After 500 Hours of Exposure

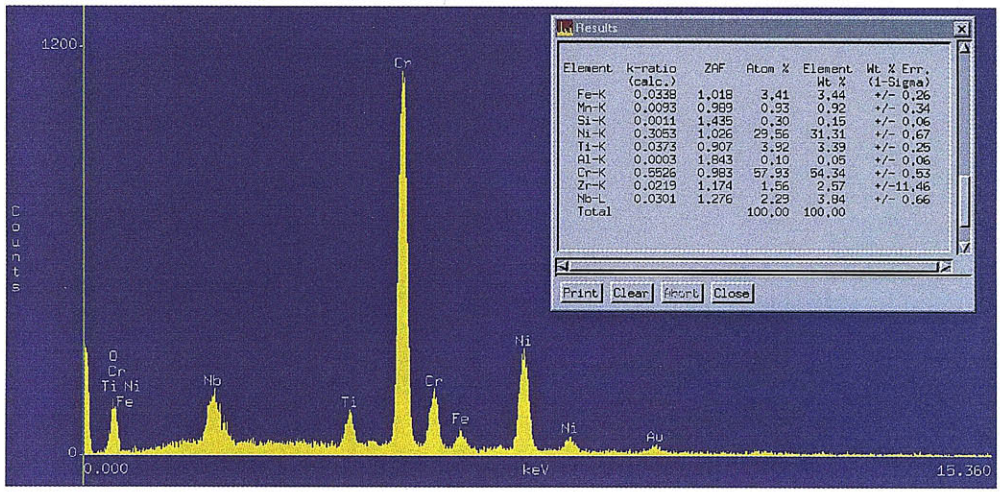

Figure C.61: EDX at 40000x of the Oxide on LA3-82

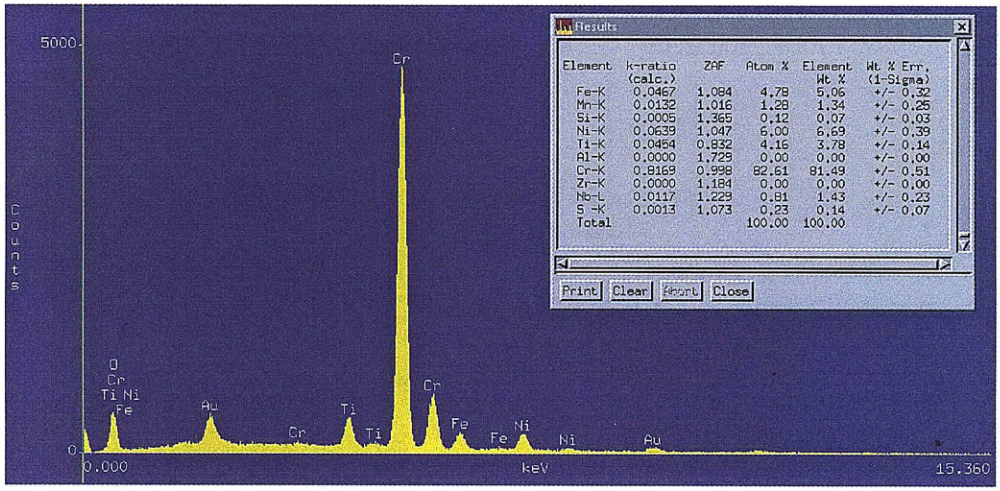

Figure C.62: EDX at 5000x of the Grain Boundary on LA3-82

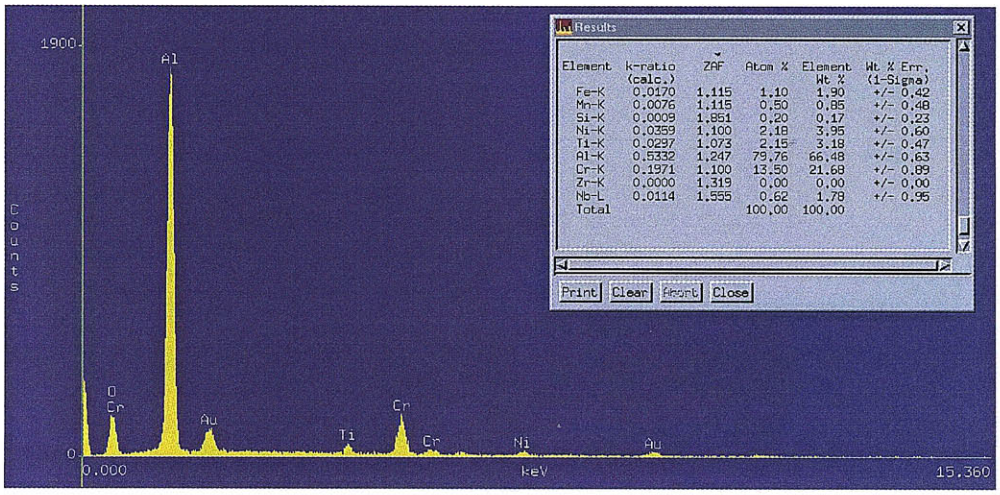

Figure C.63: EDX at 100000x of the Al-Cr Precipitates on LA3-82